UNIVERSIDADE DE LISBOA

FACULDADE DE CIÊNCIAS

Departamento de Química e Bioquímica

GALLIUM COMPOUNDS FOR THE DESIGN OF (NANO)RADIOPHARMACEUTICALS

Francisco França A. C. Silva

Doutoramento em Química

(Química Inorgânica)

2014

UNIVERSIDADE DE LISBOA

FACULDADE DE CIÊNCIAS

Departamento de Química e Bioquímica

GALLIUM COMPOUNDS FOR THE DESIGN OF (NANO)RADIOPHARMACEUTICALS

Francisco França A. C. Silva

Tese orientada pelo Dr.António Rocha Paulo e Dra.Maria Helena Garcia, especialmente elaborada para a obtenção do grau de doutor em Química Inorgânica

2014

The work described in this thesis was performed in Centro de Ciências e Tecnologias Nucleares (C^2TN) in the Campus Tecnológico e Nuclear, Instituto Superior Técnico, Universidade de Lisboa, under the supervision of Dr. António Rocha Paulo and Dra. Maria Helena Garcia of the Faculdade de Ciênicas, Universidade de Lisboa. This work also involved the collaboration of the Department of Radiology of the University of Missouri, Columbia, USA, with Dr. Raghuraman Kannan.

Acknowledgements

I would like to thank Dr.António Paulo for being my PhD supervisor. I am very grateful for his dedication, guidance and thoroughness in every stage of my PhD.

To Prof.Helena Garcia, I thank her for accepting to be responsible for this PhD thesis in the Faculty of Sciences of the University of Lisbon.

To Dr.Raghuraman Kannan, I am very grateful for the opportunity I had to work at the Allton laboratory and the great hospitality during my stay abroad.

I thank Dra.Isabel Santos for the opportunity to do my PhD at C^2TN at CTN/IST.

I would like to thank Paula Campello, Célia Fernandes and Dra.Lurdes Gano for all the help they have provided during the course of this PhD, as well as for their friendship.

I thank Ajit Zambre for all the support and friendship. To everyone else in the Allton laboratory in Columbia, I am very grateful for their hospitality.

To Sofia and Filipa, I thank them for all the support during the course of this PhD as well as for their friendship. To everyone else in the C^2TN center, I thank their support.

Finally, to my family and friends, I thank their support during the long years of this PhD.

Abstract

The work presented in this thesis focus on the design of targeted nanosized and molecular tools, for the design of gallium radiopharmaceuticals with potential application in cancer theranostics.

The first part describes gold nanoparticles (AuNPs) stabilized with thiolated derivatives of acyclic and macrocyclic chelators, and functionalized with bioactive peptides for specific targeting of Gastrin Releasing Peptide (GRP) and Epidermal Growth Factor (EGF) receptors. For GRPr targeting, the AuNPs were decorated with a bombesin (BBN) analog and stabilized with derivatives of diethylene triamine pentaacetic acid (DTPA) or 1,4,7,10-tetraazacyclododecane-1,4,7,10-tetraacetic acid (DOTA) chelators for ^{67}Ga complexation. From the evaluated radiolabeled nanoconstructs, the ones containing a dithioctic derivative of BBN and a thiolated DOTA chelator is the most promising one for the design of ^{67}Ga (nano)radiopharmaceuticals, due to its high *in vitro*/*in vivo* stability, high cellular internalization in GRPr-positive PC3 cells, and significant tumor uptake in prostate cancer tumor xenografts. For EGFr targeting, the AuNPs were decorated with GE-11 peptide that was incorporated in a thiolated DOTA derivative. The resulting AuNPs were labeled with ^{67}Ga using pre- and post-labeling approaches. Those obtained based on the pre-labeling approach showed an enhanced *in vitro* stability towards release of ^{67}Ga while maintaining a high cellular internalization in A431 cells overexpressing EGFr.

The second part describes new N_4O_2-donor acyclic chelators of the Schiff base type and the respective reduced amines, which contain pyridyl or pyrazolyl coordinating units at the central nitrogen atom of diethylenetriamine and phenol groups introduced at the terminal amines. The Schiff bases undergo decomposition reactions, while the corresponding amine derivatives give well defined monocationic Ga(III) complexes. However, only a pyridyl-containing amine derivative was able to effectively coordinate ^{67}Ga. Biodistribution studies in mice showed that the corresponding radiocomplex displays a high *in vivo* stability and favourable pharmacokinetics, being a good candidate for further evaluation in radiopharmaceutical research.

Resumo

O objectivo deste trabalho de doutoramento consistiu no estudo de novas sondas nanométricas e moleculares para o desenho de radiofármacos de gálio com potencial aplicação na *teranóstica* do cancro. Para este efeito, a investigação desenvolvida centrou-se em dois tópicos principais. O primeiro envolveu o estudo de nanopartículas de ouro funcionalizadas com agentes quelantes e com péptidos biologicamente activos, tendo em vista obter nanoradiofármacos inovadores para entrega dirigida de gálio radioactivo a tecidos tumorais. O segundo tópico centrou-se no estudo das propriedades de coordenação de novos agentes quelantes, doadores N_2O_4, face a centros metálicos de Ga(III) com o intuito de investigar o seu interesse para a química radiofarmacêutica, nomeadamente na concepção de radiofármacos específicos ou de perfusão.

Concretamente, o primeiro tópico envolveu a síntese, caracterização e avaliação biológica de nanopartículas de ouro (AuNPs) marcadas com ^{67}Ga e funcionalizadas com análogos da bombesina (BBN) ou do péptido GE11, dirigidos aos receptores do péptido libertador da gastrina (GRPr) e do factor do crescimento epidérmico (EGFr), respectivamente, que se encontram sobre-expressos numa grande variedade de tumores. A marcação com ^{67}Ga destas AuNPs foi efectuada por complexação do radiometal com derivados do ácido dietilenotriaminopentacético (DTPA) ou do ácido 1,4,7,10-tetraazaciclododecano-1,4,7,10-tetraacético (DOTA), os quais foram ainda utilizados para estabilizar as nanopartículas.

Inicialmente, foram sintetizadas AuNPs estabilizadas com um derivado sulfurado do DTPA, designado **DTDTPA**. O **DTDTPA** contém dois grupos tiol que permitem formar ligações covalentes com os átomos de ouro à superfície das nanopartículas e simultaneamente formar grupos disulfureto, levando a um processo de catenação e à formação de uma camada polimérica de **DTDTPA**. As nanopartículas resultantes, **AuNP-DTDTPA**, apresentam um "core" de ouro esférico e de tamanho pequeno (2.28 ± 1.32 nm), tendo capacidade para coordenar Ga(III) através do revestimento de **DTDTPA**. Em solução apresentam um tamanho hidrodinâmico relativamente elevado (100.6 nm, PDI (índice de polidispersividade) = 0.111) e uma carga superficial negativa (-80.7 ± 15.6 mV). As **AuNP-DTDTPA** foram funcionalizadas com um derivado do ácido tióctico contendo a

sequência BBN[7-14] (**TA-BBN**), o que permitiu obter nanopartículas com um péptido biologicamente activo (**BBN-AuNP-DTDTPA**).

A reacção de **AuNP-DTDTPA** e **BBN-AuNP-DTDTPA** com $^{67}GaCl_3$ levou à formação das nanopartículas marcadas **AuNP-DTDTPA-^{67}Ga** e **BBN-AuNP-DTDTPA-^{67}Ga**, que foram sintetizadas com elevado rendimento e pureza radioquímica. No entanto, estas AuNPs apresentam tendência para libertar o ^{67}Ga, nomeadamente na presença de meio de cultura de células ou de *apo*-transferrina. Ensaios de internalização celular em células do carcinoma da próstata (PC3), que sobre-expressam o GRPr, indicaram uma baixa captação para ambas as AuNPs marcadas com ^{67}Ga. Estudos de biodistribuição em ratinhos Balb/c com tumor induzido, inoculados com células PC3, mostraram que **BBN-AuNP-DTDTPA-^{67}Ga** apresentam uma razoável captação tumoral (5.8 ± 0.7% I.D. (dose injectada)/g às 4 h p.i. (pós-injecção)). No entanto, esta captação pode estar relacionada com a tendência que estas AuNPs apresentam para libertar o ^{67}Ga *in vivo* com possível *trans*-quelatação para a transferrina circulante.

De forma a superar as dificuldades observadas na capacidade de coordenação ao ^{67}Ga das AuNPs estabilizadas com **DTDTPA**, decidiu explorar-se um derivado do DOTA (**TDOTA**). Esperava-se que este derivado pudesse estabilizar as nanopartículas de ouro, tendo em conta a presença de um grupo tiol na sua estrutura, e simultaneamente melhorar a capacidade de coordenação ao ^{67}Ga. As AuNPs resultantes (**AuNP-TDOTA**) também apresentam um "core" de ouro esférico pequeno (4.29 ± 1.60 nm) mas, comparativamente a **AuNP-DTDTPA**, têm um tamanho hidrodinâmico significativamente maior (489.3 nm, PDI = 0.520) e uma carga negativa menor (-20.4 ± 5.5). **AuNP-TDOTA** foram funcionalizadas com **TA-BBN** e com outro derivado da BBN (**C-KKK-BBN**) que apresenta uma cisteína terminal para ligação covalente à superficie das nanopartículas de ouro. A conjugação destes péptidos biologicamente activos a **AuNP-TDOTA** foi efectuada com sucesso, tendo levado à formação de AuNPs funcionalizadas designadas por **BBN-AuNP-TDOTA** e **CBBN-AuNP-TDOTA**, respectivamente.

A marcação com ^{67}Ga de **AuNP-TDOTA**, **BBN-AuNP-TDOTA** e **CBBN-AuNP-TDOTA** foi efectuada com elevado rendimento radioquímico e permitiu obter as nanopartículas **AuNP-TDOTA-^{67}Ga**, **BBN-AuNP-TDOTA-^{67}Ga** e **CBBN-AuNP-TDOTA-^{67}Ga**, respectivamente. As AuNPs estabilizadas com **TDOTA** apresentam, comparativamente às AuNPs congéneres estabilizadas com **DTDTPA**, uma capacidade significativamente superior para manter a coordenação ao ^{67}Ga em condições fisiológicas.

Nos ensaios de internalização celular realizados com células PC3, destacaram-se as nanopartículas **BBN-AuNP-TDOTA-^{67}Ga** com uma elevada percentagem de radioactividade internalizada (≈ 25% aos 15 min). Estudos de biodistribuição demonstraram uma moderada captação tumoral para **BBN-AuNP-TDOTA-^{67}Ga** e **CBBN-AuNP-TDOTA-^{67}Ga** (3.7 ± 0.5% e 3.3 ± 0.8% I.D./g às 24 h p.i., respectivamente) em ratos Balb/c inoculados com células PC3. No entanto, também foi observada uma elevada acumulação no fígado, baço e pulmões, muito provavelmente devido ao elevado tamanho hidrodinâmico destas nanopartículas.

Com o intuito de desenvolver nanopartículas dirigidas ao EGFr, explorou-se um conjugado peptídico derivado do GE11 (**TA-GE11-DOTA**), o qual possui um grupo tióctico que permite a ligação à superfície das nanopartículas de ouro e um grupo quelante do tipo DOTA para complexação de Ga(III). Inicialmente, utilizaram-se AuNPs estabilizadas com citrato para conjugação do **TA-GE11-DOTA** e de polietilenoglicol (PEG). As AuNPs obtidas (**PEG-AuNP-GE11-DOTA**) apresentam um "core" de ouro esférico de 11.99 ± 1.49 nm e um tamanho hidrodinâmico razoavelmente baixo (49.3 nm, PDI = 0.382), em particular quando comparado com as AuNPs estabilizadas com **DTDTPA** e **TDOTA**. No entanto, não foi possível marcar **PEG-AuNP-GE11-DOTA** com ^{67}Ga com um rendimento radioquímico adequado, muito provavelmente devido à baixa concentração de **TA-GE11-DOTA** à superfície das AuNPs.

Alternativamente, decidiu utilizar-se **AuNP-DTDTPA** para conjugação do **TA-GE11-DOTA**, com o objectivo de sintetizar AuNPs com afinidade e especificidade para o EGFr e, simultaneamente, contendo unidades DOTA para obtenção de uma complexação estável do ^{67}Ga. As AuNPs sintetizadas, designadas **DTAu-GE11-DOTA**, apresentam um tamanho hidrodinâmico (167.2 nm, PDI = 0.228) e uma carga superficial (-53.1 ± 10 mV) muito próximos dos verificados para **BBN-AuNP-DTDTPA**. A marcação directa de **DTAu-GE11-DOTA** com ^{67}Ga foi efectuada com sucesso e conduziu às nanopartículas marcadas **Post-DTAu-GE11-DOTA-^{67}Ga**. Paralelamente, explorou-se ainda uma estratégia de pré-marcação. Neste caso, o composto **TA-GE11-DOTA** foi marcado com ^{67}Ga e conjugado posteriormente a **AuNP-DTDTPA**, obtendo-se, com sucesso, **Pre-DTAu-GE11-DOTA-^{67}Ga**.

Ensaios de estabilidade *in vitro* de **Post-DTAu-GE11-DOTA-^{67}Ga** e **Pre-DTAu-GE11-DOTA-^{67}Ga** demonstraram que as primeiras têm uma tendência relativamente elevada para libertar o ^{67}Ga, de forma semelhante ao comportamento previamente

observado para **BBN-AuNP-DTDTPA-^{67}Ga**. Pelo contrário, **Pre-DTAu-GE11-DOTA-^{67}Ga** possui uma estabilidade muito favorável. Estes resultados sugerem que o ^{67}Ga se apresenta coordenado preferencialmente pelas unidades de **DTDTPA**, no caso de **Post-DTAu-GE11-DOTA-^{67}Ga**, enquanto para **Pre-DTAu-GE11-DOTA-^{67}Ga** essa coordenação é efectuada pelo DOTA.

Ensaios de internalização celular de **Post-DTAu-GE11-DOTA-^{67}Ga** e **Pre-DTAu-GE11-DOTA-^{67}Ga** em células do carcinoma cervical (A431), que sobre-expressam o EGFr, mostraram que estas nanopartículas apresentam uma elevada percentagem de radioactividade internalizada (72.1% e 35.7% às 3 h, respectivamente). Ensaios de internalização celular com bloqueio simultâneo com EGF não afectaram a internalização de **Post-DTAu-GE11-DOTA-^{67}Ga** mas conduziram a um decréscimo moderado no caso de **Pre-DTAu-GE11-DOTA-^{67}Ga**. Este resultado sugere que a internalização destas últimas é mediada, em parte, pela interacção com o EGFr. Estudos de biodistribuição de **Pre-DTAu-GE11-DOTA-^{67}Ga** e **Post-DTAu-GE11-DOTA-^{67}Ga** em ratinhos normais indicaram que as primeiras apresentam um perfil de biodistribuição mais favorável, em particular uma eliminação da corrente sanguínea mais rápida (1.3 ± 0.1 *vs*. 5.0 ± 0.1 %I.D./g à 1 h p.i.), surgindo como as mais promissoras para desenvolvimento de nanoradiofármacos dirigidos ao EGFr.

A parte final desta tese descreve a síntese e caracterização de agentes quelantes dadores N_4O_2, do tipo base de Schiff (**H_2L^1** e **H_2L^3**) e respectivos análogos reduzidos (**H_2L^2** e **H_2L^4**). Estes agentes quelantes foram desenhados com base na estrutura da dietilenotriamina (dien), com a introdução de braços pirazolo ou piridilo na amina central e de grupos fenol nas aminas terminais. Esperava-se obter novos ligandos adequados para estabilização de centros metálicos de Ga(III) e com interesse para desenho de radiofármacos de ^{67}Ga/^{68}Ga.

Estudaram-se reacções dos compostos **H_2L^1**-**H_2L^4** com $Ga(NO_3)_3$ em metanol, com o objectivo de avaliar a sua capacidade de coordenação face ao ião metálico Ga(III). Verificou-se que as bases de Schiff (**H_2L^1** e **H_2L^3**) apresentam tendência para sofrer processos de hidrólise. No entanto, no caso de **H_2L^1** foi possível isolar o complexo **$GaL^{1,OMe}$** que contém um ligando hexadentado do tipo hemiaminal, como resultado do ataque do metanol a um dos grupos imina. No caso dos correspondentes ligandos amina

(**H_2L^2** e **H_2L^4**), as reacções levaram à formação dos complexos esperados (**GaL^2** e **GaL^4**), que foram caracterizados pela análise por difracção de raios-X de cristal único e pelas técnicas espectroscópicas usuais em Química Inorgânica. Estudos de RMN multinuclear, incluindo experiências bidimensionais e a temperatura variável, confirmaram que o complexo **GaL^4**, contendo um ligando com um braço coordenante piridilo, existe em solução como uma mistura de isómeros de coordenação. Pelo contrário, para o complexo congénere **GaL^2**, contendo um braço pirazolilo, foi detectada a presença de um único isómero.

Foi estudada a reacção de **H_2L^2** e **H_2L^4** com ^{67}Ga, ao nível *carrier-free*. Somente **H_2L^4** permitiu obter o radiocomplexo pretendido, **$^{67}GaL^4$**, com um rendimento radioquímico adequado (> 95%). A identidade química de **$^{67}GaL^4$** foi confirmada por comparação do seu comportamento em HPLC com o complexo correspondente sintetizado ao nível macroscópico com gálio natural. **$^{67}GaL^4$** apresenta uma estabilidade elevada, *in vitro* e *in vivo,* e uma biodistribuição e farmacocinética favoráveis com uma taxa de excreção elevada e uma rápida eliminação sanguínea. Estas características incentivam uma investigação mais aprofundada desta nova classe de agentes quelantes no âmbito da química radiofarmacêutica do gálio.

Keywords

Gold nanoparticles

Gallium

Polydentate Chelators

Bombesin Analogs

GE11 derivatives

Radiopharmaceuticals

Cancer Theranostic

Palavras-Chave

Nanopartículas de Ouro

Gálio

Agentes Quelantes Polidentados

Análogos da Bombesina

Derivados do GE11

Radiofármacos

Teranóstica do Cancro

General Index

Figures

Tables

Schemes

List of Symbols and Abreviations

A

α	Alpha
AAS	Atomic Absorption Spectrometry
AuNP	Gold Nanoparticle

B

β	Beta
b	Broad
BBN	Bombesin
BOC	Tert-Butyloxycarbonyl

C

CHN	Elemental Analysis
CME	Clathrin Mediated Endocytosis
COSY	Correlation Spectroscopy
CT	Computed Tomography

D

d	Doublet
$D_{o/w}$	Partition Coefficient
DLS	Dynamic Light Scattering
DMF	Dimethylformamide
DOTA	1,4,7,10-Tetraazacyclododecane-1,4,7,10-Tetraacetic Acid
DTDTPA	Dithiol Diethylene Triamine Triacetic Acid
DTPA	Diethylene Triamine Pentaacetic Acid

E

EDS	Energy Dispersive X-ray
EELS	Electron Energy Loss Spectroscopy
EGF	Epidermal Growth Factor
EGFr	Epidermal Growth Factor Receptor
EPR	Enhanced Permeability Retention
EtOH	Ethanol

ESI-MS Electronspray Ionisation – Mass Spectrometry

G

γ Gamma

GRP Gastrin Releasing Peptide

GRPr Gastrin Releasing Peptide Receptor

H

HAADF High Angle Annular Dark Field

HCl Hydrochloric Acid

HPLC High Performance Liquid Chromatography

HR High Resolution

HSQC Heteronuclear Single Quantum Coherence

I

IC_{50} Half Maximal Inhibitory Concentration

ICP-OES Inductively Coupled Plasma – Optical Emission Spectrometry

I.D. Injected Dose

IR Infrared

i.p. Intraperitoneal

ITLC-SG Instant Thin Layer Chromatography – Silica Gel

i.v. Intravenous

M

m Multiplet

MeOH Methanol

MRI Magnetic Resonance Imaging

MTT 3-(4,5-Dimethylthiazol-2-yl)-2,5-diphenyltetrazolium bromide

N

NMR Nuclear Magnetic Resonance

NOE Nuclear Overhauser Effect

NOESY Nuclear Overhauser Effect Spectroscopy

NP Nanoparticle

NTA	Nanoparticle Tracking Analysis

O

OI	Optical Imaging
o.n.	Overnight

P

PBS	Phosphate Buffered Saline
PEG	Polyethylene Glycol
PET	Positron Emission Tomography
p.i.	Post-Injection

R

RES	Reticuloendothelial System
RP-TLC	Reverse Phase – Thin Layer Chromatography
R_f	Retention Factor
r.t.	Room Temperature

S

s	Singulet
SD	Standard Deviation
SPECT	Single-Photon Emission Cumputed Tomography
STEM	Scanning Transmission Electron Microscopy

T

t	Triplet
$T_{1/2}$	Half-life
TA	Thioctic Acid
TEM	Transmission Electron Microscopy
Tf	Transferrin
TFA	Trifluoracetic Acid
THF	Tetrahydrofuran

TLC	Thin Layer Chromatography
TOCSY	Total Correlation Spectroscopy
t_R	Retention Time

U

UV-Vis	Ultraviolet – Visible

X

XPS	X-ray Photoelectron Spectroscopy

Chapter 1: Introduction

1.1 Aim and Scope of the Thesis

Molecular imaging is nowadays recognized as a very important tool in all stages of cancer management. The development of molecular imaging over the years allowed the introduction of more efficient and faster cancer diagnosis techniques, making it crucial for the successful diagnosis, treatment and follow up of this malignant disease. Among the available molecular imaging techniques, nuclear imaging is an expanding field that has contributed greatly for cancer diagnosis, through the use of the non-invasive modalities Single Photon Emission Computed Tomography (SPECT) and Positron Emission Tomography (PET).

The development of nuclear imaging techniques has been closely accompanied by the discovery of new agents and strategies for cancer treatment. In the past, these two areas of cancer management, diagnosis and therapy, have mostly followed a parallel course of development, being developed agents solely for diagnosis or therapy.

Nowadays, there is an increasing interest in merging diagnostic and therapeutic functions in the same tool, which is on the basis of a new field in contemporary biomedical research designated as theranostics. Combining diagnosis and therapy in a single tool allows for the possibility of acquiring real time information on the effects, either positive or negative, of therapeutic agents when administered to patients. Hence, theranostics can pave the way to make personalized medicine a reality.

In this context, nanoparticles have emerged as a boon for theranostics, due to their unique and versatile ability to combine in the same tool therapeutic and diagnostic functions. Many nanoparticles already display therapeutic or diagnostic properties but, in addition, well-developed surface chemistry enables an easy loading with different targeting/(radio)pharmaceutical agents. In particular, radiolabeled nanoparticles can be among the most relevant theranostic tools to foster the progress on cancer management in the early 21st century, profiting from the great variety of medically relevant radioisotopes available for nuclear imaging and/or therapy.

This PhD work has been developed within this area of research, and its main goal was to introduce new nano and molecular tools for the coordination and delivery of gallium radionuclides ($^{67/68}$Ga) relevant for SPECT and PET imaging. To achieve this goal the performed research work was focused in the two following topics: 1) Radiolabeled gold nanoparticles functionalized with bioactive peptides for tumor targeting; 2) Design of new molecular chelators for stable complexation of radiogallium.

The first topic was focused on the study of different gold nanoparticles (AuNPs) containing acyclic or macrocyclic polyaminocarboxylic chelators for gallium coordination, and bombesin analogs or GE11 peptide derivatives for the targeting of gastrin releasing peptide receptors (GRPr) or epidermal growth factor receptors (EGFr), respectively, which are overexpressed in different tumor cells. In this way, it was expected to obtain novel platforms suitable for specific targeting of cancer and for the design of potential theranostic agents.

The second topic involved the evaluation of the coordination capability towards Ga(III) for new families of N_4O_2-donor acyclic ligands, bearing two phenolate coordinating groups and a N-heterocyclic pendant arm of the pyridyl and pyrazolyl type. This basic-applied research was expected to identify new chelator systems suitable for the design of perfusion or target-specific gallium radiopharmaceuticals, a subject of great importance in contemporary radiopharmaceutical sciences.

Altogether, the work described in this PhD thesis intended to obtain chemical, radiochemical and biological scientific knowledge useful for the design of innovative gallium (nano)radiopharmaceuticals for diagnostics of cancer.

1.2 Cancer

1.2.1 Incidence

Cancer is one of the leading causes of death worldwide. The European Cancer Observatory (ECO) has estimated that in 2012 over 1.9 million people in Europe were diagnosed with cancer, and the total mortality was over 975 thousand. The most incident types of cancer are, prostate cancer for men, and breast cancer for women (Figure 1.1); in 2012, over 416 thousand cases of prostate cancer, and over 463 thousand of breast cancer, were reported.[1]

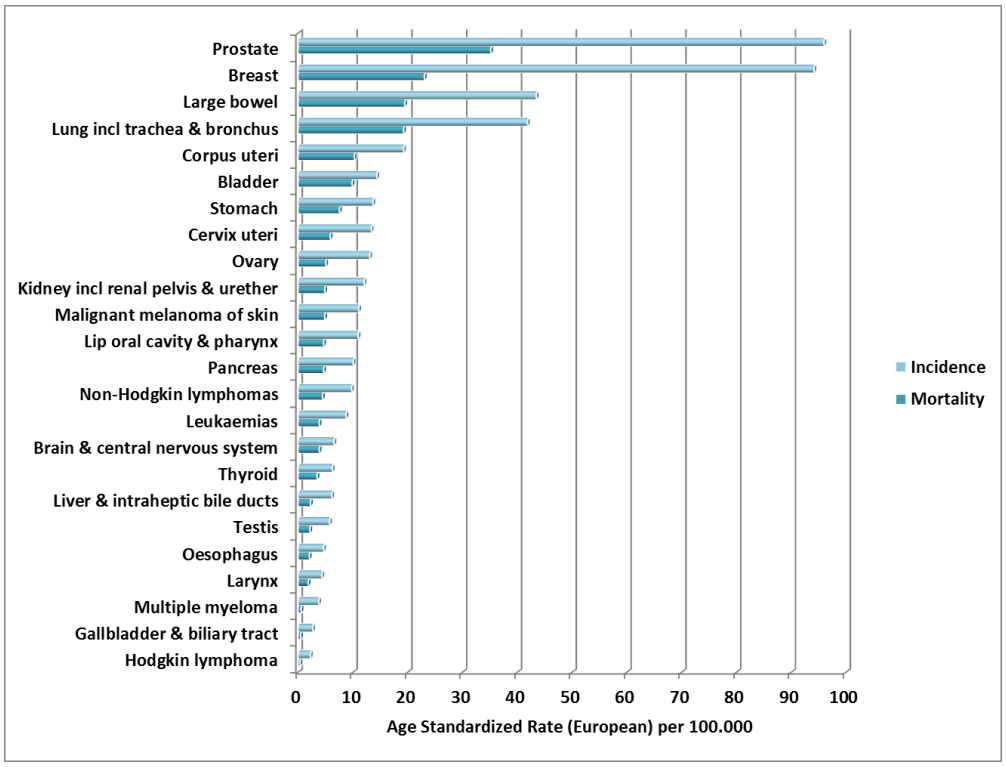

Figure 1.1: *Estimated incidence and mortality for both sexes in Europe, 2012, for different cancers.*

The International Agency for Research on Cancer (IARC) estimates that by 2030, the global incidence is expected to grow to 21.4 million new cancer cases per year with 13.2 million cancer deaths, based on the growth and aging of the population, and taking into account reductions in childhood mortality and deaths from infectious diseases.[2]

There has been some progress in the overall control of cancer cases in the latest decades, with better cancer screening and early detections, and improved and targeted cancer therapies. As a result, patients are surviving longer. But despite this achievement, the incidence of some cancers is still increasing, to the point that it is overwhelming much of the progress that has been made. It is therefore crucial to develop new and efficient drugs and methodologies for cancer diagnosis and therapy in order to effectively control this malignant disease.

1.2.2 Etiology and Biology of Cancer

Cancer is a class of diseases characterized by an up-regulated biological process of cell growth. In fact, growth factors are synthesized by cells in order for these to replicate, and when there is no need for further replication, these growth factors are

inhibited; cancer cells, however, lose the need for growth factors and therefore replicate constantly, and consequently, they do not behave as part of the tissue and become independent cells.[3]

This increased and uncontrolled cell growth generally leads to the formation of lumps or masses of tissue called tumors, which can grow and interfere with different biological functions from the digestive, nervous, circulatory systems, and can even release hormones that alter body function.[4]

There are over 100 different types of cancer, and each is classified by the type of cell that is initially involved. Cancer represents a heterogeneous population of diverse diseases, and recent advances have shed further insight on the molecular heterogeneity found between cancers of the same type, between a primary tumor and its metastases, and even between the cells that constitute individual tumors. Since a multitude of cancer phenotypes exist within a given tumor, there is a large probability for subpopulations of cancer cells to evade monotherapy. This molecular diversity, combined with the prevalence of resistant phenotypes of cancer cells towards treatment, is a major challenge when facing this disease.[5]

Tumors also possess different physicochemical properties and physiology when compared with normal tissues. For instance, normal cells have contact inhibition, that is, they respond to contact with other cells by ceasing their division. Hence, they can divide to fill in a gap, but stop dividing as soon as there are enough cells to fill that gap; this characteristic is not present in cancer cells, leading to a continuous growth, even when in contact with other cells, which generally causes the formation of tumors.[6,7] Consequently, the vascularization of tumors is heterogeneous. Some regions display a very low presence of blood vessels leading to signs of necrosis and hemorrhages. Other regions have a very high vascularized system, due to the formation of new blood vessels (angiogenesis) to increase the supply of nutrients and oxygen for the rapid tumor growth.[8] Compared to normal physiological blood vessels, those generated by tumor angiogenesis present several abnormalities, such as high proportion of proliferating endothelial cells, low linearity of the vessels, deficiency in pericytes (contractile cells that wrap around the endothelial cells of capillaries and venules throughout the body) and an abnormal basement membrane formation (Figures 1.2 and 1.3).[9-11]

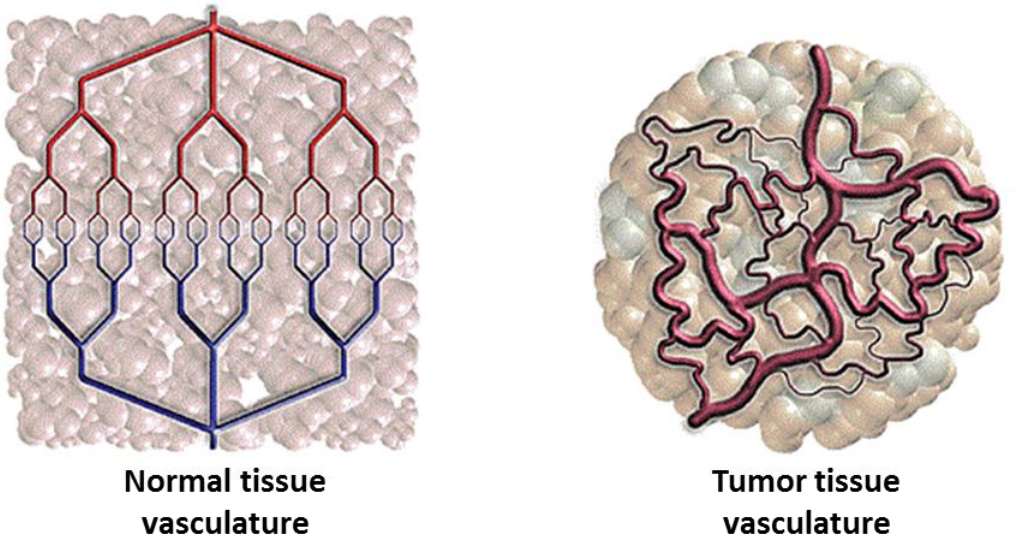

Figure 1.2: *Normal tissue vasculature vs tumor tissue vasculature.*[12]

Macromolecular transport pathways across these tumor vessels have been shown to occur via open gaps, vesiculo vacuolar organelles and fenestrations. It is known that normal tissues have tight, continuous vessel walls generally with pores of approximately 9 nm in diameter, and only a few 50 nm pores. This allows for an easy penetration of small molecules into tissues in contrast to large molecules, such as polymers and nanoparticles. On the other hand, tumor tissues, and even inflammatory tissues and organs with rich reticuloendothelial system (RES) (i.e. liver, spleen), generally display pores of 100 nm or wider diameters, because of their discontinuous capillary walls that have no basal lamina.[13,14]

Another significant difference between tumor tissues compared to normal ones is their interstitium. The interstitial compartment of tumors is generally large, with high collagen content, low proteoglycan and hyaluronate concentrations, and absence of anatomically well-defined functioning lymphatic network (Figure 1.3). These factors are responsible for a high interstitial pressure and bulk fluid flow, as well as high effective interstitial diffusion coefficient of macromolecules. Therefore, the transport of an anticancer drug for instance, is not only dependent on the physicochemical properties of the molecule, but also on the physiological properties of the interstitium.[14,15]

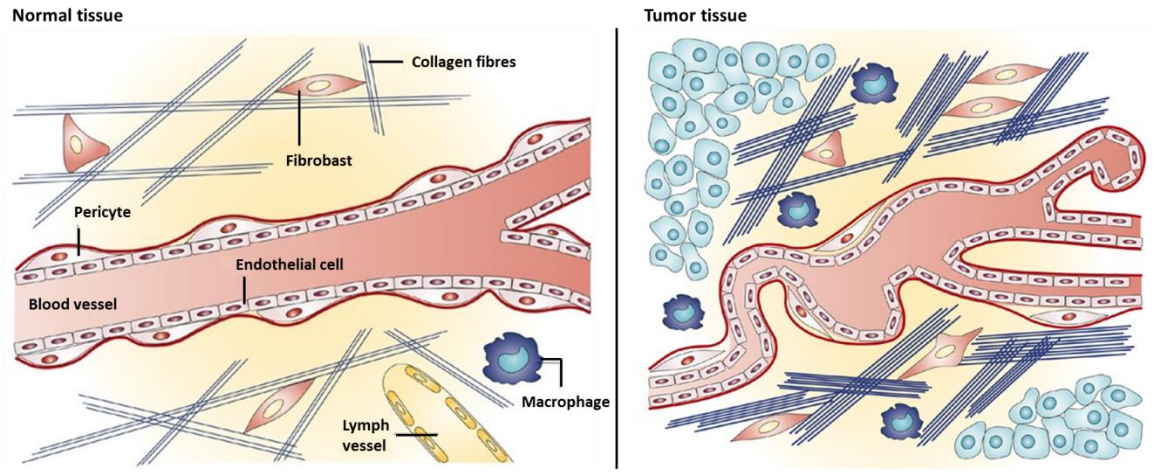

Figure 1.3: *Physiology of normal tissue* vs *tumor tissue.*[16]

1.2.3 Cancer Biomarkers and Cancer Targeting

Identifying cellular markers and understanding their relevance in cancer is a very crucial process in drug development. There are different types of known biomarkers related to cancer, such as a single gene, a gene product, or a molecular signaling pathway that have been identified on the basis of genetic analysis or biological observations (Figure 1.4). Cytogenetic and cytokenetic markers are derived from structural and numerical alterations in the chromosomes; genetic markers are, as the name implies, related with alterations at the gene level, which can lead to a gain or loss of the gene function. Modification of genes and their functional products can also occur by epigenetic modifications that alter the gene function itself. Cancer cells are known to release different proteins or other biomolecules into circulation, which can also be explored as biomarkers, like Prostate Specific Antigen (PSA) and Carcinoembryonic Antigen (CEA), among others.[17,18]

A great number of biomarkers are known but, not all of them are suitable as potential biological targets for cancer management. A biomarker is essentially a characteristic that can be measured and evaluated as an indicator of a biological process, while a target is a biological entity (e.g. enzymes, ion channels, receptors, and even DNA) to which another entity, like a drug, can be directed to and/or bind to it.[18]

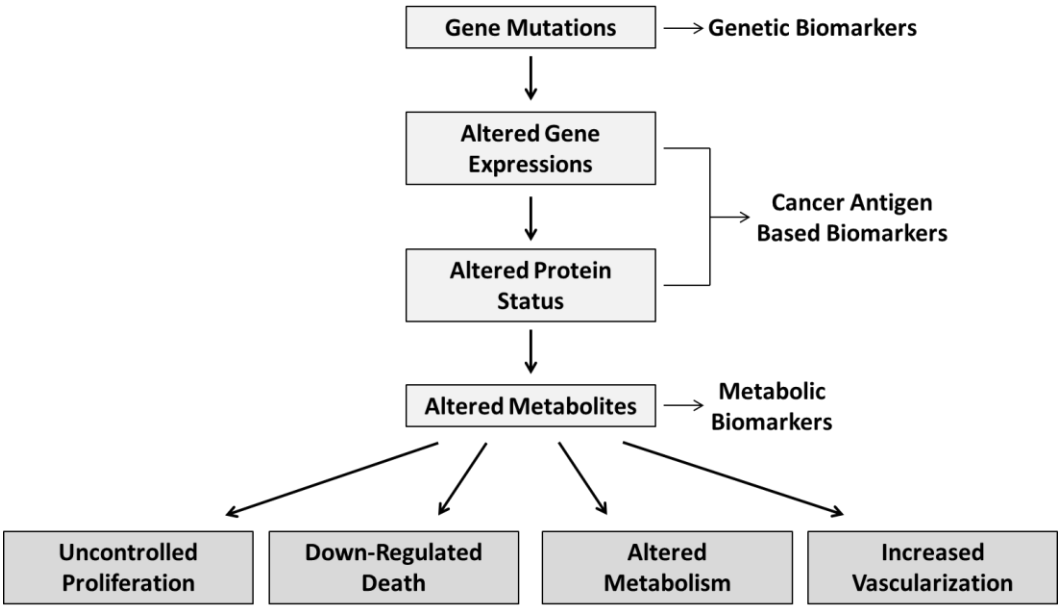

Figure 1.4: *The process of carcinogenesis and different types of biomarkers associated with cancer.*[17]

In drug development there is a great focus on exploiting membrane receptors for targeted therapy and imaging. These receptors are overexpressed in cancer cells, which make them potential molecular targets to enhance selectivity and signal of imaging techniques and/or mediate the action of anticancer agents. Relevant examples of membrane receptors include, Gastrin Releasing Peptide (GRP) receptors, Epidermal Growth Factor (EGF) receptors, integrin receptors, α-Melanocyte-Stimulating Hormone (α-MSH) receptors, somatostatin (sst) receptors, among others (Table 1.1). These receptors can be targeted with biomolecules that have high affinity and/or specificity towards them, like antibodies or peptides.[19-22]

Small peptides have attracted a lot of attention as biological vectors for the specific targeting of membrane receptors overexpressed in tumor cells, either for diagnosis or therapy. The biological action of the peptides is mediated upon binding with high affinity to specific receptors, which facilitates its retention in the receptor-expressing tissues. Receptor-binding peptides can be characterized into two categories: agonists and antagonists; upon binding of an agonist peptide the receptor is activated and a biological response is produced, whereas an antagonist peptide blocks the action of the receptor.[23,24] Earlier studies were mostly focused on agonist peptides due to their efficient internalization

into the cells; however, recent cases have shown that antagonist peptides can display higher levels of cellular uptake compared with its agonist analogs.[25,26]

Table 1.1: *Selected examples of membrane receptors and expressing tumor types.*[20-22]

Membrane receptors	Receptor subtypes	Expressing tumor type
Somatostatin	sst1, sst2, sst3, sst4 and sst5	Neuroendocrine tumor, adenoma, glioma
Bombesin/gastrin-releasing peptide (GRP)	BB1, BB2, BB3 and BB4	Renal cell, breast and prostate carcinomas
Neurotensin	NTR1, NTR2 and NTR3	Neuroblastoma, small cell lung, pancreatic and colonic cancers
Integrin	$\alpha_v\beta_3$	Melanoma, Breast and prostate carcinoma
EGF	EGFR, HER2, HER3 and HER4	Glioblastoma, lung and colon cancers
α-MSH	MC1, MC3, MC4 and MC5	Melanoma

For drug development, peptides display some distinct advantages over proteins and antibodies: i) they are small sized and easier to prepare; ii) more resistant to degradation in harsh conditions of chemical modification or radiolabeling; iii) offer a more straightforward conjugation to other molecules of interest; iv) more rapid clearance from blood and non-target tissues; v) show higher tumor penetration and low toxicity. The disadvantage with peptides is often their short biological half-life, since they can be rapidly degraded *in vivo* by peptidases and proteases. Hence, most peptides have to be molecularly engineered to inhibit their enzymatic degradation. The resulting synthetic peptides however must retain the same or even higher receptor affinity than the original natural peptide.[24]

1.3 Nuclear Modalities for Cancer Imaging and Theranostics

1.3.1 Nuclear Imaging Modalities and Radionuclide Therapy

Although natural radioisotopes of radon and radium have been used in medicine in the early years of the twentieth century, the systemic use of radioisotopes for medical

means had only begun in the 1930's, with the development of the cyclotron and the nuclear reactor. This equipment allowed the production of a wide range of artificial radionuclides with physicochemical properties adequate for medical application, which led to the establishment of Nuclear Medicine as a medical specialization. Nowadays, Nuclear Medicine makes use of a great variety of radiopharmaceuticals for diagnostic and therapeutic applications.[27]

Radiopharmaceuticals are drugs that incorporate a radionuclide in its constitution, and do not display a pharmacological effect since they are administrated in a subnanomolar concentration range. Most of them are organic, inorganic or organometallic compounds of well-defined structure. However, radiopharmaceuticals can also be obtained in the form of nanostructures (ex: nanoparticles), or even macromolecules (e.g. antibodies). Most of the approved radiopharmaceuticals are used for diagnostic application, while only a small percentage is used in therapy.[28]

Radiopharmaceuticals are generally classified into two categories, perfusion radiopharmaceuticals or specific radiopharmaceuticals (Figure 1.5). Perfusion radiopharmaceuticals are delivered into the organs of interest with no specific interaction occurring between the radiopharmaceutical compound and a target located in the accumulating tissue; hence the localization occurs by simple diffusion, phagocytosis, entrapment, or cell sequestration mechanisms. Specific radiopharmaceuticals possess biologically active molecules that can bind specifically to cellular targets, like membrane receptors or antigenes.[29]

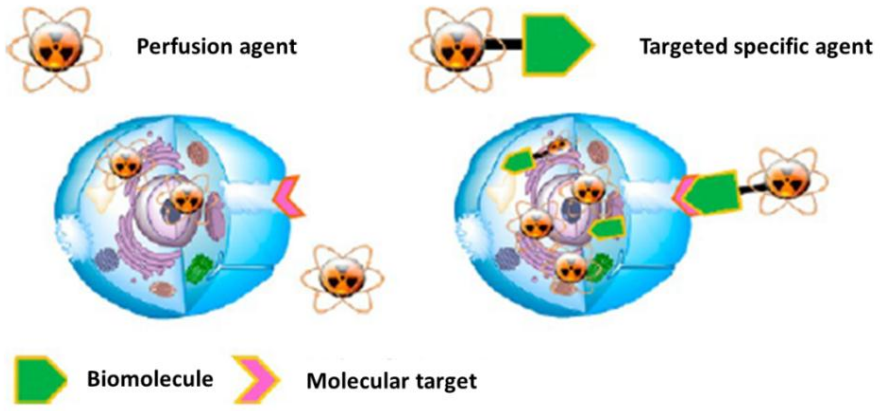

Figure 1.5: *Schematic representation of perfusion and specific radiopharmaceuticals.*[30]

The radionuclide is the fundamental component of any radiopharmaceutical. It is an atom with an unstable nucleus that contains an excess of energy. To release this excess of energy, the radionuclide undergoes a radioactive decay that leads to the emission of gamma (γ) rays or alpha (α) and beta (β^+, β^-) subatomic particles (Figure 1.6). Each radionuclide has its own half-life ($T_{1/2}$), which represents the time it takes for the number of unstable nucleus to reduce to half. The known radionuclides exhibit a wide variety of half-life's, ranging from mere fractions of a second to millions of years. To select a radionuclide for diagnosis of therapy one has to take into consideration its physico-chemical properties, being the half-life and the nature of emitted radiation and/or particles the most relevant ones.[28,31]

Radionuclides that are α or β^- emitters are the ones used for the development of therapeutic radiopharmaceuticals. Due to the high ionizing capabilities and low tissue penetration, these particles can destroy the target tissues.[28,31] Most radiopharmaceuticals approved for medical application contain β^- emitting radionuclides (Table 1.2), being the most commonly used ^{131}I, ^{90}Y, ^{153}Sm, ^{89}Sr and ^{32}P.[32] In recent years, $^{223}RaCl_2$ has been evaluated for bone metastases therapy, becoming the first ever FDA approved alpha emitting radiopharmaceutical.[33]

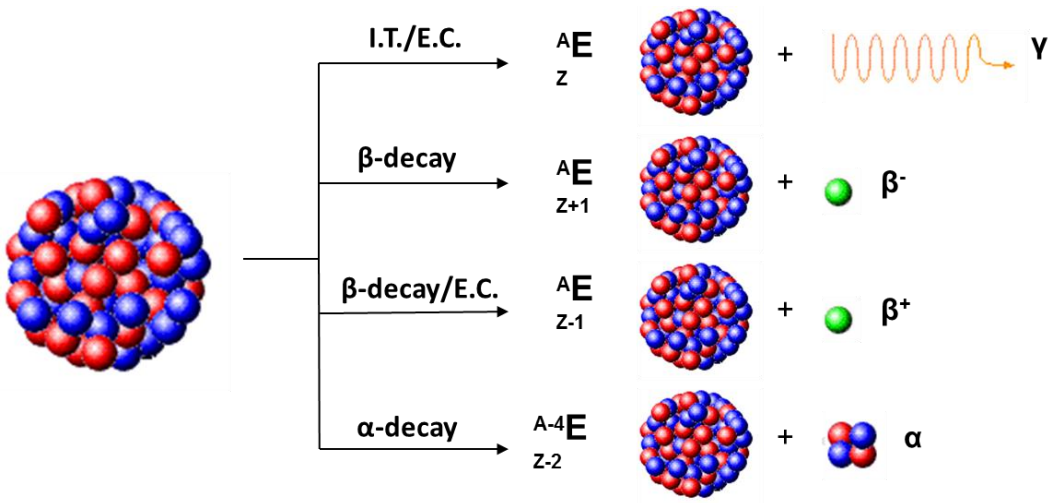

Figure 1.6: *Radioactive decay routes (I.T.- Isomeric Transition; E.C. – Electron Capture).*

In some cases of radioisotopes that decay by either electronic capture or internal conversion, vacancies are created on an internal atomic shell of the isotope and a cascade of electron transitions from higher energy shells occurs to fill those vacancies. This

process is accompanied by the emission of low energy electrons which, depending on the atomic shells involved, can be classified of the Auger type. For many years the biological relevance of Auger electrons was disregarded since the energy associated with these particles is very low when compared to the total energy released by the radionuclide during decay. However, in later years, it was shown that Auger electrons can lead to molecular fragmentation, which can make Auger-emitting radionuclides potentially relevant for selective and targeted radiotherapy. Most of the radioisotopes that emit Auger electrons are already used in diagnostic Nuclear Medicine: ^{67}Ga, ^{99m}Tc, ^{111}In, ^{123}I, ^{125}I and ^{201}Tl.[34,35]

Radionuclides that decay with emission of γ photons or β^+ particles are best suited for the development of radiopharmaceuticals aiming at diagnosis, either by Single Photon Emission Computed Tomography (SPECT) or Positron Emission Tomography (PET) (Table 1.2)

SPECT radionuclides are γ emitters with adequate radiation energy (30-300 KeV), which decay by electronic capture or isomeric transition. γ photons with an energy lower than 30 KeV, are absorbed by tissues and are not detected efficiently outside the body. On the other hand, photons with an energy higher than 300 KeV do not undergo an efficient collimation process, or might even pass through the detector without any interaction.[27,28,31] Due to its favourable physicochemical properties, easy and economic availability from ^{99}Mo/^{99m}Tc generators, ^{99m}Tc still remains the most used SPECT radionuclide. Nevertheless, there is available a variety of approved radiopharmaceuticals based on other SPECT radionuclides (e.g. ^{67}Ga, ^{123}I and ^{111}In) (Table 1.2).[28,36]

PET is the alternative nuclear imaging technique to SPECT. PET imaging relies on the use of radionuclides that are positron (β^+) emitters and on the simultaneous detection of two 511 KeV photons produced from the annihilation reaction between the positron and the electrons from the medium. Currently, the most used PET radionuclide is ^{18}F ($T_{1/2}$ = 110 min); however, in latest years, there has been a lot of focus on PET radiometals due to their attractive physicochemical properties (Table 1.2). In this matter, ^{68}Ga stands out as one of the most promising, since it can be obtained *in loco* by elution of the ^{68}Ge/^{68}Ga generator, making it easily accessible.[28,37]

Table 1.2: *Examples of medically relevant radionuclides.*

Radionuclide	Emission type	$T_{1/2}$	Application
^{67}Ga	γ	78.3 h	SPECT
^{99m}Tc	γ	6.01 h	SPECT
^{111}In	γ	2.83 h	SPECT
^{123}I	γ	13.2 h	SPECT
^{52}Fe	β^+	8.3 h	PET
^{62}Cu	β^+	9.7 min	PET
^{68}Ga	β^+	68 min	PET
^{18}F	β^+	109.7min	PET
^{131}I	β^-	8.0 d	Therapy
^{89}Sr	β^-	50.5 d	Therapy
^{186}Re	β^-	3.71 d	Therapy
^{188}Re	β^-	0.71 d	Therapy
^{153}Sm	β^-	1.93 d	Therapy
^{32}P	β^-	14.3 d	Therapy
^{90}Y	β^-	2.7 d	Therapy
^{223}Ra	α	11.4 d	Therapy

1.3.2 Nuclear Imaging *vs* Other Modalities

Biomedical imaging is one of the main pillars for effective cancer management. It has become a crucial tool in all phases of cancer treatment, including prediction, screening, biopsy guidance, staging, prognosis, therapy planning, therapy guidance, therapy response, recurrence and palliation. The advantages associated with cancer imaging are real time monitoring, accessibility without tissue destruction, minimal or no invasiveness, and can function on a wide range of size scales, from organs or a whole organism to the molecular and cellular range.[38]

Some of the most used imaging techniques for cancer management are shown in Table 1.3. Each technique has its inherent advantages and handicaps, generally associated with their sensitivity, spatial resolution and tissue depth penetration.

Table 1.3: *Characteristics of medical imaging techniques.*

Imaging Technique	Spatial Resolution	Depth Penetration	Sensitivity (mol/L)
PET	1 - 2 mm	No limit	10^{-11} to 10^{-12}
SPECT	0.3 - 1 mm	No limit	10^{-10} to 10^{-11}
OI	1 - 2 mm	< 5 cm	10^{-6} to 10^{-12}
MRI	50 - 250 µm	No limit	10^{-3} to 10^{-5}
X-ray, CT	25 - 150 µm	No limit	-

As mentioned before, SPECT and PET make use of low doses of radioactive compounds to visualize specific biological processes in the body or in certain types of tissues, such as tumors. This high level of sensitivity allows the identification of cancer cells in tissue and bone (Figure 1.7), thus allowing for a precise diagnostic. Compared with the other imaging approaches, the nuclear techniques SPECT and PET are highly sensitive and specific, allowing accurate quantification since there is no limit to tissue penetration of γ photons emitted from any organ.[39]

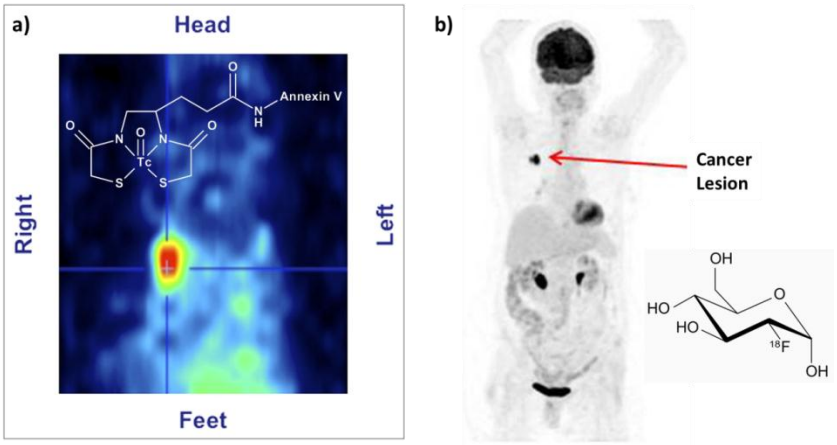

Figure 1.7: a) *SPECT imaging of a breast cancer bearing mouse injected with ^{99m}Tc-annexin V,*[40] *and* ***b)*** *PET imaging of a patient with a cancer lesion injected with F-18 FDG.*[41]

Optical Imaging (OI) uses light propagation through the tissues and is one of the most economic imaging techniques available, which provides fast results and a sensitive and non-invasive imaging approach (Figure 1.8). Although being used in clinical imaging diagnosis, it can be applied to very limited types of cancers due to the small depth

penetration of light photons. This means that OI can be suited to study surface malignancies, but not for whole-body imaging. Moreover, it is necessary to take into consideration that different tissue components (i.e tumors) have distinct scattering and absorption characteristics for each wavelength.[42-44]

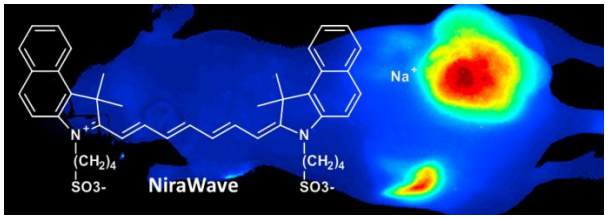

Figure 1.8: *Whole body Near-Infrared fluorescence of a tumor bearing mouse injected with NiraWave.*[45]

Computed Tomography (CT) is an imaging technique that makes use of X-rays to obtain detailed images of the body. Each image created during a CT analysis shows the organs, bones, and other tissues in a thin "slice" of the body; these slices are then stacked in order to create a wider image of the body, but they can also be analyzed individually in order to provide more detailed information. Unlike OI, CT has no depth penetration limit, and provides a very good spatial resolution; however, this technique is limited by its sensitivity. There are different types of contrast agents explored for CT; iodine based agents were some of the first water-soluble imaging agents to be used, due its high atomic number (Z = 53) which allows for higher levels of X-ray attenuation than those observed for biological tissue, not to mention the easy incorporation of a iodine atom into other molecular structures of biological relevance. Gold nanoparticles display ideal properties as CT contrast agents (Figure 1.9), presenting very favorable X-ray attenuation properties due to the high density and high atomic number of gold. Other CT contrast agents worth mentioning are lanthanide and bismuth based agents.[46-49]

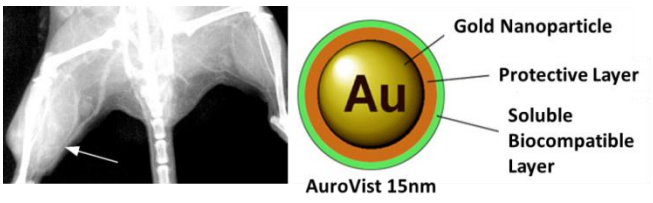

Figure 1.9: *X-ray of mouse hind legs showing accumulation of AuroVist 15nm with contrast in tumor growing on left leg.*[50]

Magnetic Resonance Imaging (MRI) uses radio frequency waves in the presence of a strong magnetic field in order to build up detailed images of various parts of the body by picking up signals sent out by water molecules (Figure 1.10). These radio waves are used to induce tissues to emit radio waves of their own, and different tissues (like tumors) emit a more or less intense signal based on their chemical makeup. Much like CT, MRI can produce three-dimensional images of sections of the body, but MRI has a higher sensitivity that allows a better distinction of soft tissues than CT. The high sensitivity of MRI is however not comparable to that of nuclear imaging techniques (SPECT and PET).[51-53]

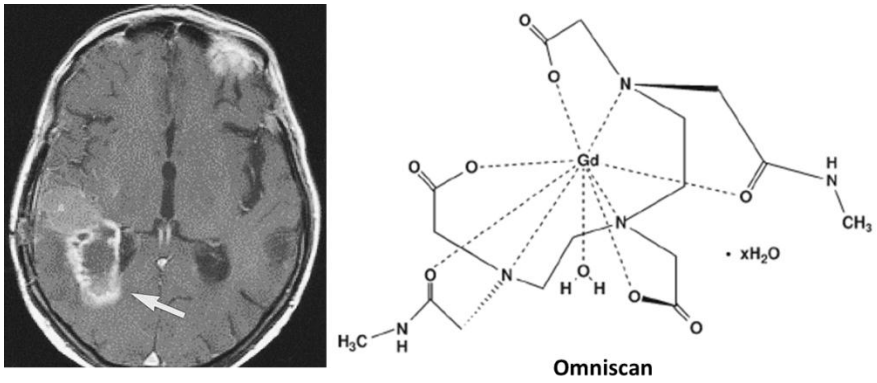

Figure 1.10: *MRI image showing a brain tumor using Omniscan contrast agent.*[54]

The most well-known type of MRI contrast agents are gadolinium based, due to its efficient capability to shorten relaxation times of bulk water protons.[55] In order to enhance the sensitivity of MRI analysis researchers have been exploring nanoparticles as MRI contrast agents with promising results, either profiting from their inherent magnetic properties (e.g. superparamagnetic iron oxide (SPIO) nanoparticles) or as carriers for gadolinium to increase metal payload.[56,57]

Most times the individual imaging techniques cannot provide all the information required to develop a thorough cancer management. As each imaging modality is characterized by different spatial resolution and sensitivity, an integrated multimodal imaging system eliminates the shortcomings of individual imaging modalities and offers a wider range of imaging possibilities. The integration of different imaging modalities is a solution to easily obtain both anatomical and functional information. Hence, conjugation of SPECT or PET with CT or MRI imaging can provide an excellent tissue contrast and information about functional, structural and morphological changes in cancer diagnosis.

The association of SPECT or PET with CT provides information about both morphological and functional changes and has been a major breakthrough in cancer imaging. This conjugation offers great potential in the planning of radiation therapy when tumor regions are difficult to define.[58,59] This combination however maintains the limitation of CT, which is inadequate for soft-tissue contrast. In such cases, the association of SPECT or PET with MRI can overcome this limitation, and provide sufficient spatial resolutions and high sensitivity. Also, MRI does not require the use of ionizing radiation like CT, and therefore the radiation dose required for imaging is less.[60,61]

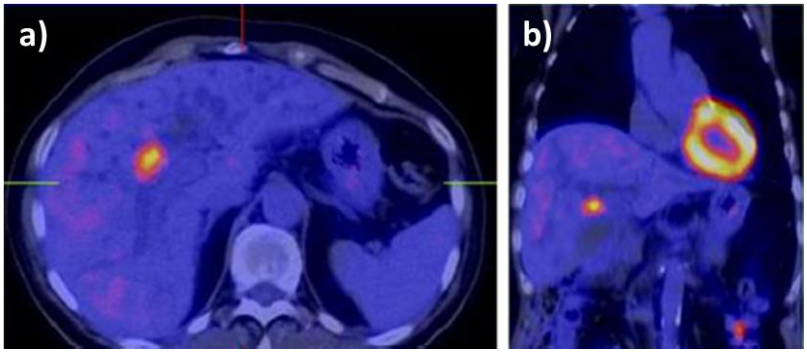

Figure 1.11: *SPECT/CT imaging of a patient with adenocarcinoma injected with ^{18}F-FDG:* ***a)*** *axial and* ***b)*** *coronal slices.*[62]

Multimodal agents, i.e. compounds than display more than one imaging modality property, might play an important role in the development of new strategies for cancer management. For instance, having a probe that possesses a SPECT or PET radionuclide, and that can be simultaneously used as a CT or MRI contrast agent, will provide an identical biodistribution profile for both imaging moieties.[63-65]

Nuclear imaging is arising also as a prominent tool for theranostics.[66,67] The concept of theranostic was introduced in 2002 by Funkhouser, and it is defined as a combination of therapy and diagnostics in a single treatment.[68] This integration of diagnostic imaging capability with therapy can be critical when approaching malignant diseases like cancer due to its heterogeneity and adaptation.

There are already some nuclear imaging procedures that can be considered theranostics. Na^{131}I has probably been the first theranostic compound available in medical application, since it has the ability to detect the uptake of iodine in thyroid carcinoma metastases and at the same time it can allow medical staff to identify patients that could

benefit from therapeutic doses of ^{131}I. The well-known chemistry of ^{99m}Tc and its similarities with that of rhenium offer the possibility to easily translate from a SPECT imaging compound (^{99m}Tc) to a therapeutic agent (^{188}Re) by replacement of the radioisotope in isostructural radiocomplexes, assuming the same biodistribuion profile for Tc and Re congener compounds. The field of theranostics is however relatively recent and some issues related to ambiguity and difference between therapeutic and imaging agent doses still needs further work.[67,69]

1.4 Chemistry and Radiochemistry of Gallium Relevant for Radiopharmaceutical Design

1.4.1 PET and SPECT Gallium Radionuclides

Natural gallium consists of a mixture of two stable isotopes, ^{69}Ga and ^{71}Ga. However different gallium radionuclides can be produced, including ^{67}Ga and ^{68}Ga that are useful for nuclear imaging, and, for this reason, are those that are the most commercially important ones.

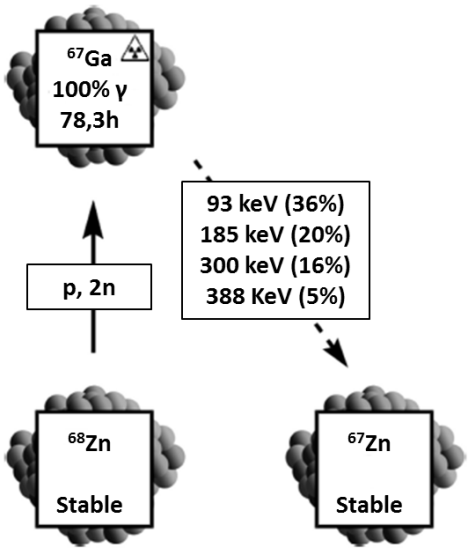

Figure 1.12: *Production and decay of ^{67}Ga.*[70]

^{67}Ga has several characteristics that make it interesting for SPECT imaging. It is produced by cyclotron through the ^{68}Zn (p, 2n) → ^{67}Ga reaction, being therefore available in a carrier-free state. It has a half-life of 78.3h and its mode of decay is by electron capture, with the emission of four main γ rays having energies of 93, 185, 300 and 388 keV.[70]

^{68}Ga ($T_{1/2}$ = 67.71 min) decays by positron emission (89%) and electron capture (11%) with an average positron energy per disintegration of 1899 keV. The major advantage of this radioisotope is its easy availability from the transportable ^{68}Ga/^{68}Ga generator, as Ge(IV) and Ga(III) have significantly different chemical properties which allows for an efficient separation of both isotopes (Figure 1.13). ^{68}Ge/^{68}Ga generators have emerged in recent years as an economic source of ^{68}Ga without the dependence of a nearby cyclotron. The parent isotope, ^{68}Ge, has a half-life of 270.8 days and the generator can be used over 1-2 years. The recent development of ^{68}Ga/^{68}Ga generators following the Good Manufacturing Practice (GMP) conditions allowed for its use in clinics. This is expected to confer an important role to ^{68}Ga in PET imaging, as observed in the past for ^{99m}Tc that became the most important SPECT radionuclide mainly due to its availability from ^{99}Mo/^{99m}Tc generators. Despite the increasing role of ^{68}Ga in nuclear imaging, it is still common however the use of ^{67}Ga in radiopharmaceutical development due to its accessibility and easier manipulation ($T_{1/2}$ ≈ 78.3h vs 68 min for ^{68}Ga).[70,71]

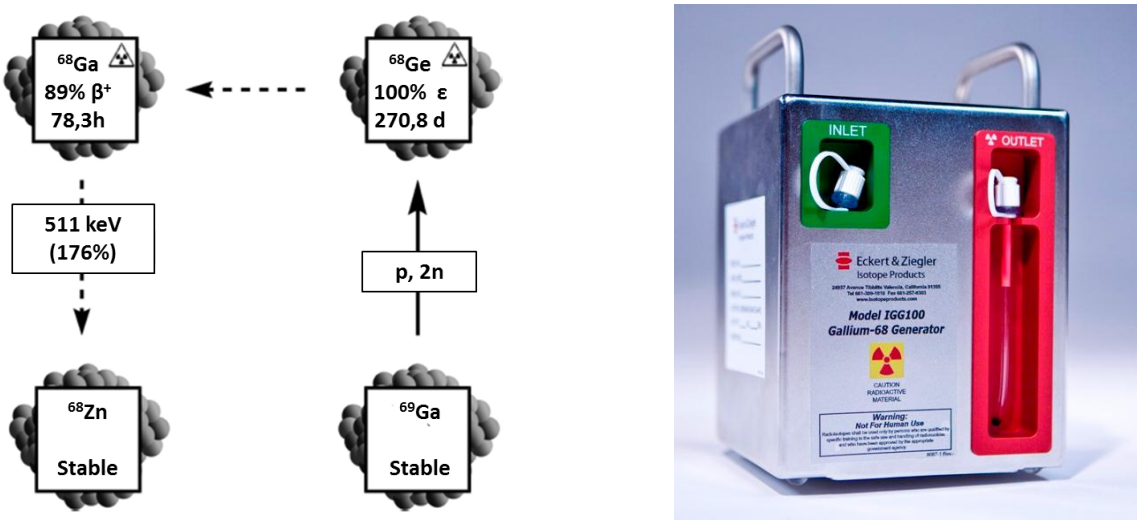

Figure 1.13: *Production and decay of ^{68}Ge and ^{68}Ga (left),[70] and an example of a commercial ^{68}Ge/^{68}Ga generator (right).[72]*

1.4.2 Gallium Chelators and Radiopharmaceuticals

Gallium is a metallic element of the 13th group of the periodic table with the [Ar]3d^{10}4s^{2}4p^{1} electronic configuration, which has been discovered in 1875 by the chemist Leqoc de Boisbaudran. Gallium in aqueous medium is found predominantly in the stable oxidation state +3 (Ga(III)), while the low-valent state +1 (Ga(I)) is not significant under

aqueous conditions. Hence, Ga(III) is the only oxidation state of relevance in radiopharmaceutical development.[73]

The accurate control of pH is an important factor in gallium chemistry. In the absence of stabilizing ligands, Ga(III) undergoes hydrolysis at pH ≈ 3-7 to insoluble $Ga(OH)_3$ and at pH > 7 it re-dissolves as $[Ga(OH)_4]^-$. The more common gallium reagents used for radiopharmaceutical development are Ga-citrate and $GaCl_3$. In the preparation of gallium radiopharmaceuticals citrate is used as a weak stabilizing agent for ligand-exchange reaction, in order to avoid hydrolysis and formation of gallium hydroxide. In an acidic hydrochloric medium (pH < 3), gallium is used in the form of $GaCl_3$, which is more reactive than Ga-citrate.[70,74]

The first study of a Ga(III) radioactive complex towards imaging of tumor tissues remotes to the end of the 1960's, when ^{67}Ga-citrate (Figure 1.14) was injected into tumor-bearing mice with accumulation of ^{67}Ga in the malignant cells.[75] A few years later ^{67}Ga-citrate started to be used for the detection of malignant tumors in patients. Over the last two decades, ^{67}Ga-citrate scanning has been used frequently in patients with Hodgkin's and non-Hodgkin's lymphomas for detection of residual disease or monitoring signs of relapse following treatment with chemotherapy or radiotherapy.[76,77]

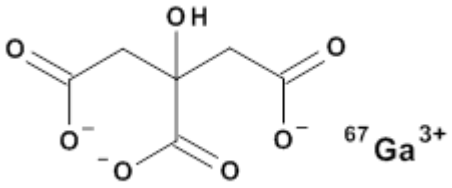

Figure 1.14: *^{67}Ga-citrate.*

However, ^{67}Ga-citrate is not specific towards tumor tissues and it is also known to accumulate in inflammatory tissue;[78] ^{67}Ga-citrate can be seen as a pro-radiopharmaceutical because ^{67}Ga transchelates *in vivo* to transferrin, immediately after injection and almost quantitatively. Therefore, the biodistribution of ^{67}Ga-citrate is directly related with that of transferrin, which is a 79570 Da iron carrier protein with two homologous regions for iron coordination.[79]

In vivo studies using ^{67}Ga as a tracer indicated that most of the Ga(III) is bonded to transferrin, in the absence of strongly coordinating chelators. For this reason, it is assumed

that the uptake and distribution of gallium in the cells occurs through mechanisms similar to those involved in the transport of iron.[80,81] Fe(III) and Ga(III) present great similarity in their physicochemical properties, like the ionic radius, electronegativity, electronic affinity, coordination geometry and affinity to the same type of ligands, The ionic radius of octahedral Ga(III) (0.62 Å) is comparable to that of high-spin octahedral Fe(III) (0.645 Å). Both these metals are hard Lewis acids, which present a strong affinity for hard Lewis bases, in particular to oxygen and nitrogen donors. For these reasons, it is no wonder that Ga(III) displays a biochemical behavior similar to that of Fe(III). There are however, some differences regarding their redox behavior *in vivo*.[74,82,83]

Transferrin (Tf) can coordinate up to two Fe(III) ions (or Ga(III)), along with a carbonate or bicarbonate anion per metallic ion.[83,84] Tf carries the metallic ions to the cells through Tf receptors, a protein located at the surface of the cells that can bind two molecules of Tf. All nucleated cells in the organism express Tf receptors, but the concentrations vary significantly depending on the type of cell. Cancer cells generally have a very high Tf receptor expression, since these cells have high need for iron that is essential for DNA synthesis. For this reason, gallium is preferably located in proliferating tissues (including most tumors), expressing high amounts of Tf receptors, when compared with normal tissues. Nevertheless, the *in vivo* biodistribution of gallium is a more complex issue, since gallium is not equally distributed in all proliferating tissues, and it is also located in bone formation regions that do not possess any iron carrier proteins.[83]

^{67}Ga-citrate had some considerable success in medical nuclear imaging. To further expand the biomedical applications of gallium radioisotopes, either for SPECT (^{67}Ga) or PET (^{68}Ga), the availability of chelator systems capable of a fast complexation of ^{67}Ga/^{68}Ga, under highly diluted concentrations of the metal, and forming complexes with high kinetic inertness is a crucial issue. Such chelators must avoid the *in vivo* dissociation of the radiometal, particularly transchelation to transferrin. The nature of the chelator has an important influence on the structure and physicochemical properties of the resulting radioactive chelates with a consequent large impact on the overall pharmacokinetic properties of the putative radiopharmaceuticals.

The macrocycle 1,4,7,10-tetraazacyclododecane-1,4,7,10-tetraacetic acid (DOTA) (Figure 1.15) is one of the most important chelators in radiopharmaceutical chemistry,

being extensively used with a large variety of trivalent radiometals that include $^{67/68}$Ga. Its coordination to Ga(III) affords complexes with good thermodynamic stability, still remaining free carboxylic acid arms for the conjugation of targeting molecules.[85,86] Another well-known cyclic chelator is 1,4,7-triazacyclononane-1,4,7-triacetic acid (NOTA) (Figure 1.15), one of the oldest and most successful chelators for Ga(III). It is widely accepted that NOTA complexes of Ga(III) are more stable thermodynamically than their DOTA counterparts (log K_{ML} = 31.0 for NOTA and log K_{ML} = 21.3 for DOTA)[87]. However, sometimes NOTA may not be the optimal choice for certain applications, since kinetic stabilization is often a more important factor in radiopharmaceutical design than thermodynamic stabilization. In fact, due to differences in charge and physical properties, DOTA may provide superior *in vivo* properties with certain targeting vectors.[85,88]

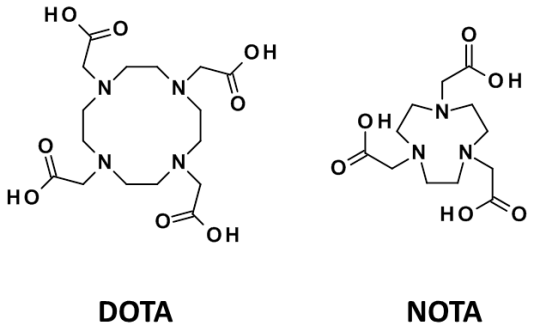

Figure 1.15: *Chemical structures of DOTA and NOTA.*

In the field of acyclic chelators, 2-[bis[2-[bis(carboxymethyl)amino]ethyl]amino] acetic acid (DTPA) (Figure 1.16) is one of the most used in radiopharmaceutical development. One of its most relevant features is the fact that it can be radiolabeled with many different radiometal ions at room temperature in a few minutes, including $^{67/68}$Ga. Recently, other acyclic chelators have shown very promising results in the stabilization of Ga(III) under the conditions required for the synthesis of radiopharmaceuticals, such as the poly(amino) carboxylic derivatives 1,2-[(6-(carboxylato-)pyridin-2-yl)methylamino]-ethane (H2dedpa) and N,N-bis(2-hydroxybenzyl) ethylenediamine-N,N-diacetic acid (HBED) (Figure 1.16).[85]

H2dedpa belongs to a family of ligands known as the “pa family”, being crafted around two picolinic acid (pa) coordinating moieties. It has a very good coordination capability towards $^{67/68}$Ga, being able to quantitatively coordinate the radiometal in less than 10 min at room temperature. The resulting radiocomplex demonstrates excellent

stability in blood serum and resistance to transchelation by apo-transferrin, and has been considered quite promising for the design of specific $^{67/68}$Ga radiopharmaceuticals.[87,89] Studies with HBED, a phenolic aminocarboxylic acid derivative, demonstrated that phenol donor groups can be effective for Ga(III) complexation. HBED has received limited attention in the design of specific $^{67/68}$Ga radiopharmaceutcals and, in recent years has been supplanted by a plethora of new ligands. Nevertheless, one HBED derivative (HBED-CC, Figure 1.16) has been conjugated to antibodies and allowed a much faster radiolabeling than NOTA.[85,90]

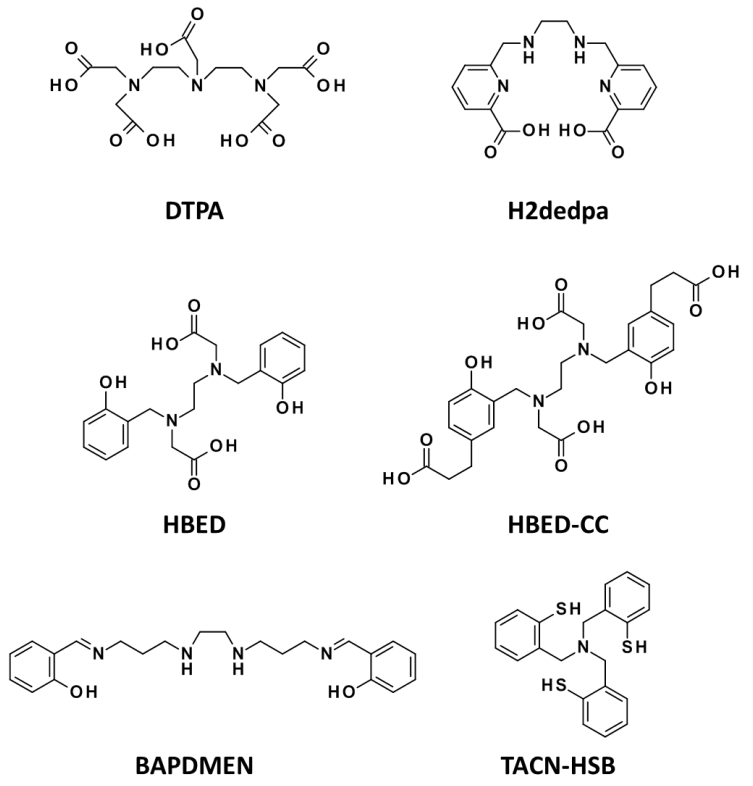

Figure 1.16: *Chemical structures of selected acyclic chelators.*

Acyclic chelators have also been applied in the design of perfusion $^{67/68}$Ga radiopharmaceuticals with a main focus on myocardial imaging agents. The pioneering work of M.A. Green and co-workers with hexadentate salycilaldimine derivatives, such as BAPDMEN (N,N′-Bis(3-aminopropyl)-N,N′-dimethyl-ethylenediamine, Figure 1.16), demonstrated the potential of this class of chelators to obtain $^{67/68}$Ga complexes suitable for myocardial imaging.[91,92,93] A series of thiol containing chelators, including TACN-HSB (tris(2-mercaptobenzyl)-amine, Figure 1.16) and related derivatives, have been used in the

synthesis of neutral and lipophilic Ga(III) complexes aiming at the design of $^{67/68}$Ga radiopharmaceuticals for brain imaging.[94] Despite some encouraging results, the evaluated $^{67/68}$Ga complexes did not emerge as good candidates for clinical use.

Several target specific gallium complexes have shown promising as radiopharmaceuticals for cancer imaging. These progresses were fuelled by the availability of ^{68}Ge/^{68}Ga generators, the booming development of bifunctional chelators for linkage to target specific vectors and the increasing demand for ^{68}Ga-based probes for PET imaging. A major breakthrough was the development of several ^{68}Ga-labeled somatostatin analogs for imaging of neuroendocrine tumors, namely the radiopeptide ^{68}Ga-DOTATOC (Figure 1.17). Nowadays, this radiometallated peptide is used in medical diagnosis to image somatostatin receptor-positive tumors, and has proved to be superior to CT and/or MRI for detection and staging of neuroendocrine tumors.[95]

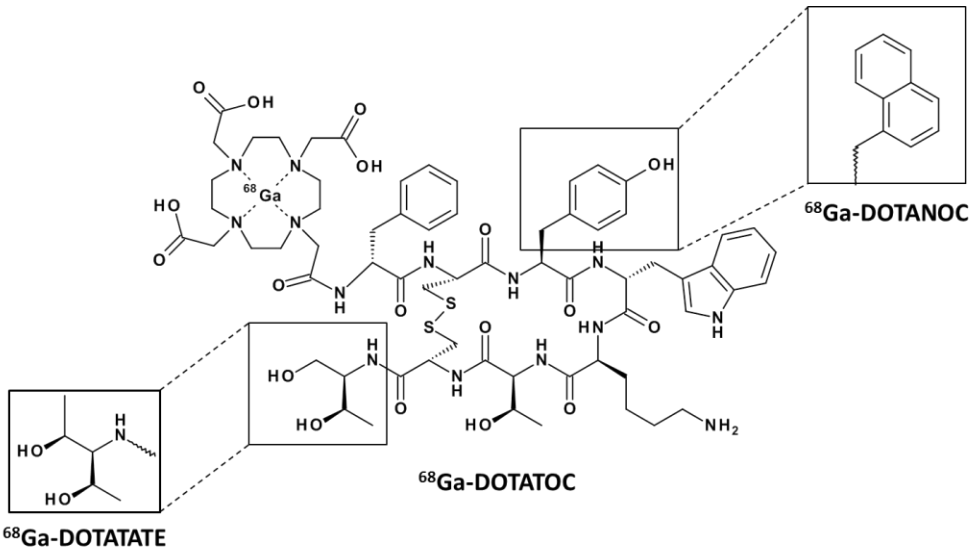

Figure 1.17: *Chemical structures of ^{68}Ga-DOTATOC, DOTATATE and DOTANOC.*

The success of ^{68}Ga-DOTATOC prompted the development of other somatostatin analogs, like ^{68}Ga-DOTATATE and ^{68}Ga-DOTANOC (Figure 1.17). These radiopeptides are used in PET nuclear oncology for *in vivo* targeting of tumors overexpressing somatostatin receptors, although displaying different radiopharmacological properties: ^{68}Ga-DOTATATE displays a higher affinity for somatostatin receptor type 2 (sstr2) compared with ^{68}Ga-DOTATOC. ^{68}Ga-DOTANOC is reported to have a more favorable

dosimetry and acts as a pan-somatostatin ligand with good affinity towards somatostatin receptor type 3 (sstr3).[96-98]

Besides the successful story of somatostatin analogs, other classes of ^{68}Ga-labeled peptides also led to encouraging results. For instance, Melanocyte-Stimulating Hormone (MSH) derivatives were labeled with ^{67}Ga and the resulting metallated peptides were evaluated as radioprobes for specific targeting of melanoma cells overexpressing melanocortin (MC1) receptors. PET studies with the radiolabeled MSH analog ^{68}Ga-DOTA-NAPamide (Figure 1.18) have shown a very high contrast image in mouse B16F1 melanoma models, just one hour post-injection. However, the MC1 receptor density in human melanomas is much lower than in the murine-melanoma, which justifies that the preliminary experience in human patients gave negative results.[99]

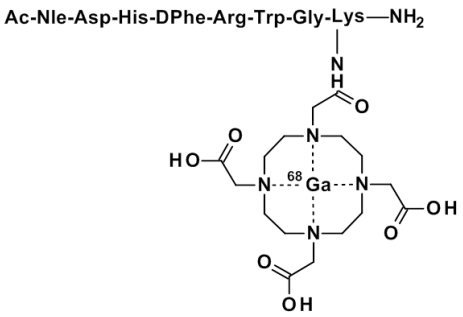

Figure 1.18: *Chemical structures of ^{68}Ga-DOTA-NAPamide and ^{68}Ga-BZH3.*

Bombesin (BBN) analogs correspond to another class of clinically relevant peptides that have been labeled with $^{67/68}$Ga. BBN is a tetradecapeptide with high affinity to Gastrin Releasing Peptide (GRP) receptors that are overexpressed in some tumors, particularly prostate and breast cancers, and for this reason BBN derivatives can be explored as carriers for *in vivo* tumor targeting, as discussed in more detail in Chapter 2. For instance, the evaluation of ^{68}Ga-DOTAPEG2-[D-Tyr6,Ala11,Thi13,Nle14]-bombesin (BZH3) (Figure

1.18) in a pancreatic carcinoma model showed very good uptake by the tumor with a significant tumor-to-background ratio, indicating a great potential for clinical practice.[100]

1.5 Nanoparticles and the Design of Nanoradiopharmaceuticals

1.5.1 General Considerations on Nanoparticles and Nanomedicine

Nanotechnology is defined as the design, characterization, production and application of structures, devices and systems by controlling shape and size at the nanoscale (1-100 nm). It is an interdisciplinary research field involving chemistry, engineering, biology, and medicine. In the last decades there has been a considerable increase of interest in nanotechnology with the development of promising strategies to overcome technological impasses incurred in various fields of science.[101,102]

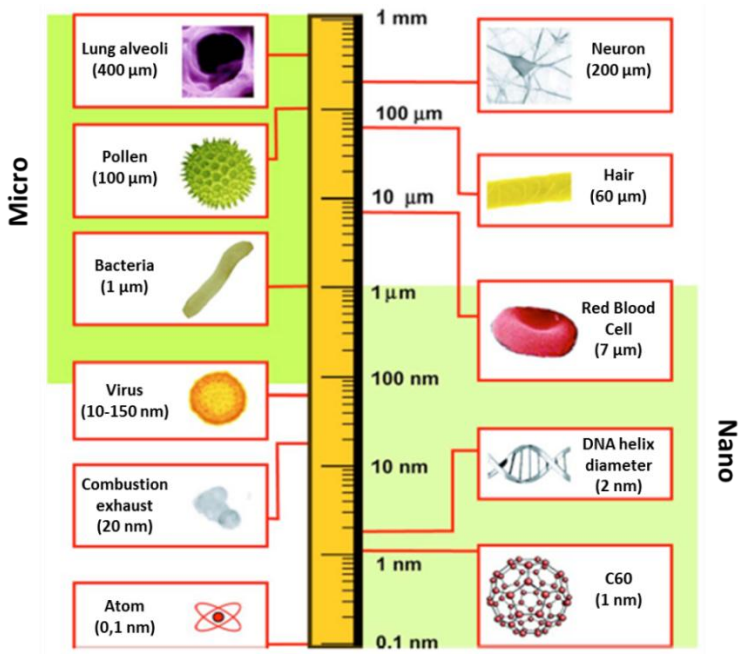

Figure 1.19: *Logarithmical length scale of nanomaterial size compared with biological components.*[103]

In the past, microsized structures of well-defined nature, shapes and functionalities have been well documented (Figure 1.19). Microparticles and nanoparticles vary in their conception only by their size, but by shrinking the size of the particles to the nano scale causes these materials to behave significantly different than their micro counterparts; this is mainly due to surface and quantum effects that affect chemical reactivity of materials as well as their mechanical, optical, electric and magnetic properties.[103-106]

Compared to microparticles, nanoparticles (NPs) have a very large surface area and high particle number per unit mass. As the material in nano structures presents a much larger surface area for chemical reactions, reactivity is normally enhanced. But while chemical reactivity generally increases with decreasing particle size, surface coatings and other modifications can have reverted effects, leading to a reduction of reactivity with decreasing particle size in some instances.[105,107] Also, the atoms situated at the surface have less neighboring atoms than those in microparticles, resulting in a lower binding energy per atom.[103] Nanoparticles can be obtained with a wide variety of different materials including inorganic compounds or organic polymers, among others (Figure 1.20). The use of different materials provides nanoparticles with different physico-chemical properties, as well as with different shapes which may also be relevant in some fields of application, namely in biomedicine.[108]

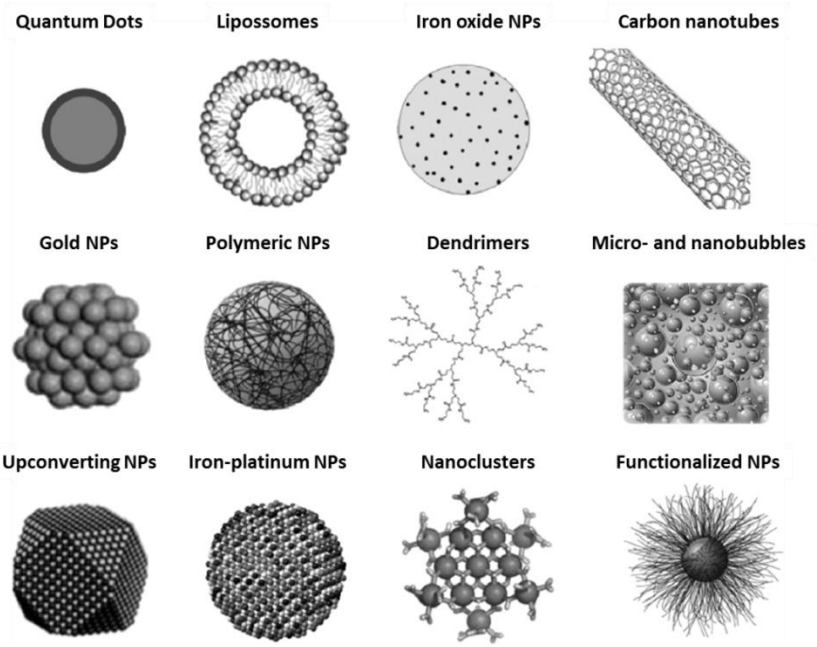

Figure 1.20: *Selected examples of different types of nanoparticles.*[109]

Nanotechnology is a discipline of science and engineering that has led to innovative approaches in many areas of medicine. Its applications in the screening, diagnosis, and treatment of disease are collectively referred to as “nanomedicine”, an emerging field that has demonstrated great potential to revolutionize individual and population wide health in the future. It can be seen as a refinement of molecular medicine,

integrating innovations in genomics and proteomics on the path to a more personalized medicine. The main applications of nanomedicine are summarized in Figure 1.21.[110,111]

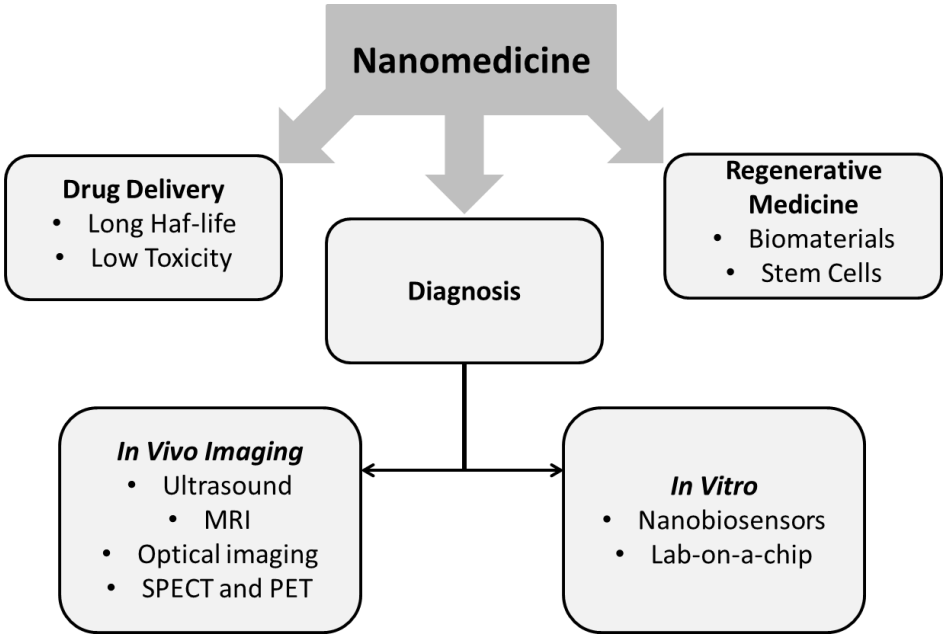

Figure 1.21: *Main application fields of nanomedicine.*

Conventional drugs suffer from the major limitation of adverse effects, the result of the non-specificity of their action, and from a lack of effectiveness due to improper or ineffective dosage, e.g., in cancer chemotherapy. Due to their small size, nanoparticles can efficiently penetrate tissue/cell barriers, allowing a more efficient drug accumulation at the target site. Therefore, the unwanted adverse effects and the toxicity of the therapeutic agent can be reduced. Drugs can be loaded onto nanoparticles by various methods, such as encapsulation, surface attachment or entrapment. This possibility can be used to optimize drug formulations and open new opportunities for therapeutic agents that cannot be used effectively as conventional drug formulations due to poor bioavailability or drug instability.[112,113]

Nanotechnology can also play a major role in the development of new and efficient diagnostic tools, either for *in vitro* or *in vivo* applications.[110-113] Gold nanoparticles have shown promising results as contrast agents for CT due to their remarkable properties, since they display a high X-ray absorption coefficient, but also a low cytotoxicity, good biocompatibility, and well defined surface chemistry.[114-117] Superparamagnetic iron oxide (SPIO) nanoparticles are assuming an increasing importance in the development of MRI

contrast agents, because of their high transverse relaxivity.[118-122] Promising results have been reported for ultrasound and optical imaging based on a variety of nanoparticles.[123-125]

Radiolabeled nanoconstructs present also a new approach, with great potential, for the development of radiopharmaceuticals for SPECT and PET imaging and for cancer theranostics, as discussed below.[39,126-132]

1.5.2 Biological Properties of Nanoparticles

Most nanoparticles have high *in vivo* stability. For some of them (*e.g.* quantum dots), their inherent toxicity is a potential drawback, but for many others (*e.g.* iron oxide and gold NPs) toxicity issues are less relevant. Nanoparticle biodistribution can vary greatly depending on the type and size of the particle, as well as on their surface chemistry.[133]

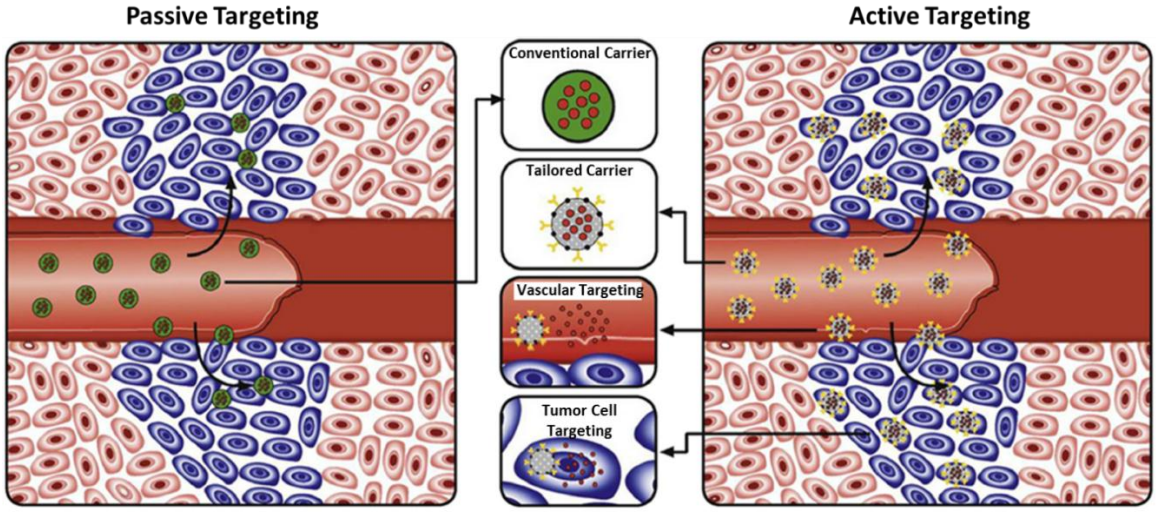

Figure 1.22: *Nanoparticle passive* vs *active targeting.*[134]

A major advantage of using nanocarriers in imaging and/or theranostics of cancer is that they can increase selectively the uptake of a drug or radionuclide in tumor tissues due to two major factors: i) their nanosize (<100 nm) and the Enhanced Permeability and Retention (EPR) effect allows passive targeting of the leaky tumor tissue; ii) surface conjugation of biological vectors can promote a specific targeting of tumors (Figure 1.22).[39,101]

The EPR effect is a result of the leakiness of the newly forming blood vessels and poor lymphatic drainage in growing tumors. During the angiogenesis, the endothelial cells

from the blood vessel walls do not seal tightly against each other, leaving fenestrations of approximately 200 - 800 nm in diameter. These factors lead to a passive accumulation of nanoparticles in tumor tissues.[135]

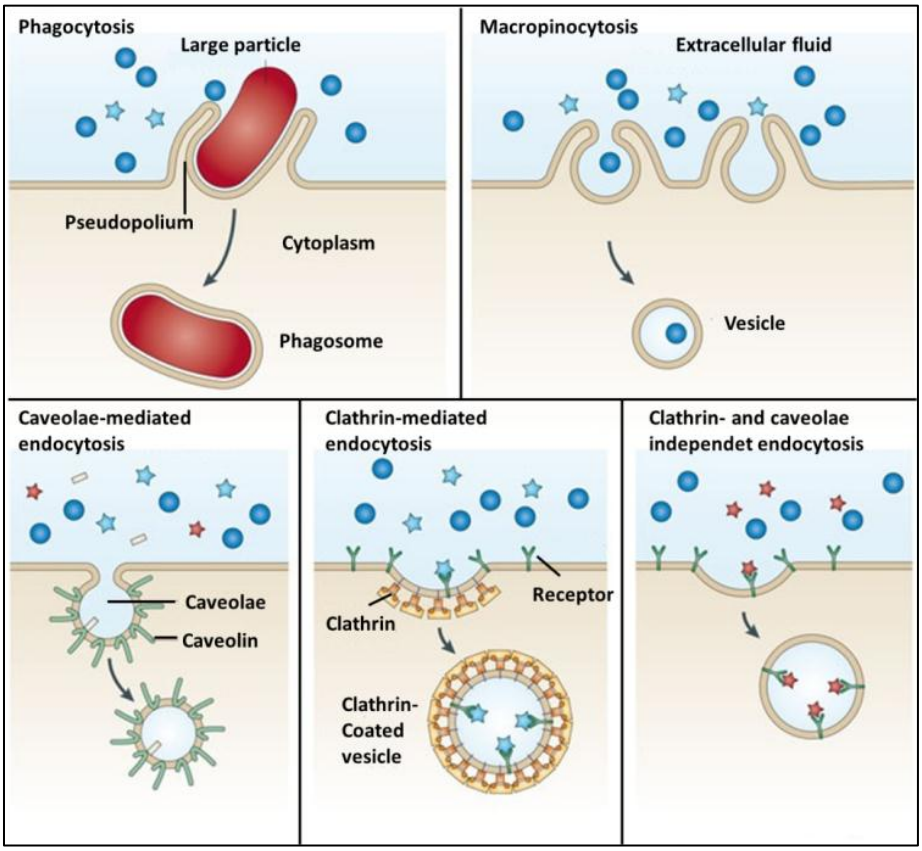

Figure 1.23: *Mechanisms of cellular internalization of nanoparticles.*[136]

At the cellular level, it is known that most of the nanoparticles are uptake through endocytic pathways. Endocytosis is a conserved mechanism where extracellular particles are taken into the cell by invagination of the plasma membrane with formation of vesicles. Two of the most common endocytic mechanisms for nanoparticle uptake are phagocytosis and pinocytosis. The first occurs mostly when dealing with large size particles (>500 nm), the later one is observed for smaller sized particles and can occur by different pathways: i) macropinocytosis, an invagination of the cell membrane to form a pocket that occurs for particles of >200 nm size; ii) clathrin-mediated endocytosis, a mechanism by which the endocytic process occurs though inward budding of the cell membrane vesicles due to specific binding of molecules to cell receptors; iii) caveolae-mediated endocytosis, which involves the cholesterol-binding protein caveolin and is more commonly found in non-

clathrin-coated cell membrane regions; iv) clathrin- and caveolae-independent mechanisms, which are mediated by specific receptor interaction.[137-139]

The inherent size of nanoparticles results in a rapid entrapment in the RES organs (liver, spleen and lymph nodes), which are responsible for clearing, processing and degrading foreign materials from circulation. This implies a lowering of the available dose of therapeutic nanoparticles in a target site, and it can also lead to inflammation, compromised host defense, release of toxic byproducts, and redistribution of the nanoparticles to sensitive areas of the body. Therefore, uptake by the RES is avoided as much as possible when developing new nanopharmaceuticals.[140] It is possible to tamper with the RES uptake of nanoparticles by modification of certain parameters, namely, their size, surface charge and coating.

Small size nanoparticles are known to have a reduced uptake by the RES organs when compared to larger ones. Studies suggest that if they are small enough (<5-6 nm) nanoparticles can display renal excretion in their biological profile.[141,142] However, when designing nanoparticles for specific receptor targeting, one needs to take into consideration that small nanoparticles (size <40 nm) are more dependent on receptor distribution along the membrane due to their small surface area. The receptors need to be in close proximity to each other in order to occur sufficient nanoparticle-receptor interactions to produce enough free energy that will allow membrane wrapping and induce cell uptake.[101]

Particles with 40-50 nm size have a higher surface area, and are generally capable of binding to enough receptors that cell membrane wrapping will occur without being overly dependent of receptor distribution along the membrane. Larger size particles (>50 nm) can bind to such a large number of receptors that can lead to a depletion of the receptors in the cell membrane and this may limit the binding of additional nanoparticles to the same cell.[101]

Regarding the surface charge of nanoparticles, it has been seen in some cases (e.g. iron oxide NPs) that positively charged nanoparticles display a faster cell uptake when compared to neutral or negatively charged ones. This can explained by a slightly negative charge of the cell membrane and by a cell uptake driven by electrostatic interactions.[143]

The nature of the molecules coating a nanoparticle is another parameter that greatly influences nanoparticle biodistribution and cellular uptake. Polyethylene glycol (PEG) is one of the most commonly used compounds to enhance nanoparticle biodistribution; when attached to the nanoparticle surface, PEG normally reduces RES uptake and increases circulation time. PEG is also known to increase particle stability and reduce aggregation and association of non-targeted proteins, which enables a type of "stealth" behavior to the nanoparticles.[144]

To date, three generations of nanoparticles have been engineered for biomedical application. The first generation consisted of nanomaterials obtained based on basic surface chemistry to assess biocompatibility and toxicity, which normally are rapidly trapped in the RES organs. The second generation corresponds to nanomaterials with optimized surface chemistry and improved stability, which can evade the RES of the liver and spleen, display a prolonged circulation in the blood, and allow for passive targeting through the EPR effect in leaky tumor tissues. The third generation of nanocarriers exhibits surface modification by bioconjugation, using for instance specific antibodies or peptides, to actively target tumor tissues.[101,145]

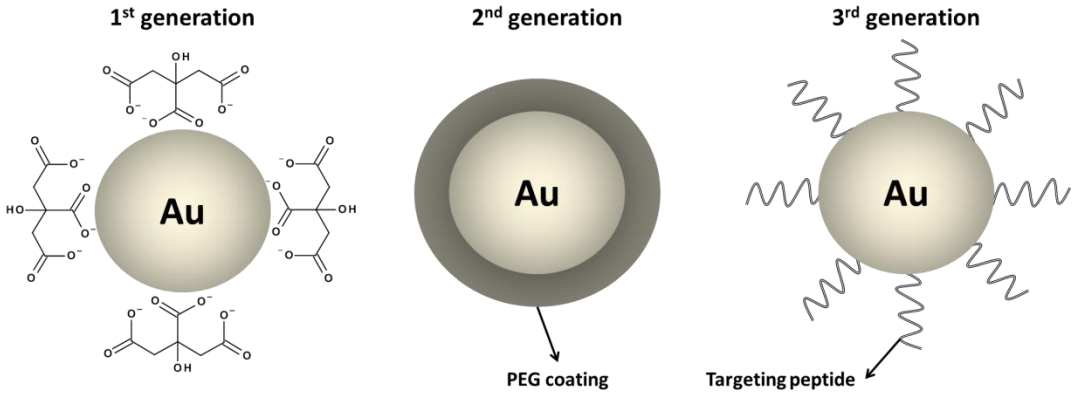

Figure 1.24: *Examples of the three generations of gold nanoparticles.*

For all the generations of nanoparticles (Figure 1.24), there has been a significant focus on the study of gold nanoparticles (AuNPs), as these metallic nanomaterials show great potential for optical, electronic, magnetic, catalytic, and biomedical applications.[144,146,147]

1.5.3 Synthesis and Medical Use of Gold Nanoparticles

1.5.3.1 Historical Background and Synthetic Methodologies

The use of AuNPs can be retraced back to the 5th century B.C. in Egypt and China, for mostly aesthetic purposes. Colloidal gold was used to make ruby glass and for coloring ceramics and these applications are still used today. A very famous example is the Lycurgus Cup, which due to the presence of AuNPs in its composition displays a ruby red color in transmitted light and a green color in reflected light (Figure 1.25).[148]

Figure 1.25: *Lycurgus Cup with reflected (left) and transmitted light (right).*

The first recorded medicinal application of AuNPs remotes to the Middle Ages, as reported in 1618 in a book by the medical doctor Francisci Antonii. Francisci Antonii claimed that, at the time, soluble gold was used to cure a great variety of diseases, including heart and venereal problems, dysentery, epilepsy and tumors, as well as for diagnosis of neuro-syphilis through precipitation of colloidal gold by pathological cerebrospinal fluids. Later on, in 1676, the German chemist Johann Knuckles has also described the curative properties of “drinkable gold” for several diseases.[149]

The first description of AuNPs dates from 1857 and is due to Michael Faraday, who has reported on the formation of deep-red solutions of colloidal gold by reduction of an aqueous solution of tetrachloroaurate ($AuCl_4^-$) using phosphorus in CS_2 (two-phase system).[149] During the 20th century, many methods have been reported for the preparation of gold colloids. Based on these different methods, it is possible nowadays to manipulate

the size and shape of gold nanoparticles, spanning from shapes like nanospheres (or nanoshells), nanorods, nanocages to nanostars (Figure 1.26).[39,102]

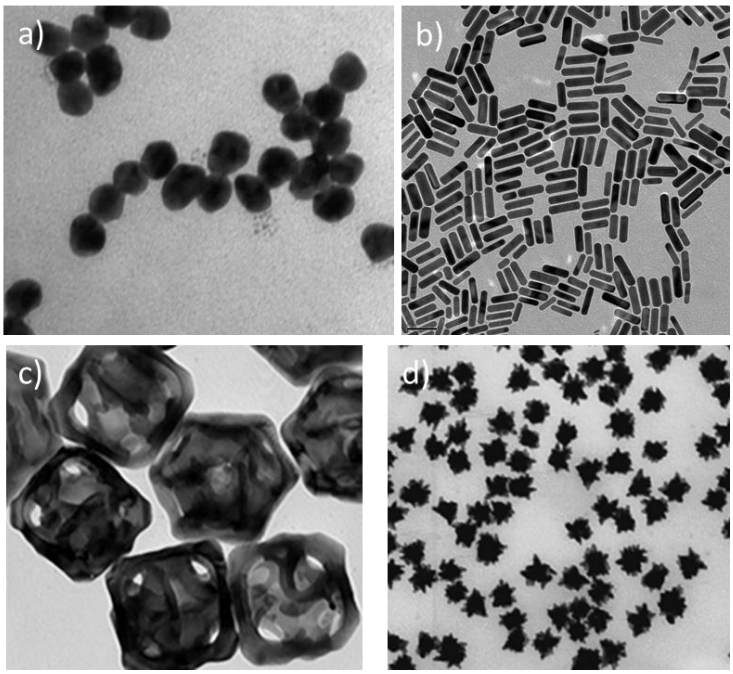

Figure 1.26: *Gold nanoparticle shapes:* ***a)*** *nanosphere,* ***b)*** *nanorod,* ***c)*** *nanocage and* ***d)*** *nanostar.*

One of the most conventional routes for AuNPs synthesis, developed by Turkevitch et al. in 1951, but still in use, consists on the reduction of Au(III) in $HAuCl_4$ by citrate in water. It is known as the citrate reduction method, which allows the formation of citrate stabilized AuNPs and a controlled size of the particles by varying the citrate/gold ratio.[150] This method provides nanoparticles that can be used as precursors in the synthesis of other AuNPs due to the non-covalent nature of the citrate-gold binding, which can be easily replaced with other molecules of interest, namely with thiol or even amine functional groups.[149,151]

An important breakthrough was due to Brust et al., who introduced in 1994 a new procedure for the efficient synthesis of stable gold nanoparticles with reduced dispersity and controlled size. This procedure is based on the use of thiolated ligands that strongly bind to gold due to the soft character of both Au and S. After addition of a reducing agent (*e.g.* $NaBH_4$), the Au(III) is reduced to Au(I) and the AuNPs are formed. This opened the opportunity to develop AuNPs using a great variety of thiolated ligands. This method allows the control of core nanoparticle size by shifting the ratio of thiol/Au in the reaction

mixture; for instance, the use of larger thiol/Au ratios affords smaller core sizes with less polydispersity. The obtained AuNPs can be repeatedly isolated and re-dissolved in common solvents without irreversible aggregation or decomposition, while maintaining the capability of being functionalized with different bioactive molecules, namely therapeutic drugs or target specific vectors.[149,152,153]

1.5.3.2 Gold Nanoparticles in Cancer Imaging and Theranostics

In the biomedical field, AuNPs possess particular properties that make them very compelling for pharmaceutical development. They have very good biocompatibility (non-toxic) as gold is resistant to oxidation under physiological conditions. AuNPs present unique optical properties by their localized surface plasmon resonance, which are dependent on the size and shape of the nanoparticles. Moreover, they offer versatile functionalization with biomolecules for the targeting of tumor cells. Based on these interesting and unique properties, AuNPs have been investigated in diverse areas of cancer imaging and therapy.[102,147,149]

One of the major applications of AuNPs as therapeutic agents is in the field of photothermal therapy. When irradiated with focused laser pulses of suitable wavelength the AuNPs can reach temperatures of 70 - 80 ºC, thus killing the cancer cells and destroying tumor tissue.[154-156] When using absorbance wavelength in the visible range only large sized nanoparticles (>300 nm) exhibit sufficient light absorbance to induce cell death. However, with the development of near-infrared (NIR) lasers, smaller sized AuNPs were also shown to induce cell death. Thus, NIR lasers opened the possibility for a wider range of AuNPs in photothermal therapy.[157]

AuNPs have been applied as drug delivery platforms for cytotoxic molecules, as for example Tumor Necrosis Factor-Alpha (TNF-α) or doxorubicin. In this case, the nanoparticle itself is not the therapeutic agent, but it can lead to the enhancement of the cytotoxic effect of the molecule it is carrying, by increasing the drug payload, increasing its bioavailability or “protecting” the drug from degradation in the biological medium. In addition, the use of AuNPs for drug delivery can minimize adverse side effects or overcome Multidrug Resistance (MDR).[158,159,160]

As *in vivo* imaging agents, AuNPs have shown promising results as contrast agents for CT imaging, due to their high absorption coefficient, and for Surface-Enhanced Raman Spectroscopy (SERS), an optical technique based on Raman scattering by molecules adsorbed on metal surfaces or nanostructures. SERS offers advantages over traditional technologies like fluorescence, since it has better sensitivity, high levels of multiplexing, robustness, and superior performance in blood and other biological matrices.[161]

Although some studies have already shown significant potential for AuNPs in Raman imaging, it should be noted that this technique is still limited by tissue penetration of the optical signal. Hence, Raman spectroscopy imaging is only clinically relevant to image tissues that are close to the surface of the skin (breast cancer), are accessible by endoscopy (esophagus and colon cancer), or for intraoperative visualization in image guided surgery.[162,163]

Another optical imaging that is explored using AuNPs is NIR, a technique that uses the near-infrared region of the electromagnetic spectrum. Used in combination with SERS, NIR imaging can allow for multiplexed and simultaneous imaging of many tumor if an efficient targeting can be achieved.[164]

The rapidly advancing field of cancer nanotechnology has generated several innovative radionuclide delivery systems to improve and enhance their targeted transport to the tumor sites, including nanocarriers like AuNPs.[39,145,165]

Incorporation of the radionuclide can be done with or without modification of the nanoparticle surface. In some cases chelator molecules are conjugated to the nanoparticle core for the coordination of radiometals, while another possibility is to encapsulate the radionuclide inside the nanoparticle, which is more commonly found in liposomes. For nuclear imaging or radionuclide therapy it is of great importance that the incorporation of the radioisotope remains stable during *in vivo* administration in order to exercise properly its function. Otherwise, radioisotope biodistribution will no longer reflect that of the nanoparticles, which means the imaging data will not be useful to predict the fate of the nanoparticles.[39,165]

Table 1.4 presents a selection of various nanocarriers other than AuNPs that have been labeled with radionuclides and evaluated as (nano)radipharmaceuticals for SPECT and PET imaging.

Table 1.4: *Selected examples of radiolabeled nanoparticle in cancer studies.*

Type of Nanoparticle	Radionuclide	Imaging Applications	Reference
Liposome	^{111}In	SPECT imaging of breast, head and neck, glioma and lung cancers. Mammary carcinoma in mice. Lung carcinoma and breast adenocarcinoma in mice.	166-168
Liposome	^{99m}Tc	Kaposi's sarcoma in mice. Mammary cancer in mice.	169,170
Liposome	^{67}Ga	Yoshida sarcoma in rats.	171
Liposome	^{64}Cu	Human colon adenocarcinoma in mice. Human neuroendocrine tumors in mice.	172,173
Liposome	^{18}F	Colorectal carcinoma in mice. Glioma in mice.	174,175
Iron Oxide Nanoparticles	^{64}Cu	PET/MRI imaging of human glioblastoma in mice.	176
Iron Oxide Nanoparticles	^{18}F	PET/CT imaging in mice.	132
Quantum Dots	^{64}Cu	PET/NIRF imaging of human glioblastoma in mice	177,178
Quantum Dots	^{18}F	Multimodal imaging in mice.	179
Carbon Nanotubes	^{111}In	SPECT imaging of lymphoma in mice.	180

As mentioned above, over the last decade there has been a considerable research effort in the application of AuNPs for multimodal tumor imaging and cancer theranostics. In particular, several reports have been made on the potential of AuNPs for the development of SPECT and PET radiopharmaceuticals, using a great variety of radioisotopes and gold nanoplatforms (Table 1.5). However, so far, most of the reported studies are of the proof-of-principle type, and have not been translated to the clinical stage.

Table 1.5: *Selected examples of AuNPs radiolabeled with different radionuclides.*

Nanoconstruct	Radionuclide	Study	Reference
HYNIC-GGC-AuNP-c[RGDfK(C)]	^{99m}Tc	Molecular imaging of tumor $\alpha_v\beta_3$ expression.	181
EDDA/HYNIC-GGC-AuNP-Lys^3-bombesin	^{99m}Tc	Molecular imaging of tumor GRPR expression	182
Au@DTDTPA	^{99m}Tc/^{111}In	Nanoparticle tracking in healthy mice.	183
AuNP-OPSS-DOTA/DTPA	^{64}Cu/^{111}In	T cell nanoparticle uptake analysis.	184
DTPA-IgG-HAuNS	^{111}In	.Molecular imaging of EGFR-positive tumors.	185
NS-RGDfK	^{64}Cu	$\alpha v\beta_3$ expressing tumor targeting.	186
ICAM-GdNRs	^{125}I	Targeted imaging of inflammation.	187
cRGD-PEG-AuNP	^{125}I	Targeting and imaging of RGD receptor expression tumor.	188
AuNP-Tat-BN	^{99m}Tc + ^{177}Lu	Targeted radiotherapy and imaging of prostate cancer.	189
Lip-EnkGNP	^{68}Ga	Molecular imaging of brain.	190

To apply AuNPs in the design of SPECT and PET nanoradiopharmaceuticals, some key factors still need to be addressed, like the uptake in the RES organs, which is a major challenge for *in vivo* imaging. The development of chelators with the capability to maintain a stable radionuclide coordination *in vivo* is also important in order to avoid non-specific uptake in non-targeted organs. Also, to increase the specific binding of the radiolabeled AuNPs to the tumors, the choice of targeting moieties such as peptides or antibodies, needs to be thoroughly studied.[39,165]

1.6 Thesis Outline

The work presented in this thesis was aimed at developing AuNP platforms for the target-specific delivery of $^{67/68}$Ga to tumor tissues, having in mind the design of new theranostic tools for cancer imaging and/or therapy. Gold nanoparticles containing DTPA and DOTA derivatives and decorated with target specific peptides towards GRPr and

EGFr (BBN and GE11, respectively) were synthesized and characterized. Their capacity to coordinate ^{67}Ga was evaluated and their biological properties were studied.

Also, a new family of N_4O_2-donor acyclic ligands was developed in this work, and its coordination capability evaluated towards Ga(III), aiming to assess their suitability for applications in radiopharmaceutical research.

Chapters 2 and 3 will focus on the synthesis, characterization, and *in vitro*/*in vivo* biological evaluation of ^{67}Ga-labeled BBN-containing gold nanoparticles stabilized with DTPA and DOTA derivatives. These studies were performed to get insight on their usefulness to design new tools for prostate cancer theranostics.

Chapter 4 describes the conjugation of GE11 to different types of gold nanoparticles, evaluation of their capability to coordinate ^{67}Ga, and *in vitro* and *in vivo* biological studies, aiming to identify the most promising ones for the specific targeting of EGFr-postive tumors.

Chapter 5 will focus on the synthesis and characterization of new families of N_4O_2-donor acyclic ligands containing a dien backbone and bearing a pyridyl or pyrazolyl unit in the central nitrogen and phenol groups at the terminal amines. It also comprises the studies performed to assess their suitability for radiogallium coordination under the condition required in the preparation of radiopharmaceuticals.

Finally, main conclusions and detailed experimental procedures will be described in Chapters 6 and 7, respectively.

Chapter 2: BBN-containing Gold Nanoparticles Stabilized with a DTPA derivative for the Targeting of GRPr-positive Tumors

2.1 Introduction

As referred in the introductory Chapter, one of the goals of this PhD work was to develop ^{67}Ga-labeled AuNPs that could target *in vivo* Gastrin-Releasing Peptide receptors (GRPr). By focusing in this particular target, it was taken into consideration that GRPr are overexpressed in a great variety of cancers, including prostate, breast, pancreas, gastrointestinal and small lung cancer, being a prime target for the diagnostic and therapy of cancer.[191]

GRP is a mammalian neuropeptide that is present in a variety of tissues including brain, spinal cord and in the gastrointestinal tract where it is present in higher concentrations. GRP performs a wide variety of functions from regulation of circadian rhythm to modulation of the activity of the immune system. In the gastrointestinal tract it is responsible for the stimulation of the release of gut hormones, including gastrin. GRP is structurally related to the amphibian peptide bombesin (BBN) (Figure 2.1).[192,193]

BBN is a 14-amino acid peptide that displays a very high affinity for GRPr, which mediates its biological effect. Therefore, BBN derivatives have emerged as very attractive targeting vectors for the diagnostic and therapy of cancers that overexpress GRPr.[23,194,195] The specificity of BBN towards GRPr is directly related to the amino acid sequence Trp-Ala-Val-Gly-Hist-Leu-Met (BBN[7-14]). Therefore, any structural alterations undergone when developing a BBN derivative should take this into account.[196]

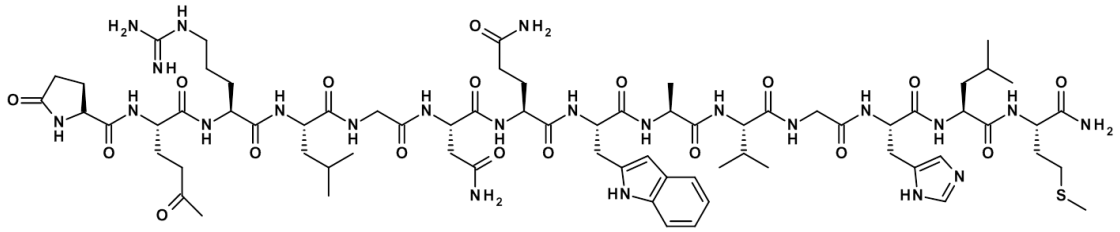

Pyr-Gln-Arg-Leu-Gly-Asn-Gln-Trp^{8}-Ala-Val-Gly-His-Leu-Met^{14}-NH_2

Figure 2.1: *Chemical structure of Bombesin and respective amino acid sequence.*

BBN derivatives are a class of molecules that present remarkable targeting properties for cancer management, being useful to provide enhanced delivery of therapeutic drugs or diagnostic agents to tumor sites. A particular field in which the development of BBN derivatives has a very high impact is in radiopharmaceutical

development, being reported several examples of BBN derivatives that gave promising results in the target-specific delivery of radionuclides to tumor tissues (Table 2.1).

Table 2.1: *Selected examples of radiolabeled BBN derivatives studied as diagnostic or therapeutic radiopharmaceuticals.*

BBN derivative	Radionuclide	Amino acid sequence	Reference
HYNIC-Bombesin	^{99m}Tc	NQWAVGHLM-NH_2	197
GGG-BBN[7-14]	^{99m}Tc	GGGQWAVGHLM-NH_2	198
[DTPA-Pro1,Tyr4]BN	^{111}In	PQRYGNQWAVGHLM-NH_2	199
SarAr-SA-Aoc-GSG-bombesin(7-14)	^{64}Cu	GSGQWAVGHLM-NH_2	200
BZH3	^{68}Ga	YQWAVH-Thi-Nle-NH_2	100
FB-[Lys^3]BBN	^{18}F	Glp-QKLGNQWAVGHLM-NH_2	201
DOTA-BN[2-14]NH(2)	^{177}Lu, ^{90}Y	QRLGNQWAVGHLM-NH_2	202

The use of BBN derivatives has also been explored in the targeted delivery of nanoparticle platforms to tumor tissues. Different types of nanoparticles, ranging from liposomes and iron oxide to polymeric and gold nanoparticles, have been successfully conjugated with BBN derivatives. In general, the resulting BBN containing nanoparticles displayed good affinity and specificity towards GRPr overexpressing cell lines and/or cancer tissue, and showed improved cellular and/or tumor uptake when compared with their non-BBN functionalized analogs.[203-205]

Regarding gold nanoparticles, the group of Kannan et al. has demonstrated that the BBN loading into the surface of AuNPs can effectively enhance the target specific delivery of AuNPs to prostate cancer PC3 cells. They have also studied the same AuNPs labeled with ^{198}Au, which is a β^- emitter. The use of radioactive gold allowed a more straightforward study of the biological fate of these BBN-containing AuNPs, offering also the possibility of exploring these AuNPs as targeted radiotherapy agents.[146,206]

Radiolabeled BBN-containing AuNPs have been further explored by Morales-Avila and co-workers. These authors have successfully labeled this type of nanoparticles with ^{99m}Tc, and reported that the resulting ^{99m}Tc-labeled AuNPs show significant uptake in the pancreas and GRPr positive tumors in athymic mice induced with prostate cancer PC3

cells. Altogether, these findings indicate that AuNPs decorated with BBN derivatives have great potential for the *in vivo* target specific delivery of radionuclides to tumor cells.[182]

In this PhD work it was reasoned that BBN-containing AuNPs could be suitable platforms for the target specific delivery of radiogallium ($^{67/68}$Ga), providing innovative tools for SPECT/PET imaging, and for potential theranostic applications.

To attain such goal, the first explored strategy has been based on AuNPs stabilized with a DTPA derivative (Figure 2.2) and conjugated with a BBN targeting vector. This type of AuNP platform has been introduced by Roux et al., who have synthesized AuNPs stabilized with a thiolated amino-carboxylate designated **DTDTPA** (Dithiolated Diethylenetriamine Pentaacetic Acid).[207]

These authors have shown that these AuNPs can coordinate to gadolinium and showed very promising results as contrast agents for MRI imaging. Very recently, during the later course of this PhD work, they have also proved that these **DTDTPA** stabilized AuNPs can be directly labeled with ^{99m}Tc and ^{111}In, indicating that they could have potential for the design of (nano)radiopharmaceutical.[183,207,208] It was hypothesized that these AuNPs could also present the necessary requisites to achieve a stable coordination of gallium and, at the same time, allow the conjugation with receptor-specific targeting vectors, particularly with BBN derivatives.

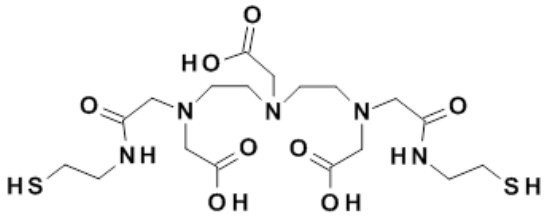

Figure 2.2: *Chemical structure of* ***DTDTPA****.*

The evaluation of the potential interest of AuNPs stabilized with **DTDTPA** and decorated with BBN analogs (Figure 2.3) for the target-specific delivery of gallium radioisotopes comprised the following studies, as described in this Chapter:

i) Synthesis and characterization of **DTDTPA** stabilized AuNPs (**AuNP-DTDTPA**).

ii) Evaluation of the capacity of **AuNP-DTDTPA** to coordinate natural gallium: Synthesis and characterization of **AuNP-DTDTPA-Ga**.

iii) Functionalization of **AuNP-DTDTPA** with a thiolated BBN derivative: Synthesis and characterization of **BBN-AuNP-DTDTPA**.

iv) Radiolabelling studies of **AuNP-DTDTPA** and **BBN-AuNP-DTDTPA** using ^{67}Ga.

v) Biological evaluation: *in vitro* studies with human prostate cancer PC3 cells and *in vivo* studies with PC3 xenografted Balb/c mice.

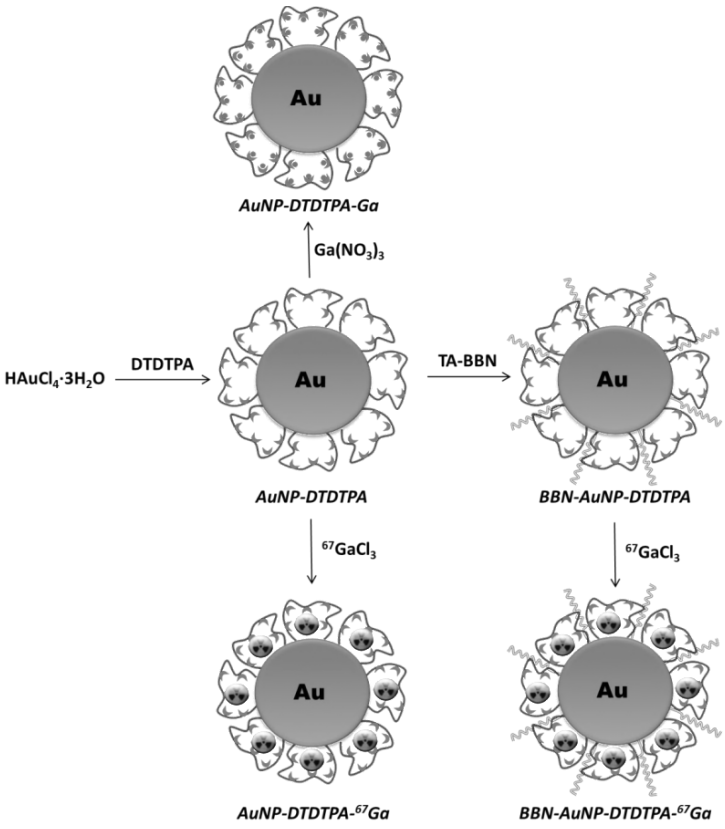

Figure 2.3: *Schematic representation on the synthetic strategies used to obtain the different AuNPs described in Chapter 2.*

2.2 Synthesis of AuNP-DTDTPA and Evaluation of its Coordination Capability Towards Ga(III)

The **AuNP-DTDTPA** nanoconstructs were obtained based on the method reported by Roux et al. using **DTDTPA**, which forms a polymeric coating around the gold core and stabilizes the nanoparticle while still maintaining its coordination capability towards metal ions.[208]

Briefly, **AuNP-DTDTPA** was synthesized by reduction of $HAuCl_4 \cdot 3H_2O$ with $NaBH_4$ in the presence of excess **DTDTPA** (1:1.8 Au/**DTDTPA**), and were obtained in the form of a black precipitate after adequate purification. Their purification was done by centrifugation and washing with 0.01 M HCl, H_2O and diethyl ether.

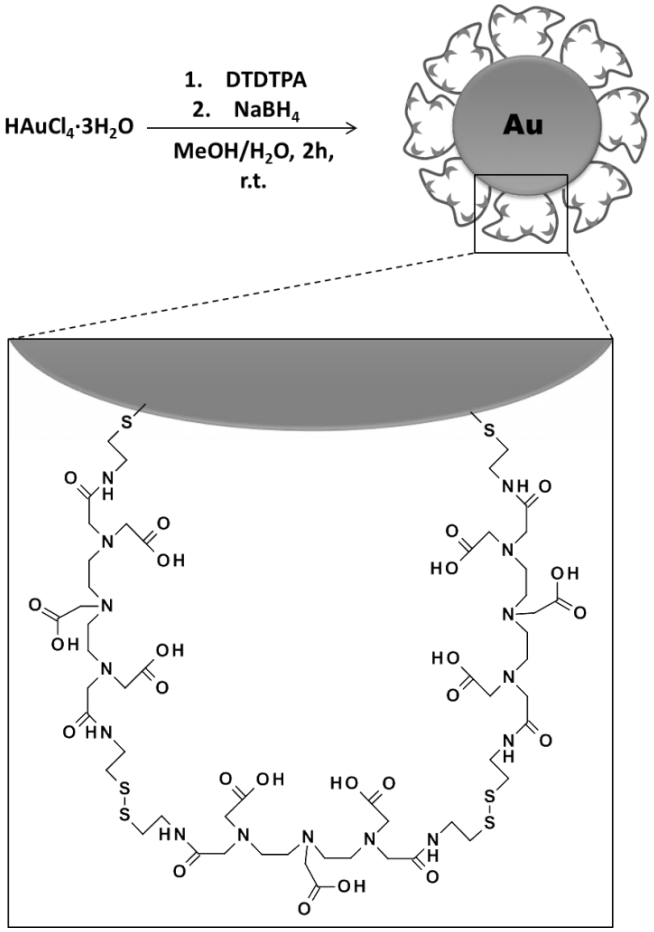

Scheme 2.1: *Synthesis of* ***AuNP-DTDTPA****.*

Prior to the evaluation of the coordination capability of **AuNP-DTDTPA** towards Ga(III), it was important to assess the amount of **DTDTPA** attached to the nanoparticle surface, and in particular the number of conjugated **DTDTPA** per nanoparticle. This has been done based on the determination of the amount of gold by Atomic Absorption Spectrometry (AAS) and on the assessment of the nanoparticle concentration by Nanoparticle Tracking Analysis (NTA).

The AAS analysis of the gold content of **AuNP-DTDTPA** has shown that the synthesized nanoparticles contain 45% of gold (w/w). Taking into consideration that these nanoconstructs consist solely of the gold core and the **DTDTPA** coating, the measured amount of gold led to an estimation of 55% of **DTDTPA** (w/w) in these nanoconstructs.

NTA is a technique for visualization and analysis of nanoparticles in solution, by correlation of the rate of Brownian motion to the particle size. Laser light is used to illuminate the particles, which in turn are visualized due to the scattering of the incident light. The light scattered by the particles is captured using a digital camera and the motion of each particle is tracked from frame to frame (Figure 2.4). It is important to use diluted solutions since overly concentrated solutions will lead to an overlap of the scattered light. By taking the average number of particles per frame it is possible to determine the nanoparticle concentration in solution.[209]

The NTA analysis of a diluted aqueous solution of **AuNP-DTDTPA** (6.66×10^{-2} mg/mL) showed that there are 1.67×10^{14} NP/mg. Combining this result with the AAS analysis, it is possible to estimate the number of **DTDTPA** molecules per nanoparticle, which corresponds to ≈ 260 **DTDTPA**/NP.

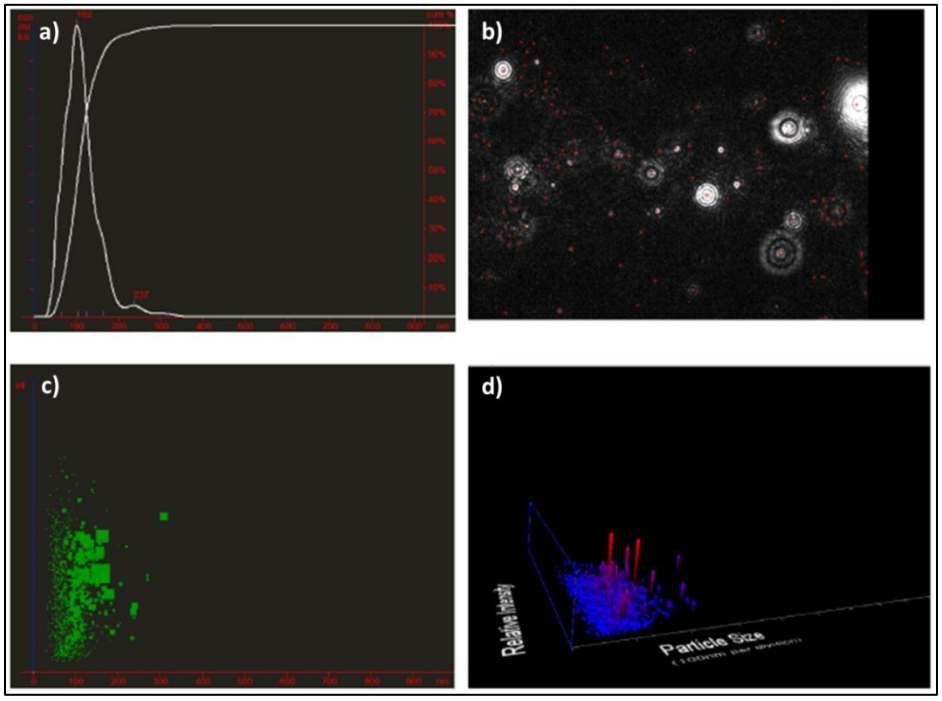

Figure 2.4: *NTA analysis of* ***AuNP-DTDTPA*** *nanoparticles:* ***a)*** *Particle size/concentration,* ***b)*** *Sample video frame,* ***c)*** *Particle size/relative intensity and* ***d)*** *Particle size/relative intensity 3D plot.*

After confirming the concentration of **DTDTPA**, it has evaluated the coordination capability of **AuNP-DTDTPA** towards Ga(III), aiming to assess the maximum amount of gallium that could be loaded into the nanoparticles. This study was done by reaction of **AuNP-DTDTPA** with $Ga(NO_3)_3$ at pH ≈ 6 (Scheme 2.2), and by determining the amount of unreacted Ga(III) by ^{71}Ga-NMR as described below.

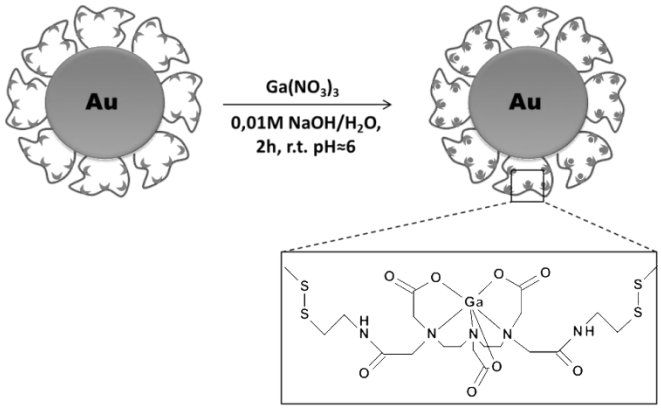

Scheme 2.2: *Synthesis of* ***AuNP-DTDTPA-Ga****.*

To determine the amount of unreacted Ga(III), a calibration curve has been established based on the ^{71}Ga-NMR analysis of aqueous $Ga(NO_3)_3$ solutions with known concentrations, in the range 0.0001 - 0.1 M. To obtain the calibration curve the ^{71}Ga-NMR spectra of the different solutions were recorded using the same acquisition parameters. An integration value of 100 has been assigned to the ^{71}Ga-NMR signal of the solution with the highest gallium concentration (0.1 M). The obtained calibration curve is shown in Figure 2.5.

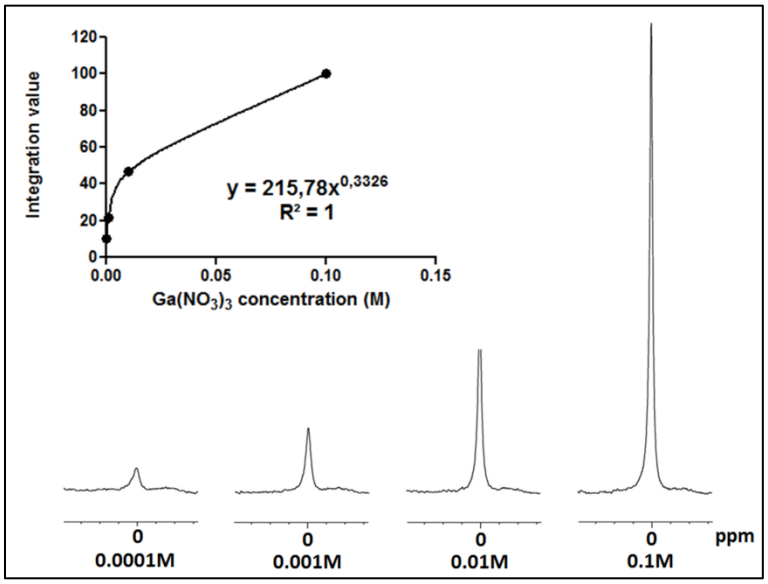

Figure 2.5: *^{71}Ga-NMR spectra of the standard solutions of $Ga(NO_3)_3$ in D_2O with concentrations in the range of 0.0001 - 0.1 M. Inset graph shows the standard curve of the integration of the ^{71}Ga-NMR peaks as a function of the $Ga(NO_3)_3$ concentration.*

Instead of a linear regression line fit for the standard curve, it was observed however that while the concentrations of the solutions were prepared in ten-fold dilutions the integration values obtained had only two-fold variations. Hence, it was verified that a quadratic non-linear regression curve afforded a more adequate fit for the standard curve with a $R^2 = 1$.

As shown in Scheme 2.2, the coordination capability of **AuNP-DTDTPA** towards Ga(III) was studied by reacting aqueous solutions containing 5 mg of the nanoparticles with different amounts of $Ga(NO_3)_3$ (7.5 - 30 mg), at room temperature for 2 h. After centrifugation of the reaction mixtures, the supernatants were analyzed by ^{71}Ga-NMR,

which allowed the estimation of unreacted Ga(III) based on the calibration curve presented in Figure 2.5.

Taking into account the starting amount of gallium, it was possible to calculate the amount of Ga(III) loaded into the AuNPs for the different concentrations under study. The results obtained are shown in Figure 2.6, and indicates that the saturation threshold of coordinated gallium corresponds to a total of ≈ 0.15 mg of gallium per mg of nanoparticles.

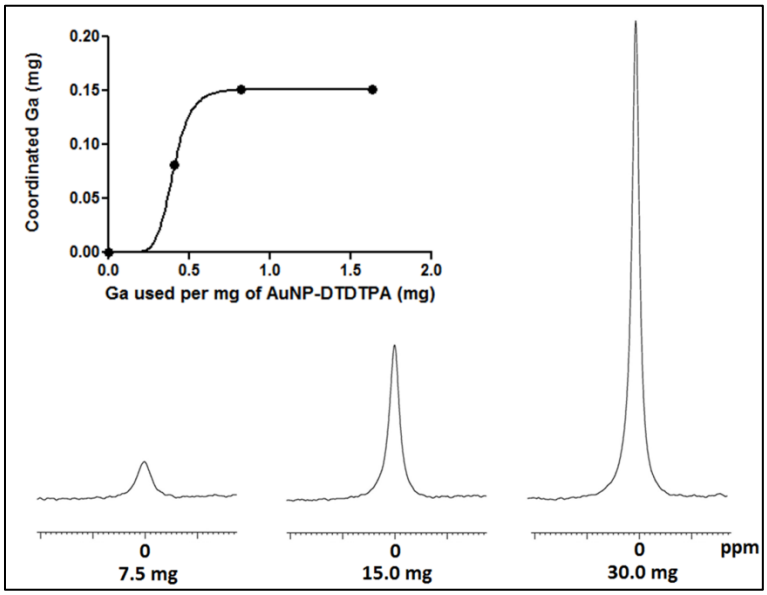

Figure 2.6: *^{71}Ga-NMR spectra of the supernatants of the reactions of* ***AuNP-DTDTPA*** *with different amounts of reacted $Ga(NO_3)_3$. Inset graph shows the amount of gallium coordinated to 1 mg of* ***AuNP-DTDTPA*** *for the various concentrations of gallium under study.*

The ^{71}Ga-NMR studies were used as an indirect approach to determine the maximum amount of coordinated gallium per mg of nanoparticles. Alternatively, the saturation threshold of coordinated gallium was also assessed by ICP-OES, which allowed the direct determination of the amount of Ga(III) coordinated to the **AuNP-DTDTPA**.

For the studies using ICP-OES analysis, aqueous solutions containing 1 mg of **AuNP-DTDTPA-Ga** were treated with different amounts of $Ga(NO_3)_3 \cdot 4H_2O$ (0.1 - 5.5 mg). After reaction, the AuNPs were separated by ultra-filtration and washed with distilled water. The recovered AuNPs were digested in an *aqua regia* solution (HNO_3/HCl (3:1)) under microwave heating, and then analyzed by ICP-OES. The results obtained are shown in Figure 2.7.

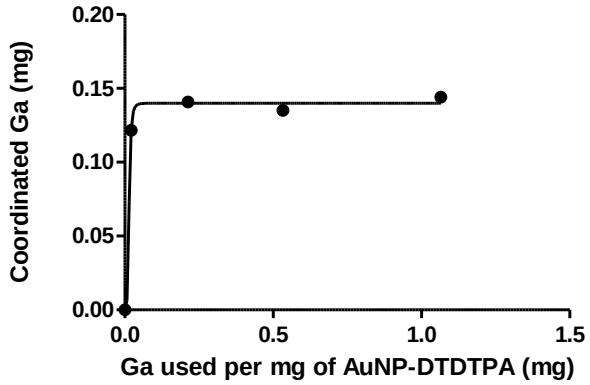

Figure 2.7: *Determination of gallium coordinated to* ***AuNP-DTDTPA*** *by ICP-OES analysis: results obtained upon treatment of 1 mg of* ***AuNP-DTDTPA*** *with different amounts of* $Ga(NO_3)_3 \cdot 4H_2O$.

The results obtained by ICP-OES indicate that the maximum amount of gallium that can be loaded to **AuNP-DTDTPA** is ≈ 0.14 mg per mg of nanoparticles (Figure 2.7), which is in agreement with the value obtained in the ^{71}Ga-NMR studies (≈ 0.15 mg per mg of nanoparticles) (Figure 2.8).

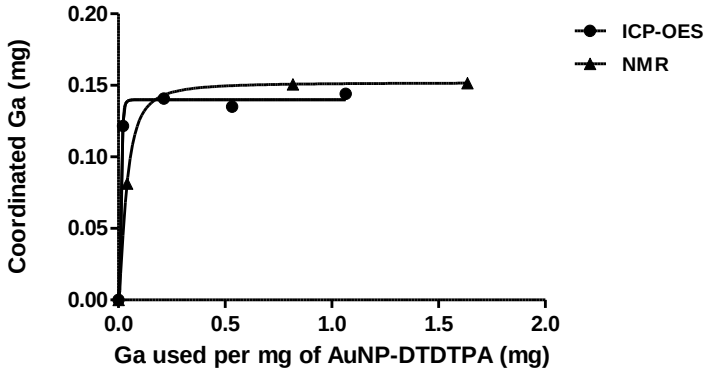

Figure 2.8: *Comparison of the amount of coordinated gallium per mg of* ***AuNP-DTDTPA*** *determined by ICP-OES and ^{71}Ga-NMR as a function of the amount of reacting Ga(III).*

The molar amount of gallium loaded per mg of **AuNP-DTDTPA**, determined either by ^{71}Ga-NMR (0.15 mg, 2.1×10^{-3} mmol) or ICP-OES (0.14 mg, 2.0×10^{-3} mmol), is roughly two-fold higher than the molar amount of conjugated **DTDTPA** determined by AAS analysis (0.55 mg, 1.1×10^{-3} mmol). This finding indicates that each Ga(III) ion is not just

coordinated to one individual unit of the **DTDTPA** chelator, which is most probably due to the presence of a polymeric **DTDTPA** coating that allows the interaction of each Ga(III) ion with N, O or S atoms from different **DTDTPA** units.

2.3 Characterization of AuNP-DTDTPA and AuNP-DTDTPA-Ga

The nanoconstructs **AuNP-DTDTPA** and the congener nanoparticles containing Ga(III), herein designated as **AuNP-DTDTPA-Ga**, were further characterized by a variety of techniques, spanning from conventional ones (UV-Vis and TEM) to more sophisticated and multiple analytical tools (DLS, XPS, EDX, HAADF and EELS). In this way, it was intended to obtain a detailed and precise structural characterization of the AuNPs including at the atomic level, aiming also to evaluate the influence of the presence of the Ga(III) ions in the physico-chemical properties of the nanoparticles.

The **AuNP-DTDTPA-Ga** that **were** submitted to the characterization by several analytical techniques corresponded to those having a saturated amount of gallium, and were obtained using a 2:1 ratio (w/w) of Ga/Au.

2.3.1 UV-Vis Spectroscopy

UV-Vis analysis of **AuNP-DTDTPA** and **AuNP-DTDTPA-Ga** were performed in order to provide information regarding the size and shape of the gold core of the nanoparticles.

UV-Vis is one of the most commonly used techniques for AuNP characterization. AuNPs have optical properties that are sensitive to size, shape, concentration, agglomeration state, and refractive index near the nanoparticle surface, which makes UV-Vis spectroscopy a valuable tool for identifying, characterizing, and studying these types of nanoparticles.[210]

As shown in Figure 2.9, the UV-Vis spectrum of **AuNP-DTDTPA** shows a small absorption band centered at ≈ 520 nm, which corresponds to the surface plasmon resonance band. This band is observed in UV-Vis spectrum of AuNPs due to the interaction of incident electromagnetic radiation with the free electrons at the interface between the particle and the medium surrounding the particle. Such interaction causes a concerted oscillation of electron charge in resonance with the frequency of visible light,

leading to resonant oscillations that are known as surface plasmons.[210] A single plasmon absorption band was observed for **AuNP-DTDTPA**, which indicates that the particles are spherical shaped and larger than 2 nm, since in the case of smaller sized AuNPs (< 2 nm) the absorption band is generally not possible to visualize. The absorption band however, has a very low intensity for the concentration of nanoparticles used ($8x10^{-2}$ mg/mL), which means that the AuNPs are not very large (< 10 nm).[211]

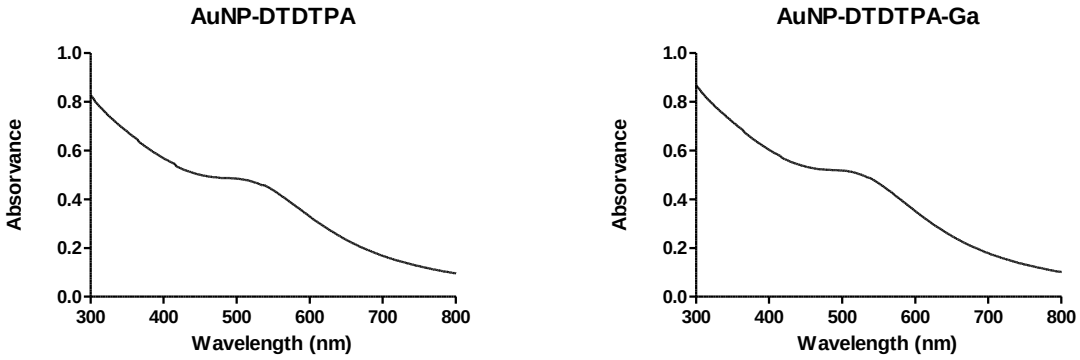

Figure 2.9: *UV-Vis spectra of* ***AuNP-DTDTPA*** *and* ***AuNP-DTDTPA-Ga*** *($8x10^{-2}$ mg/mL).*

UV-Vis analysis of **AuNP-DTDTPA-Ga** also showed the presence of a single broad absorption band centered at ≈ 520 nm (Figure 2.9), almost superimposable with the one exhibited by **AuNP-DTDTPA**. This result indicates that the loading of the AuNPs with gallium did not cause any significant alterations in the core size and shape of the nanoparticles.

2.3.2 Transmission Electron Microscopy (TEM)

As seen above, UV-Vis is an easy and accessible tool that can provide an estimation on the size and shape of AuNPs. However, to have more detailed data on these two parameters it is necessary to use more advanced techniques like TEM.

TEM is a very important tool in the characterization of nanoparticles; it allows direct imaging and quantitative measurements of particle size, size distribution, and morphology. This technique is based on the transmission of a focused beam of electrons through a sample, forming an image in an analogous way to a light microscope. However, the use of

electrons instead of light grants TEM a significantly higher resolution when compared to light-based imaging techniques.[212]

AuNP-DTDTPA and **AuNP-DTDTPA-Ga** were studied by TEM and the images obtained are shown in Figure 2.10. TEM analysis of **AuNP-DTDTPA** (Figure 2.10a) confirmed the UV-Vis results, showing the presence of spherical nanoparticle with small-sized core (2.28 ± 1.32 nm) and with a relatively narrow size distribution. High Resolution-TEM analysis of **AuNP-DTDTPA** showed the presence of lattice planes (Figure 2.10b) indicating a crystalline structure for these AuNPs. TEM analysis of **AuNP-DTDTPA-Ga** (Figure 2.10c) confirmed that the core size of the nanoparticles remains in the same size range (2.61 ± 1.31 nm) after coordination of Ga(III).

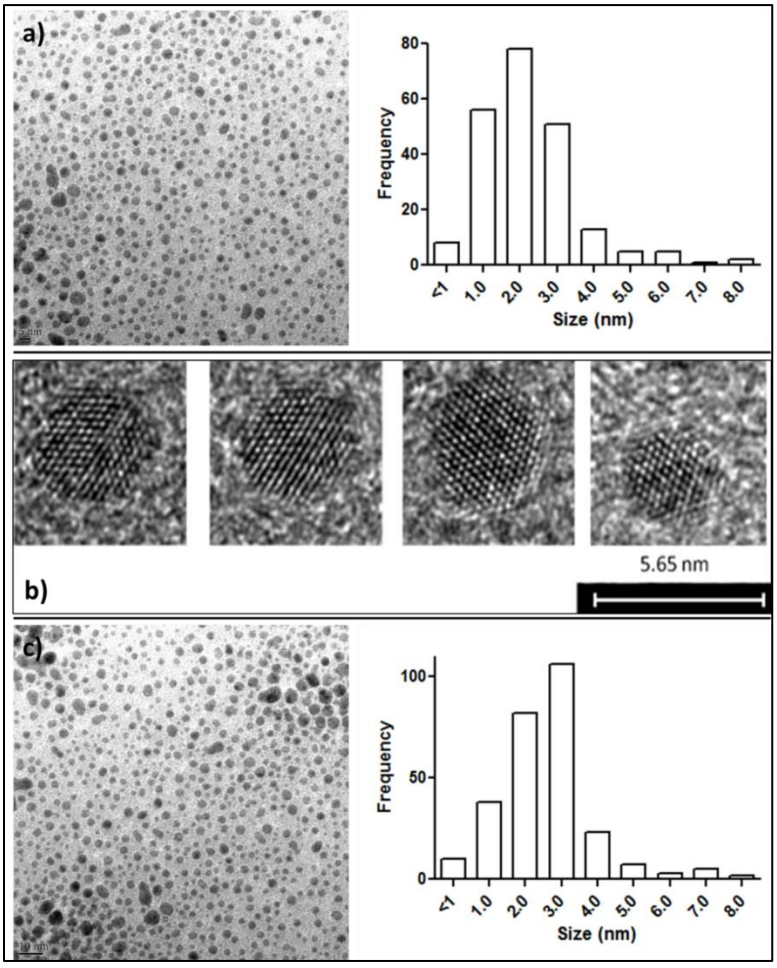

Figure 2.10: *TEM image with respective size histogram (**a**) and HR-TEM (**b**) of **AuNP-DTDTPA**; **c)** TEM image with respective size histogram of **AuNP-DTDTPA-Ga**.*

2.3.3 Dynamic Light Scattering (DLS) Analysis and Zeta-Potential Measurement

The data obtained by the characterization of **AuNP-DTDTPA** and **AuNP-DTDTPA-Ga** by UV-Vis and TEM provided detailed information on its general core size and shape. However, these parameters do not take into account the presence of the **DTDTPA** coating around the gold core of the nanoparticles. Most importantly, one should take into account that it is common for nanoparticles in solution to aggregate, and the level of aggregation can vary with the surrounding medium. When nanoparticles aggregate their behavior will be more resembling of larger sized particles, which is something that should be taken into consideration when performing biological studies, since the level of aggregation can influence the biological profile of the nanoparticles.

In order to gather information on the size of the nanoparticles in solution (hydrodynamic size) and on its potential tendency to aggregate, their characterization usually involves DLS analysis and the determination of the zeta-potential.

DLS relies on the measurement of scattered light from a laser that passes through a colloidal solution. By analyzing the modulation of the scattered light intensity as a function of time, the hydrodynamic size of the particles and particle agglomerates can be determined. Generally associated to the value of hydrodynamic size is the PolyDispersity Index (PDI) which is a measurement of the heterogeneity of the size of the nanoparticles in solution.[213]

Zeta potential analysis is a technique useful to determine the surface charge of nanoparticles in solution. Nanoparticles have a surface charge that attracts a thin layer of ions of opposite charge to its surface; this double layer of ions travels with the nanoparticles as it diffuses throughout the solution. The electrical potential at the boundary of the double layer is known as the zeta potential, and its value typically ranges from +100 mV to -100 mV. The magnitude of the zeta potential is predictive of the stability of the nanoparticles in solution, and generally the further away from zero the more stable a nanoparticle is in solution.[214]

Determination of the hydrodynamic size and zeta-potential analysis of **AuNP-DTDTPA** and **AuNP-DTDTPA-Ga** in H_2O were performed in a Malvern Zetasizer. The results obtained are presented in Figure 2.11 and Table 2.2.

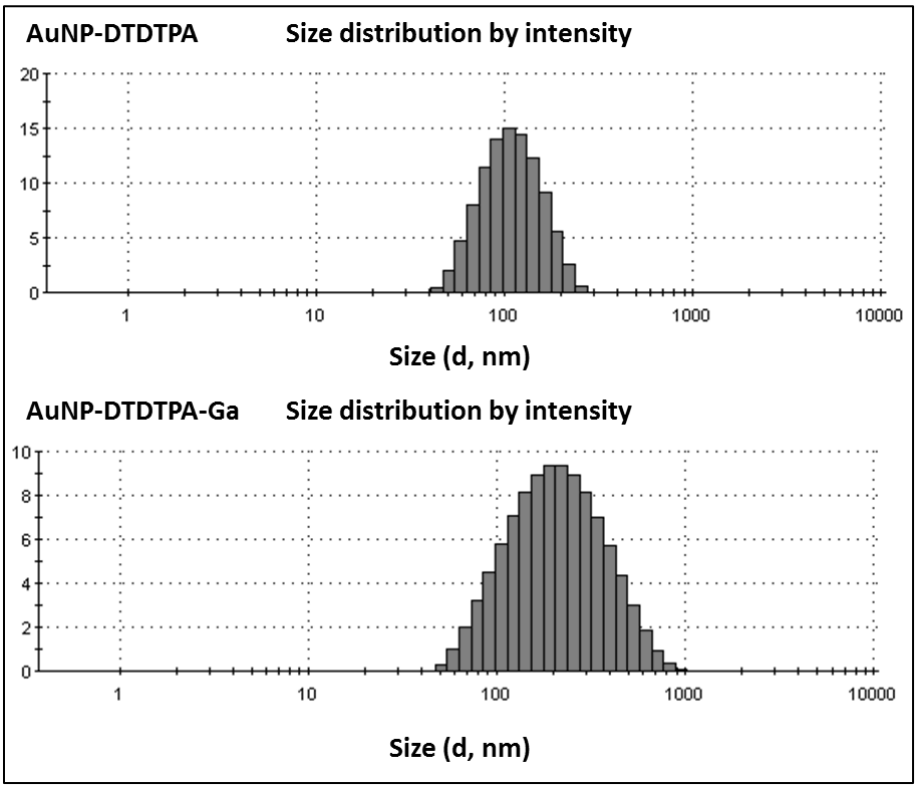

Figure 2.11: *Hydrodynamic size distribution of* ***AuNP-DTDTPA*** *and* ***AuNP-DTDTPA-Ga*** *in H_2O ($8x10^{-2}$ mg/mL).*

Table 2.2: *Hydrodynamic size (*PDI) and zeta-potential measurement of* ***AuNP-DTDTPA*** *in H_2O ($8x10^{-2}$ mg/mL).*

Nanoconstruct	Hydrodynamic Size (nm)	Zeta-Potential (mV)
AuNP-DTDTPA	100.6 (0.111)*	-80.7 ± 15.6
AuNP-DTDTPA-Ga	177.3 (0.226)*	+27.1 ± 5.4

DLS analysis of **AuNP-DTDTPA** (Figure 2.11 and Table 2.2) showed that these nanoparticles have a hydrodynamic size of 100.6 nm (PDI = 0.111) in H_2O. The measured hydrodynamic size is much larger than the core size of 2.28 ± 1.32 nm that was found for

these AuNPs, which reflects the presence of the **DTDTPA** coating around de nanoparticle core.

The zeta-potential analysis of **AuNP-DTDTPA** (Table 2.2) shows a very high negative value of -80.7 ± 15.6 mV, in agreement with the presence of deprotonated $–COO^-$ groups of the **DTDTPA** coating. This high zeta-potential value is also indicative a very good stability of the AuNPs in H_2O.[214]

DLS analysis of **AuNP-DTDTPA-Ga** (Figure 2.11 and Table 2.2) showed a hydrodynamic size of 177.3 nm (PDI = 0.226) in H_2O, while the zeta-potential (Table 2.2) gave a value of +27.1 ± 5.4 mV. The hydrodynamic size is significantly higher than the one of **AuNP-DTDTPA**, which seems to indicate that the coordination to gallium led to an eventual enhancement of the level of aggregation in solution. This can also be justified by the zeta-potential of **AuNP-DTDTPA-Ga** that is closer to zero if compared with that of **AuNP-DTDTPA**. Moreover, the charge of the AuNPs have shifted from negative to a positive charge due to the coordination of the $-COO^-$ groups to Ga(III).

2.3.4 Characterization by other advanced microscopy and spectroscopy techniques

Further studies were performed with the intent of getting more information regarding the distribution of gallium, the nature of the Au-S bond and the elemental composition of **AuNP-DTDTPA-Ga**. Such studies involved different advanced analytical techniques, like Scanning Transmission Electron Microscopy (STEM) conjugated with Energy Dispersive X-ray Spectroscopy (EDS), High-Angle Annular Dark-Field imaging (HAADF) and Electron Energy Loss Spectroscopy (EELS), and X-ray Photoelectron Spectroscopy (XPS).

AuNP-DTDTPA-Ga was studied by EDS, which is a spectroscopic technique that provides information on the elemental composition of a sample.[215] Initially, the EDS analysis of a bulk region (100 µm x 100 µm) of a sample of these AuNPs was performed, and the resulting spectrum is shown in Figure 2.12.

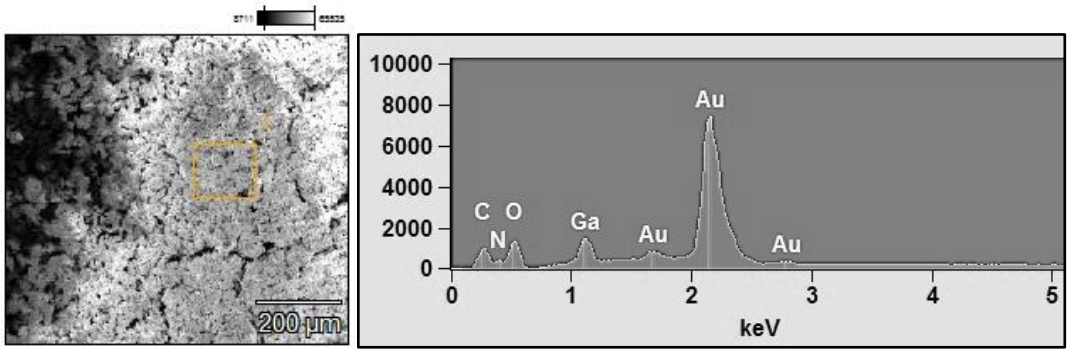

Figure 2.12: *EDS spectrum of* ***AuNP-DTDTPA-Ga*** *in a bulk area of the sample indicating a high amount of gold and also the presence of gallium.*

The EDS spectrum from a bulk region of **AuNP-DTDTPA-Ga** showed the presence of a high X-ray electron dispersion energy peak of gold (Au(M) ≈ 2.120 KeV), as well as one peak characteristic of gallium with an energy of Ga(L_α) ≈ 1.098 KeV. It is also possible to observe X-ray electron dispersion energy peaks corresponding to carbon (C(K_α) ≈ 0.277 KeV), nitrogen (N(K_α) ≈ 0.392 KeV) and oxygen (O(K_α) ≈ 0.525 KeV), confirming the presence of the DTDTPA coating.[216]

The characteristic X-ray electron dispersion energy for sulphur is found at S(K_α) ≈ 2.307 KeV, which in this case is not possible to visualize because it is overlapped with the energy peak of gold at 2.120 KeV.[216]

EDS can be conjugated with TEM and thus provide information on the elemental composition of a nanometer sized area of a sample, allowing for a more detailed information regarding the distribution of gallium within the **AuNP-DTDTPA-Ga**. As shown in Figure 2.13, two different types of scans were performed using TEM and EDS in tandem analysis of **AuNP-DTDTPA-Ga**: one directed at a region of the sample in between gold cores, and the other one pointed directly at one of the nanoparticle cores.

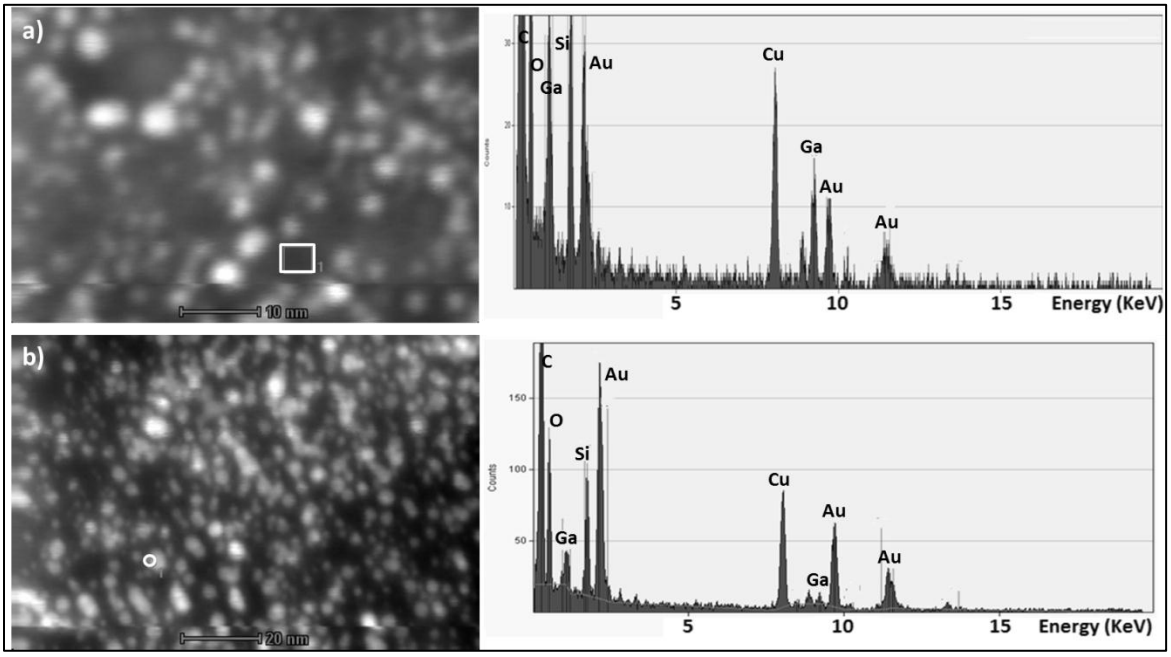

Figure 2.13: *TEM and EDS in tandem analysis of* ***AuNP-DTDTPA-Ga a)*** *in a region in between gold cores with the EDS spectrum showing low amounts of gold but high levels of gallium as well as carbon and nitrogen; and* ***b)*** *directed at one of the nanoparticle cores with the resulting EDS spectrum indicating high amounts of gold but lower levels of gallium, carbon and nitrogen.*

As can be seen in Figure 2.13a, the EDS analysis of a selective region in between the gold cores showed that the energy peaks of gold are of low intensity while the characteristic X-ray dispersion energy peaks of gallium ($Ga(L_\alpha)$ ≈ 1.098 KeV, $Ga(K_\alpha)$ ≈ 9.241 KeV) are significantly more intense. Also, the EDS spectrum displays intense energy peaks of carbon ($C(K_\alpha)$ ≈ 0.277 KeV) and oxygen ($O(K_\alpha)$ ≈ 0.525 KeV), arising from the atoms of the **DTDTPA** coating. This indicates that Ga(III) is indeed coordinated by the **DTDTPA**, as the spatial distribution of the gallium atoms and atoms of the chelator is similar.

In agreement with this finding, the analysis directed at one of the gold cores gave an EDS spectrum showing very high X-ray dispersion energy peaks characteristic of gold (Au(M) ≈ 2.120 KeV, $Au(L_\alpha)$ ≈ 9.712 KeV), and a much lower presence of gallium, carbon and oxygen (Figure 2.13b).

To have further insight on the distribution of gallium within **AuNP-DTDTPA-Ga**, Scanning TEM (STEM) imaging was performed in conjugation with High Angular Annular Dark-Field (HAADF) imaging and Electron Energy Loss Spectroscopy (EELS).

HAADF is a technique in which the unscattered electron beam of the STEM analysis is excluded from the obtained image, and thus the field around the sample is darkened. It is a technique that provides atomic resolution images where the contrast is directly related to the atomic number of the elements present in the sample.[217] EELS is a spectroscopic technique that also provides data on the elemental composition of a sample.[218] These techniques are advantageous in terms of signal acquisition, since the main beam from HAADF can pass through an EELS detector, allowing that both types of measurements can be performed simultaneously.

Two different types of scans were performed using STEM and EELS in tandem analysis of **AuNP-DTDTPA-Ga** (Figures 2.14a and 2.14b); one directed at a region of the sample in between gold cores, and the other one pointed directly at one of the nanoparticle cores. The EELS spectra obtained corroborate the results seen previously with EDS; on a selective region in between the gold cores (Figure 2.14a) it is observed the presence of a broad signal for gallium at 1100 - 1300 eV and no gold. In contrast, the analysis directed at one of the gold cores (Figure 2.14b) shows the presence of a broad peak for gold at 2300 - 2600 eV, while the gallium band was not observed.

The conjugation of EELS analysis with STEM allowed for the projection of an elemental mapping for **AuNP-DTDTPA-Ga** where it was possible to distinguish between the different metal atoms, and verify the distribution of gallium around the gold core, as seen in Figure 2.14c.

HR-STEM image of **AuNP-DTDTPA-Ga** (Figure 2.14d) allowed for the visualization of lattice planes on the nanoparticle cores, which indicates that the coordination of Ga(III) maintains the crystalline structure of the AuNPs.

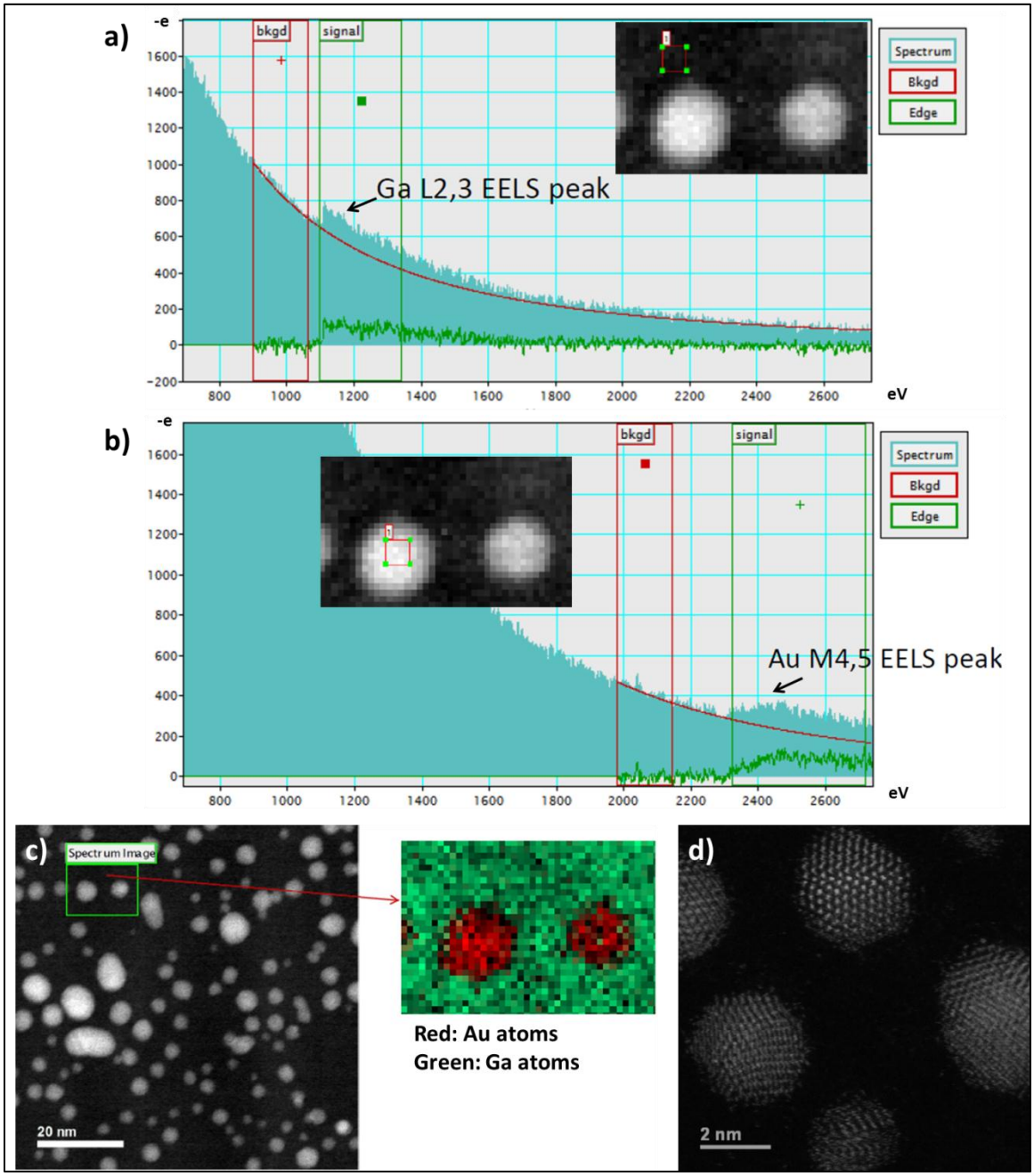

Figure 2.14: *STEM and EELS in tandem analysis of* ***AuNP-DTDTPA-Ga a)*** *in a region in between gold cores and* ***b)*** *directed at one of the nanoparticle cores, with the respective EELS spectra.* ***c)*** *STEM image with associated elemental mapping of* ***AuNP-DTDTPA-Ga*** *showing the distribution of the gold atoms in red and gallium atoms in green.* ***d)*** *HR-STEM image of* ***AuNP-DTDTPA-Ga****.*

Finally, samples of **AuNP-DTDTPA-Ga** have been analyzed by XPS analysis in order to assign the nature of the Au-S bonds, as well as to provide additional information regarding the elemental composition of the AuNPs. XPS is a technique used for surface analysis of samples, where the specimen is irradiated with mono-energetic X-rays which cause photoelectrons to be emitted from the sample surface. These photoelectrons are then detected in an electron energy analyzer that determines their binding energy, and respective intensity.[219] Figure 2.15 shows the XPS spectrum of **AuNP-DTDTPA-Ga** with the respective high resolution spectra of relevant atoms.

XPS analysis of **AuNP-DTDTPA-Ga** in the S2p region indicates a broad binding energy band expanding between 159 - 164 eV. The covalent binding energy range for S-Au in the S2p 3/2 region is around 161 - 163 eV,[220] which means that there is covalent binding of sulphur to the gold surface of the nanoparticles. However, the band observed in the XPS spectrum is much broader than this region, and this is most likely due to the presence of the disulfide bonds of the **DTDTPA** coating as their binding energies appear between 163 - 164 eV.[220]

Other atoms belonging to the **DTDTPA** coating are also present in the XPS spectrum. Regarding the C1s region, it is observed a broad band centered at 285 eV, with a shoulder at higher binding energy levels around 287 - 288 eV. The main peak at 285 eV is due to the presence of the methylenic groups of **DTDTPA**, as both C-C and C-H binding energies appear in this range; the binding energy for C-N groups is also found in this region (286 eV).[220] The presence of the shoulder at around 287 - 288 eV can be attributed to the COOH and CONH groups of **DTDTPA**, which have a higher binding energy.[220] The presence of N and O are also seen in the XPS spectrum, being observed bands in the N1s (399 eV) and O1s (530 eV) characteristic regions.

The XPS spectrum of **AuNP-DTDTPA-Ga** also indicates the presence of gold and gallium in the composition of the nanoconstruct. However, in order to distinguish between different types of gallium bonds it would have required a higher resolution XPS and the respective deconvolution to obtain such data.

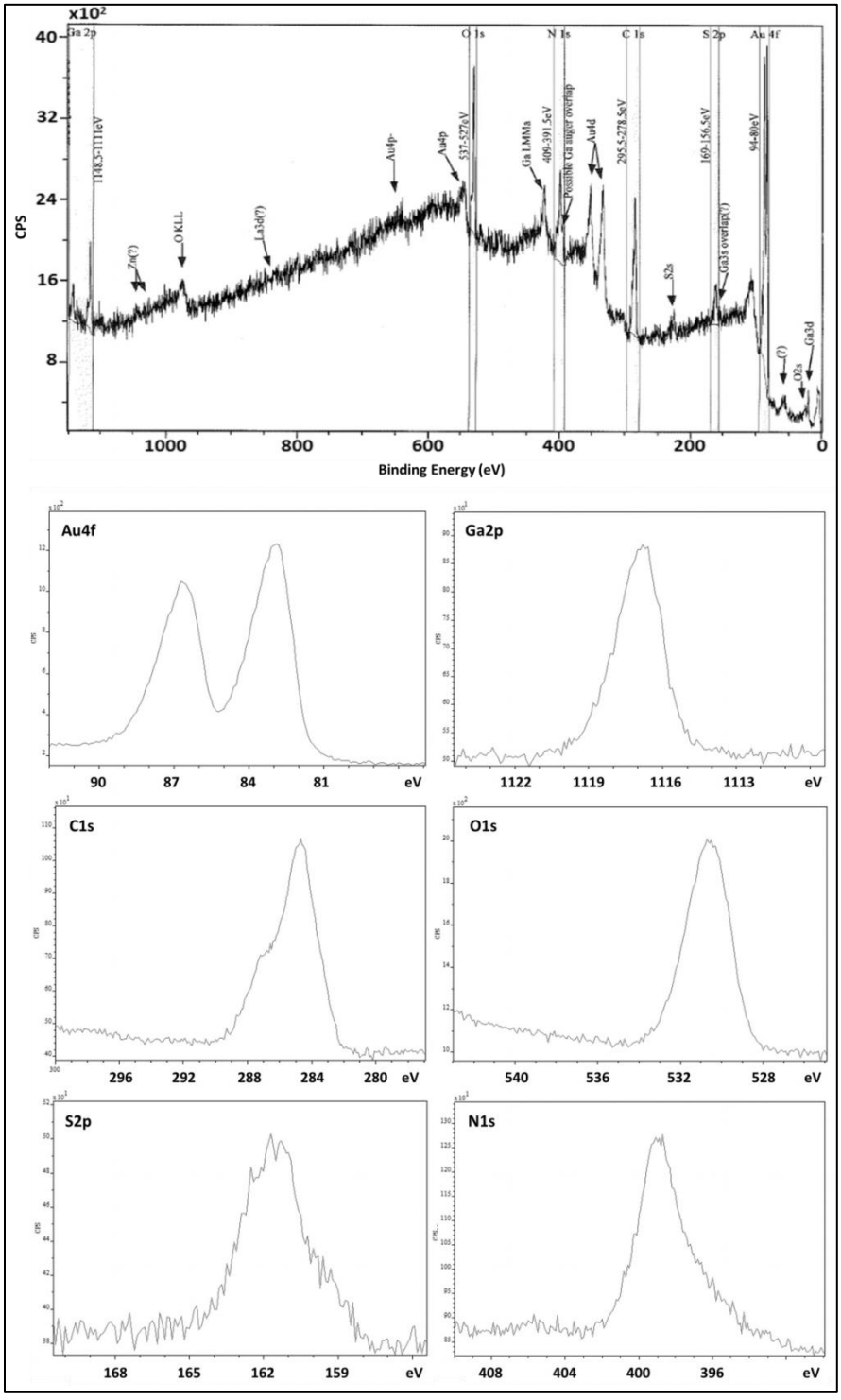

Figure 2.15: *XPS spectra of* ***AuNP-DTDTPA-Ga****, and high resolution spectrum for Au4f, S2p, C1s and Ga2p regions.*

The extensive characterization performed for **AuNP-DTDTPA** as confirmed that these AuNPs have a well-defined structure and are suitable for the coordination of natural Ga(III) through its **DTDTPA** molecules. In light of these results, it was reasoned that these AuNPs were suitable to be functionalized with a target specific molecule and used to coordinate ^{67}Ga, as planned in this PhD work.

2.4 Synthesis, Characterization and *In Vitro* Evaluation of BBN-AuNP-DTDTPA

2.4.1 Synthesis, Assessment of Peptide Loading and Binding Affinity

Aiming to obtain nanoconstructs with targeting specificity towards GRPr, the surface of **AuNP-DTDTPA** was loaded with a thiolated BBN derivative (Scheme 2.3). This BBN derivative (**TA-BBN**) contains a thioctic acid moiety at the N-terminal side of the peptide and was custom synthesized by CPC Scientific, which has confirmed its formulation and purity (> 95%) by ESI-MS and HPLC analysis.

As shown in Scheme 2.3, the loading of **AuNP-DTDTPA** with **TA-BBN** was achieved by reacting **AuNP-DTDTPA** with the peptide in methanol at room temperature using different Au:**TA-BBN** molar ratios (1:0.24, 1:0.4, 1:0.8, 1:2 and 1:4). After 2 h of reaction, the desired nanoconstructs (**BBN-AuNP-DTDTPA**) were separated from the supernatant by filtration, followed by washing with MeOH to remove any non-reacted **TA-BBN**, and finally were washed with H_2O.

The first step towards the characterization of **BBN-AuNP-DTDTPA** was to confirm the conjugation of the peptide and to determine the maximum amount of **TA-BBN** that could be conjugated.

The amount of **TA-BBN** conjugated to **AuNP-DTDTPA** was determined based on the HPLC analysis of the supernatants of the different reaction mixtures and upon comparison with the starting **TA-BBN** solutions, as exemplified in Figure 2.16. The differences in the peak areas due to **TA-BBN**, before and after reaction, were used to ascertain the different amounts of TA-BBN that were conjugated to the AuNPs. The results obtained are shown in Figure 2.17.

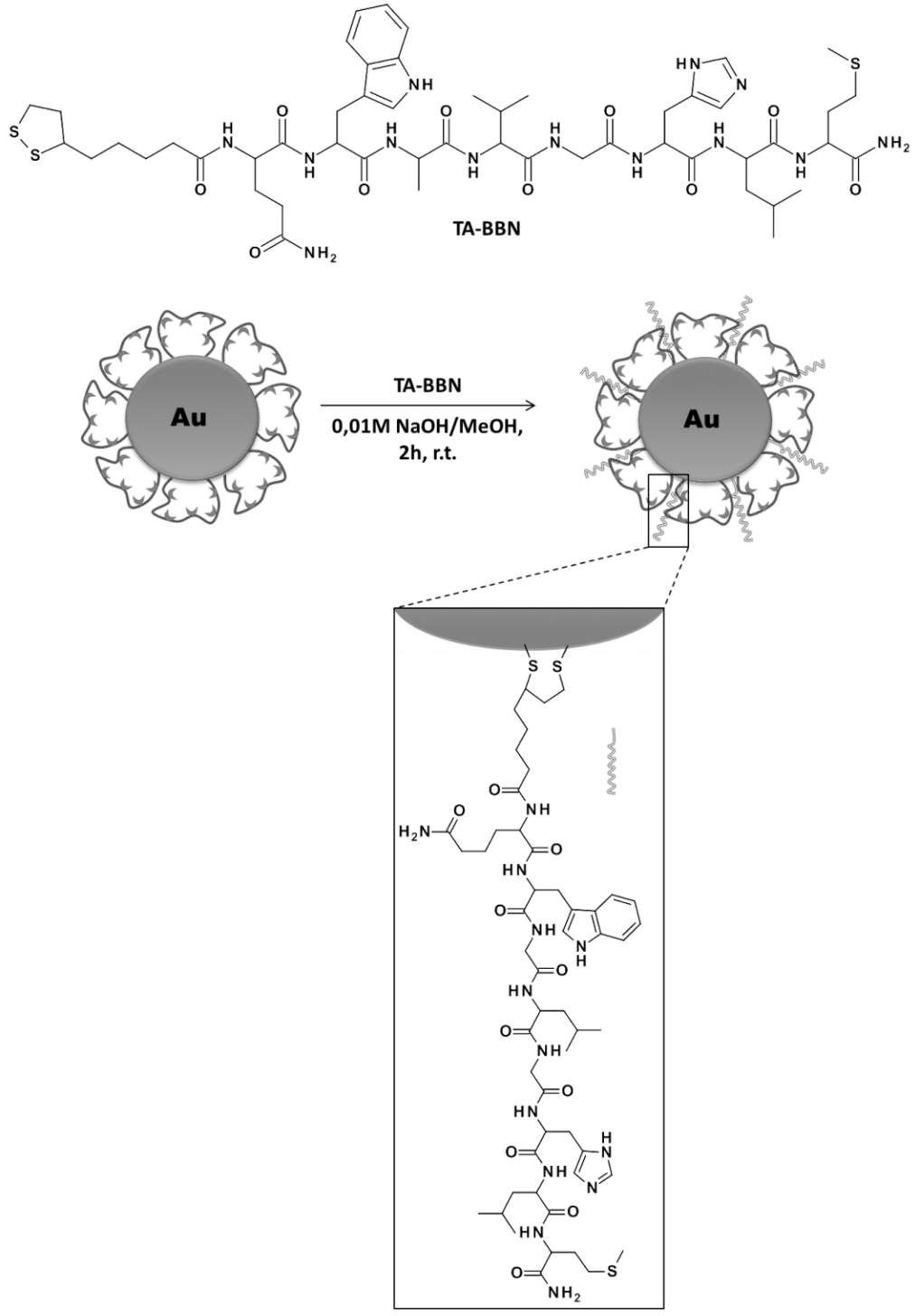

Scheme 2.3: *Structure of* ***TA-BBN*** *and synthesis of* ***BBN-AuNP-DTDTPA****.*

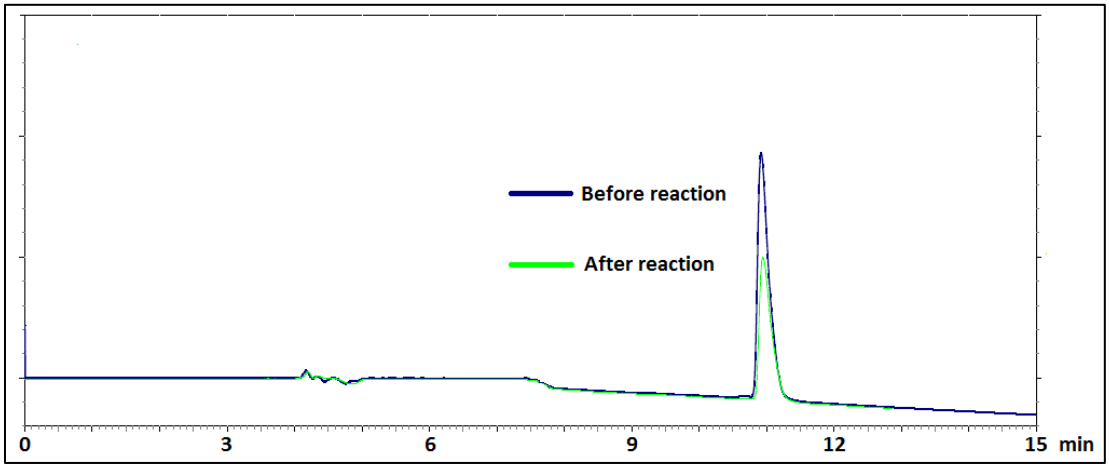

Figure 2.16: *HPLC chromatogram (100-10 C18, 0.1% TFA aqueous/CH_3CN) of* ***TA-BBN*** *(t_R = 10.92 min) before and after the reaction with* ***AuNP-DTDTPA*** *using a molar ratio of 1:0.4 (Au:****TA-BBN****).*

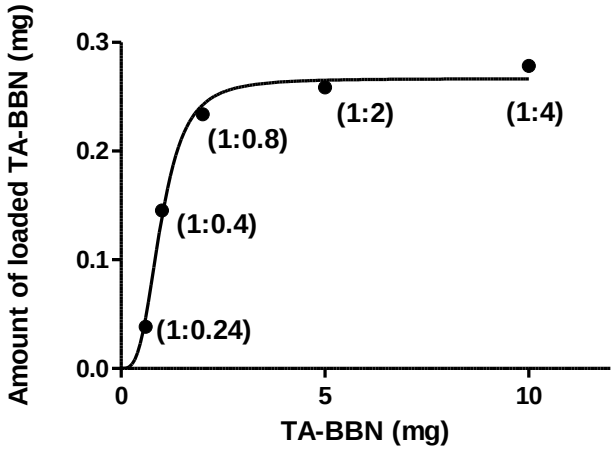

Figure 2.17: *Amounts of* ***TA-BBN*** *loaded into 1 mg of* ***AuNP-DTDTPA*** *as a function of the Au:****TA-BBN*** *molar ratio.*

The maximum amount of **TA-BBN** that can be conjugated to **AuNP-DTDTPA** is ≈ 0.26 mg per mg of nanoparticles. Saturation of the AuNP surface with **TA-BBN** is achieved when the conjugation of the peptide is performed using a Au:**TA-BBN** molar ratio of 1:2 (Figure 2.17). As discussed previously, the NTA analysis of **AuNP-DTDTPA** indicated that there are 1.67×10^{14} nanoparticles per mg; based on this value it was possible to estimate the number of **TA-BBN** molecules conjugated to each AuNP, which is ≈ 53 **TA-BBN**/NP.

It was studied if the conjugation of **TA-BBN** to the nanoparticles did not compromise the *in vitro* affinity of the bioactive peptide towards GRPr. This study has been done by competition binding experiments with the commercially available radiopeptide ^{125}I-Tyr$_4$-BBN using prostate cancer PC3 cells that are known to overexpress GRPr.[221] In these studies, it has also been assessed how the amount of conjugated **TA-BBN** affects the affinity of the AuNPs towards PC3 cells. The binding affinity towards PC3 cells was evaluated for the nanoconstructs prepared using a Au:**TA-BBN** molar ratio of 1:0.4, 1:2 and 1:4 and the results are shown in Figure 2.18.

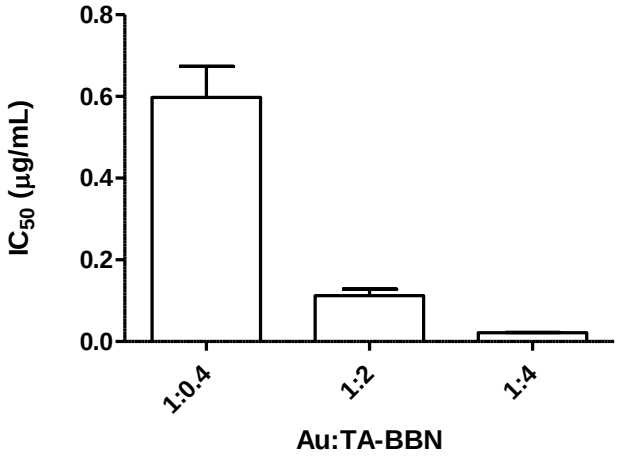

Figure 2.18: *IC_{50} affinities of **BBN-AuNP-DTDTPA** obtained using different Au:**TA-BBN** molar ratios. Measurements were done in prostate cancer PC3 cells by competition binding experiments with the radiopeptide ^{125}I-Tyr$_4$-BBN.*

The measurement of the binding affinity of the different nanoconstructs has indicated that there is a significant difference in their affinity towards the GRPr-expressing PC3 cells depending on the amount of conjugated **TA-BBN**. The measured affinities spanned between IC_{50} ≈ 0.6 µg/mL for the nanoconstructs obtained with Au:**TA-BBN** molar ratio of 1:0.4 to IC_{50} ≈ 0.02 µg/mL for those obtained using a Au:**TA-BBN** molar ratio of 1:4.

These results are clearly consistent with the conjugation of **TA-BBN** to the AuNPs, being observed an increasing affinity towards PC3 as the amount of attached **TA-BBN**

increases. The **BBN-AuNP-DTDTPA** nanoconstruct that was used for further characterization and ^{67}Ga-labeling studies was the one obtained using a Au:**TA-BBN** molar ratio of 1:2, which already correspond to nanoparticles saturated with **TA-BBN** and having a high binding affinity (IC_{50} ≈ 0.1 μg/mL).

2.4.2 Characterization by Microscopy and Spectroscopy Techniques

The **BBN-AuNP-DTDTPA** nanoconstruct was analyzed by XPS, in the same way as described above for **AuNP-DTDTPA-Ga**. The XPS analysis was expected to further confirm the attachment of the BBN derivative at the surface of the AuNPs. The XPS spectrum and high-resolution XPS spectra obtained for **BBN-AuNP-DTDTPA** are presented in Figure 2.19.

The deconvoluted S2p spectrum shows two S2p 3/2 and S2p 1/2 regions suggesting that there are two different S2p species in the AuNPs. For the designated Specie 1, the S2p 3/2 and S2p 1/2 energy bands appear at ≈ 162.3 eV and ≈ 163.5 eV, respectively, and are most likely due to the presence of covalent Au-S bonds, which are found in the 161-163 eV range.[220] Specie 2 displays binding energies of S2p 3/2 ≈ 163.2 eV and S2p 1/2 ≈ 164.4 eV; these energy bands are most likely due to the presence of the disulfide bonds of the **DTDTPA** coating; however, this range of energy is also characteristic of thioether bonds, which are present in the methionine group of the BBN derivative.[220]

The high resolution XPS spectrum of the C1s region indicates two distinct binding energy bands, one centered at ≈ 285 eV and the other at ≈ 288 eV. The deconvolution of the former shows the presence of two types of C1s bindings, one with binding energy ≈ 285 eV, which is attributed to the presence of C-C and C-H from methylenic groups, and another one at slightly higher binding energy levels, at ≈ 286 eV, characteristic of C-N groups.[220]

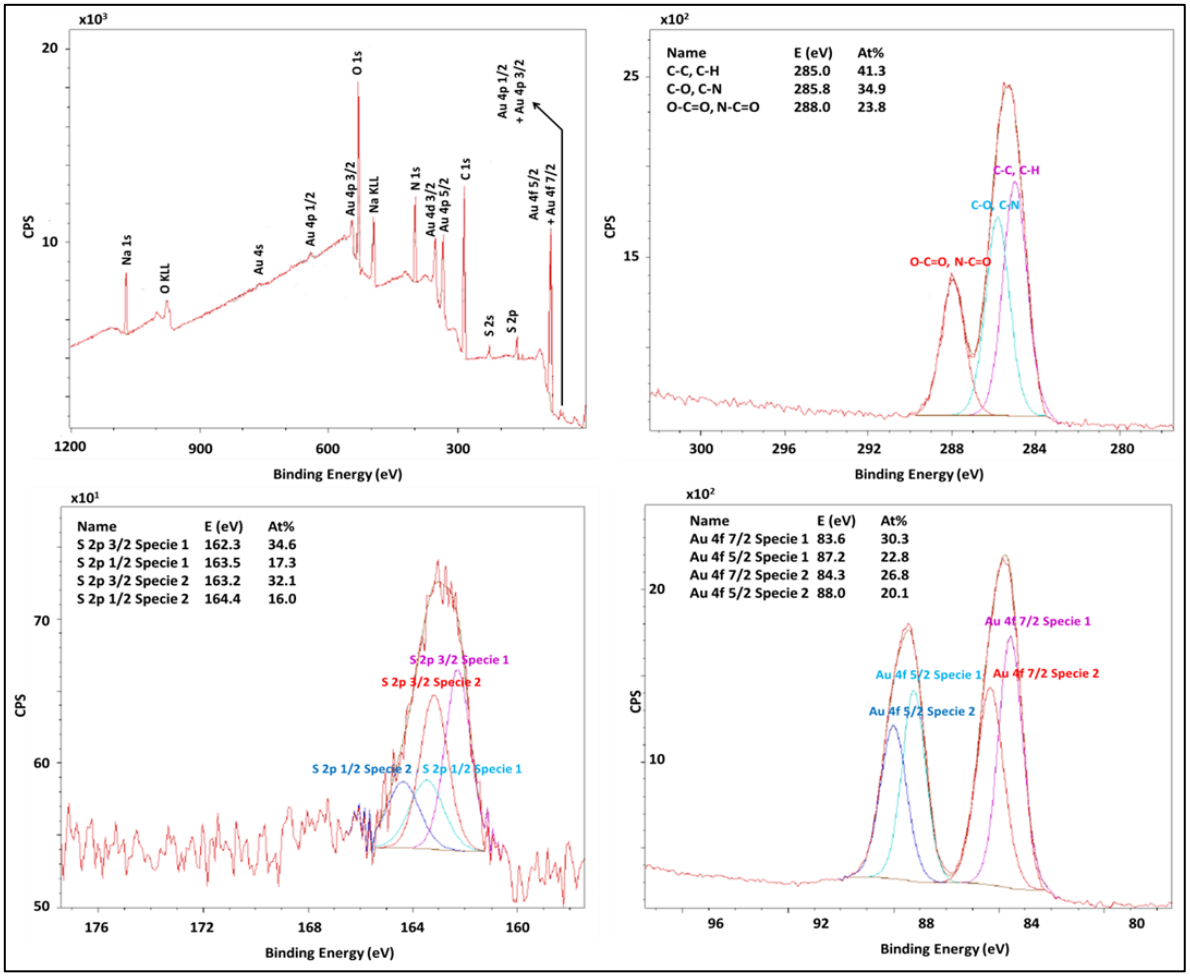

Figure 2.19: *XPS spectrum and high-resolution XPS spectrum in the C1s, S2p and Au4f regions, for* ***BBN-AuNP-DTDTPA****.*

The second C1s band, centered at ≈ 288 eV, is attributed to the C-O binding energies of COOH and CONH, which are found in this region.[220] When compared with the XPS spectrum of **AuNP-DTDTPA-Ga** (Figure 2.15), it is verified that the intensity of this band characteristic of C-O bonds is much higher. This is most likely due to the presence of the peptide which has a high amount of amino acid residues.

Analysis of the high resolution XPS spectrum in the Au4f 7/2 and Au4f 5/2 regions also indicates the presence of two distinct species. Specie 1 with energy bands of Au4f 7/2 ≈ 83.6 eV and Au4f 5/2 ≈ 87.2 eV, and Specie 2 with energies of Au4f 7/2 ≈ 84.3 eV and Au4f 5/2 ≈ 88.0 eV. The values observed for Specie 1 are likely due to the gold in metallic form,[220] which is not conjugated to any organic molecule, which can be attributed to the

existence of gold atoms on the nanoparticle surface that do not display any S-Au bonding. Specie 2 on the other hand is characteristic of the covalent Au-S bond which was also confirmed by the high resolution XPS spectrum of S2p 3/2 and S2p 1/2.[220]

The characterization of **BBN-AuNP-DTDTPA** comprised also UV-Vis spectroscopy, TEM analysis, DLS and zeta-potential measurements, aiming to assess the influence of the incorporation of the BBN peptide in the physico-chemical properties of the AuNPs.

UV-Vis and TEM analysis of **BBN-AuNP-DTDTPA** are shown in Figure 2.20. The UV-Vis spectrum of **BBN-AuNP-DTDTPA** shows the presence of a broad absorption band centered at ≈ 520 nm, with a profile identical to the one found for **AuNP-DTDTPA**. This finding indicated that the conjugation of **TA-BBN** to the AuNPs did not alter the gold core of the nanoparticles, which was further corroborated by the TEM image of **BBN-AuNP-DTDTPA** that ascertained a core size of ≈ 2.02 ± 0.88 nm for the BBN-containing nanoparticles.

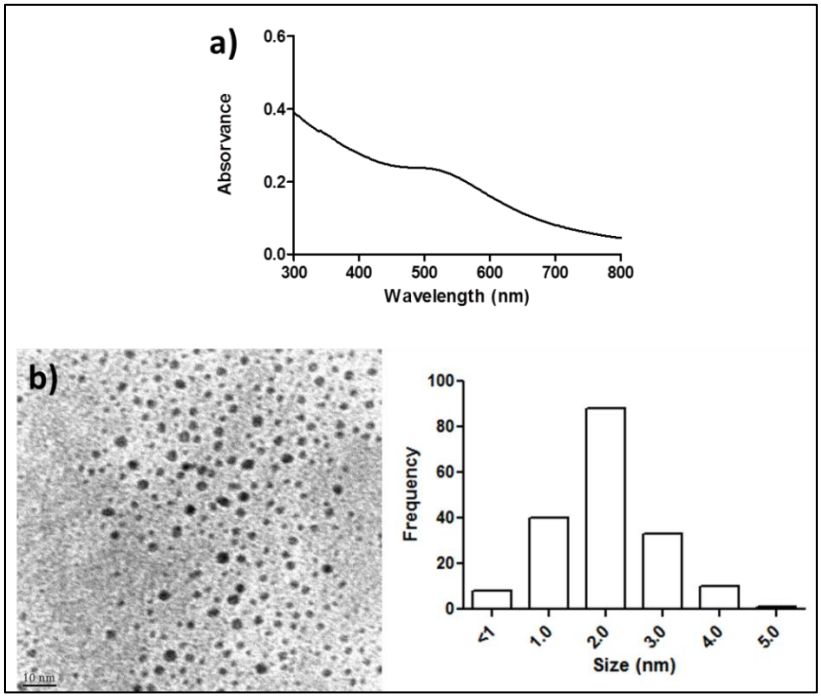

Figure 2.20: a) *UV-Vis spectrum (8x10^{-2} mg/mL) and* ***b)*** *TEM image with respective size histogram of* ***BBN-AuNP-DTDTPA****.*

DLS analysis (Figure 2.21) and zeta-potential measurements were performed in a solution of **BBN-AuNP-DTDTPA** in H_2O ($8x10^{-2}$ mg/mL), in order to evaluate the influence of the conjugated peptide on the hydrodynamic size and surface charge of the nanoparticles.

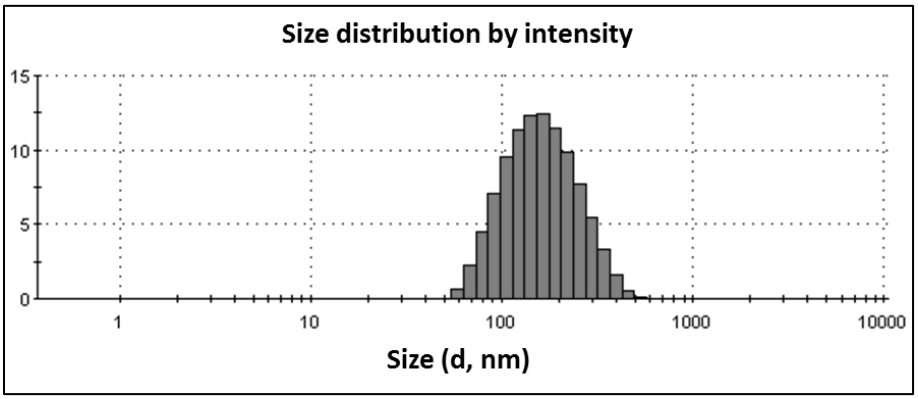

Figure 2.21: *Hydrodynamic size distribution of* ***BBN-AuNP-DTDTPA*** *in H_2O ($8x10^{-2}$ mg/mL).*

The hydrodynamic size found for **BBN-AuNP-DTDTPA** in H_2O was 146.2 nm (PDI = 0.162) and the measured zeta-potential was -71.5 ± 9.1 mV.

The hydrodynamic size of **BBN-AuNP-DTDTPA** in H_2O is higher than the one found for **AuNP-DTDTPA** (100.6 nm (PDI = 0.111)), which can be justified by the increasing of the AuNP coating due to the conjugation of **TA-BBN** to the AuNPs. However, one can not exclude that the presence of the peptide imbues a slightly higher level of aggregation when compared to the peptide free AuNPs.

On the other hand, the zeta-potential of -71.5 ± 9.1 mV measured for **BBN-AuNP-DTDTPA** in H_2O can be considered comparable to that of **AuNP-DTDTPA** (-80.7 ± 15.6 mV), showing that the presence of **TA-BBN** did not affect the highly negative charge of the nanoconstruct and indicating that the AuNPs present a high stability towards aggregation in solution.

2.5 Synthesis, Characterization and *In Vitro*/*In Vivo* Evaluation of AuNP-DTDTPA-^{67}Ga and BBN-AuNP-DTDTPA-^{67}Ga

As discussed above, it was shown that **DTDTPA** stabilized AuNPs have the capability to coordinate Ga(III) and its decoration with **TA-BBN** provides nanoconstructs (**BBN-AuNP-DTDTPA**) with high affinity towards GRPr.

These encouraging results prompted the study of the ^{67}Ga-labeling of **BBN-AuNP-DTDTPA** aiming to assess their relevance as platforms for the target specific delivery of radiogallium to GRPr-overexpressing tumor tissues. In parallel, the same studies were also performed for **AuNP-DTDTPA** to have an insight on the influence of the BBN peptide in the *in vitro*/*in vivo* stability and biodistribution of the ^{67}Ga-labeled AuNPs.

2.5.1 Radiolabeling and *In Vitro* Stability Studies

The ^{67}Ga-labeling of the nanoconstructs was attempted by reacting **AuNP-DTDTPA** or **BBN-AuNP-DTDTPA** with $^{67}GaCl_3$ in ammonium acetate buffer (pH ≈ 7) solution. The labeling concentrations used for both nanoconstructs were identical (0.16 mg/mL); for lower concentrations (0.08 mg/mL), the radiolabeling of these AuNPs proceeded with low radiochemical yields (≈ 40%). The successful radiolabeling of **AuNP-DTDTPA** was achieved by heating the reaction mixture to 50 ºC for 15 min, while for **BBN-AuNP-DTDTPA**, 15 min at room temperature guaranteed the maximum radiochemical yield (Scheme 2.4).

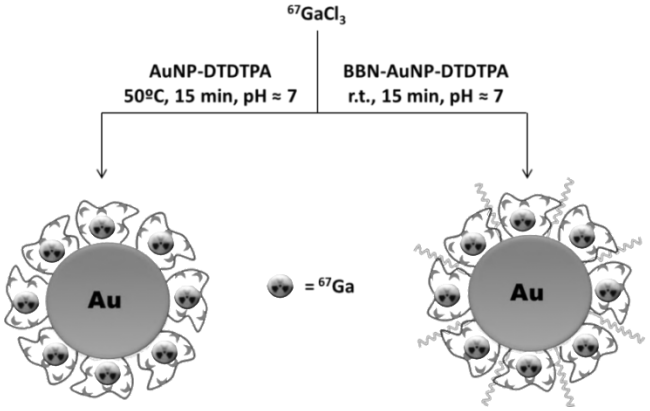

Scheme 2.4: *Radiolabeling of* ***AuNP-DTDTPA*** *and* ***BBN-AuNP-DTDTPA*** *with* ^{67}*Ga.*

After the labeling reaction, the ^{67}Ga-labeled AuNPs were purified by ultra-filtration to remove any unreacted $^{67}GaCl_3$, and recovered by dissolution in H_2O. The radiochemical purity of the resulting **AuNP-DTDTPA-^{67}Ga** and **BBN-AuNP-DTDTPA-^{67}Ga** was assessed by TLC using 6 M HCl/MeOH (5:95) as eluent (Figure 2.22). In this system, the ^{67}Ga-labeled AuNPs have $R_f \approx 0$ while $^{67}GaCl_3$ displays $R_f \approx 1$. Under the optimized labeling conditions, **AuNP-DTDTPA-^{67}Ga** and **BBN-AuNP-DTDTPA-^{67}Ga** were obtained in radiochemical yields of 85% and 80%, respectively, and with high radiochemical purity (> 95%).

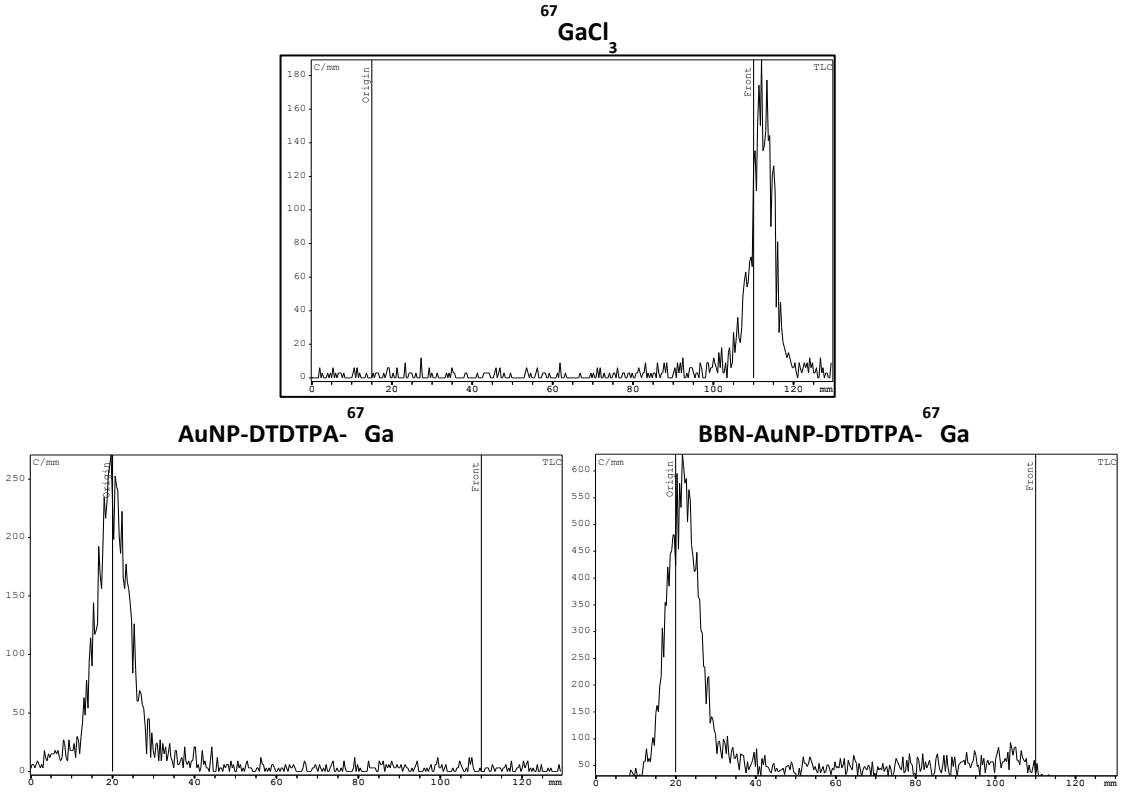

Figure 2.22: *Radiochromatograms of $^{67}GaCl_3$ (R_f = 1),* ***AuNP-DTDTPA-^{67}Ga*** *(R_f = 0) and* ***BBN-AuNP-DTDTPA-^{67}Ga*** *(R_f = 0) obtained using ITLC-SG plates with 6 M HCl/MeOH (5:95) as eluent.*

The *in vitro* stability of the two types of radiolabeled AuNPs, **AuNP-DTDTPA-^{67}Ga** and **BBN-AuNP-DTDTPA-^{67}Ga**, was studied in the presence of several media: NaCl 0.9%, PBS 0.1 M, cell medium and *apo*-transferrin (3 mg/mL, in 10 mM $NaHCO_3$), at 37 ºC. The AuNP concentration in the solutions used for these studies was ≈ 0.11 mg/mL. These

media were chosen in order to mimic the physiological conditions and the presence of biologically relevant substrates.

These studies intended to check the stability towards release of ^{67}Ga and, therefore, the different mixtures were analyzed by radio-TLC analysis in order to verify any change in the amount of radiolabeled AuNPs. The results obtained upon radio-TLC analysis of the different reaction mixtures are presented in Figure 2.23.

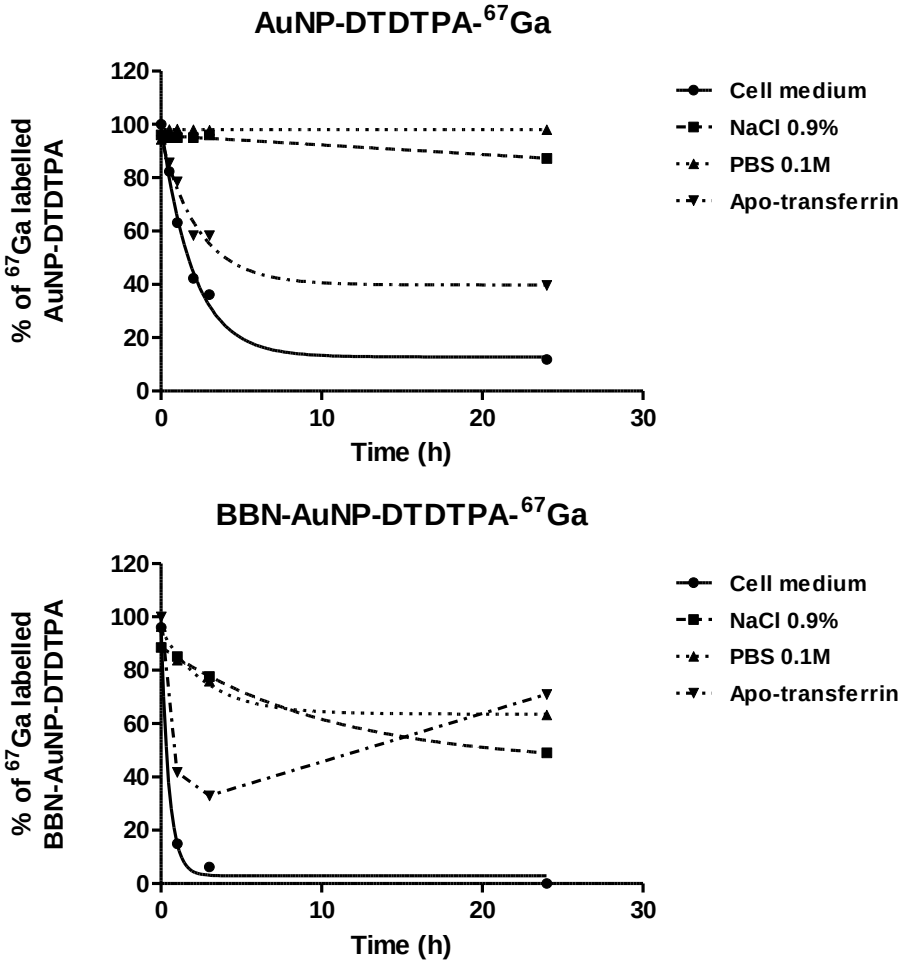

Figure 2.23: In vitro *stability of* ***AuNP-DTDTPA-^{67}Ga*** *and* ***BBN-AuNP-DTDTPA-^{67}Ga*** *in the presence of physiological and biologically relevant media.*

The stability studies performed for **AuNP-DTDTPA-^{67}Ga** (Figure 2.23) showed that in physiological conditions (NaCl 0.9% and PBS 0.1 M), the AuNPs display an adequate

stability with > 80% of the ^{67}Ga still coordinated to the nanoconstructs, after an incubation time of 24 h. For **BBN-AuNP-DTDTPA-^{67}Ga**, the release of ^{67}Ga is more pronounced in the presence of the same media but nevertheless, still ≈ 60% of the radioactivity is retained by the nanoconstruct at 24 h.

In cell medium and in the presence of *apo*-transferrin, both radiolabeled nanoconstructs retain a high percentage of coordinated ^{67}Ga for short incubation times (> 80% at 15 min). However, there is a relatively fast release of ^{67}Ga from the AuNPs overtime. In general, this release is more accentuated for **BBN-AuNP-DTDTPA-^{67}Ga** if compared with **AuNP-DTDTPA-^{67}Ga** and more significant in the case of cell medium.

A particular phenomenon was observed when **BBN-AuNP-DTDTPA-^{67}Ga** was incubated with *apo*-transferrin, it has been observed an increase of the amount of ^{67}Ga-labeled AuNPs, from ≈ 35% to ≈ 70%, between the 3 h and 24 h incubation times. The reasons for this behavior were not fully understood but one possibility could be related with the eventual slow interaction of ^{67}Ga-transferrin, resulting from trans-chelation reactions, with the surface of the BBN-containing AuNPs. Apparently, the presence of BBN has some role in such eventual interactions, as this behavior was not observed for **AuNP-DTDTPA-^{67}Ga**.

2.5.2 Biological Evaluation: Cell Studies and Biodistribution

After successfully radiolabeling **AuNP-DTDTPA** and **BBN-AuNP-DTDTPA** and getting insight on their *in vitro* stability, it has been proceed with the biological evaluation of the corresponding ^{67}Ga-labeled AuNPs. As discussed before, **AuNP-DTDTPA-^{67}Ga** and **BBN-AuNP-DTDTPA-^{67}Ga** do not display optimal ability to maintain a stable ^{67}Ga coordination in the presence of certain challenging media, namely in cell medium. Nevertheless, it has been considered relevant to perform their biological evaluation, in order to verify any influence of the presence of the BBN derivative on the biological behavior of the AuNPs.

The biological evaluation of **AuNP-DTDTPA-^{67}Ga** and **BBN-AuNP-DTDTPA-^{67}Ga** included cell internalization studies in PC3 cells and biodistribution studies in human PC3 xenograft Balb/c mice, as well as cell viability studies by MTT assays for the non-radioactive counterparts. These studies were intended to obtain data on eventual toxicity

issues associated with the use of these AuNPs, internalization in GRPr-overexpressing cells, and finally to have some insight on their ability to target *in vivo* GRPr-positive tumors.

2.5.2.1 Cell Studies: Citotocicity Assays and Cell Uptake

The evaluation of the cytotoxicity of **AuNP-DTDTPA** and **BBN-AuNP-DTDTPA** against human prostate cancer PC3 cells has been done by exposing the cells, for 24h at 37 ºC, to increasing concentrations of both types of AuNPs. These studies were performed using the MTT assay, which is a colorimetric assay that is based on the conversion of the tetrazolium dye MTT into insoluble formazan crystals, by enzymes in living cells. The number of viable cells is proportional to the amount of formazan crystals, which is quantified by measurement of the UV-Vis absorbance at 570 nm.

The results obtained for both nanoconstructs are presented in Figure 2.24. No cytotoxic activity against PC3 cells was observed, either for **AuNP-DTDTPA** and **BBN-AuNP-DTDTPA**, up to concentrations as high as 40 µg/mL. It is worthwhile to notice that this concentration is much higher than those involved in the further *in vitro* and *in vivo* biological studies of the ^{67}Ga-labeled congeners of these nanoparticles.

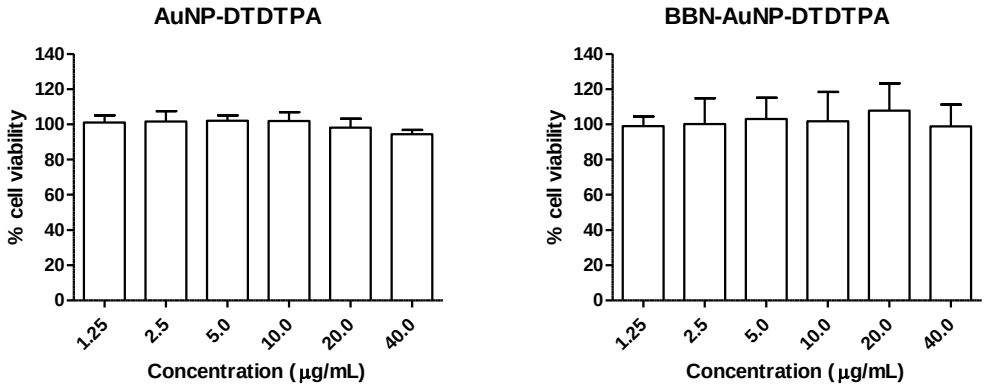

Figure 2.24: *Cell viability (mean ± SD, n=3) of PC3 cells exposed to increasing concentrations.of* ***AuNP-DTDTPA*** *and* ***BBN-AuNP-DTDTPA*** *as assessed by the MTT assay.*

Internalization studies of **AuNP-DTDTPA-^{67}Ga** and **BBN-AuNP-DTDTPA-^{67}Ga** were performed in PC3 cells in order to have some insight on the influence of the presence of the BBN derivative on their ability to deliver radiogallium to GRPr-positive tumor cells. In these studies, solutions containing the radiolabeled AuNPs were added to

plated PC3 cells and left to incubate at 37 ºC for different intervals of time: 15 min - 3 h. The cells were washed with PBS and lysed with 0.1 M NaOH, and the cellular extracts were counted for radioactivity in a gamma counter. The cellular internalization results expressed as a percentage of total cell radioactivity added and normalized per million of cells, are presented in Figure 2.25.

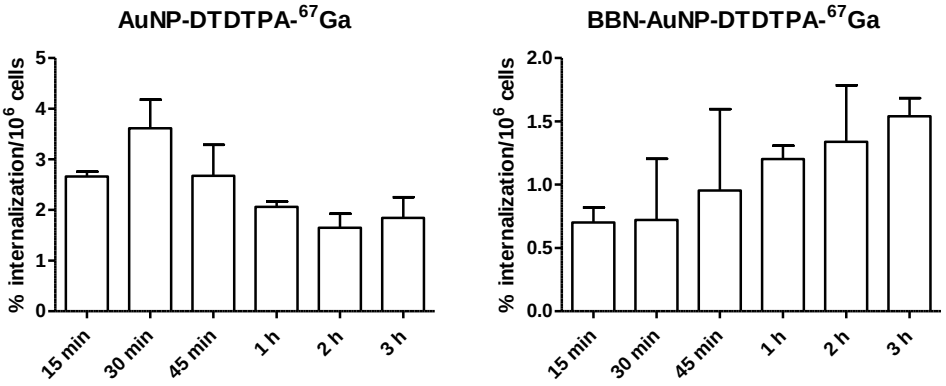

Figure 2.25: *Cellular internalization (mean ± SD, n=4) of* ***AuNP-DTDTPA-^{67}Ga*** *and* ***BBN-AuNP-DTDTPA-^{67}Ga*** *in PC3 cells after incubation at 37 ºC for different intervals of time. Internalization is expressed as percentage of the total radioactivity added to the cells.*

Both nanoconstructs, **AuNP-DTDTPA-^{67}Ga** and **BBN-AuNP-DTDTPA-^{67}Ga**, show a low uptake in PC3 cells. **AuNP-DTDTPA-^{67}Ga** has a faster uptake (≈ 2.6% at 15 min) with a maximum value (≈ 3.6%) at 30 min of incubation, which is followed by a slow washout. In the case of **BBN-AuNP-DTDTPA-^{67}Ga**, the cell uptake steadily increases with time attaining a maximum value of ≈ 1.5% of internalized activity after 3 h of incubation. This profile can be considered more compatible with a receptor-mediated uptake, despite the low uptake observed for **BBN-AuNP-DTDTPA-^{67}Ga**.

Overall, these results indicate that the presence of the BBN derivative in **BBN-AuNP-DTDTPA-^{67}Ga** does not enhance the cellular uptake of the AuNPs. However, taking into account the poor stability of these AuNPs in cell medium, it may occur a fast release of ^{67}Ga from the nanoconstructs and, therefore, the cellular internalization is not being mediated by the nanoparticles themselves.

2.5.2.2 Biodistribution in Tumor-Bearing Mice

In vivo biodistribution studies were carried out in human PC3 xenograft Balb/c mice. The animals were injected in the tail vein with 100 µL of radiolabeled AuNPs saline solutions (≈ 80 µCi). The mice were measured in a gamma counter in order to determine the injected dose (I.D.). After specific post-injection times (15 min - 24 h), the animals were sacrificed by cervical dislocation. Tissue samples of the main organs were removed and weighted, and the radioactivity was measured in a gamma counter. Results are expressed as percentage of injected dose per gram of organ (%I.D./g) (Table 2.3 and Figures 2.26 and 2.27). For blood, bone and muscle, this value was calculated assuming a compostion of 6%, 10% and 40% of the total weight, respectively. The values of excretion were measured by the difference between the administered radioactivity and the whole body radioactivity at the time of sacrifice.

The biodistribution profile of **AuNP-DTDTPA-^{67}Ga** (Figure 2.26) indicates a very fast liver uptake (36.5 ± 2.2 %I.D./g at 30 min p.i.) and also a significant uptake in the spleen (7.9 ± 2.7 %I.D./g at 30 min p.i.). This is characteristic of nanoparticles with an hydrodynamic size over 100nm.[101] Practically no renal excretion is observed and the tumor uptake is very low, with a maximum of 1.1 ± 0.6 %I.D./g at 24h p.i..

The main features of the *in vivo* behaviour of **BBN-AuNP-DTDTPA-^{67}Ga** (Figure 2.27) are the relatively slow blood clearance (11.9 ± 1.5 %I.D./g and 9.8 ± 0.7 %I.D./g, at 15 min and 4 h respectively), which is considerably slower than that of **AuNP-DTDTPA-^{67}Ga** that exhibits a blood uptake of 3.7 ± 0.2 %I.D./g at 30 min p.i.. At 24 h p.i., the liver uptake of the BBN-containing AuNPs (4.8± 1.2 %I.D./g) is significantly lower than that showed by **AuNP-DTDTPA-^{67}Ga** (48.2 ± 6.2 %I.D./g). On the other hand, there is a more significant renal excretion component for the former, as evidenced by its highest kidney uptake ranging from 12.4 ± 3.3 %I.D./g at 15 min p.i. to 7.5 ± 1.8 %I.D./g at 24 h p.i..

Table 2.3: *Biodistribution results (mean ± SD, n=3; expressed as %I.D./g of organ) for* ***AuNP-DTDTPA-^{67}Ga*** *and* ***BBN-AuNP-DTDTPA-^{67}Ga*** *after i.v. administration in human PC3 xenograft Balb/c mice.*

Organ	%I.D./g					
	15 min	30 min		4 h	24 h	
	BBN-AuNP-DTDTPA-^{67}Ga	AuNP-DTDTPA-^{67}Ga	BBN-AuNP-DTDTPA-^{67}Ga	BBN-AuNP-DTDTPA-^{67}Ga	AuNP-DTDTPA-^{67}Ga	BBN-AuNP-DTDTPA-^{67}Ga
Blood	11.9 ± 1.5	3.7 ± 0.2	10.3 ± 3.1	9.8 ± 0.7	0.8 ± 0.1	1.7 ± 0.4
Liver	7.1 ± 3.0	36.5 ± 2.2	5.0 ± 1.0	8.4 ± 1.6	48.2 ± 6.2	4.8 ± 1.2
Intestine	1.6 ± 0.3	0.3 ± 0.2	1.3 ± 0.06	2.1 ± 0.4	0.41 ± 0.07	1.6 ± 0.5
Spleen	3.0 ± 1.2	7.9 ± 2.7	2.8 ± 0.5	4.5 ± 0.6	6.4 ± 1.9	3.0 ± 0.4
Heart	3.2 ± 0.3	1.09 ± 0.04	3.00 ± 0.09	3.0 ± 0.8	0.8 ± 0.2	0.9 ± 0.1
Lung	6.6 ± 1.7	3.4 ± 0.3	5.0 ± 0.4	3.7 ± 0.4	1.2 ± 0.06	2.1 ± 0.5
Kidney	12.4 ± 3.3	2.4 ± 0.4	9.9 ± 2.4	11.3 ± 1.1	1.8 ± 0.1	7.5 ± 1.8
Muscle	1.8 ± 0.2	0.3 ± 0.2	1.8 ± 0.2	1.1 ± 0,2	0.26 ± 0.04	0.4 ± 0.1
Bone	2.9 ±1.4	0.76 ± 0.05	3.3 ± 0.4	3.2 ± 0.4	2.2 ± 0.2	5.8 ± 0.4
Stomach	1.3 ± 0.5	0.47 ± 0.04	0.7 ± 0.3	1.4 ± 0.5	0.4 ± 0.2	1.1 ± 0.1
Pancreas	2.1 ± 0.6	0.8 ± 0.69	1.8 ± 0.4	2.4 ± 0.4	0.1 ± 0.07	2.2 ± 0.2
Brain	0.35 ± 0.07	0.13 ± 0.05	0.29 ± 0.06	0.25 ± 0.06	0.07 ± 0.02	0.16 ± 0.03
Tumor	4.8 ± 0.1	0.8 ± 0.4	4.7 ± 0.9	4.5 ± 1.3	1.1 ± 0.6	5.8 ± 0.7
Excretion (%I.D.)	14.9 ± 12.0	13.4 ± 17.7	31.1 ± 7.7	44.8 ± 0.9	2.9 ± 2.4	57.1 ± 2.5

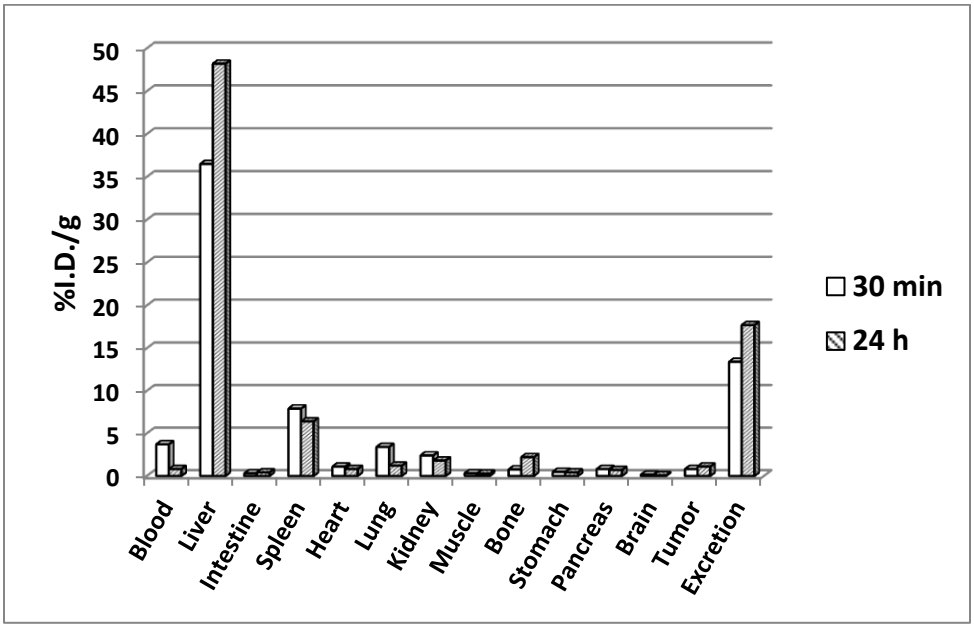

Figure 2.26: *Biodistribution results (mean, n=3; expressed as %I.D./g of organ) for* ***AuNP-DTDTPA-^{67}Ga*** *after i.v. administration in human PC3 xenograft Balb/c mice.*

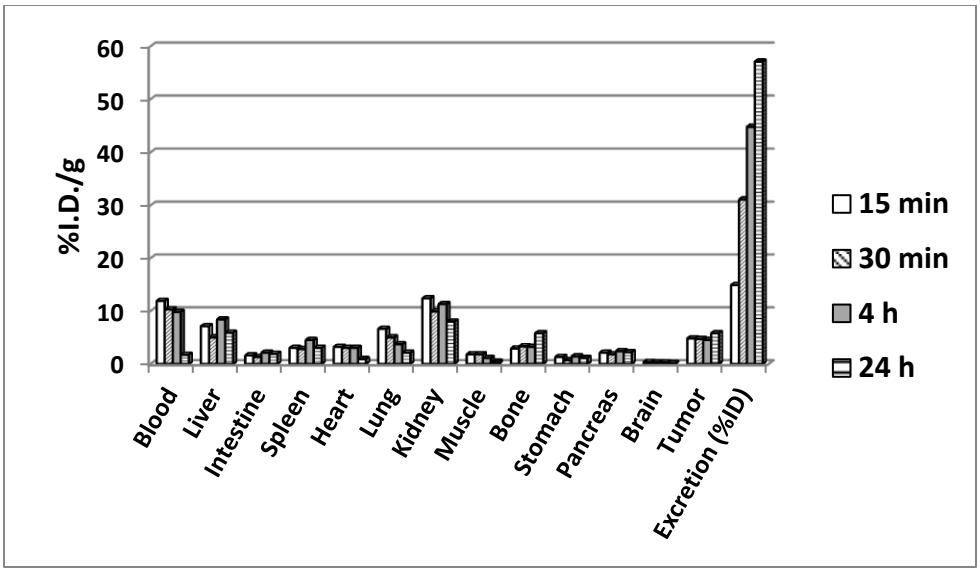

Figure 2.27: *Biodistribution results (mean ± SD, n=3; expressed as %I.D./g of organ) for* ***BBN-AuNP-DTDTPA-^{67}Ga*** *after i.v. administration in human PC3 xenograft Balb/c mice,.*

Pancreas and tumor uptake are also increased in the biodistribution of **BBN-AuNP-DTDTPA-^{67}Ga** if compared with **AuNP-DTDTPA-^{67}Ga**. For the former, tumor and pancreas uptake values of 5.8 ± 0.7% I.D./g and 2.2 ± 0.2 %I.D./g were observed at 24 h p.i.,

respectively. The higher pancreas and tumor uptake observed for **BBN-AuNP-DTDTPA-^{67}Ga** could be due to the presence of the BBN derivative, as these tissues express significant quantities of GRPr.[221] In fact, the GRPr densiy in mice is assumed to follow the order: pancreas > tumor > intestine,[100] and consequently it is common to observe high pancreas uptake for BBN derivatives.[182,222] However, the pancreas uptake of **BBN-AuNP-DTDTPA-^{67}Ga** is very low when compared with other BBN functionalized nanoparticles reported in the literature.[146,181] For instance, the group of Morales-Avila *et al.* described AuNPs targeted at GRPr with a pancreatic uptake as high as ≈ 39.83 %I.D./g at 1 h p.i..[182]

Blockade studies were done for **BBN-AuNP-DTDTPA-^{67}Ga** in order to have an insight on the possible involvement of receptor-mediated pancreas and tumor uptake. A separate set of animals were firstly treated with cold BBN and then injected with **BBN-AuNP-DTDTPA-^{67}Ga**. These assays were also run in parallel with non-treated mice. The uptake in the pancreas and tumor for both groups at 4 h p.i. is graphically presented in Figure 2.28.

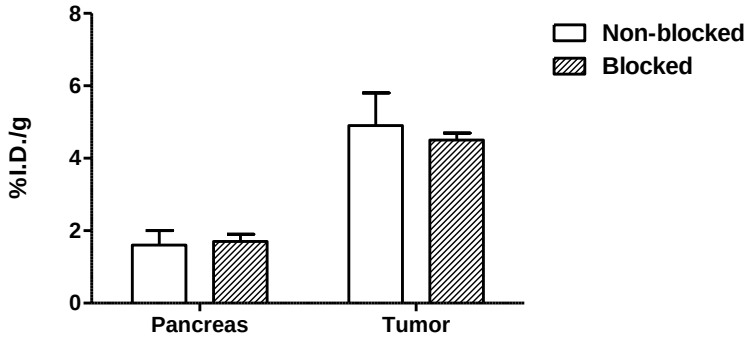

Figure 2.28: *Comparison of pancreas and tumor uptake (mean ± SD, n=3; expressed as %I.D./g of organ) for* ***BBN-AuNP-DTDTPA-^{67}Ga*** *at 4 h p.i. in human PC3 xenografts Balb/c mice treated (blocked) or non-treated with BBN.*

As can be seen in Figure 2.28, the tumor and pancreas uptake of **BBN-AuNP-DTDTPA-^{67}Ga** is not altered by blocking GRPr with BBN. This finding seems to indicate that the tumor and pancreas uptake of these radiolabeled AuNPs is not receptor-mediated.

It was reasonable to hypothesize that the greatest tumor and pancreas uptake exhibited by **BBN-AuNP-DTDTPA-^{67}Ga** could reflect its lower *in vivo* stability compared to **AuNP-DTDTPA-^{67}Ga**. The bone uptake of **BBN-AuNP-DTDTPA-^{67}Ga** reaches a relatively high value of 5.8± 0.4% I.D./g at 24 h p.i., which can be considered indicative of such *in vivo* instability. In fact, it is known that free gallium accumulates in the hydroxylapatite of the bone matrix.[223]

To have a further insight in this aspect, it has been assessed the pancreas and tumor uptake of cold **BBN-AuNP-DTDTPA** in the same animal model used to evaluate the ^{67}Ga-labeled counterparts. Hence, 100 µL of the **BBN-AuNP-DTDTPA** aqueous solutions were administerd in human PC3 xenograft Balb/c mice, which were sacrificed at 4 h p.i.. The pancreas and tumor were collected, lyophilized and analysed by ICP-OES to determine the amount of gold present in these samples. For control purposes, 100 µL of the injected nanoparticle solution was also analysed by ICP-OES in order to determine the total amount of injected gold in the mice.

Figure 2.29 shows the results obtained for the amount of gold found in the pancreas and tumors of the mice injected with **BBN-AuNP-DTDTPA**. A comparison between the uptake of gold and ^{67}Ga in the pancreas and tumor, expressed as %I.D./g, is also shown in Figure 2.30.

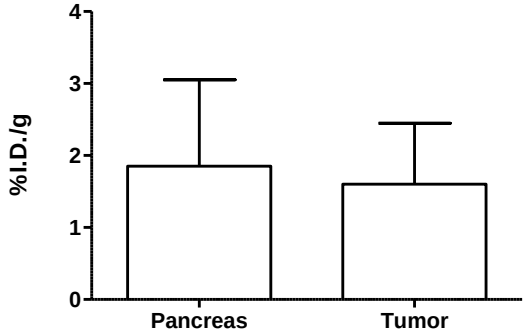

Figure 2.29: *Comparison of pancreas and tumor gold uptake (mean ± SD, n=2; expressed as %I.D./g of organ) for* ***BBN-AuNP-DTDTPA*** *at 4 h p.i., in human PC3 xenograft Balb/c mice.*

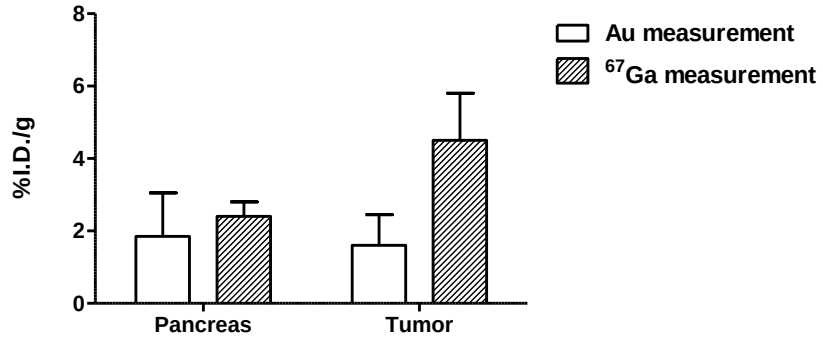

Figure 2.30: *Comparison of pancreas and tumor gold (mean ± SD, n=2; expressed as %I.D./g of organ) and ^{67}Ga (mean ± SD, n=3; expressed as %I.D./g of organ) uptake for* ***BBN-AuNP-DTDTPA*** *and* ***BBN-AuNP-DTDTPA-^{67}Ga****, respectively, at 4 h p.i., in human PC3 xenograft Balb/c mice.*

The percentage amount of gold found in the pancreas for **BBN-AuNP-DTDTPA** is very similar to that of ^{67}Ga in the biodistribution study of **BBN-AuNP-DTDTPA-^{67}Ga** (Figure 2.30). By contrast, in the case of the tumor uptake, the percentage amount of gold is significantly lower than that determined for ^{67}Ga (1.6 ± 0.85% I.D./g *vs* 4.5 ± 1.3 % I.D./g at 4 h p.i.). This indicates that ^{67}Ga is not following the biodistribution of the corresponding AuNPs, pointing out for the release of ^{67}Ga from the AuNPs with eventual *in vivo* transchelation to transferrin.

To have a better insight in this issue, the biodistribution of ^{67}Ga-citrate has been evaluated in human PC3 xenograft Balb/c mice. As mentioned in the introductory Chapter, ^{67}Ga-citrate undergoes an almost quantitive transchelation to transferrin upon intravenous injection. Therefore, if transchelation processes to transferrin were playing an important role in the biodistribution of **BBN-AuNP-DTDTPA-^{67}Ga**, it was expectable that these AuNPs and ^{67}Ga-citrate present a similar biodistribution profile.

To compare the biodistribution profiles of **BBN-AuNP-DTDTPA-^{67}Ga** and ^{67}Ga-citrate, the later was injected intravenously in human PC3 xenograft Balb/c mice and its biodistribution was assessed at 4 h p.i.. The results obtained are presented in Table 2.4. Figure 2.31 shows the comparison of the uptake in the tumors and relevant organs for **BBN-AuNP-DTDTPA-^{67}Ga** and ^{67}Ga-citrate.

Table 2.4: *Biodistribution results (mean ± SD, n=3; expressed as %I.D./g of organ) for ^{67}Ga-citrate at 4 h p.i in human PC3 xenograft Balb/c mice.*

Organ	%I.D./g
Blood	8.6 ± 0.8
Liver	5.6 ± 0.7
Intestine	3.9 ± 0.5
Spleen	3.5 ± 0.8
Heart	3.7 ± 0.3
Lung	5.1 ± 0.7
Kidney	7 ± 0.8
Muscle	1.5 ± 0.1
Bone	7.9 ± 0.2
Stomach	1.9 ± 0.5
Pancreas	3.0 ± 0.2
Brain	0.4 ± 0.2
Tumor	8.0 ± 0.8
Excretion (%I.D.)	18.7 ± 0.9

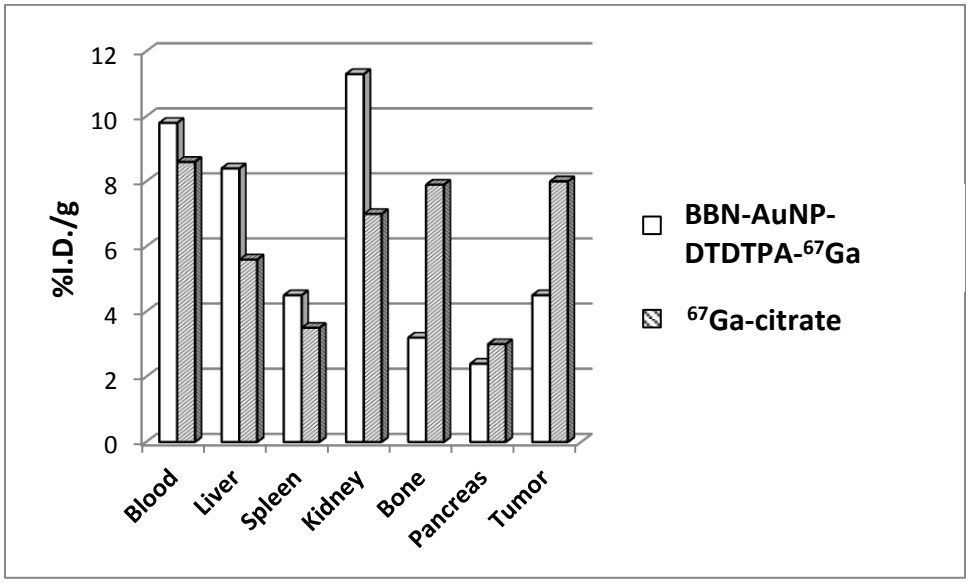

Figure 2.31: *Comparison of the biodistribution (mean, n=3; expressed as %I.D./g of organ) of* ***BBN-AuNP-DTDTPA-^{67}Ga*** *and ^{67}Ga-Citrate at 4 h p.i., in human PC3 xenograft Balb/c mice.*

As can be seen in Figure 2.31, the biodistribution profile of ^{67}Ga-citrate at 4 h p.i. is rather similar to that obtained for **BBN-AuNP-DTDTPA-^{67}Ga**, despite a slightly higher tumor (8.0 ± 0.8 I.D./g) and bone (7.9 ± 0.2 I.D./g) uptake.

These findings could indicate that **BBN-AuNP-DTDTPA-^{67}Ga** is undergoing *in vivo* transchelation to transferrin, in the same way as ^{67}Ga-citrate, and the resulting ^{67}Ga-labeled transferrin (Tf) is accumulated by the tumors upon interaction with Tf receptors and subsequent internalization. However, it is not possible to exclude the involvement of other processes in the tumor accumulation observed for **BBN-AuNP-DTDTPA-^{67}Ga**, namely the EPR effect.

Chapter 3: BBN-containing Gold Nanoparticles Stabilized with a DOTA derivative for the Targeting of GRPr-positive Tumors

3.1 Introduction

As discussed in the previous Chapter the **DTDTPA** coated AuNPs have shown some tendency to release ^{67}Ga, either *in vitro* and/or *in vivo*. It was hypothesized that the replacement of **DTDTPA** by an appropriate thiolated macrocyclic chelator would still enable the stabilization of the AuNPs while providing a more stable coordination of radiogallium. For this purpose, a new DOTA derivative functionalized with a thiol group (2-[4,7-bis(carboxymethyl) -10-[2-(3-sulfanylpropanoylamino)ethyl] - 1,4,7,10 - tetrazacyclododec-1-yl] acetic acid, **TDOTA**, Figure 3.1) was developed and evaluated in the stabilization of AuNPs and subsequent coordination of radiogallium.

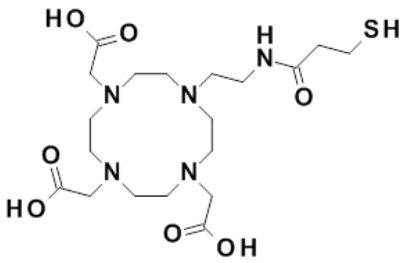

Figure 3.1: *Chemical structure of* ***TDOTA****.*

DOTA has been extensively used in the field of radiopharmaceutical development, and its capability to coordinate gallium is well known.[85,86] Moreover, there are several studies with nanoparticles decorated with DOTA derivatives that have shown promising results in which concerns the coordination of medically relevant metals or radiometals.[145,165] However, studies where DOTA derivatives are used as stabilizers of AuNPs are scarcer.

In this Chapter, it is described the synthesis of **TDOTA**, its use to stabilize AuNPs, as well as the decoration of the AuNPs with BBN derivatives and its labeling with ^{67}Ga. It is also reported on the *in vitro* and *in vivo* biological evaluation of the resulting BBN decorated AuNPs, aiming to assess their suitability for the targeted delivery of ^{67}Ga to GRPr-positive tumor, particularly in comparison with **BBN-AuNP-DTDTPA-^{67}Ga** described in Chapter 2.

3.2 Synthesis and Characterization of TDOTA

As depicted in Scheme 3.1, the multistep synthetic strategy used to obtain **TDOTA** relied on the introduction of a single 2-ethylamine pendant arm in the cyclen framework, for further coupling to a thiolated pendant arm.

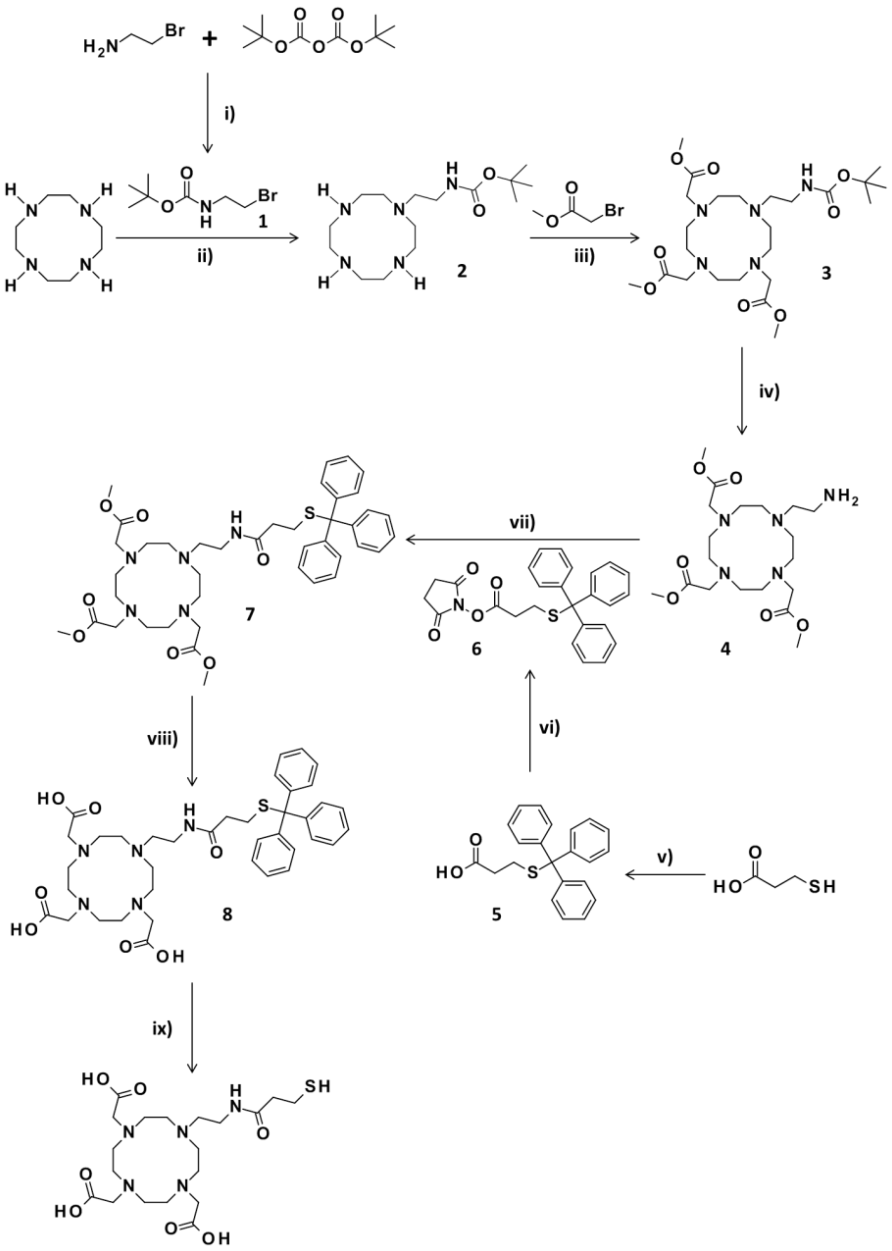

Scheme 3.1: *Synthesis of* ***TDOTA****:* ***i)*** *MeOH, 24 h, r.t.;* ***ii)*** *Toluene, 24 h, reflux;* ***iii)*** *CH_3CN, Na_2CO_3, 8 h, 70 ºC;* ***iv)*** *TFA/CH_2Cl_2, 2 h, r.t.;* ***v)*** *THF, Ph_3CSH, NaH, 30 min, r.t.;* ***vi)*** *CH_2Cl_2, NHS, EDC, DIPEA, 24 h, r.t.;* ***vii)*** *DMF/CH_2Cl_2, DIPEA, 24 h, r.t.;* ***viii)*** *THF/MeOH/H_2O, LiOH, 24 h, r.t.;* ***ix)*** *TFA:H_2O:thioanisole:1,2-dithiolethane, 2 h, r.t..*

The synthesis of compound **TDOTA** started with the N-alkylation of tert-butyl N-(2-bromoethyl)carbamate (**1**) with excess of cyclen (Scheme 3.1). The resulting monoalkylated cyclen derivative (compound **2**), containing a BOC protected pendant arm, was treated with methyl 2-bromoacetate to afford **3**. Then, removal of the BOC protecting group from **3** with TFA gave compound **4** displaying a terminal amino function for coupling of 3-mercaptopropionic acid. Treatment of **4** with a NHS activated ester of 3-mercaptopropionic acid (**6**), having the terminal thiol protected with a trityl group, yielded the amide derivative **7**. Basic hydrolysis of the methyl ester fucntions of **7** followed by acid deprotection of the trityl protecting groups led to the desired final compound (**TDOTA**).

TDOTA has been synthesized with a global yield of 4.5% and has been recovered in the form of a yellow viscous oil. Characterization of **TDOTA** was done by ESI-MS, ^{1}H and ^{13}C-NMR, as well as by COSY and HSQC. The ^{1}H and ^{13}C-NMR spectra of **TDOTA** in D_2O are shown in Figures 3.2 and 3.3, respectively, with assignment of the different resonances. This assignment was done based on COSY and HSQC experiments (A1 and A2 of the Annex section).

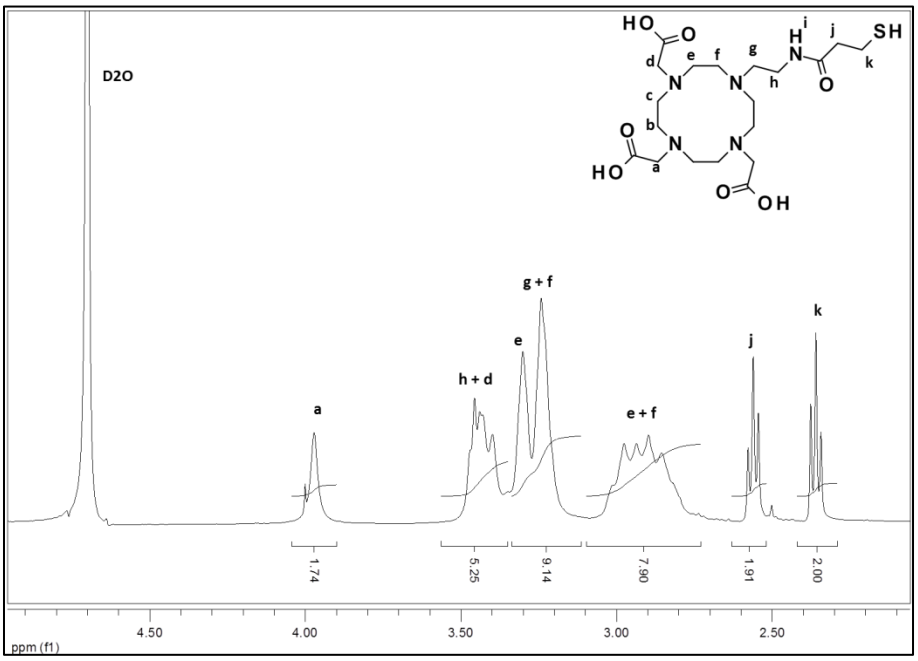

Figure 3.2: *^{1}H-NMR spectrum (D_2O) of* ***TDOTA****.*

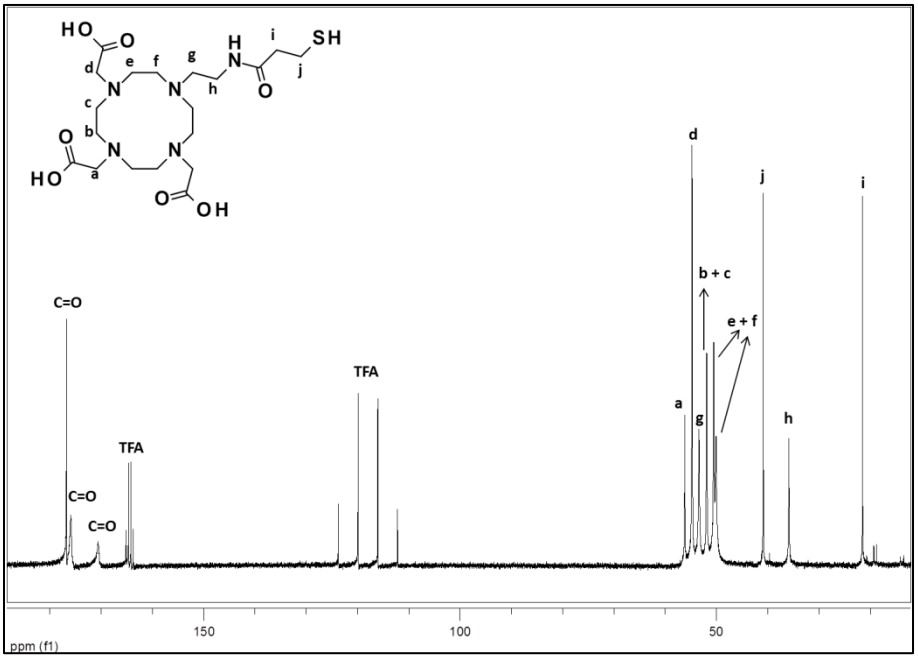

Figure 3.3: *^{13}C-NMR (D_2O) spectrum of* ***TDOTA****.*

In solution, **TDOTA** presents a virtual plane of symmetry that contains the thiolated pendant arm and the correspondent *trans* carboxylate group. Therefore, the remaining acetate arms and the methylenic groups in opposite positions are magnetically equivalent, giving rise to only one set of resonances in the ^{1}H and ^{13}C-NMR spectra of **TDOTA**.

All the expected resonances are present in the ^{1}H-NMR spectrum of **TDOTA**; in particular, there are two distinct triplets at 2.36 and 2.56 ppm, due to the **j** and **k** methylenic protons (Figure 3.2), which confirms the presence of the thiolated am in the compound. This is also corroborated by the three distinct signals that are observed in the ^{13}C-NMR spectrum (Figure 3.3), resonating at 170.56, 175.90 and 176.75 ppm, which are due to the carbonyl groups of the several magnetically different pendant arms.

The ESI-MS analysis of **TDOTA** confirmed the proposed formulation as indicated by the presence of a prominent peak at m/z = 478.4 corresponding to the protonated molecular ions ($[M+H]^+$) and showing the expected isotopic distribution pattern (Figure 3.4).

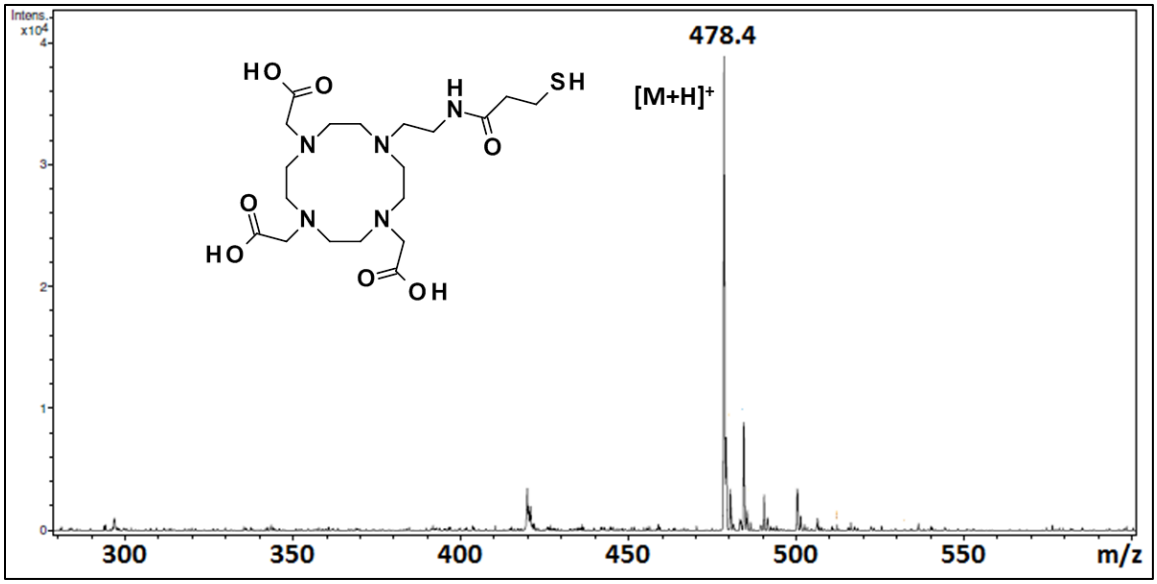

Figure 3.4: *ESI-MS spectrum of* ***TDOTA****.*

3.3 Synthesis and Characterization of AuNP-TDOTA

The strategy for the synthesis of the AuNPs stabilized with **TDOTA** has also been based on the method of Brust *et al.*. As shown in Scheme 3.2, this involved the reduction of $HAuCl_3 \cdot 3H_2O$ with $NaBH_4$ in the presence of **TDOTA** using a molar ratio of 1:2.5 (Au:**TDOTA**), which led almost immediately to the formation of a dark brown solution of AuNPs. The mixture was placed in a dialysis membrane and dialysed for three days in Millipore water. After dialysis, the mixture was centrifuged, washed with H_2O and freeze-dried.

Characterization of **AuNP-TDOTA** was performed by an array of microscopy and spectroscopic techniques (e.g. TEM, DLS and XPS) aiming to assess their physico-chemical properties, namely their elemental composition, size and shape of the core, as well as the nature of the Au-S bond involved in the attachment of **TDOTA** to the gold surface.

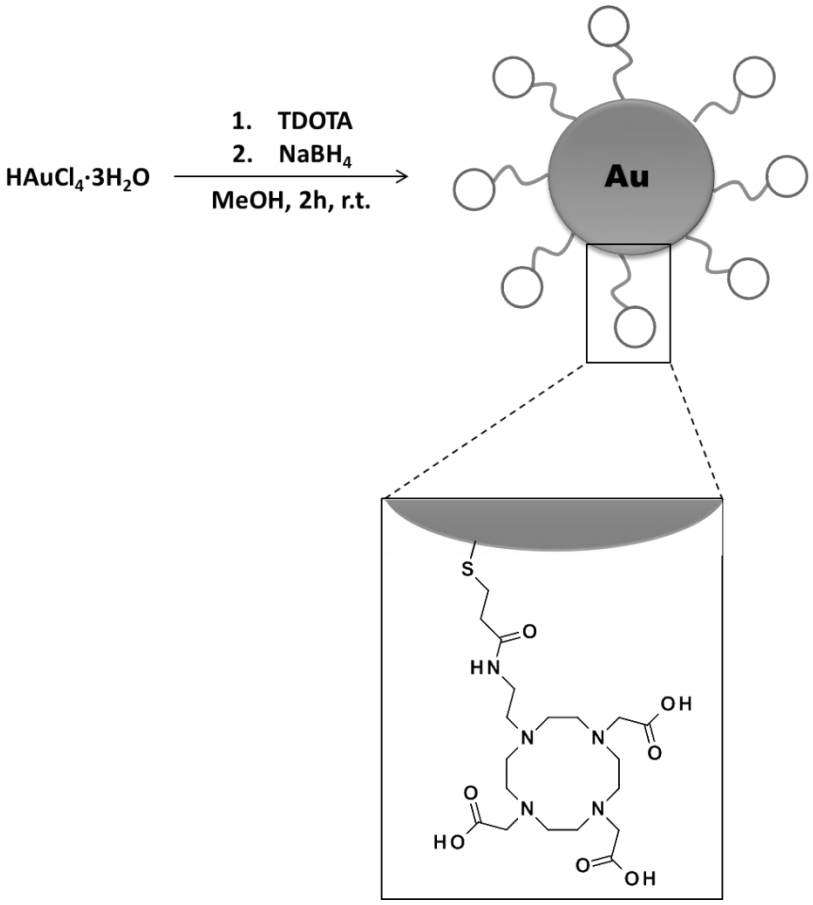

Scheme 3.2: *Synthesis of* ***AuNP-TDOTA****.*

ICP-OES analysis of the gold content of **AuNP-TDOTA** showed that the synthesized nanoconstruct contains 60% of gold (w/w). Assuming that the nanocontruct is essentially constituted by the gold core and the **TDOTA** coating, it is possible to estimate that the AuNP contain contains 40% (w/w) of **TDOTA**.

AuNP-TDOTA was studied by UV-Vis and TEM analysis (Figure 3.5) in order to characterize the size and shape of the respective gold core. The UV-Vis spectrum of **AuNP-TDOTA** in H_2O ($8x10^{-2}$ mg/mL) shows the presence of a broad and low intense absorption band centered at ≈ 520 nm. These results indicate that the core size of the AuNPs is larger than 2 nm, although only slightly. TEM imaging of **AuNP-TDOTA** confirmed a 4.29 ± 1.60 nm size for the core of the AuNPs, and a narrow size distribution.

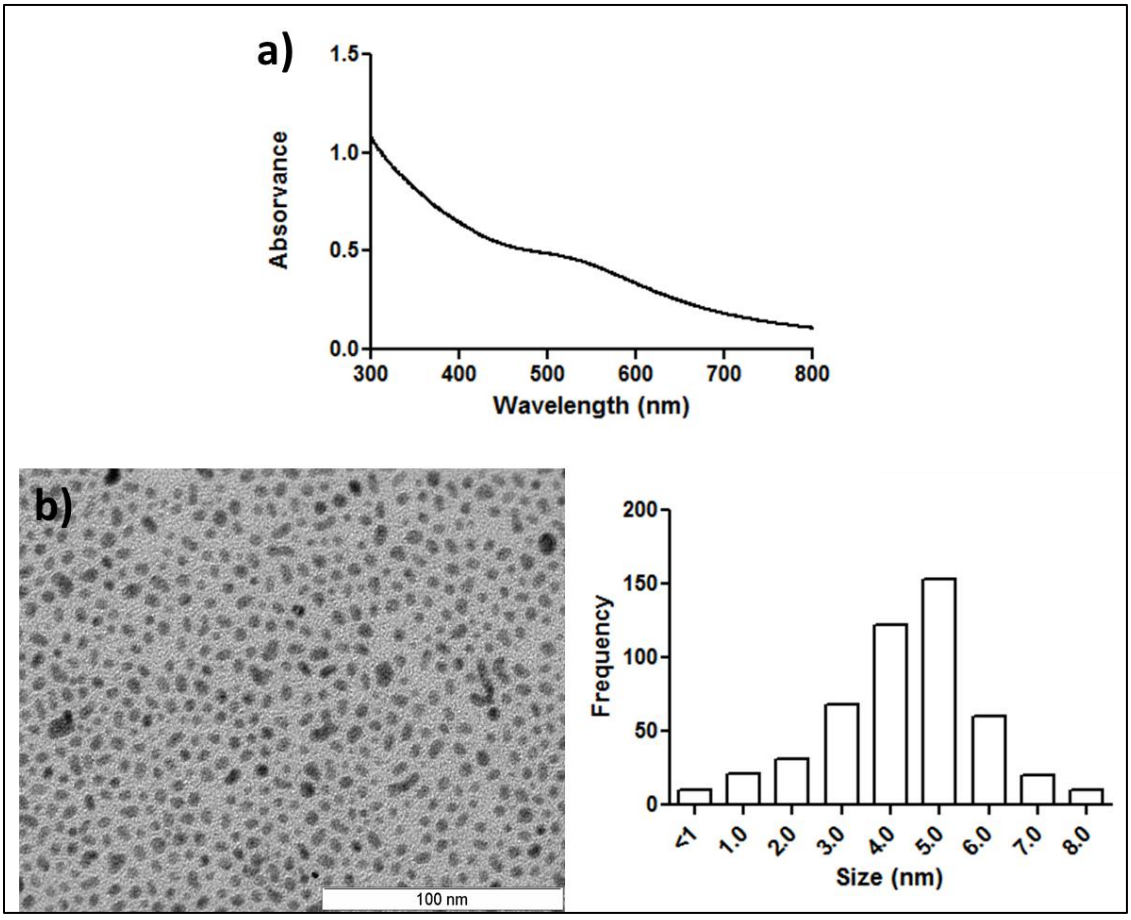

Figure 3.5: a) *UV-Vis spectrum (8x10^{-2} mg/mL) and* ***b)*** *TEM image with respective size histogram, of* ***AuNP-TDOTA****.*

DLS and zeta-potential analysis of **AuNP-TDOTA** were performed in H_2O (8x10^{-2} mg/mL), in order to assess its hydrodynamic size in solution and its surface charge. The DLS analysis showed the opresence of nanoparticles with a large hydrodynamic size of 489.3 nm (PDI = 0.520) (Figure 3.6), which is indicative that **AuNP-TDOTA** have significant tendency to aggregate in solution. If compared with **AuNP-DTDTPA**, the greatest tendency to aggregate exhibited by **AuNP-TDOTA** can be rationalized by its zeta-potential (-20.4 ± 5.5 mV) which is significantly less negative than the one observed for **AuNP-DTDTPA** (-80.7 ± 15.6 mV).

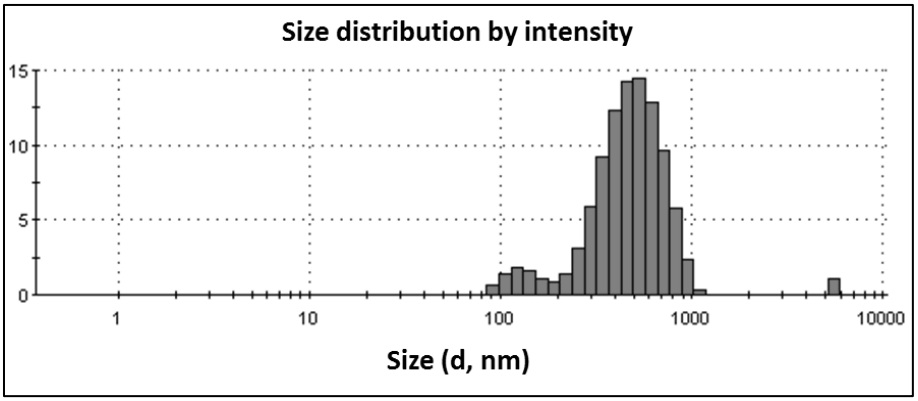

Figure 3.6: *Hydrodynamic size distribution of* ***AuNP-TDOTA*** *in H_2O ($8x10^{-2}$ mg/mL).*

XPS analysis of **AuNP-TDOTA** was done in order to gather further information regarding the presence of the thiolated chelator at the surface of the nanoparticles, namely in which concerns the nature of the Au-S bonds. The high-resolution XPS spectra of **AuNP-TDOTA** obtained for several relevant spectral regions are presented in Figure 3.7.

The C1s photoelectron spectrum of **AuNP-TDOTA** displays two bands in the regions 283-286 eV and 286-289 eV. As shown in Figure 3.7, the deconvolution of the first band shows the presence of two peaks that correspond to C-C and C-H binding energies (284 - 285 eV) and to the C-N binding energy (285 - 286 eV), respectively. The deconvolution of the higher energy C1s band originates binding energy bands, at 286 - 287 eV and 288 - 289 eV, which are due to N-C=O and O-C=O bonds, respectively. The XPS spectrum in the O1s region is consisted with the presence of the C-O (≈ 532eV) and C=O (≈ 531eV) bonds.[220] All these spectral features support the presence of **TDOTA** at the surface of the nanoparticles.

The S2p region of the XPS spectrum of **AuNP-TDOTA** shows a shoulder of low intensity at 162 eV correspondent to the binding energy of sulphur in the form of thiolate. The spectrum shows also a more intense peak at ≈ 163 eV with a shoulder at ≈ 165 eV, which are binding energy values characteristic of S2p 3/2 and S2p 1/2 for thiols.[220] The relative intensities of these bands seem to indicate that the sulphur atom from **TDOTA** is predominatly in the thiol form. This finding seems to indicate that **TDOTA** is bound to the gold atoms mainly by formation of S-H-Au bonds instead of S-Au thiolate bonds, which nevertheless have also been detected. It is worthwhile to mention that the formation of S-H-Au between gold surfaces and thiol derivatives has been invoked previously.[224]

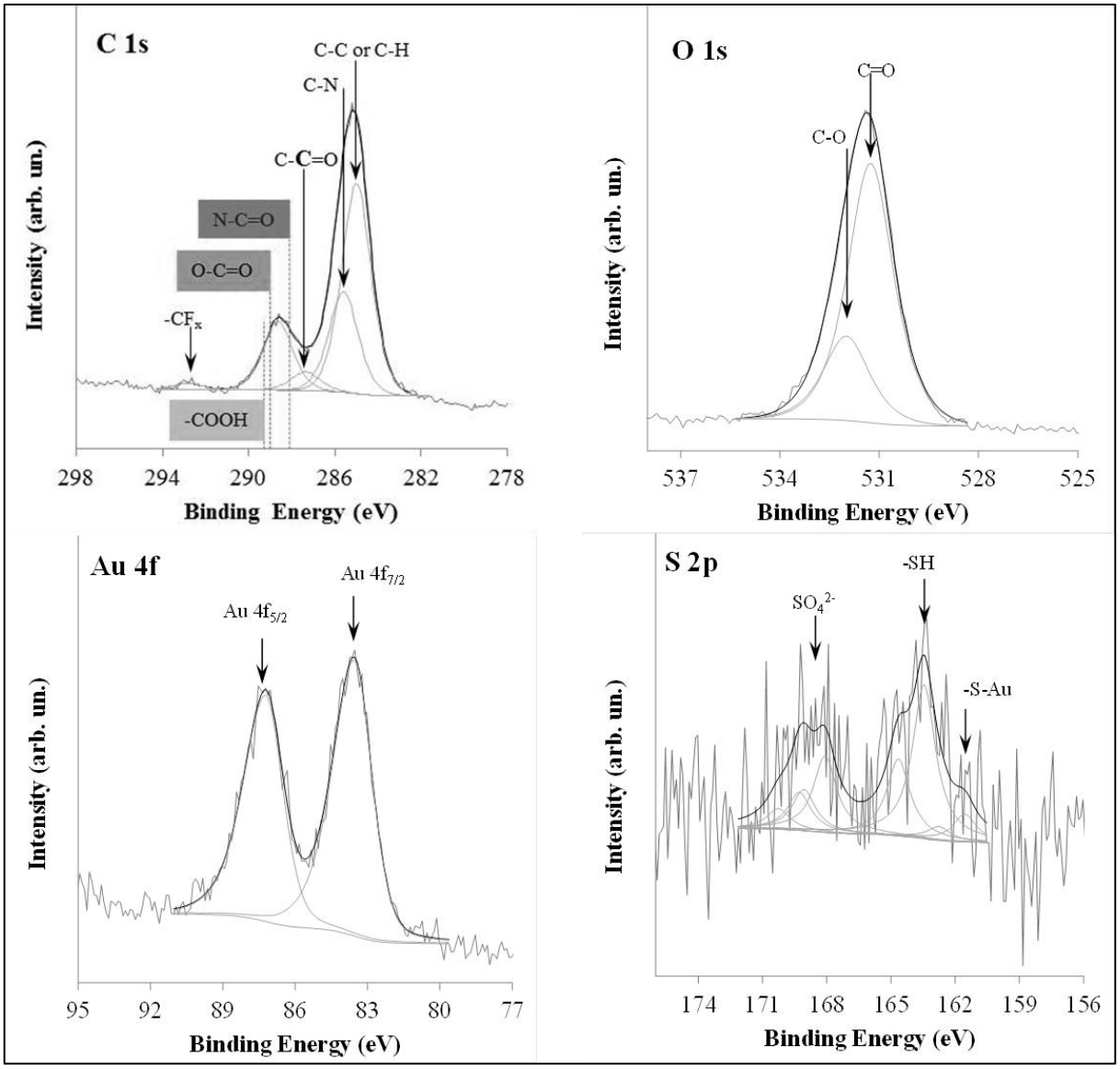

Figure 3.7: *High-resolution XPS spectra of* ***AuNP-TDOTA*** *in the C1s, O1s, Au4f and S2p regions.*

The XPS spectrum of **AuNP-TDOTA** shows the presence of another rather intense band appearing at binding energies in the range 167 - 171 eV (Figure 3.7), which can be assigned to SO_4^{2-} as the binding energies of oxidized sulphur are higher than 166 eV.[220] As can be seen in Figure 3.8, the intensity of this band increases with the duration of the exposition of the sample to the X-rays. Therefore, the detection of oxidized forms of sulphur is most likely due to the effect of the X-ray irradiation of the sample during analysis.

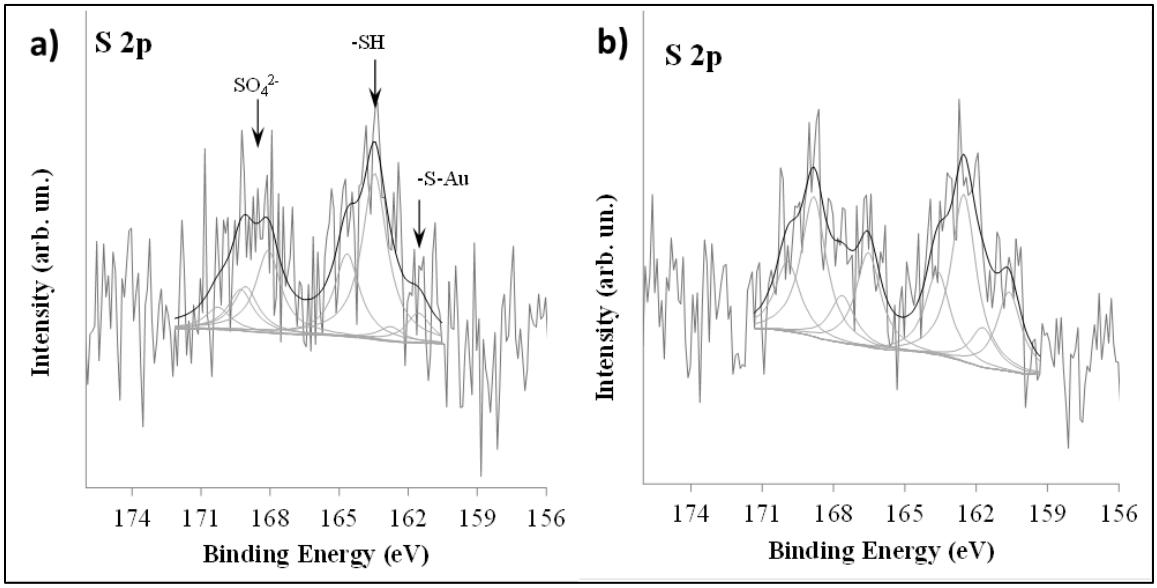

Figure 3.8: *High-resolution XPS spectra of* ***AuNP-TDOTA*** *in the S2p region,* ***a)*** *at the beginning of the analysis and* ***b)*** *after longer X-ray irradiation of the sample.*

3.4 Functionalization of AuNP-TDOTA with BBN Derivatives: Synthesis, Characterization and Biological Evaluation of BBN-AuNP-TDOTA and CBBN-AuNP-TDOTA

After the synthesis and characterization of **AuNP-TDOTA**, the next goal was to proceed with its decoration with BBN derivatives in order to obtain AuNPs with specific targeting capability towards GRPr-positive tumor tissues. For this purpose, it was used **TA-BBN**, that has been applied in the functionalization of **AuNP-DTDTPA**, as described in Chapter 2. For the functionalization of **AuNP-TDOTA**, another BBN derivative (**C-KKK-BBN**) was also studied. This derivative contains the sequence BBN[7-14] but with three additional lysines and a N-terminal cysteine for coupling to the gold surface (Figure 3.9).

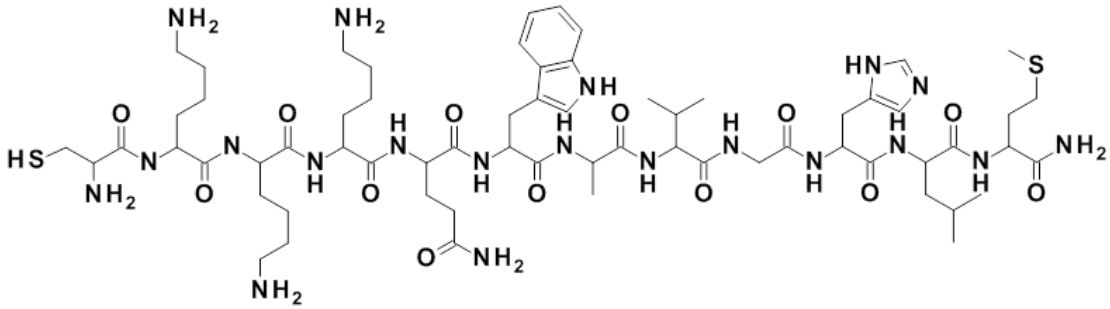

Figure 3.9: *Chemical structure of* ***C-KKK-BBN****.*

By performing a comparative study using **TA-BBN** and **C-KKK-BBN**, it was hypothesized that the use of cysteine instead of thioctic acid would allow the loading of the AuNPs with a higher amount of BBN, as cysteine only possesses a single thiol group and consequently will establish a single S-Au interaction per molecule of peptide attached to the nanoparticle. By contrast, in the case of thioctic acid two of such interactions are involved in the coupling of each molecule of peptide. The possibility of increasing the load of peptide was expected to enhance the targeting ability of the BBN-containing AuNPs.

3.4.1 Synthesis of C-KKK-BBN

The synthesis of **C-KKK-BBN** was accomplished using solid phase peptide synthesis (SPPS) methodologies in a microwave assisted peptide synthesizer (CEM) using standard Fmoc solid-phase chemistry. This approach is based on the use of a resin that is insoluble in the solvents used for the synthesis, which displays a functional group that allows its conjugation to the first amino acid in the peptide sequence. The resin used to synthesize **C-KKK-BBN** was a rink amide resin designated MBHA (Figure 3.10), which consists of a polystyrene matrix with 1% divinylbenzene and it is used in the synthesis of peptides with an amide functional group in the C-terminal of the sequence.

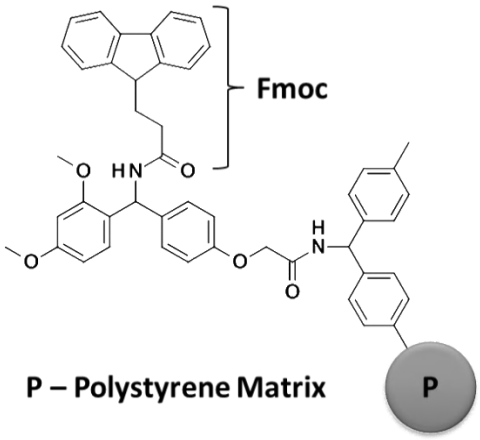

Figure 3.10: *Schematic drawing of rink amide MBHA.*

The procedure was initiated by the removal of the Fmoc protecting group of the resin with a solution of 20% piperidine in DMF. After Fmoc removal, the resin displayed a primary amine group that has been used for the conjugation of the C-terminal carboxylic acid of the first amino acid in the sequence. To perform this conjugation it was necessary to activate the carboxylic functional group of the amino acid. This has been done using O-

(Benzotriazol-1-yl)-N,N,N′,N′-tetramethyluronium hexafluorophosphate (HBTU), which is an activator commonly used in peptide synthesis. Hydroxybenzotriazole (HOBt) was used as an auxiliary nucleophile to suppress racemization reactions and improve the peptide yield.

After conjugation of the first amino acid the process was repeated restarting with the removal of the Fmoc protection group and proceeding to the conjugation of the next amino acid until the peptide sequence was complete.

The final step consisted in removing the peptide from the resin and removal of the protection groups still present in the amino acids of the peptide sequence. First the resin was thoroughly washed with CH_2Cl_2 to eliminate any trace amount of DMF and to swollen the resin in order to guarantee the acidic removal of the peptide. The resin was then treated with a highly acidic solution of TFA:thioanisole:1,2-dithiolethane:H_2O (96:2:1:1), which simultaneously removed the peptide from the resin and the protection groups from the amino acids. The acid solution containing the peptide was then mixed with cold diethyl-ether which led to the precipitation of the peptide. The mixture was centrifuged and the peptide was purified by HPLC.

The characterization of the purified **C-KKK-BBN** has been done by ESI-MS, which confirmed the presence of the desired peptide. The spectrum obtained in the positive mode (Figure 3.11) shows three prominent peaks found at m/z = 1429.2, 714.9 and 477.0, which correspond to the $[M+H]^+$, $[M+2H]^{2+}$ and $[M+3H]^{3+}$ ions, respectively.

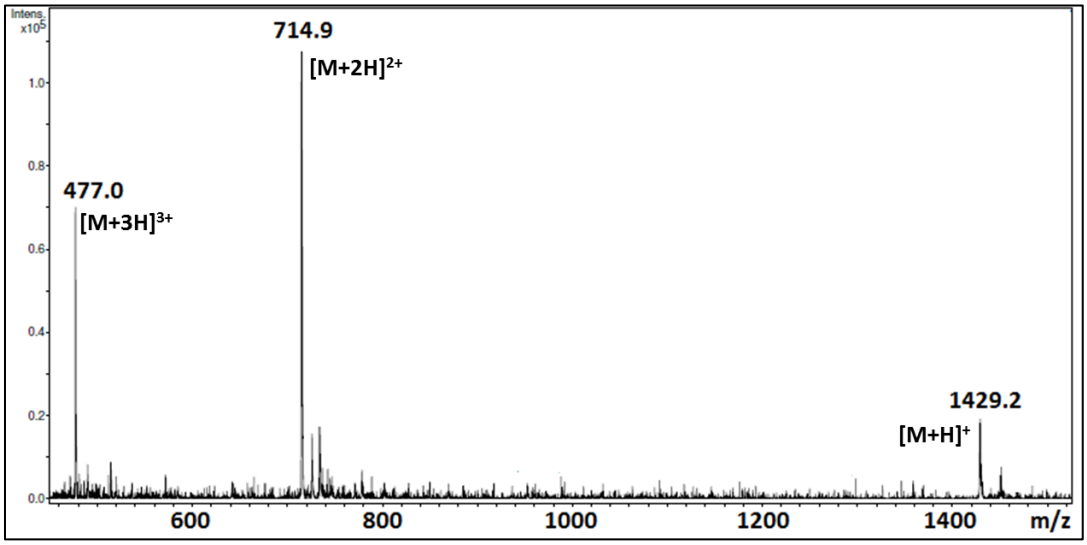

Figure 3.11: *ESI-MS spectrum of* ***C-KKK-BBN****.*

3.4.2 Synthesis of BBN-AuNP-TDOTA and CBBN-AuNP-TDOTA

The synthesis of **BBN-AuNP-TDOTA** and **CBBN-AuNP-TDOTA** has been done by reacting **AuNP-TDOTA** with the desired thiolate peptides (Scheme 3.3), as described previously for the congener **BBN-AuNP-DTDTPA**. The reactions were done using a 1:2 mass ratio of **AuNP-TDOTA** and each BBN derivative. The resulting BBN-containing AuNPs were separated from the supernatant by ultra-filtration and recovered by dissolution in distilled water.

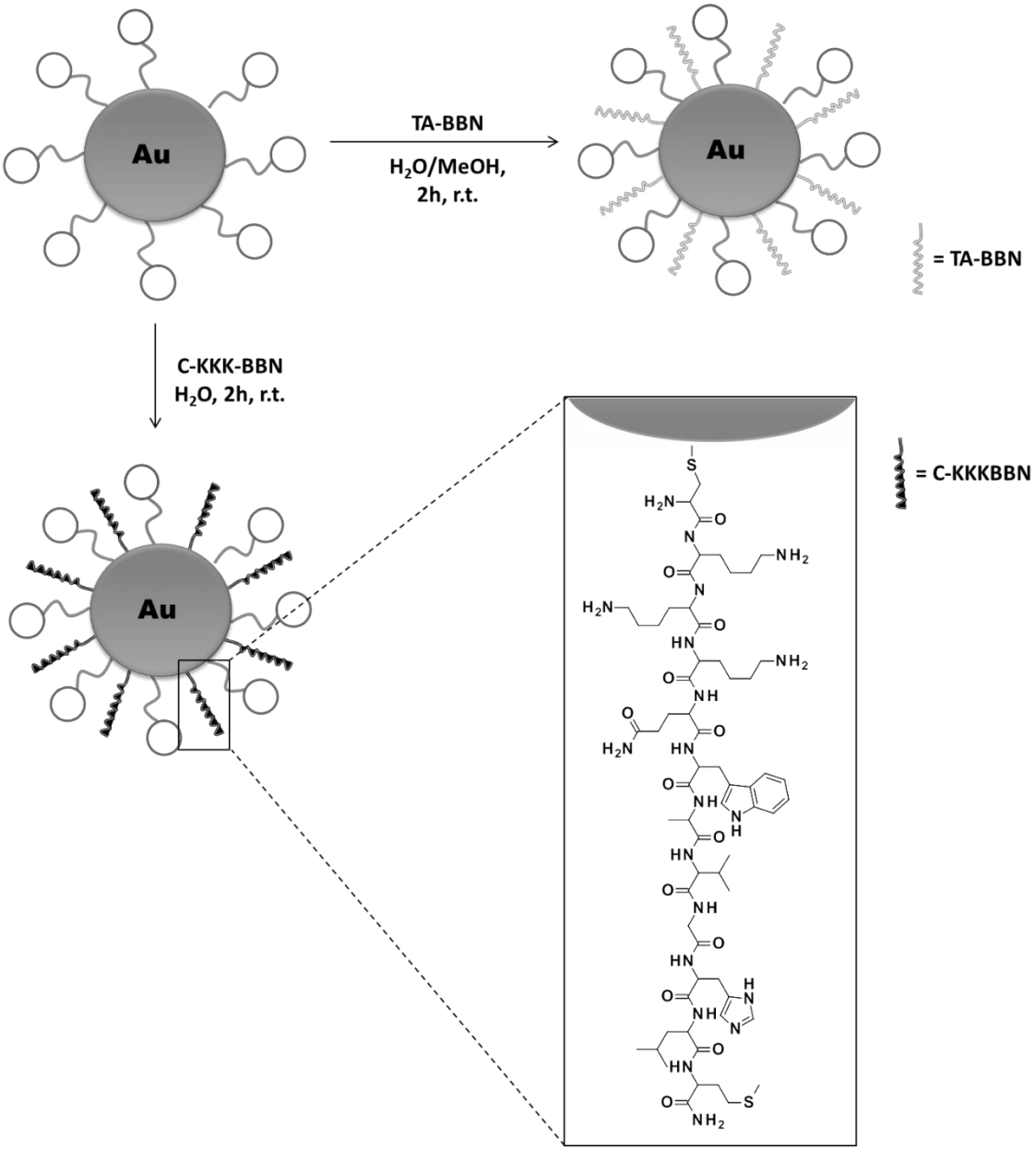

Scheme 3.3: *Synthesis of* ***BBN-AuNP-TDOTA*** *and* ***CBBN-AuNP-TDOTA****.*

HPLC analysis of he supernatant from each conjugation reaction was used to estimate the amount of BBN derivative that has been coupled to **AuNP-TDOTA**, using the procedure described in the previous Chapter for conjugation of **TA-BBN** to **AuNP-DTDTPA**.

Based on the HPLC chromatograms of the supernatants of the reaction mixtures and control solutions of the starting peptides, it was possible to estimate that the amounts of **TA-BBN** and **C-KKK-BBN** attached to **AuNP-TDOTA** were 0.98 mg ($8.58x10^{-4}$ mmol) and 0.24 mg ($1.68x10^{-4}$ mmol) per mg of nanoparticle, respectively. As mentioned above, the conjugation of **C-KKK-BBN** to the AuNPs involves uniquely the formation of one Au-S bond and, therefore, the coupling of the same number of peptide molecules involves less number of gold atoms if compared with **TA-BBN**. This is why one could expect that it should be possible to attach a high number of peptide molecules to the AuNPs in the case of **C-KKK-BBN**. However, the involvement of two suphur atoms per molecule in the conjugation of **TA-BBN** to the AuNPs can lead to a more stable binding, which eventually justifies the higher payload that has been achieved in the case of this BBN derivative.

3.4.3 Physico-Chemical Characterization

UV-Vis and TEM analysis of **BBN-AuNP-TDOTA** and **CBBN-AuNP-TDOTA** were done in order to verify if the conjugation of the peptides induced any significant alteration on the core size and shape of the AuNPs. The obtained UV-Vis spectra and TEM images are presented in Figures 3.12 and 3.13, respectively.

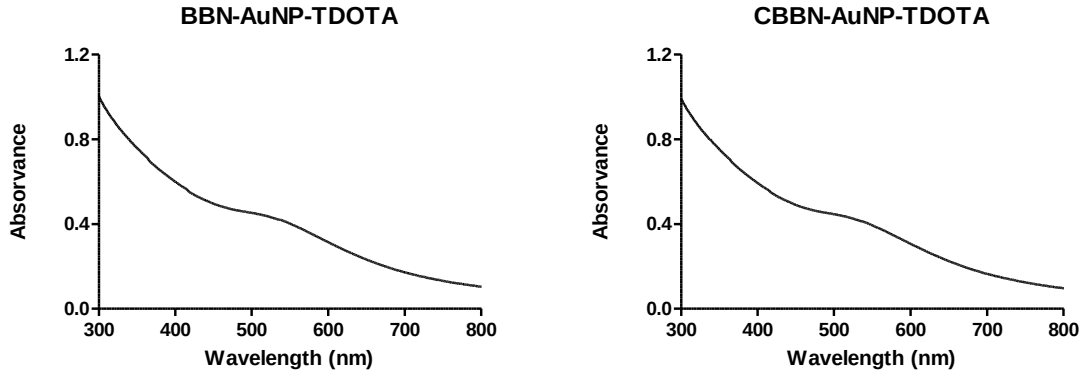

Figure 3.12: *UV-Vis spectra of* ***BBN-AuNP-TDOTA*** *and* ***CBBN-AuNP-TDOTA*** *($8x10^{-2}$ mg/mL).*

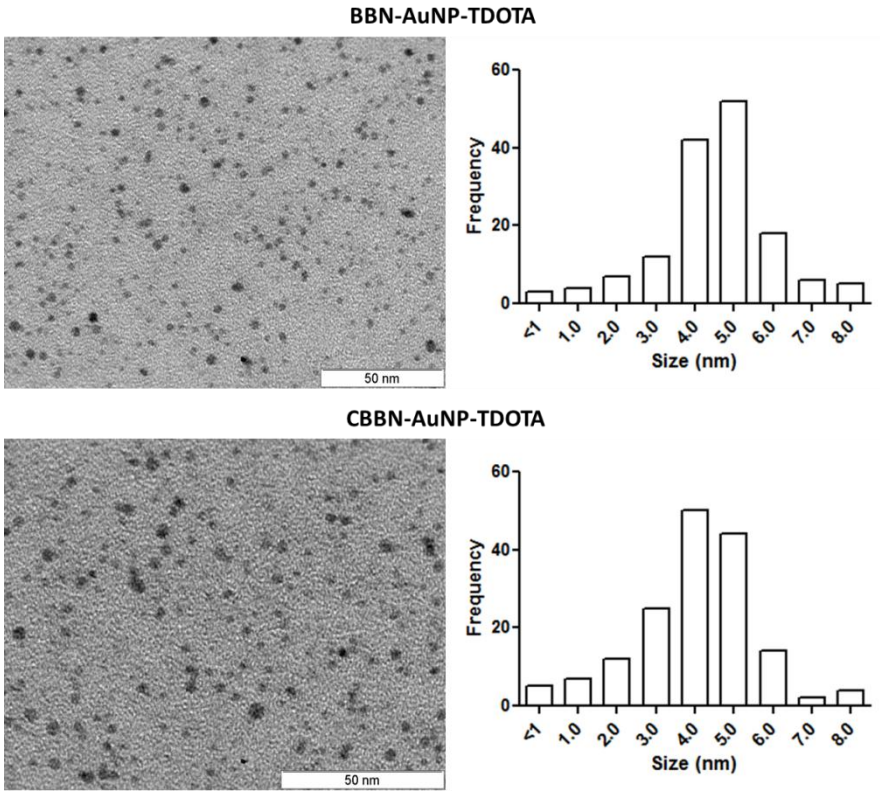

Figure 3.13: *TEM images with respective size histograms of* ***BBN-AuNP-TDOTA*** *and* ***CBBN-AuNP-TDOTA****.*

UV-Vis spectra of **BBN-AuNP-TDOTA** and **CBBN-AuNP-TDOTA** (Figure 3.12) show a band centered at ≈ 520 nm, identical to that of **AuNP-TDOTA**, which indicates that the conjugation of the BBN derivatives did not alter the core size or shape of the AuNPs. This result was further confirmed by TEM analysis (Figure 3.13) being obtained a size of 4.79 ± 1.50 and 4.04 ± 1.52 nm for the core size of **BBN-AuNP-TDOTA** and **CBBN-AuNP-TDOTA**, respectively.

The DLS analysis of **BBN-AuNP-TDOTA** and **CBBN-AuNP-TDOTA** in H_2O (Figure 3.14 and Table 3.2) has shown that these nanoparticles have hydrodynamic sizes of 214 nm (PDI = 0.269) and 313.0 nm (PDI = 0.37), respectively. These values are relatively large but are significantly lower than that exhibited by **AuNP-TDOTA** (489.3 nm (PDI = 0.52)). The zeta-potential values that have been measured for **BBN-AuNP-TDOTA** (-22.6 ± 5.6 mV) and **CBBN-AuNP-TDOTA** (-15.0 ± 8.7 mV) are both negative and can be considered comparable to the zeta-potential of **AuNP-TDOTA** (-20.4 ± 5.5 mV).

The trend observed in the hydrodynamic size of the different **TDOTA** stabilized AuNPs is not directly related with their zeta-potential values, which can be considered rather similar. Apparently, the conjugation of the peptides led to a decrease on the hydrodynamic size of the nanoparticles, contributing for the stabilization with reduction of the levels of aggregation in solution. This can also account for the higher hydrodynamic size of **CBBN-AuNP-TDOTA** compared with **BBN-AuNP-TDOTA**, as the amount of conjugated peptide per mg of nanoparticle is much lower for **C-KKK-BBN** than for **TA-BBN** ($1.68x10^{-4}$ mmol *vs* $8.58x10^{-4}$ mmol).

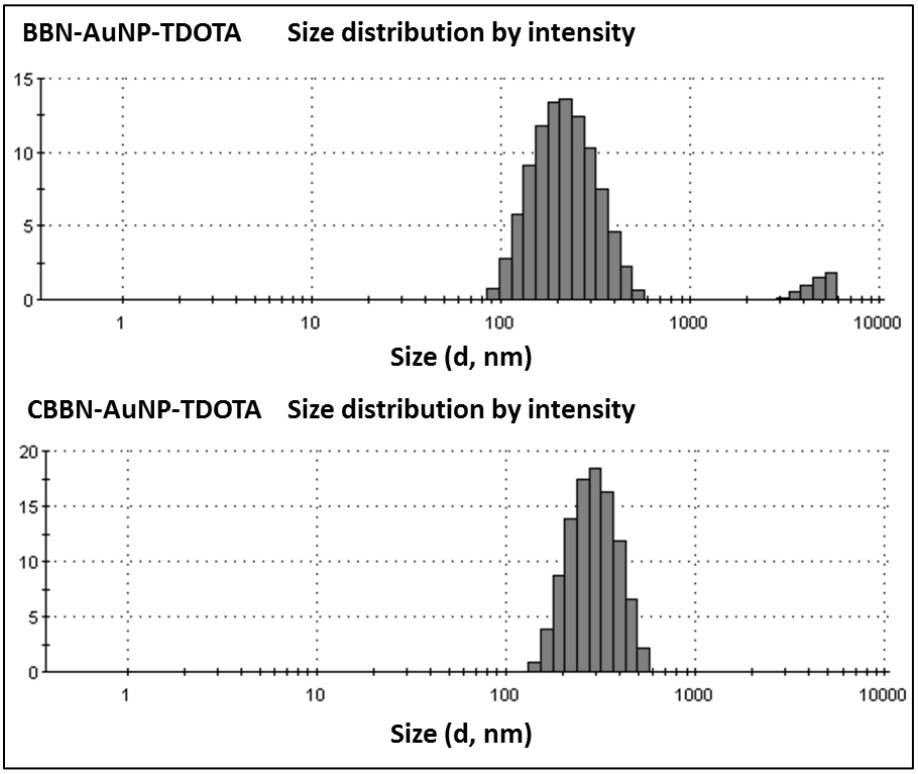

Figure 3.14: *Hydrodynamic size distributions of* ***BBN-AuNP-TDOTA*** *and* ***CBBN-AuNP-TDOTA*** *in* H_2O *(*$8x10^{-2}$ *mg/mL).*

Table 3.1: *Hydrodynamic size (*PDI) and zeta-potential measurements in* H_2O *of* ***BBN-AuNP-TDOTA*** *and* ***CBBN-AuNP-TDOTA****.*

Nanoconstruct	Hydrodynamic Size (nm)	Zeta-Potential (mV)
BBN-AuNP-TDOTA	214.7 (0.269)*	-22.6 ± 5.6
CBBN-AuNP-TDOTA	313.0 (0.37)*	-15.0 ± 8.7

3.4.4 Binding Affinity and Cytotoxicity Assays

Cell viability studies for **AuNP-TDOTA**, **BBN-AuNP-TDOTA** and **CBBN-AuNP-TDOTA** were performed in order to determine the toxicity displayed by these AuNPs. These studies were performed by MTT assays in PC3 cells (Figure 3.15) using the same methodology as for the **DTDTPA** stabilized AuNPs (Chapter 2) and according to a more detailed protocol that is described in the experimental section of this thesis.

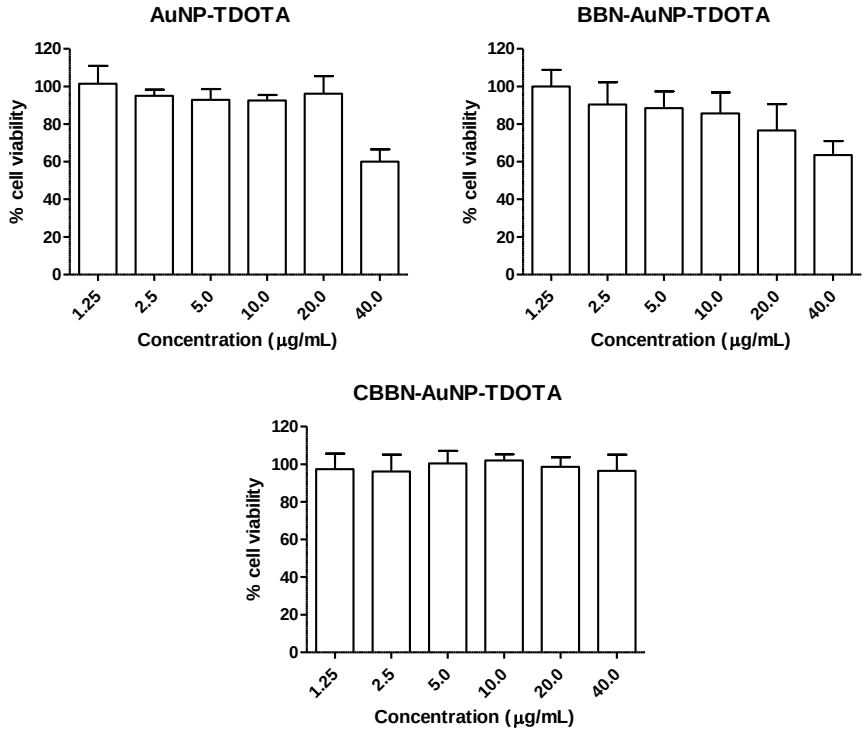

Figure 3.15: *Cell viability (mean ± SD, n=4) of PC3 cells exposed to increasing concentrations of* ***AuNP-TDOTA****,* ***BBN-AuNP-TDOTA*** *and* ***CBBN-AuNP-TDOTA****, evaluated using the MTT assay.*

Overall, **AuNP-TDOTA**, **BBN-AuNP-TDOTA** and **CBBN-AuNP-TDOTA** display low cytotoxic properties, however, at the highest concentration used (40.0 µg/mL) **AuNP-TDOTA** and **BBN-AuNP-TDOTA** led to some significant cell death. It should be noted that the concentrations used for the other biological studies involving these AuNPs were much lower than 40.0 µg/mL.

A competitive binding assay with ^{125}I-Tyr$_4$-BBN was used in order to assess the affinity of the BBN-containing AuNPs towards GRPr in PC3 cells. For comparison purposes, **AuNP-TDOTA** was also studied in this experiment. The procedure was similar

to the one described previously in Chapter 2. The competitive binding curves are shown in Figure 3.16.

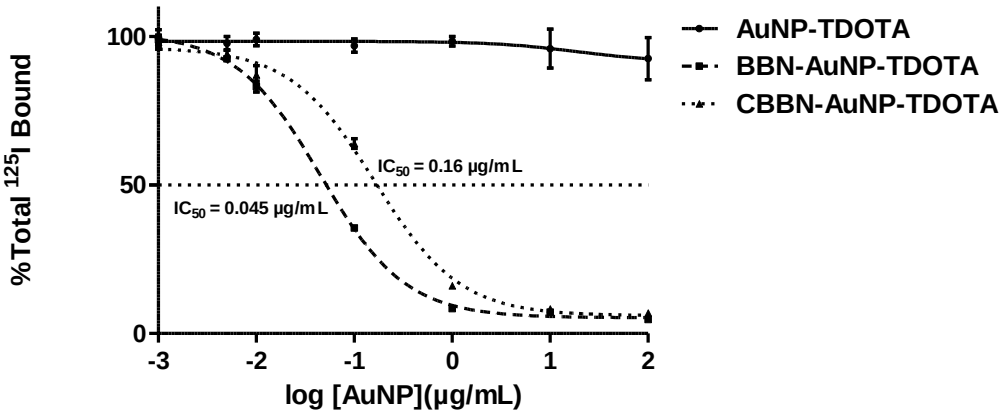

Figure 3.16: *Binding affinity (mean ± SD, n=4) of* ***AuNP-TDOTA****,* ***BBN-AuNP-TDOTA*** *and* ***CBBN-AuNP-TDOTA*** *in PC-3 cells by competitive assays with* ^{125}*I-Tyr*$_4$*-BBN.*

Competitive binding assays with ^{125}I-Tyr$_4$-BBN show that **AuNP-TDOTA** displays no affinity towards GRPr, as can be seen by its inability to displace the radioiodinated specific binding ligand (Figure 3.16). By contrast, **BBN-AuNP-TDOTA** and **CBBN-AuNP-TDOTA** display a significant affinity towards GRPr with IC_{50} values of 0.045 and 0.16 µg/mL, respectively. These results confirm that the presence of BBN in the structure of the AuNPs provides them with affinity towards GRPr. Also, the fact that **BBN-AuNP-TDOTA** has a lower IC_{50} compared with **CBBN-AuNP-TDOTA** is most likely related with the fact that **BBN-AuNP-TDOTA** has a higher amount of conjugated BBN derivative. Compared with **BBN-AuNP-DTDTPA** (IC_{50} ≈ 0.1 µg/mL), described in Chapter 2, **BBN-AuNP-TDOTA** also displays a higher affinity towards GRPr.

3.5 Synthesis, Characterization and Biological Evaluation of AuNP-TDOTA-^{67}Ga, BBN-AuNP-TDOTA-^{67}Ga and CBBN-AuNP-TDOA-^{67}Ga

3.5.1 Radiolabeling and *In Vitro* Stability Studies

After successful synthesis, characterization and functionalization with BBN derivatives of the **TDOTA** stabilized AuNPs, it has been evaluated their capacity to coordinate ^{67}Ga. These studies allowed the synthesis of **AuNP-TDOTA-^{67}Ga**, **BBN-AuNP-TDOTA-^{67}Ga** and **CBBN-AuNP-TDOTA-^{67}Ga**, which were obtained by reaction of the

desired AuNPs with $^{67}GaCl_3$ in acetate buffer (pH ≈ 7) at 50 ºC for 30 min, using a nanoparticle concentration of 0.16 mg/mL.

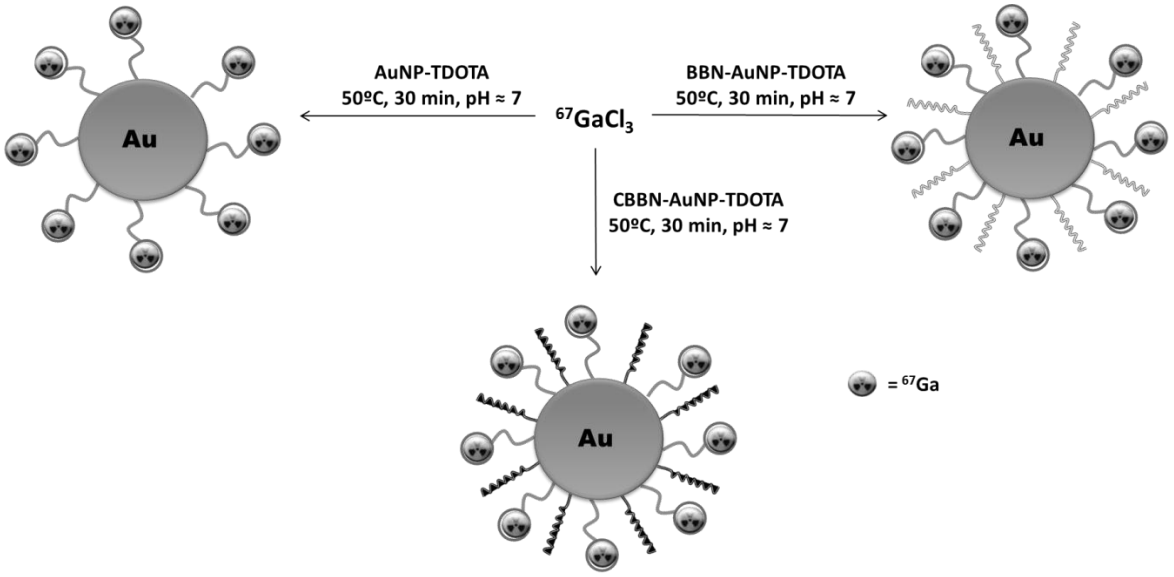

Scheme 3.4: *Radiolabeling of* ***AuNP-TDOTA****,* ***BBN-AuNP-TDOTA*** *and* ***CBBN-AuNP-TDOTA*** *with* ^{67}Ga*.*

After purification by ultra-filtration, the recovered aqueous solutions containing the radiolabeled nanoparticles were analyzed by TLC to assess the radiochemical purity of the synthesized ^{67}Ga-labeled nanoparticles (Figure 3.17). The final ^{67}Ga-labeled nanoconstructs were obtained with radiochemical yields of 86, 69 and 71%, respectively, and with a radiochemical purity >95%.

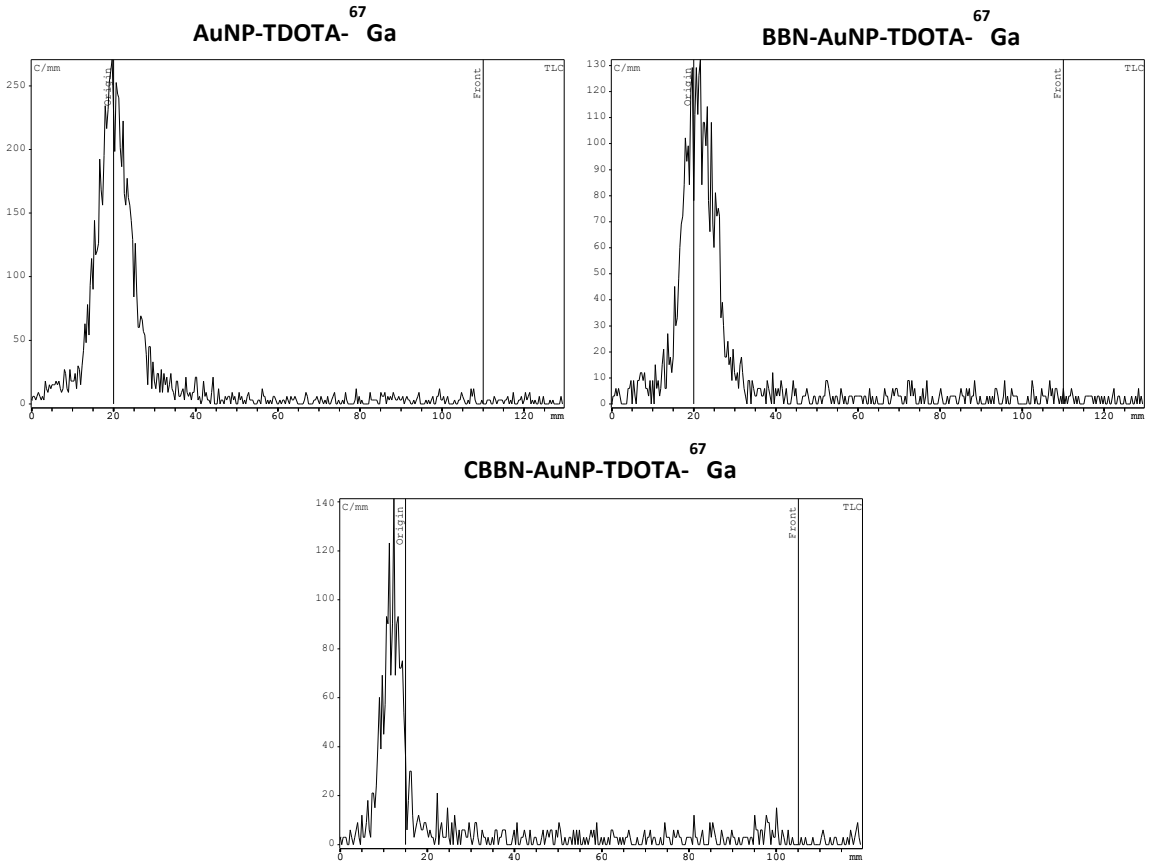

Figure 3.17: *Radiochromatograms of* ***AuNP-TDOTA-^{67}Ga*** *(R_f = 0),* ***BBN-AuNP-TDOTA-^{67}Ga*** *(R_f = 0) and* ***CBBN-AuNP-TDOTA-^{67}Ga*** *(R_f = 0) obtained using ITLC-SG plates with 6 M HCl/MeOH (5:95) as eluent ($^{67}GaCl_3$ (R_f = 1)).*

The *in vitro* stability of **AuNP-TDOTA-^{67}Ga**, **BBN-AuNP-TDOTA-^{67}Ga** and **CBBN-AuNP-TDOTA-^{67}Ga** was studied in the presence of PBS 0.1M, NaCl 0.9%, cell culture medium and apo-transferrin (3 mg/mL, in 10 mM $NaHCO_3$). The radiolabeled nanoconstructs were incubated with the several media at 37 ºC. At different intervals of time, aliquots of the several mixtures were analyzed by TLC. The results obtained for the *in vitro* stability studies of each nanoconstruct are presented in Figure 3.18.

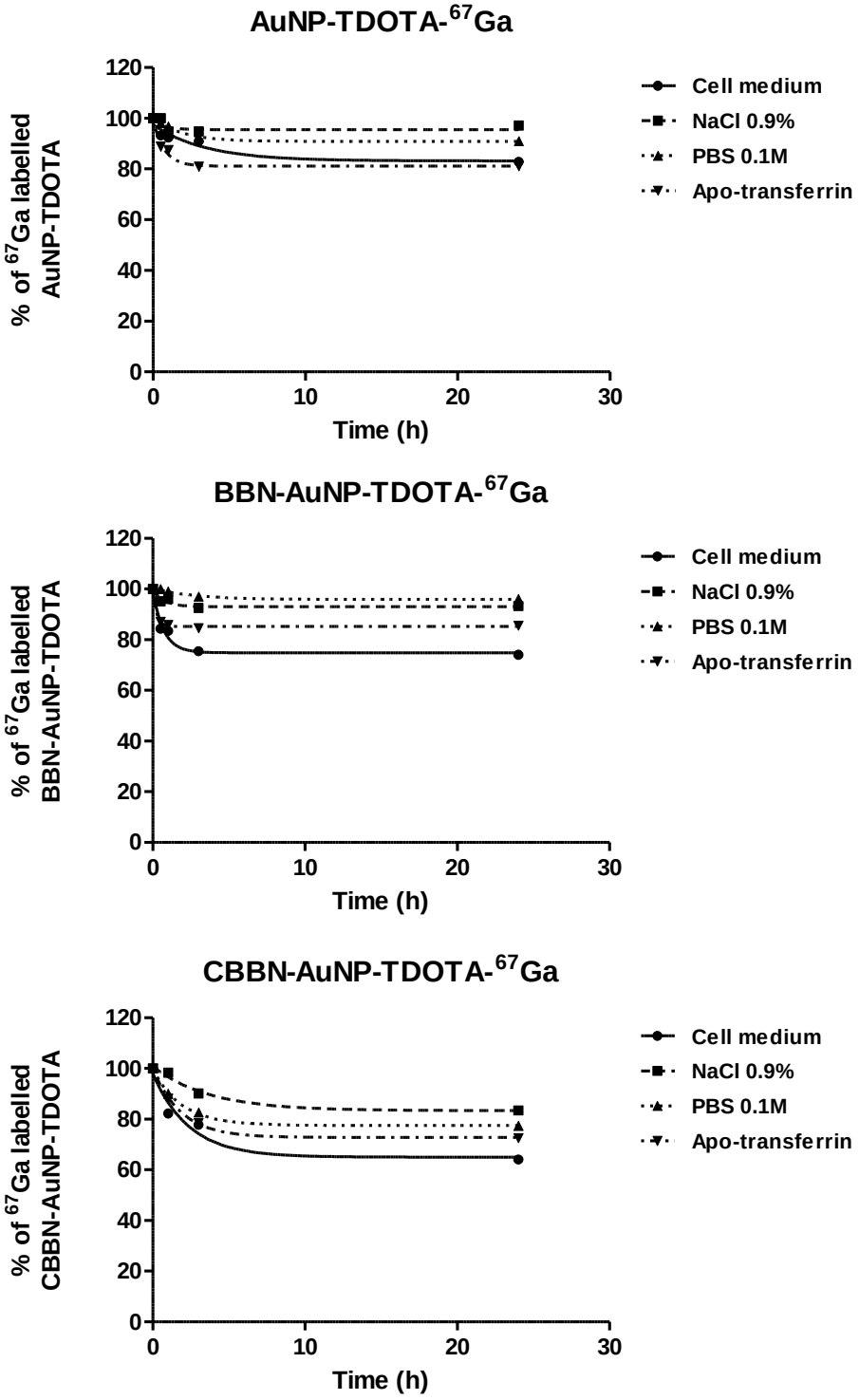

Figure 3.18: In vitro *stability of* ***AuNP-TDOTA-^{67}Ga***, ***BBN-AuNP-TDOTA-^{67}Ga*** *and* ***CBBN-AuNP-TDOTA-^{67}Ga*** *in the presence of physiological and biologically relevant media.*

As it can be observed in Figure 3.18, **AuNP-TDOTA-^{67}Ga**, **BBN-AuNP-TDOTA-^{67}Ga** and **CBBN-AuNP-TDOTA-^{67}Ga** have shown a moderate to high stability in the presence of the different challenging media. For all of them, there is some decrease in the percentage of radiolabeled nanoconstructs for the shortest incubation times but for longer incubation times such percentage remained farily constant.

The *in vitro* stability is lower in the presence of cell medium, being **CBBN-AuNP-TDOTA-^{67}Ga** the less stable nanoconstruct. Nevertheless, more than 60% of **CBBN-AuNP-TDOTA-^{67}Ga** did not release the ^{67}Ga label even after 24 h of incubation with cell medium. Overall, these results show that these **TDOTA** stabilized nanoconstructs provide a more stable coordination of ^{67}Ga when compared with the **DTDTPA** stabilized AuNPs described in Chapter 2.

3.5.2 Cell Studies

Cell uptake studies of **AuNP-TDOTA-^{67}Ga**, **BBN-AuNP-TDOTA-^{67}Ga** and **CBBN-AuNP-TDOTA-^{67}Ga** were performed in GRPr-positive human prostate cancer PC3 cells, by exposing the cells to a solution of the radiolabeled AuNPs in cell culture medium and incubation at 37 ºC for different intervals of time.

The results obtained, expressed as percentage of internalized radioactivity, are presented in Figure 3.19. The internalization observed for **AuNP-TDOTA-^{67}Ga** and **CBBN-AuNP-TDOTA-^{67}Ga** shows a very similar profile with a slow increase of the uptake radioactivity that reaches relatively low plateaued values (< 2%). However, it has been found that the maximum internalization of **CBBN-AuNP-TDOTA-^{67}Ga** is slightly higher than that of **AuNP-TDOTA-^{67}Ga**. By contrast, **BBN-AuNP-TDOTA-^{67}Ga** has shown a very high and rapid internalization into the cells with almost 25% internalization after 15 min of incubation; thereafter, there is a slow release of the radioactivity from the cells.

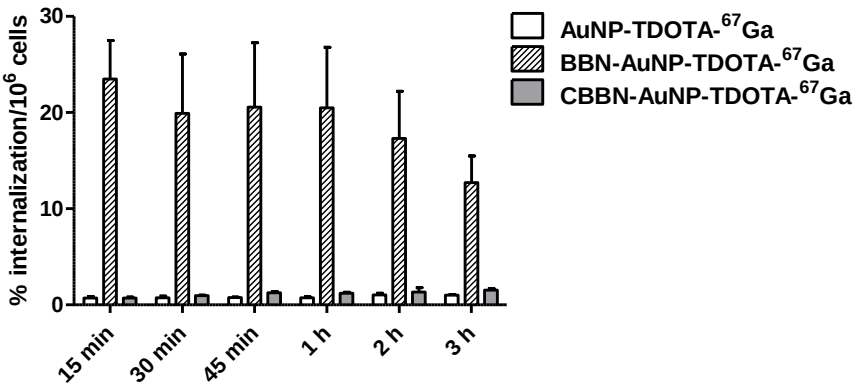

Figure 3.19: *Cellular uptake (mean ± SD, n=4) of* ***AuNP-TDOTA-^{67}Ga****,* ***BBN-AuNP-TDOTA-^{67}Ga*** *and* ***CBBN-AuNP-TDOTA-^{67}Ga*** *in PC3 cells, after incubation at 37 ºC at different intervals of time. Internalization is expressed as the percentage of the applied radioactivity internalized by the cells.*

The lowest rates of internalization were observed for **AuNP-TDOTA-^{67}Ga**, which does not contain any peptide and the highest rates were found for **BBN-AuNP-TDOTA-^{67}Ga**, presenting the highest concentration of BBN analog. As discussed before, the load of **BBN-AuNP-TDOTA** with **TA-BBN** is roughly five-fold higher than the load of **CBBN-AuNP-TDOTA** with **C-KKK-BBN**, which may justify this difference. As above discussed, this difference also affects the binding affinities of the nanoconstructs towards GRPr in PC3 cells. Altogether, these findings indicated that the internalization of **BBN-AuNP-TDOTA-^{67}Ga** should involve a receptor mediated process. To have a better insight on this aspect, the cell uptake of **BBN-AuNP-TDOTA-^{67}Ga** was further studied, which included efflux assays, blockade experiments and use of human tumor cell lines without overexpression of GRPr.

In the efflux studies, PC3 cells were incubated for 15 min with **BBN-AuNP-TDOTA-^{67}Ga** and the radioactivity retained by the cells was measured. Then, the cells were washed at different intervals of time and the radioactivity associated with the cells measured again.

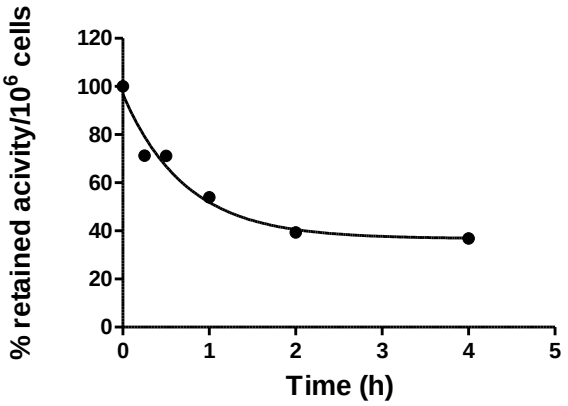

Figure 3.20: *Cellular retention of radioactivity for* ***BBN-AuNP-TDOTA-^{67}Ga*** in PC3 cells, after 15 min incubation at 37 ºC.

As can be verified in Figure 3.20, a fast washout of the radioactivity has been observed during the first 2 h. However, thereafter, the efflux rate significantly decreases and the activity present in the cells remains essentially constant after 4 h of incubation, reaching roughly 40% of the initial radioactivity. Therefore, one can consider that a reasonable amount of **BBN-AuNP-TDOTA-^{67}Ga** was retained by the PC3 cells, which was an encouraging result to further study the targeting ability of these AuNPs in GRPr-positive tumors.

Blocking studies with BBN were also performed in PC3 cells at different intervals of time, aiming to check the contribution of specific uptake in the cellular internalization of **BBN-AuNP-TDOTA-^{67}Ga**, i.e. mediated by interaction with GRPr. The results are presented in Figure 3.21a. These studies showed that there is no significant difference in the amount of internalized radioactivity between the blocked and the non-blocked cells. The presence of BBN at the surface of the AuNPs clearly influences its internalization into the cells, but apparently the process involved is not mediated merely by the specific interaction with GRPr, as indicated by the inability of cold BBN to inhibit the uptake.

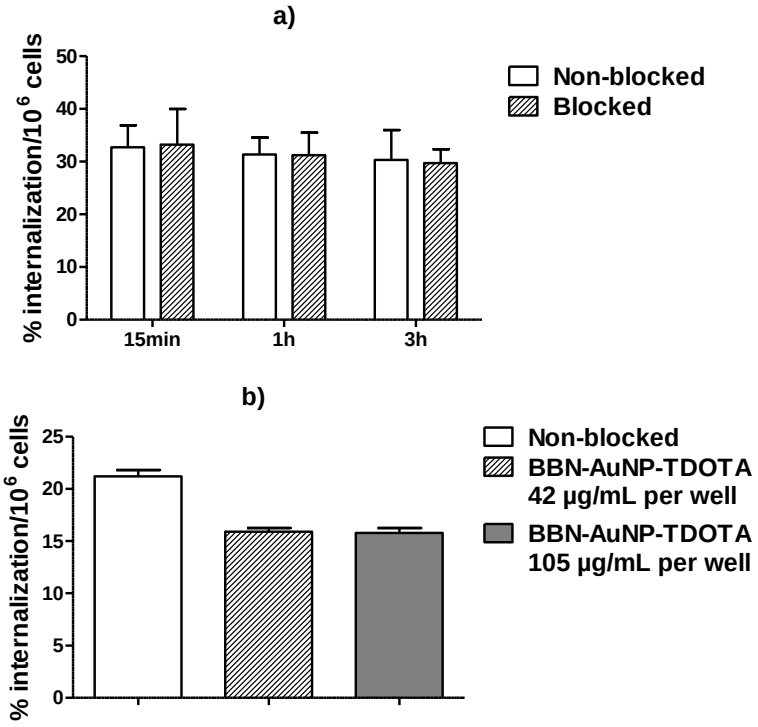

Figure 3.21: *Cellular uptake (mean ± SD, n=4) of* ***BBN-AuNP-TDOTA-^{67}Ga*** *at 37 ºC in PC3 cells in the presence of* ***a)*** *BBN (1 µM/well) and* ***b)*** *cold* ***BBN-AuNP-TDOTA*** *(42 µg/mL and 105 µg/mL per well). Internalization is expressed as the percentage of the applied radioactivity internalized by the cells.*

It has been hypothesized that the large hydrodynamic size of **BBN-AuNP-TDOTA** (214.7 nm (PDI = 0.269)) could contribute for an easier saturation of the GRPr receptors in the cell membrane. As invoked by other authors, due to their size, a single nanoparticle can block the access to several receptor molecules, even without being involved in direct and specific interactions with such molecules.[101] On the flip side, a single **BBN-AuNP-TDOTA** having several copies of the bioactive peptide can specifically interact with more than one GRPr molecule, leading to a strong binding as found often for multimerized constructs, due to the so-called concept of avidity.[225] For all these reasons, monomeric BBN can be a less effective competitor in the GRPr binding of **BBN-AuNP-TDOTA-^{67}Ga** if compared with the cold **BBN-AuNP-TDOTA** itself.

Then, it was decided to perform blockade experiments using increasing concentrations of cold **BBN-AuNP-TDOTA**. As can be seen in Figure 3.21b, the amount of internalized radioactivity decreased but the decrease was not very pronounced (roughly

25%), even using a 30-fold greater concentration (17.5 µg/mL per well) of **BBN-AuNP-TDOTA**, compared to the concentration (≈ 3.5 µg/mL per well) of the radiolabeled AuNPs.

It should also be taken into account that due to the low amount of ^{67}Ga present in the radiolabeling mixture (< 4.7×10^{-9} mmol) it is common to have non-radiolabeled AuNPs in the final **BBN-AuNP-TDOTA-^{67}Ga** solution. These non-radiolabeled AuNPs will compete for the binding with GRPr. Unfortunately, separation of the radiolabeled AuNPs form the non-radiolabeled ones was not possible with the available methodologies.

These findings confirmed that cold BBN-containing AuNPs are more effective in reducing the cell uptake of **BBN-AuNP-TDOTA-^{67}Ga** than molecular BBN. To have a different insight in this aspect, it has been studied the effect of using lower concentrations of **BBN-AuNP-TDOTA** to obtain **BBN-AuNP-TDOTA-^{67}Ga**. For this purpose, **BBN-AuNP-TDOTA-^{67}Ga** were prepared using half of the concentration of cold AuNPs (i.e. 0.08 mg/mL *vs* 0.16 mg/mL) but the same ^{67}Ga radioactivity, according to the procedure described above.

Figure 3.22 compares the cell internalization results of **BBN-AuNP-TDOTA-^{67}Ga** obtained using these two concentrations of starting AuNPs. **BBN-AuNP-TDOTA-^{67}Ga** obtained with the lowest concentration display highest cell uptake particularly for short periods of incubation (54.0% *vs* 32.74% after 15 min of incubation). It was attempted to perform the cell uptake studies using even lower concentrations of starting AuNPs but, unfortunately, it was not possible to obtain satisfactory radiochemical yields.

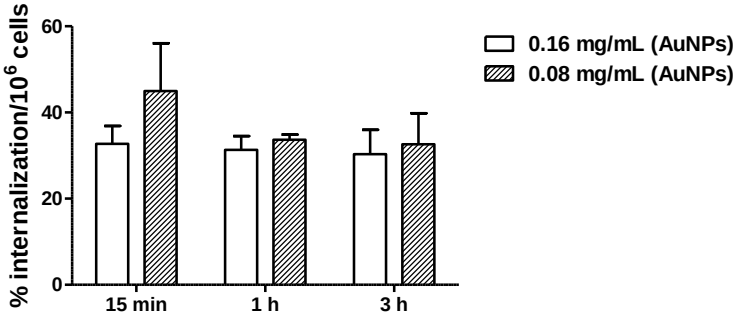

Figure 3.22: *Cellular uptake (mean ± SD, n=4) of* ***BBN-AuNP-TDOTA-^{67}Ga*** *in PC3 cells at 37 ºC, as a function of the concentration of the starting AuNPs. Internalization is expressed as the percentage of the applied radioactivity internalized by the cells.*

The cell internalization of **BBN-AuNP-TDOTA-^{67}Ga** was also studied in two alternative cell lines, human breast cancer MCF7 and mouse melanoma B16F1 cell lines, which are not considered to overexpress GRPr (Figure 3.23). The initial rate of internalization is significantly lower in these cell lines, with less than 5% internalized radioactivity at 15 min of incubation in contrast with > 20% of internalization observed for the PC3 cells. Moreover, there is a slow release of radioactivity from PC3 cells with the incubation time, while the opposite is observed for the B16F1 and MCF7 cell lines that showed a steady increase of internalization with the time of incubation. These results are indicative that the presence of GRPr influences the cellular uptake of the nanoparticles, taking into account the much faster internalization observed for the PC3 cells.

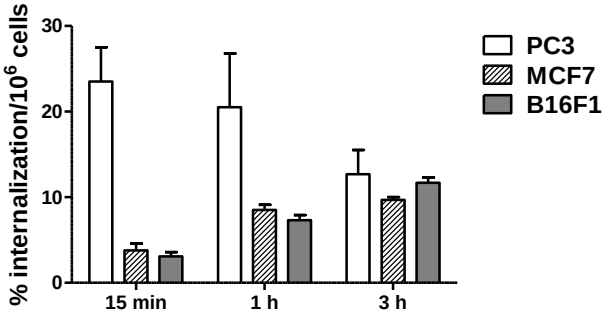

Figure 3.23: *Comparative cellular uptake (mean ± SD, n=4) for* ***BBN-AuNP-TDOTA-^{67}Ga*** at 37 ºC *in PC3, MCF7 and B16F1 cell lines. Internalization is expressed as the percentage of the applied radioactivity internalized by the cells.*

Altogether, these results indicate that the internalization of **BBN-AuNP-TDOTA-^{67}Ga** in PC3 cells is somewhat mediated by the GRPr. Eventually, in all performed internalization experiments there is already a considerable degree of GRPr saturation due to the presence of the cold BBN-containing AuNPs with high affinity/avidity for the receptor. This may explain that the blocking studies with molecular BBN did not have a significant influence in the cell uptake. Unfortunately, separation of the radiolabeled AuNPs from the non-radiolabeled was not possible, and the radiolabeling with considerably lower concentrations of starting AuNPs did not proceed properly. For these reasons, this issue was not completely clarified.

In order to attain more insight into the involvement of different energy dependent pathways in the internalization of **BBN-AuNP-TDOTA-^{67}Ga** in PC3 cells, cellular uptake was studied at low temperature (4 ºC) and in the presence of inhibitors of different cellular transport processes.

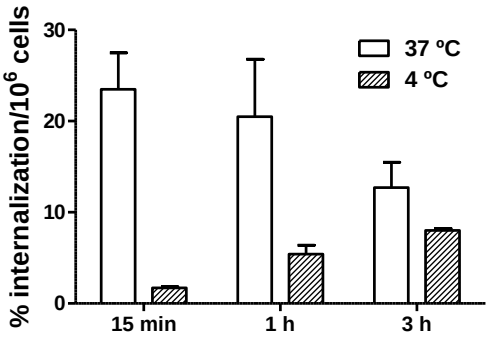

Figure 3.24: *Cellular uptake (mean ± SD, n=4) of* ***BBN-AuNP-TDOTA-^{67}Ga*** *at 4 ºC incubation in PC3 cell lines. Internalization is expressed as the percentage of the applied radioactivity internalized by the cells.*

The cellular uptake of **BBN-AuNP-TDOTA-^{67}Ga** in PC3 cells incubated at 4 ºC is considerably inferior to that observed at 37 ºC (Figure 3.24), which confirms that its cellular uptake involves energy dependant mechanisms, like phagocytic and endocytic pathways. It is worth noting that other authors have also found that BBN peptide analogs and gold nanocages decorated with BBN derivatives show decreased cellular uptake at 4 ºC in GRPr expressing cancer cells.[226]

In agreement, when the cells were placed in the presence of amiloride, phenylarsine oxide or cadaverine, which are endocytosis or phagocytosis inhibitors, there was a decrease up to 20% in the amount of internalized radioactivity (Figure 3.25). Amiloride is a Na^+/H^+ channel inhibitor that is known to block macropynocitosis and phagocytosis pathways, which correspond to non-receptor mediated pathways. Phenylarsine oxide or cadaverine, are both clathrin-mediated endocytosis (CME) inhibitors. In general, receptor based internalization of molecules involves clathrin machinery, as discussed in the introductory Chapter of this thesis.

These results indicate that the cell uptake of **BBN-AuNP-TDOTA-^{67}Ga** occurs most probably *via* active phagocytic and endocytic pathways, which in the later case might involve the internalization of GRPr. Very recently, Kannan *et al.* have shown that the

uptake in PC3 cells of BBN-conatining gold nanocages is mediated by CME, and confirmed the formation of characteristic clathrin coated pits with lisossomal release of the nanocages.[226]

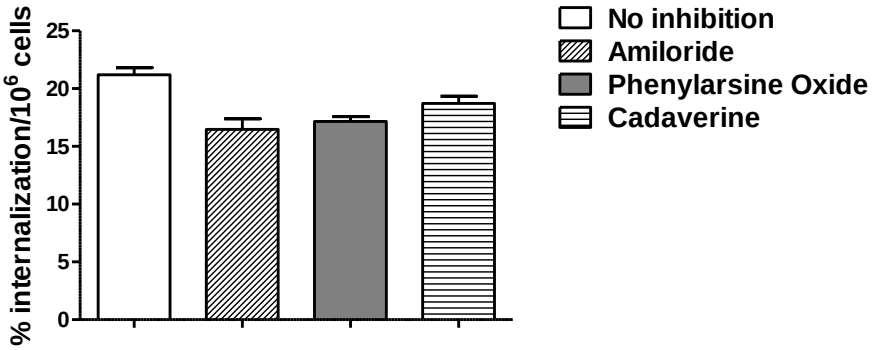

Figure 3.25: *Cellular uptake (mean ± SD, n=4) of* ***BBN-AuNP-TDOTA-^{67}Ga*** *in the presence of amiloride, phenylarsine and cadaverine at 37 ºC in PC3 cells. Internalization is expressed as the percentage of the applied radioactivity internalized by the cells.*

For **BBN-AuNP-TDOTA-^{67}Ga**, the characterization of the uptake was not so detailed, and other possibilities have to be considered, as the nature of interaction and mechanism of internalization of receptor-avid peptide nanoparticles with cells is not yet fully understood. Such possibilities may include other endocytic transport processes, namely caveolae (lipid transport) or alternative non-investigated pathways. As invoked by other authors, the involvement of these alternative pathways may result from the aggregation of the individual nanoparticles, since clathrin mediation is size dependent. In fact, it is considered that nanoparticles can utilize CME to internalize the cells when their dynamical-aggregates are not superior to a 300 nm size limit.[226] As the hydrodynamic size of **BBN-AuNP-TDOTA-^{67}Ga** was 214.7 (PDI = 0.269), it is conceivable that the internalization of **BBN-AuNP-TDOTA-^{67}Ga** will occur through CME, with involvement of GRPr, only when these AuNPs present themselves to the cell surface as individual "monomeric" nanoparticles.

3.5.3 Biodistribution Studies

The biodistribution of **BBN-AuNP-TDOTA-^{67}Ga** and **CBBN-AuNP-TDOTA-^{67}Ga** was studied in groups of three human PC3 xenograft Balb/c mice. Initially, the biodistribution studies were performed by intravenous administration of the AuNPs as

described in the previous Chapter for the **AuNP-DTDTPA** congeners. The results obtained are presented in Table 3.2 and Figure 3.26.

Table 3.2: *Biodistribution results (mean ± SD, n=3; expressed as %I.D./g of organ) for* ***BBN-AuNP-TDOTA-^{67}Ga*** *and* ***CBBN-AuNP-TDOTA-^{67}Ga*** *after i.v. administration in human PC3 xenograft Balb/c mice.*

Organ	%I.D./g					
	15 min		4 h		24 h	
	BBN-AuNP-TDOTA-^{67}Ga	CBBN-AuNP-TDOTA-^{67}Ga	BBN-AuNP-TDOTA-^{67}Ga	CBBN-AuNP-TDOTA-^{67}Ga	BBN-AuNP-TDOTA-^{67}Ga	CBBN-AuNP-TDOTA-^{67}Ga
Blood	3.4 ± 1.4	12.9 ± 3.3	1.7 ± 0.4	2.7 ± 1.4	1.1 ± 0.4	1.3 ± 0.3
Liver	58.9 ± 18.4	37.6 ± 5.7	27.1 ± 1.2	61.9 ± 3.3	13.3 ± 1.7	11.4 ± 4.2
Intestine	0.6 ± 0.2	2.0 ± 1.1	0.7 ± 0.3	0.5 ± 0.3	0.5 ± 0.2	1.0 ± 0.2
Spleen	41.4 ± 3.4	18.0 ± 1.5	10.6 ± 3.9	12.7 ± 1.4	0.7 ± 0.5	4.3 ± 2.4
Heart	1.19 ± 0.07	3.9 ± 1.1	1.3 ± 0.3	0.85 ± 0.09	0.6 ± 0.3	0.68 ± 0.08
Lung	11.8 ± 4.0	23.6 ± 8.3	38.6 ± 1.7	3.0 ± 0.1	2.0 ± 0.5	1.2 ± 0.1
Kidney	1.7 ± 0.2	32.0 ± 5.4	4.8 ± 2.0	2.2 ± 0.4	3.2 ± 0.3	11.6 ± 1.2
Muscle	0.84 ± 0.02	1.5 ± 0.1	0.3 ± 0.1	0.50 ± 0.04	0.6 ± 0.2	0.44 ± 0.03
Bone	2.7 ± 1.1	2.8 ± 0.6	1.1 ± 0.3	3.2 ± 0.7	8.1 ± 0.5	3.5 ± 0.2
Stomach	0.3 ± 0.2	2.42 ± 0.05	0.8 ± 0.2	1.0 ± 0.4	0.7 ± 0.2	0.51 ± 0.07
Pancreas	2.5 ± 0.4	3.0 ± 0.1	0.6 ± 0.2	1.6 ± 0.1	4.5 ± 1.4	1.5 ± 0.2
Brain	0.12 ± 0.01	0.41 ± 0.04	0.11 ± 0.06	0.07 ± 0.01	0.07 ± 0.01	0.11 ± 0.03
Tumor	2.60 ± 0.07	4.1 ± 0.2	2.8 ± 0.3	3.2 ± 0.7	3.7 ± 0.5	3.3 ± 0.8
Excretion (%I.D.)	1.0 ± 0.8	6.1 ± 0.8	30.2 ± 1.4	6.0 ± 2.2	33.2 ± 3.1	38.2 ± 0.5

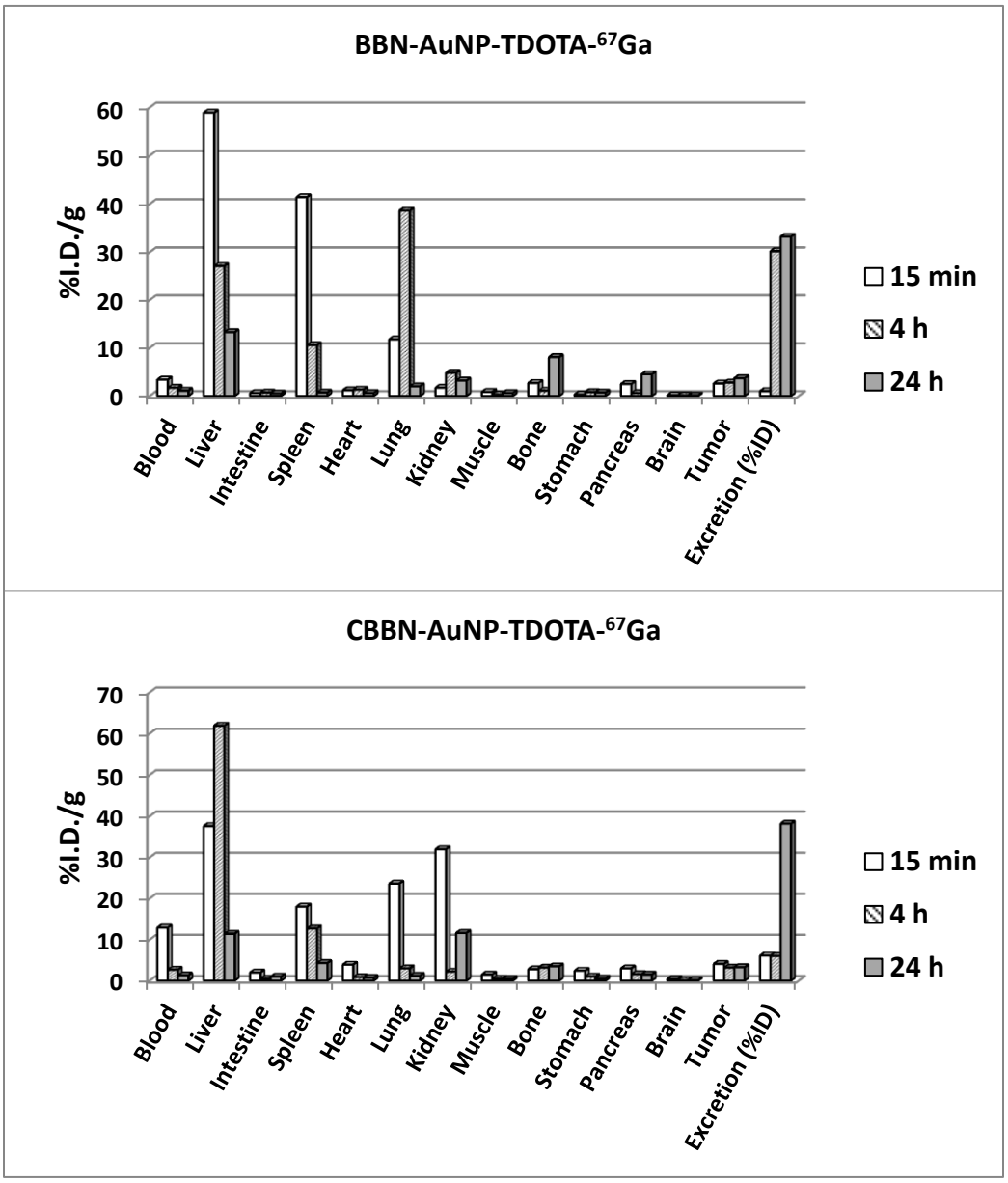

Figure 3.26: *Biodistribution results (mean, n=3; expressed as %I.D./g of organ) for* ***BBN-AuNP-TDOTA-^{67}Ga*** *and* ***CBBN-AuNP-TDOTA-^{67}Ga*** *after i.v. administration in human PC3 xenograft Balb/c mice.*

BBN-AuNP-TDOTA-^{67}Ga shows a very fast extraction by the reticuloendothelial system (RES) organs, as shown by the high uptake values of 58.9 ± 18.4 and 41.4 ± 3.4 %I.D./g observed at 15 min p.i. in the liver and spleen, respectively. There is also a significant accumulation of the radioactivity in the lungs for the early post-injection times. **CBBN-AuNP-TDOTA-^{67}Ga** displays a similar profile, although presenting lower initial uptake values in the liver and spleen (Figure 3.26). These results can be explained by the

large hydrodynamic size of both AuNPs, which are being rapidly entrapped in the RES organs.

Both nanoconstructs show significant tumor uptake, spanning between 2.60 ± 0.07 and 4.1 ± 0.2 %I.D./g for the several time points under study. The maximum tumor uptake for **BBN-AuNP-TDOTA-^{67}Ga** was observed at 24 h p.i (3.7 ± 0.8 %I.D./g), while for **CBBN-AuNP-TDOTA-^{67}Ga** it was at 15 min p.i. (4.1 ± 0.2 %I.D./g). Overall there is no remarkable difference in the tumor uptake for both nanoconstructs.

The uptake ratios tumor/blood and tumor/muscle at 24 h (Figure 3.27) are also comparable, and can be considered relatively favourable for the *in vivo* visualization of tumors.

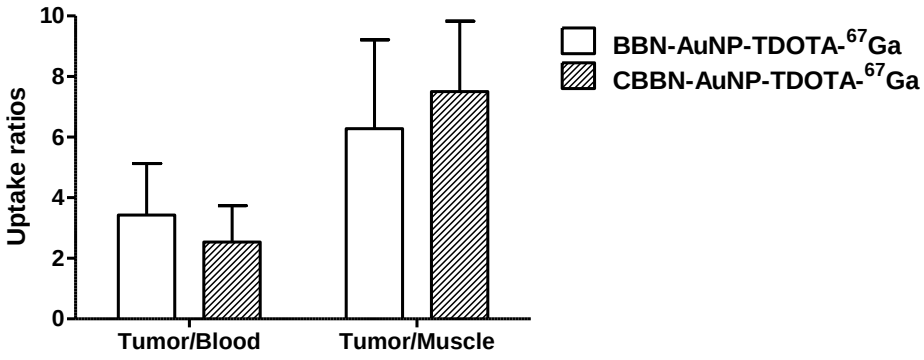

Figure 3.27: *Uptake ratios of tumor/blood and tumor/muscle in the biodistribution (mean ± SD, n=3) of* ***BBN-AuNP-TDOTA-^{67}Ga*** *and* ***CBBN-AuNP-TDOTA-^{67}Ga*** *in human PC3 xenograft Balb/c mice at 24 h p.i..*

The group of Morales-Avila *et al.* have reported that BNN-containing AuNPs tend to be uptaken by the pancreas due to the high overexpression of GRPr in the organ.[182] However, **BBN-AuNP-TDOTA-^{67}Ga** and **CBBN-AuNP-TDOTA-^{67}Ga** showed a very low uptake in pancreas, when administered i.v.. This finding indicated that the tumor uptake observed is most likely not being mediated by the GRPr. In order to verify this hypothesis, blockade studies were performed for **BBN-AuNP-TDOTA-^{67}Ga** and **CBBN-AuNP-TDOTA-^{67}Ga**. A separate set of animals were treated with cold BBN and, thereafter, injected with the nanoconstructs. These experiments were done in parallel with non-treated mice. The pancreas and tumor uptakes for both nanoparticles at 4 h p.i., with and without the blockade, are presented in Figure 3.28.

The blockade experiments have shown no significant alteration in the pancreas and tumor uptake of **CBBN-AuNP-TDOTA-^{67}Ga** and **BBN-AuNP-TDOTA-^{67}Ga** in animals injected or not with BBN. These results indicated that the uptake of these radiolabeled AuNPs in these organs is non-specific. Eventually, the observed tumor uptake is due to the enhanced permeability and retention (EPR) effect that can promote the tumor accumulation of nanoparticles, as discussed in more detail in the introductory Chapter of this thesis.

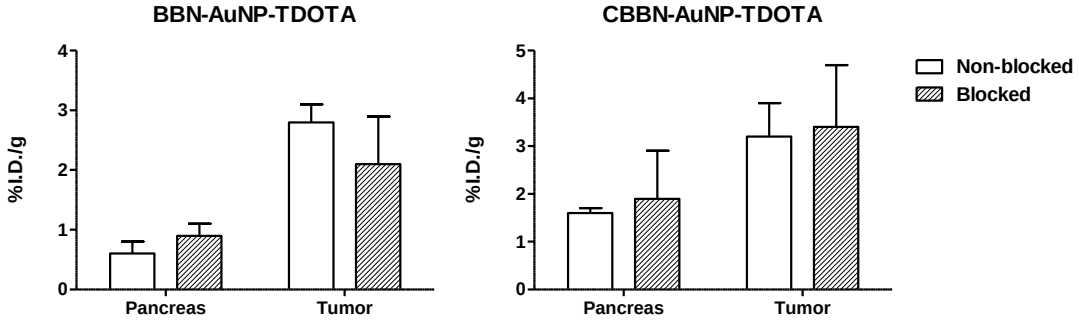

Figure 3.28: *Comparison of the pancreas and tumor uptakes (mean ± SD, n=3; expressed as %I.D./g of organ) at 4 h p.i. for* ***BBN-AuNP-TDOTA-^{67}Ga*** *and* ***CBBN-AuNP-TDOTA-^{67}Ga*** *after i.v. administration in human PC3 xenografts of Balb/c mice, treated (blocked) or non-treated with BBN.*

Taking into account the high affinity of **BBN-AuNP-TDOTA** for GRPr, the poor pancreas uptake found for **BBN-AuNP-TDOTA-^{67}Ga** was quite unexpected. It was thought that the fast uptake of the AuNPs by the RES organs, following the i.v. administration, had severly limited the amount of AuNPs available to reach the pancreas. To clarifiy this aspect, the biodistribution of **BBN-AuNP-TDOTA-^{67}Ga** was evaluated upon intraperitoneal (i.p.) administration. For comparison purposes, **AuNP-TDOTA-^{67}Ga** was also studied in the same conditions. The results obtained are presented in Table 3.3 and Figure 3.29.

The biodistribution profile of **BBN-AuNP-TDOTA-^{67}Ga** after i.p. injection is remarkably different than the one obtained after i.v. administration. In particular, the radioactivity uptakes in the liver, spleen and lung are significantly lower, with values < 5% %I.D./g for all the post-injection times. Moreover, there is a significant pancreas uptake of 9.7 ± 1.6 %I.D./g at 4 h p.i.. The biodistribution profile of **AuNP-TDOTA-^{67}Ga** can be

considered similar but displayed a lower pancreatic uptake (5.6 ± 0.6 %I.D./g at 4 h p.i.), although still significant.

The tumor uptake for **BBN-AuNP-TDOTA-^{67}Ga** after i.p. administration is slightly higher when compared with **AuNP-TDOTA-^{67}Ga** (0.95 ± 0.03 *vs* 0.65 ± 0.11 %I.D./g at 24 h p.i.), which may be related with the presence of the BBN derivatives in **BBN-AuNP-TDOTA-^{67}Ga**. However, this tumor uptake is lower than that exhibited by the same AuNPs after i.v. administration (3.7 ± 0.5 %I.D./g at 24 h p.i.). In summary, i.p. administration of the AuNPs provided a significantly reduced retention in the RES organs and higher pancreas uptake, but also led to a lower uptake in the tumor site.

Table 3.3: *Biodistribution results (mean ± SD, n=3; expressed as %I.D./g of organ) for* ***AuNP-TDOTA-^{67}Ga*** *and* ***BBN-AuNP-TDOTA-^{67}Ga*** *after i.p. administration in human PC3 xenograft Balb/c mice.*

Organ	%I.D./g				
	15 min	4 h		24 h	
	BBN-AuNP-TDOTA-^{67}Ga	AuNP-TDOTA-^{67}Ga	BBN-AuNP-TDOTA-^{67}Ga	AuNP-TDOTA-^{67}Ga	BBN-AuNP-TDOTA-^{67}Ga
Blood	11.0 ± 6.0	1.2 ± 0.7	2.3 ± 1.3	0.4 ± 0.09	1.1 ± 0.5
Liver	2.3 ± 0.4	1.2 ± 0.7	1.4 ± 0.5	1.5 ± 0.5	1.4 ± 0.4
Intestine	2.3 ± 0.4	1.7 ± 0.6	2.4 ± 0.6	1.1 ± 0.2	0.94 ± 0.03
Spleen	4.4 ± 0.3	1.7 ± 1.0	2.6 ± 1.0	1.9 ± 0.1	2.8 ± 1.3
Heart	1.0 0.1	0.44 ± 0.01	0.37 ± 0.09	0.15 ± 0.04	0.18 ± 0.01
Lung	1.9 ± 0.4	0.7 ± 0.3	0.7 ± 0.2	0.3 ± 0.2	0.5 ± 0.2
Kidney	4.4 ± 2.5	3.6 ± 1.8	2.5 ± 0.3	3.0 ± 0.4	2.4 ± 0.2
Muscle	2.5 ± 1.2	0.7 ± 0.2	1.1 ± 0.7	0.4 ± 0.2	0.8 ± 0.06
Bone	1.6 ± 0.6	0.6 ± 0.1	0.9 ± 0.1	0.65 ± 0.05	1.1 ± 0.1
Stomach	3.8 ± 0.7	1.4 ± 0.2	1.6 ± 0.6	0.8 ± 0.2	1.7 ± 0.3
Pancreas	8.8 ± 0.9	5.6 ± 0.6	9.7 ± 1.6	5.7 ± 0.3	5.9 ± 1.3
Brain	0.13 ± 0.01	0.06 ± 0.02	0.09 ± 0.02	0.019 ± 0.02	0.02 ± 0.01
Tumor	2.1 ± 0.4	0.62 ± 0.12	1.02 ± 0.13	0.65 ± 0.11	0.95 ± 0.03
Excretion (%I.D.)	18.0 ± 7.8	76.4 ± 1.3	64.2 ± 3.5	81.0 ± 0.7	71.1 ± 0.5

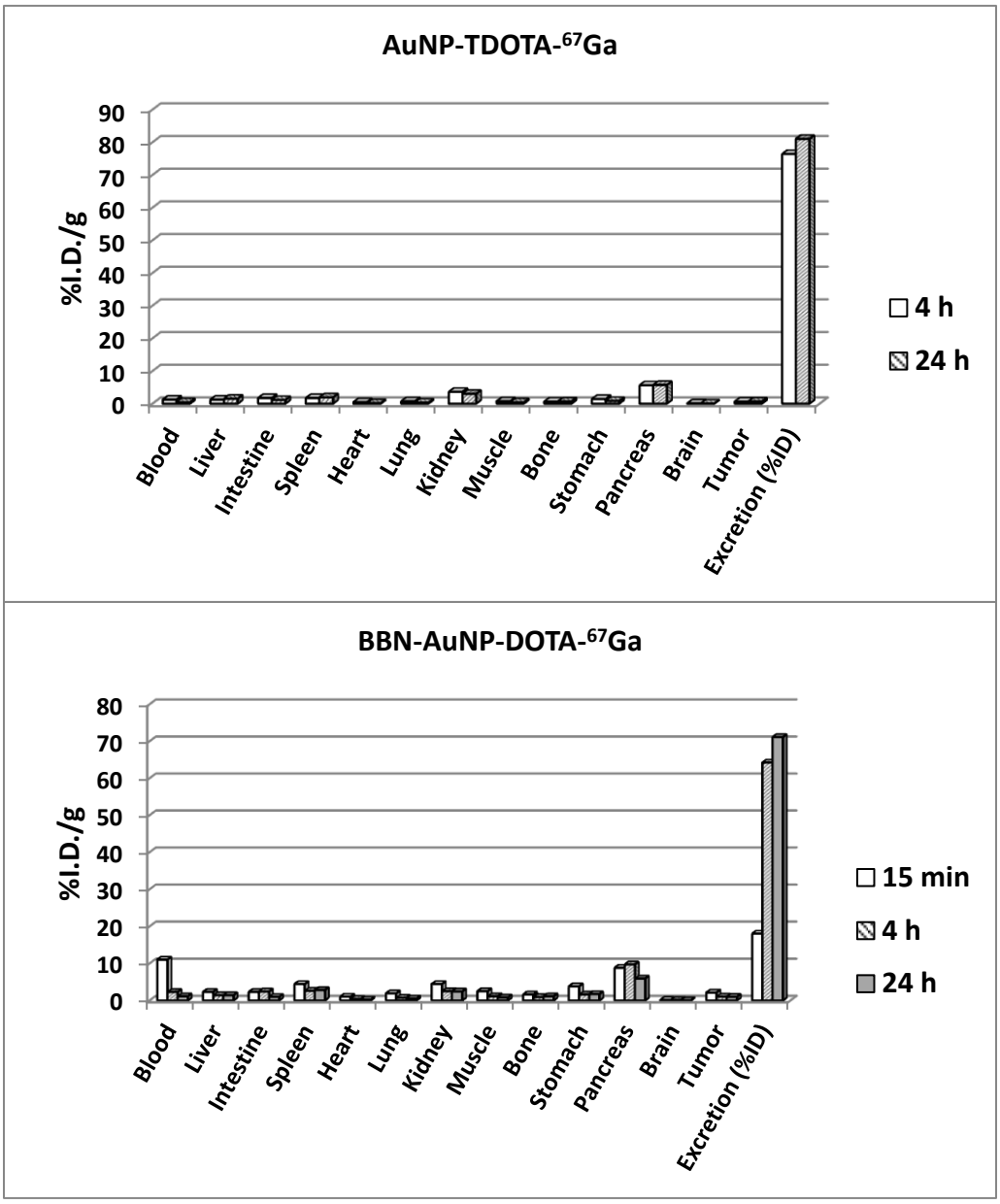

Figure 3.29: *Biodistribution results (mean, n=3; expressed as %I.D./g of organ) for* ***AuNP-TDOTA-^{67}Ga*** *and* ***BBN-AuNP-TDOTA-^{67}Ga*** *after i.p. administration in human PC3 xenograft Balb/c mice.*

Blockade experiments with BBN were also done for **BBN-AuNP-TDOTA-^{67}Ga** injected intraperitoneally. The results for the pancreas and tumor uptakes obtained for the treated and non-treated animals are depicted in Figure 3.30.

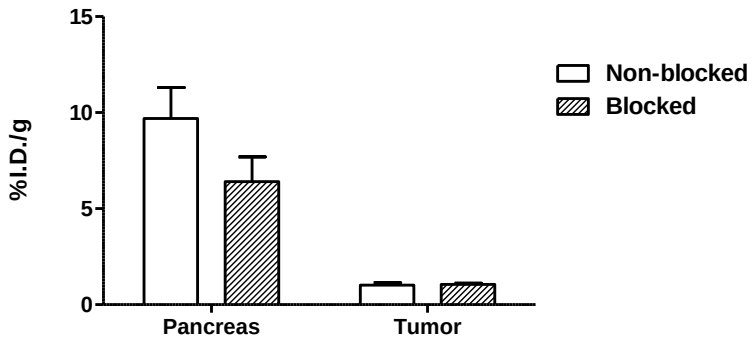

Figure 3.30: *Comparison of the pancreas and tumor uptake (mean ± SD, n=2; expressed as %I.D./g of organ) for* ***BBN-AuNP-TDOTA-^{67}Ga*** *after i.p. administration in human PC3 xenografts Balb/c mice, treated (blocked) or non-treated with BBN, at 4 h p.i..*

As shown in Figure 3.30, there is a significant decrease (≈ 34%) of the pancreas uptake of **BBN-AuNP-TDOTA-^{67}Ga**, when blocked with BBN. In contrast, no alteration was observed in the tumor uptake. These results suggest that the uptake of **BBN-AuNP-TDOTA-^{67}Ga** in the pancreas is possibly being mediated by GRPr, while in the case of the tumor uptake, the contribution of the EPR effect seems to be dominant. Nevertheless, as discussed for the cell studies, the presence of the cold **BBN-AuNP-TDOTA** can also contribute for the saturation of GRPr, and influence these results.

Chapter 4: GE11-containing Gold Nanoparticles for the Targeting of EGFr-positive Tumors

4.1 Introduction

Growth factors belong to a family of cell secreted polypeptides that are responsible for the regulation of cell growth and proliferation. One of the most commonly known growth factors is the Epidermal Growth Factor (EGF), whose biological response is mediated by the EGF receptor (EGFr) that influences cellular growth and proliferation. Mutations and overexpression of EGFr are commonly found in a great variety of cancer types including head and neck, breast, ovarian, cervical and bladder. For this reason, EGFr is a relevant target for cancer diagnostic and therapy.[227-229]

The mature human EGF, the endogenous EGFr ligand, is a 6045 Da polypeptide composed of 53 amino acids that displays three disulfide intramolecular bonds (Figure 4.1). EGF shows a very high affinity towards EGFr. However, its interaction with this receptor leads to a high mitogenic and neoangiogenic activity, which makes EGF a poor choice as a targeting vector for EGFr overexpressing cancers.[228]

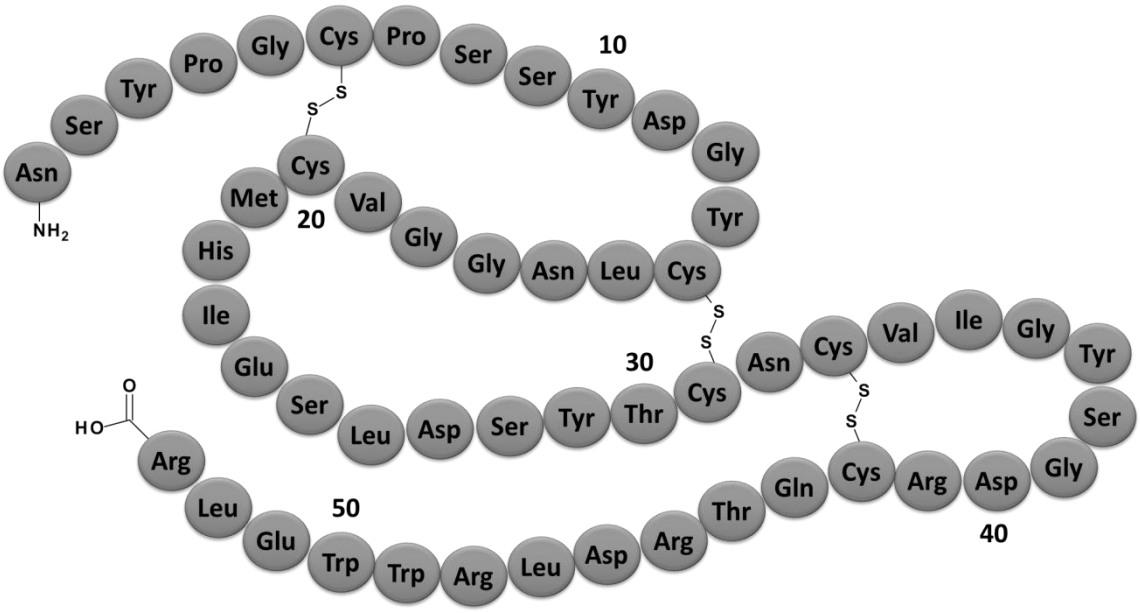

Figure 4.1: *Amino acid sequence of EGF showing the disulfide bonds.*

Recently, the group of Li et al. have identified by phage display a novel peptide composed of 12 amino acids, designated GE11, an agonist with good affinity and specificity for EGFr (Figure 4.2).[230]

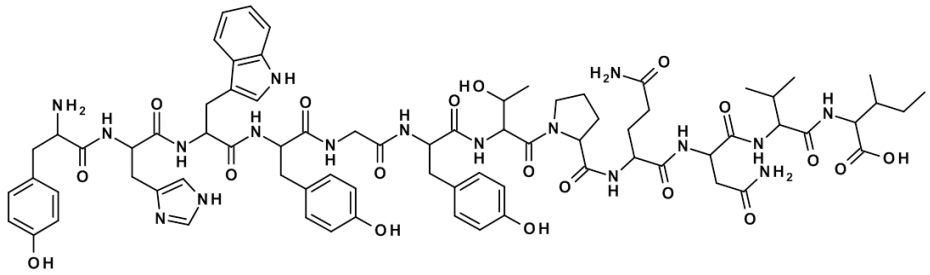

Tyr-His-Trp-Tyr-Gly-Tyr-Thr-Pro-Gln-Asn-Val-Ile-NH_2

Figure 4.2: *Chemical structure of GE11 and respective amino acid sequence.*

The EGFr binding of GE11 is inhibited by the presence of EGF and, therefore, the same binding site of EGFr is probably shared by these two molecules. As stated previously, EGFr is involved in the proliferation and differentiation of cancer cells, which is one of the reasons why GE11 is so appealing in the development of cancer targeting agents. Moreover, GE11 displays a much less significant mitogenic activity compared with EGF.[230,231]

Due to its only recent discovery in 2005, GE11 and its derivatives have not been thoroughly studied. Nevertheless, it is proving to be a promising targeting molecule towards EGFr that may lead to the development of new strategies for cancer management.[232] In particular, some research groups have evaluated the usefulness of GE11 in the design of EGFr-targeted radiopharmaceuticals, aiming at the finding of new tools for early cancer diagnosis. The group of Mishani *et al.* pioneered this field and described a variety of GE11 derivatives labeled with ^{18}F, ^{124}I and ^{111}In, although without reporting their biological behaviour.[233]

GE11 loaded nanoparticles have also been studied in recent years, and it has been shown that the presence of the peptide clearly leads to an increase in their tumor uptake compared with the peptide-free-nanoparticles. For instance, GE11-modified liposomes developed by the group of Chen *et al.* showed enhanced accumulation and prolonged retention in non-small cell lung cancer (NSCLC) tumor tissue when compared with the unmodified liposomes, making them a promising platform for targeted delivery of chemotherapeutic drugs for NSCLC.[234] The group of Kannan *et al.* have synthesized gold

nanoparticles bearing GE11 that afforded very good imaging as X-ray contrast agents for early detection of pancreatic cancer in mice models.[235]

To this date, the combination of GE11 with nanoplatforms and target-specific delivery of radionuclides was unexplored. Searching to prove the relevance of this approach for the design of target-specific (nano)radiopharmaceuticals, it was decided to study AuNPs decorated with GE11 derivatives and with DOTA chelators for ^{67}Ga complexation. For this purpose, it was designed a new molecule, designated as **TA-GE11-DOTA**, containing the GE11 peptide sequence, a DOTA unit and a thioctic acid moiety for coupling to the gold atoms.

Initially, **TA-GE11-DOTA** was conjugated to PEG-containing citrate stabilized AuNPs, but the resulting functionalized nanoconstructs have shown a poor ability to coordinate ^{67}Ga. For this reason, the studies were pursued using **AuNP-DTDTPA**, previously described in Chapter 2, which has been functionalized with **TA-GE11-DOTA** and labeled with ^{67}Ga, using the so-called pre-labeling and post-labeling approaches (Figure 4.3).

In this Chapter, it is described the synthesis and characterization of different AuNPs decorated with **TA-GE11-DOTA**, as well as their labeling with ^{67}Ga. For the AuNPs that were successfully labeled with ^{67}Ga it is also reported their biological evaluation, which comprised cell uptake studies in EGFr-positive cell lines and biodistribution in normal mice.

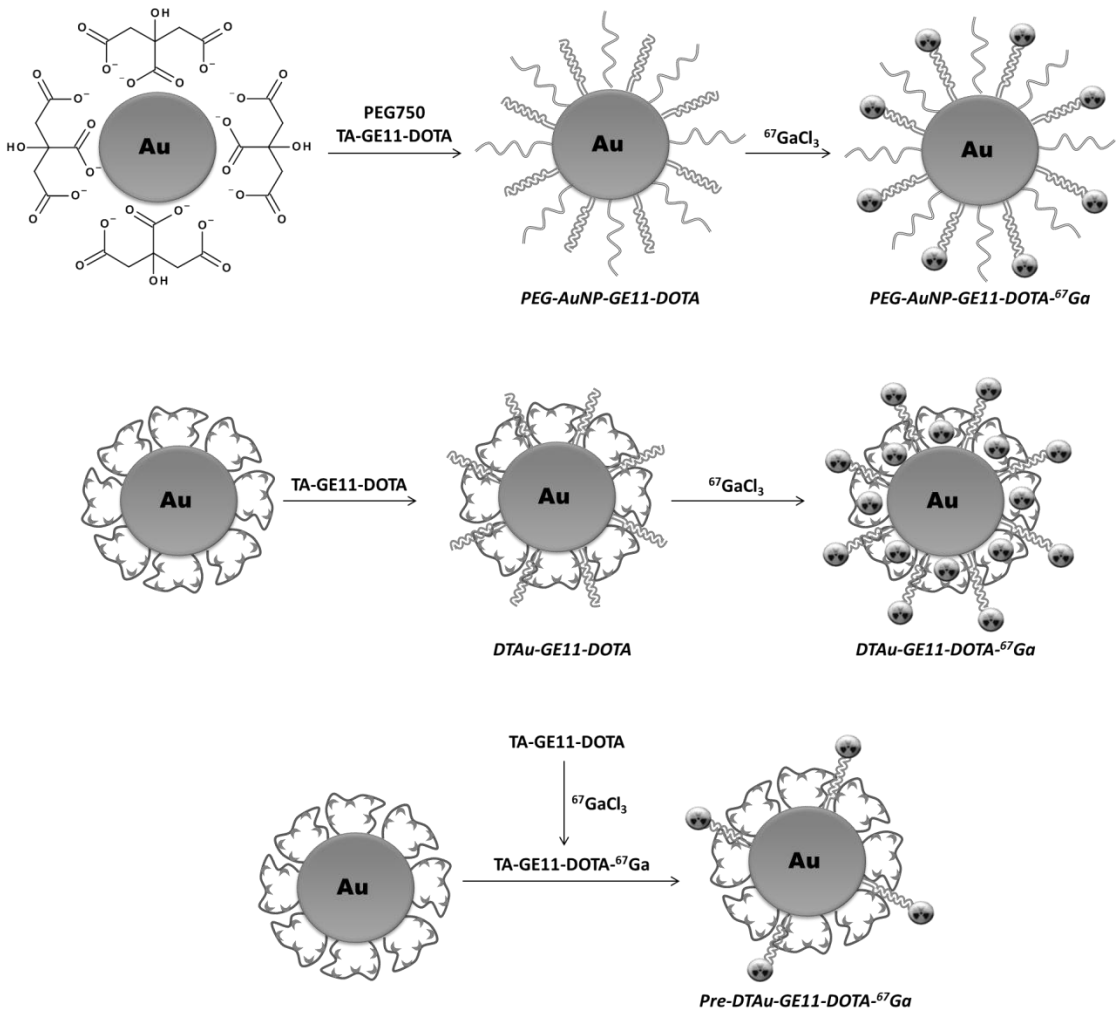

Figure 4.3: *Schematic drawing of the AuNPs studied in Chapter 4.*

4.2 Synthesis, Characterization and Radiolabeling of PEG-AuNP-GE11-DOTA

The structure of the new GE11 derivative (**TA-GE11-DOTA**) used to decorate the AuNPs is presented in Figure 4.4. **TA-GE11-DOTA** contains a PEG spacer between the GE11 amino acid sequence and the DOTA chelator, which has been introduced at the ε-amine group from one lysine. There are two more lysine residues to increase the water solubility of the conjugate and a terminal thioctic acid for attachment to the AuNPs surface. The compound was custom synthesized by CPC Scientific, which has confirmed its formulation and purity (> 95%) by ESI-MS and HPLC analysis.

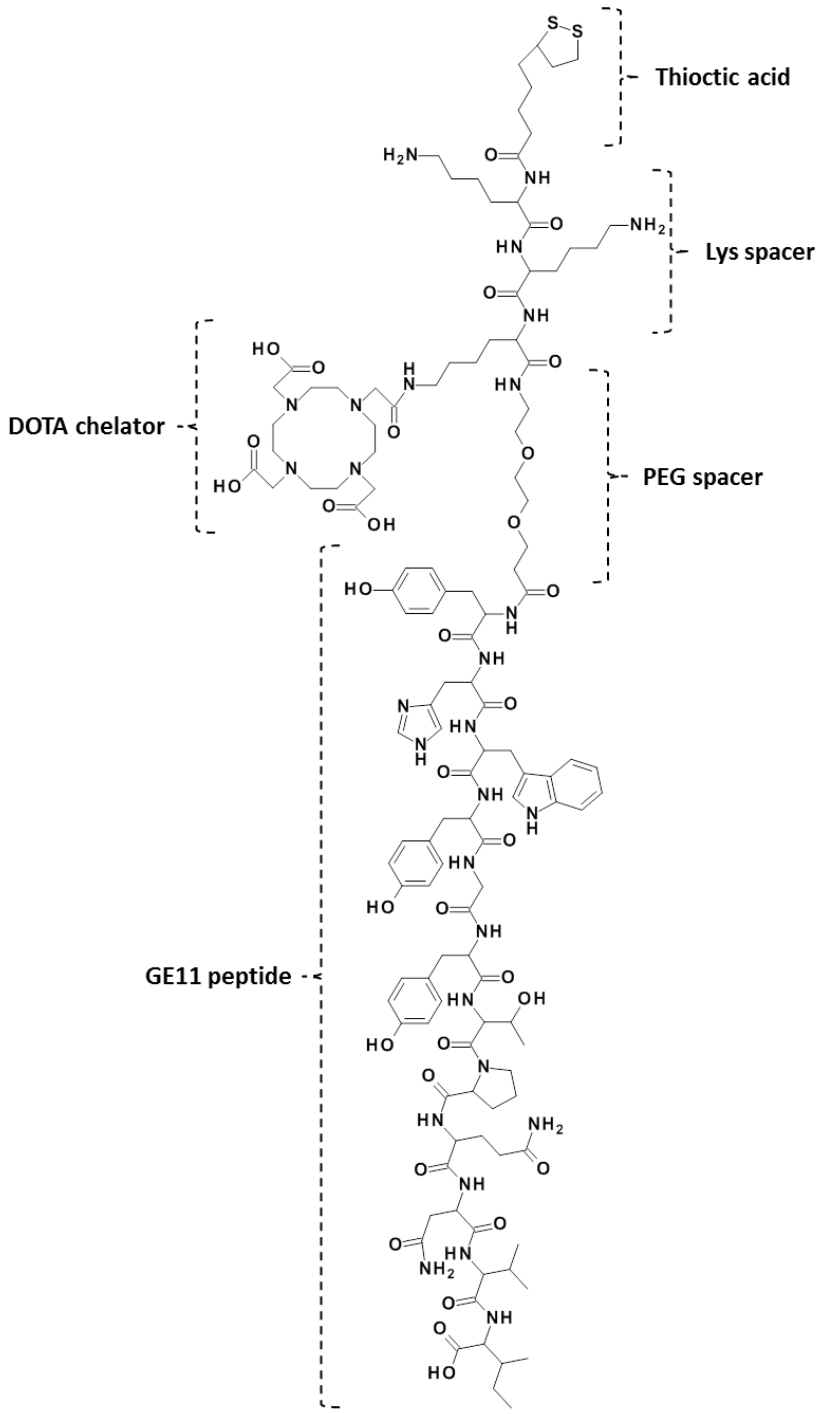

Figure 4.4: *Chemical structure of* ***TA-GE11-DOTA****.*

The initial idea was to conjugate the **TA-GE11-DOTA** to AuNPs stabilized with citrate (AuNP-citrate), which were synthesized using the method described by Turkevich *et al.*.[150] Briefly, an aqueous solution of $HAuCl_4$ was heated (70 ºC) in the presence of trisodium citrate to allow the formation of the desired nanoparticles. The size and spherical

shape of the AuNPs were confirmed by UV-Vis and TEM (11-12 nm) and the amount of gold present in solution was determined by AAS (1.86 mg(Au)/mL).

The first attempt to conjugate **TA-GE11-DOTA** to AuNP-citrate was done by reacting the nanoparticles with the thiolated peptide (Scheme 4.1). However, it has been observed a rapid aggregation of the nanoparticles in less than 5 min of reaction, and this approach proved to be inadequate to functionalize the AuNPs wih **TA-GE11-DOTA**.

To overcome this issue, AuNP-citrate was treated simultaneously with thiolated PEG chains (PEG750, Mw = 750) and **TA-GE11-DOTA** using a 1:1:0.1 (Au:PEG750:TA-GE11-DOTA) molar ratio of the reagents. Under these conditions, **PEG-AuNP-GE11-DOTA** was successfully synthesized and aggregation processes were avoided (Scheme 4.1). The reaction mixture of **PEG-AuNP-GE11-DOTA** was centrifuged in order to separate the supernatant from the AuNPs that were washed with H_2O. The supernatant was stored for posterior HPLC analysis. The synthesis was also attempted using a 1:1:1 molar ratio of the reagents, but the increase of the proportion of peptide led to aggregation of the AuNPs.

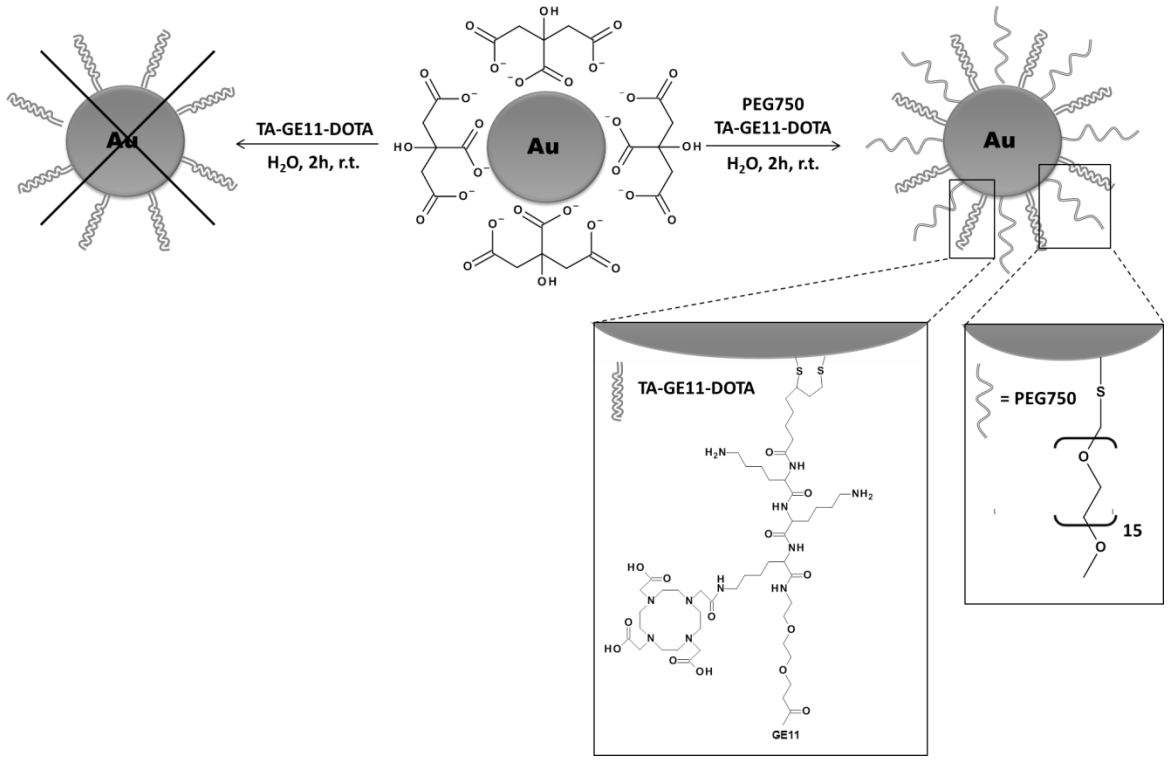

Scheme 4.1: *Synthesis of* ***PEG-AuNP-GE11-DOTA****.*

The determination of the amount of **TA-GE11-DOTA** conjugated to the AuNPs was performed by HPLC analysis of the supernatant from the reaction mixture, using the same procedure described in the previous Chapters to quantify the amount of conjugated BBN derivatives. The HPLC analysis has shown that ≈ 14% of the added **TA-GE11-DOTA** was loaded into the AuNPs, which corresponds to ≈ 0.19 mg ($7.1x10^{-5}$ mmol) of peptide per mg of gold (14.5 mmol). The low molar absorptivity of PEG750 precluded the determination of the amount of PEG750 conjugated to the AuNPs using this methodology.

The amount of conjugated **TA-GE11-DOTA** is considerably inferior to the payload of BBN derivative in the nanoconstruct **BBN-AuNP-TDOTA** ($8.58x10^{-4}$ mmol of peptide per mg of AuNP) that has been described in the previous Chapter. The presence of PEG750 is crucial to improve the stability of the AuNPs but it seems to impair the efficient conjugation of the GE11 derivative.

PEG-AuNP-GE11-DOTA was characterized using different analytical techniques including UV-Vis, TEM, DLS and zeta-potential measurements.

The UV-Vis spectrum of **PEG-AuNP-GE11-DOTA** is shown in Figure 4.5 in comparison with that of AuNP-citrate. Both spectra are relatively similar and present an intense plasmodic absorption band centered at ≈ 525 nm. This indicates that the PEG and peptide conjugation did not alter the core size of the AuNPs and points out for the presence of spherical shaped nanoparticles. **PEG-AuNP-GE11-DOTA** displays a much more intense absorption band when compared with the **DTDTPA** and **TDOTA** stabilized AuNPs previously described in this thesis, which indicates that **PEG-AuNP-GE11-DOTA** correspond to larger nanoparticles.[236] This was confirmed by the TEM imaging of **PEG-AuNP-GE11-DOTA** (Figure 4.6) that showed the presence of spherical AuNPs with a core size of 11.99 ± 1.49 nm.

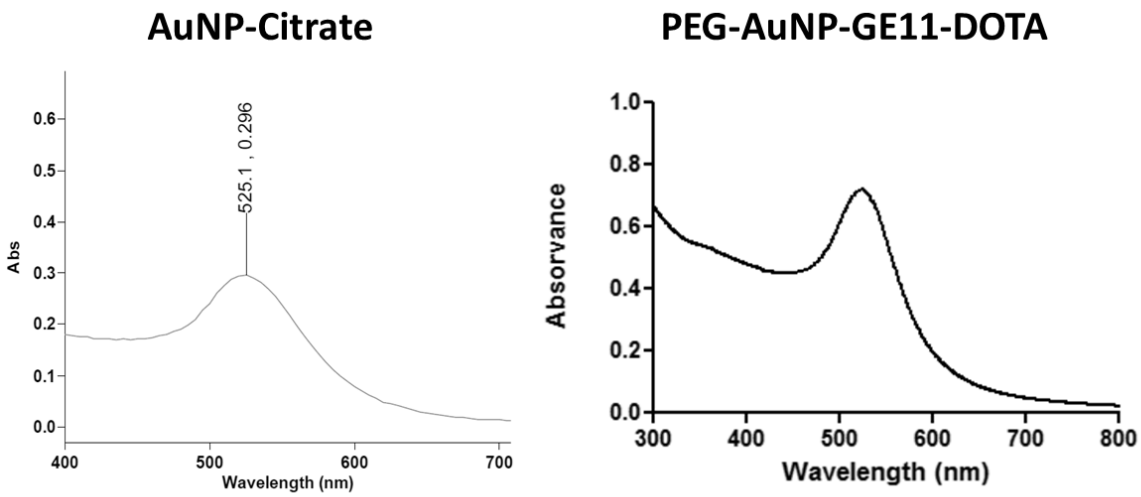

Figure 4.5: *UV-Vis spectra of AuNP-Citrate and* ***PEG-AuNP-GE11-DOTA*** *(8x10^{-2} mg/mL).*

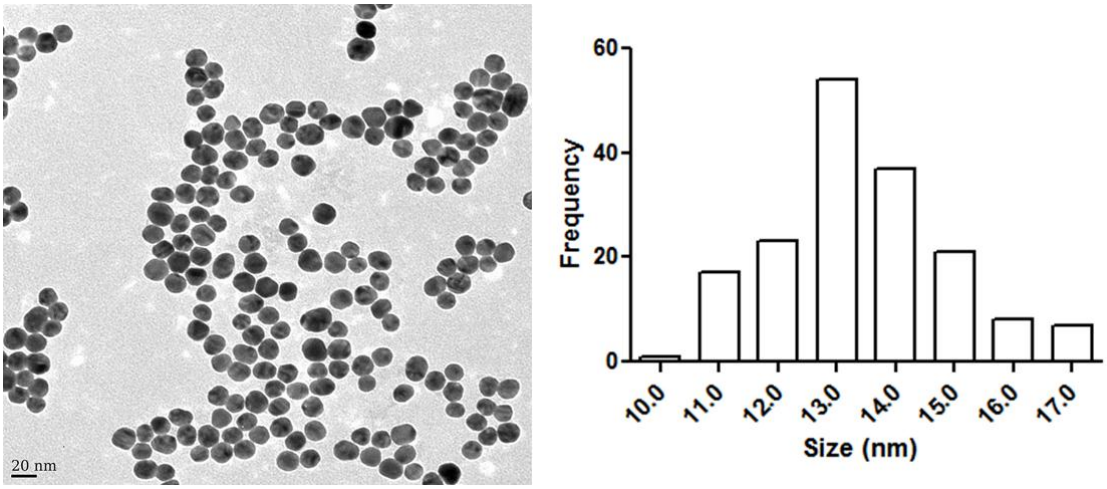

Figure 4.6: *TEM image with respective size histogram of* ***PEG-AuNP-GE11-DOTA****.*

The study of an aqueous solution of **PEG-AuNP-GE11-DOTA** by DLS and zeta-potential analysis has shown that these nanoparticles have a hydrodynamic size of 49.3 nm (PDI = 0.382) (Figure 4.7) and a charge of -65.8 ± 35.7 mV. These parameters are indicative of a very good stability of these AuNPs in solution. The measured hydrodynamic size of 49.3 nm is considerably smaller than the hydrodynamic size found for the AuNPs described in previous Chapters, meaning that **PEG-AuNP-GE11-DOTA** displays a small level of aggregation in solution. Most likely, this reflects the presence of the PEG chains at the surface of the AuNPs, which are known to enhance AuNP stability in solution.[144]

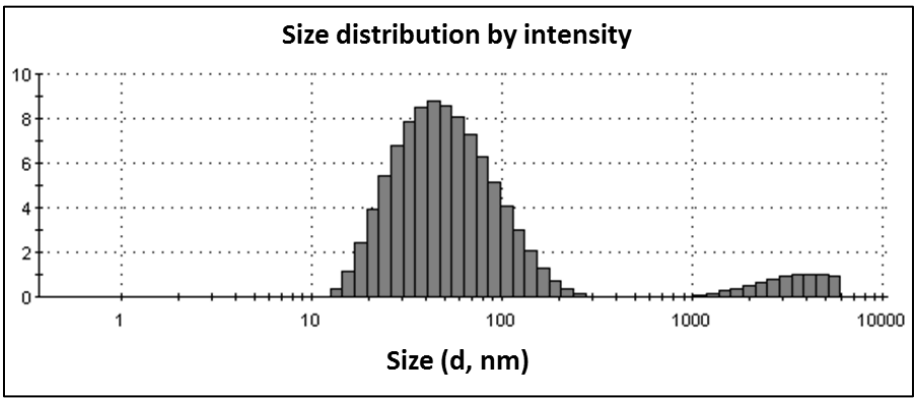

Figure 4.7: *Hydrodynamic size distribution of* ***PEG-AuNP-GE11-DOTA*** *in H_2O ($8x10^{-2}$ mg/mL).*

After synthesizing and characterizing **PEG-AuNP-GE11-DOTA**, it has been studied its capability to coordinate ^{67}Ga. However, a successful radiolabeling of **PEG-AuNP-GE11-DOTA** with ^{67}Ga was not achieved. Different attempts were done in order to optimize the radiolabeling, which included temperature variation, longer reaction times, pH variation and higher nanoparticle concentrations. However, in all the attempts made the radiochemical yields obtained were < 5%.

These results are most likely justified by the low amount of DOTA chelator that is present at the surface of the AuNPs. As discussed above, the amount of **TA-GE11-DOTA** present in **PEG-AuNP-GE11-DOTA** is relatively low and thus it does not allow an effective coordination of ^{67}Ga. This could be eventually improved by increasing the amount of DOTA incorporated in the AuNPs. However, as described previously, the attempts that have been done to increase the amount of conjugated **TA-GE11-DOTA** were not successful due to occurrence of aggregation processes.

4.3 Synthesis and Characterization of DTAu-GE11-DOTA

Due to the inability of **PEG-AuNP-GE11-DOTA** to coordinate ^{67}Ga it was hypothesized that the use of **AuNP-DTDTPA** as a platform to conjugate **TA-GE11-DOTA**, would allow the formation of EGFr-targeted AuNPs suitable for labeling with ^{67}Ga. As described in Chapter 2, **DTDTPA** stabilizes AuNPs that display favorable physico-chemical properties, regarding their hydrodynamic size and surface charge in solution. In addition, they have also proved to be suitable platforms to be functionalized with bioactive peptides (**TA-BBN**). To functionalize **AuNP-DTDTPA** with **TA-GE11-DOTA** and proceed with their labeling with ^{67}Ga, two possibilities have been considered: i) functionalization of **AuNP-**

DTDTPA with **TA-GE11-DOTA** followed by labeling with ^{67}Ga (*post-labeling approach*); ii) labeling of **TA-GE11-DOTA** with ^{67}Ga followed by the conjugation of the resulting radiopeptide to **AuNP-DTDTPA** (*pre-labeling approach*).

By studying the post-labeling and pre-labeling approaches, it was anticipated that the use of these two approaches could lead to differences on the stability of the radiolabeled AuNPs. In the case of the post-labeling approach, it has been hypothesized that ^{67}Ga could be coordinated by the **DTDTPA** layer instead of **TA-GE11-DOTA**, leading to a less stable radiolabeling. On contrary, the use of the pre-labeling approach would avoid such possibility allowing for a more stable radiolabeling. As discussed in the previous Chapter, the ^{67}Ga-labeled **AuNP-DTDTPA** have shown a poor in vitro stability on contrary to **AuNP-TDOTA-^{67}Ga**.

For the post-labeling approach, **AuNP-DTDTPA** was conjugated with **TA-GE11-DOTA** using a 1:2 AuNP:peptide ratio (w/w) (Scheme 4.2), in a same manner as used in the synthesis of **BBN-AuNP-TDOTA**. The resulting functionalized nanoparticles (**DTAu-GE11-DOTA**) were used later for labeling with ^{67}Ga.

In parallel, another experiment was performed in which **TA-GE11-DOTA** was conjugated to **AuNP-DTDTPA** following the experimental procedure used in the pre-labeling approach for the ^{67}Ga-labeling of these nanoparticles. This experiment was intended to simulate the conditions of the pre-labeling approach without the presence of the radioactive metal. The resulting AuNPs (**Pre-DTAu-GE11-DOTA**) were used to estimate the physico-chemical properties and peptide loading of the radiolabeled nanoparticles obtained using the pre-labeling approach. It is important to emphasize that ^{67}Ga is carrier-free and, therefore, it is present in a very low concentration (≤ 50 nM) that is not expected to affect the physic-chemical and biological properties of the AuNPs.

For the synthesis of **Pre-DTAu-GE11-DOTA**, a 1x10^{-4} M solution of **TA-GE11-DOTA** (0.08 mg) was heated for 30 min at 70 ºC in the presence of sodium acetate buffer (pH ≈ 5) and 0.1 M HCl, as in the case of the labeling reaction with ^{67}Ga (see 4.4.2). Then, the resulting solution was added to **AuNP-DTDTPA** (0.4 mg in 80 µL of H_2O) and the obtained mixture was stirred at room temperature for 2 h (Scheme 4.2). Both for **DTAu-GE11-DOTA** and **Pre-DTAu-GE11-DOTA**, the supernatant of each reaction mixture was separated by ultra-filtration and stored for posterior HPLC analysis; the recovered nanoparticles were washed with H_2O, freeze-dried and used for further characterization.

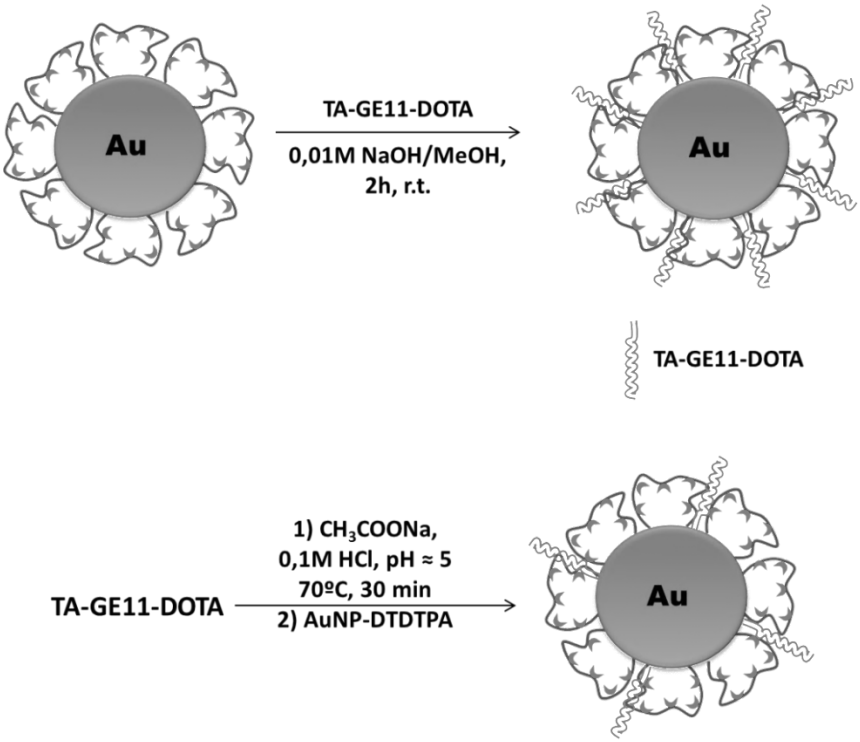

Scheme 4.2: *Synthesis of* ***DTAu-GE11-DOTA*** *(above) and* ***Pre-DTAu-GE11-DOTA*** *(below).*

The estimation of the amount of conjugated **TA-GE11-DOTA** in **DTAu-GE11-DOTA** and **Pre-DTAu-GE11-DOTA** was done by HPLC analysis of the supernatants of the reaction mixtures, as described in the previous Chapters. For **DTAu-GE11-DOTA**, the amount of conjugated **TA-GE11-DOTA** per mg of **AuNP-DTDTPA** was 1.19 mg ($4.5x10^{-4}$ mmol), while for **Pre-DTAu-GE11-DOTA** such amount was 0.25mg ($9.3x10^{-5}$ mmol). As seen in Chapter 2, NTA analysis of **AuNP-DTDTPA** indicated a nanoparticle concentration of $1.67x10^{14}$ NP/mg, which means that the number of **TA-GE11-DOTA** molecules per nanoparticle is ≈ 104 and ≈ 4-5 for **DTAu-GE11-DOTA** and **Pre-DTAu-GE11-DOTA**, respectively.

For **DTAu-GE11-DOTA**, the amount of peptide conjugated to the AuNPs is roughly the double of the one (≈ 53 molecules/NP) resulting from the conjugation of TA-BBN to the same nanoparticles, as discussed in Chapter 2. In the case of **Pre-DTAu-GE11-DOTA**, there is a much lower amount of conjugated peptide, which is a consequence of the significantly lower **TA-GE11-DOTA**:**AuNP-DTDTPA** ratio that has been used in the conjugation reaction.

To evaluate the influence of the conjugation of the GE11 derivative on their physico-chemical properties, **DTAu-GE11-DOTA** and **Pre-DTAu-GE11-DOTA** were characterizaed by UV-Vis, TEM, DLS and zeta-potential measurements.

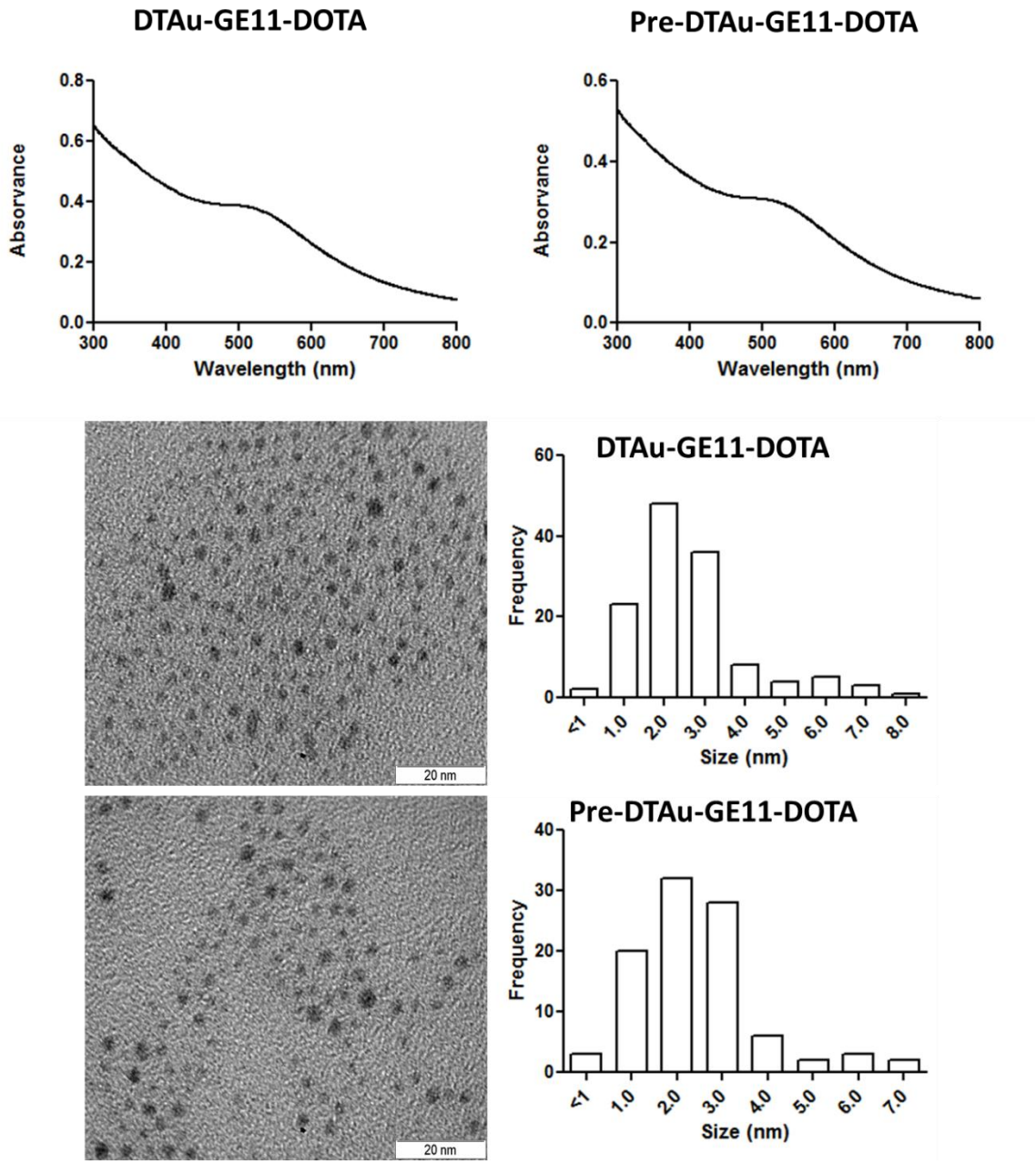

Figure 4.8: *UV-Vis spectra (8x10^{-2} mg/mL) and TEM images with respective size histograms of* ***DTAu-GE11-DOTA*** *and* ***Pre-DTAu-GE11-DOTA****.*

The UV-Vis spectra of **DTAu-GE11-DOTA** and **Pre-DTAu-GE11-DOTA** show a single broad absorption band centered at ≈ 520 nm, similar to that of **AuNP-DTDTPA**,

indicating that the conjugation of the **TA-GE11-DOTA** did not alter the core of the AuNPs in both cases. This was further confirmed by the TEM images obtained for **DTAu-GE11-DOTA** and **Pre-DTAu-GE11-DOTA** where it is possible to see the spherical shaped cores of these AuNPs with a size of 2.26 ± 1.45 and 2.45 ± 1.35 nm, respectively.

DLS analysis of **DTAu-GE11-DOTA** and **Pre-DTAu-GE11-DOTA** in H_2O led to the determination of a hydrodynamic size of 167.2 nm (PDI = 0.228) and 149.5 nm (PDI = 0.167), respectively (Fig. 4.9 and Table 4.1). The zeta-potential measurements obtained were -53.1 ± 10 and -52.9 ± 8.5 mV, respectively

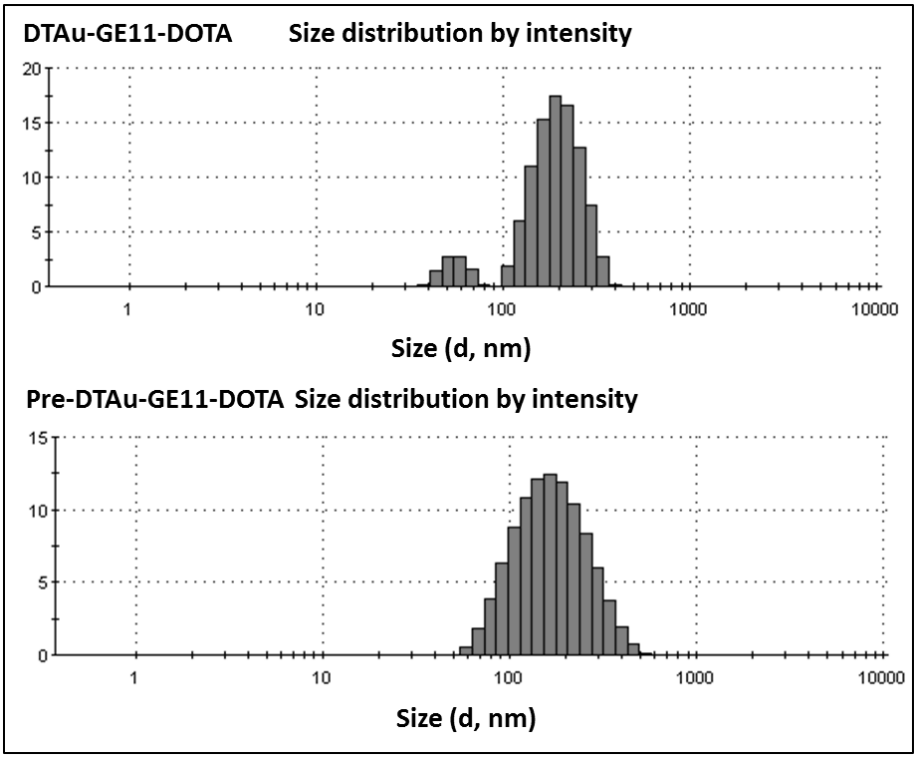

Figure 4.9: *Hydrodynamic size distributions of* ***DTAu-GE11-DOTA*** *and* ***Pre-DTAu-GE11-DOTA*** *in* H_2O *(*$8x10^{-2}$ *mg/mL).*

In Table 4.1 it is presented a comparison of the hydrodynamic size and zeta-potential values measured for **DTAu-GE11-DOTA** and **Pre-DTAu-GE11-DOTA**, with those of **AuNP-DTDTPA** and **BBN-AuNP-DTDTPA** that have been described in Chapter 2. The decoration of **AuNP-DTDTPA** with **TA-GE11-DOTA** led to a slight increase in the hydrodynamic size, in a similar way as observed for **BBN-AuNP-DTDTPA**. The zeta-

potential values remained largely negative, indicating that the GE11 containing AuNPs still maintain a good stability in solution.

Table 4.1: *Comparison of hydrodynamic size (*PDI) and zeta-potential measurements in H_2O ($8x10^{-2}$ mg/mL) of* ***DTAu-GE11-DOTA*** *and* ***Pre-DTAu-GE11-DOTA*** *with the* ***DTDTPA*** *stabilized AuNPs described in Chapter 2.*

Nanoconstruct	Hydrodynamic Size (nm)	Zeta-Potential (mV)
DTAu-GE11-DOTA	167.2 (0.228)*	-53.1 ± 10.0
Pre-DTAu-GE11-DOTA	149.5 (0.167)*	-52.9 ± 8.5
AuNP-DTDTPA	100.6 (0.111)*	-80.7 ± 15.6
BBN-AuNP-DTDTPA	146.2 (0.162)*	-71.5 ± 9.1

4.4 Radiolabeling with ^{67}Ga and *In Vitro* Stability Studies

Following the successful functionalization of **AuNP-DTDTPA** with **TA-GE11-DOTA**, it was then proceed with the radiolabeling studies, based on the pre- and post-labeling approaches. Prior to the labeling of the AuNPs, it was studied the labeling of **TA-GE11-DOTA** with ^{67}Ga, as the corresponding radioconjugate **TA-GE11-DOTA-^{67}Ga** was necessary to carry out the pre-labeling approach.

4.4.1 Synthesis, Characterization and *In Vitro* Stability of TA-GE11-DOTA-^{67}Ga

The labeling of **TA-GE11-DOTA** with ^{67}Ga was successfully achieved by reaction with $^{67}GaCl_3$ in the presence of acetate buffer (pH ≈ 5), using a peptide concentration of $1x10^{-4}$ M and by heating at 70 ºC for 30 min (Scheme 4.3). Under these conditions, **TA-GE11-DOTA-^{67}Ga** was obtained with a radiochemical yield >99% as confirmed by HPLC and TLC analyses (Figure 4.10).

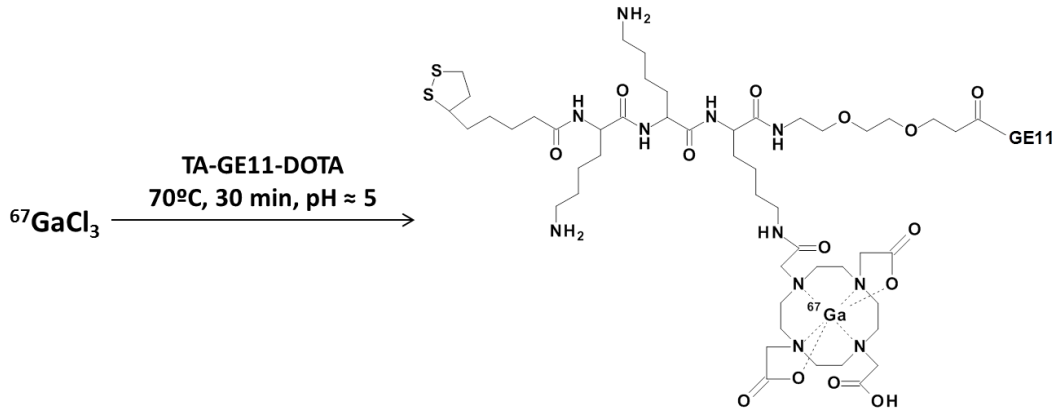

Scheme 4.3: *Radiolabeling of* ***TA-GE11-DOTA*** *with* ^{67}Ga.

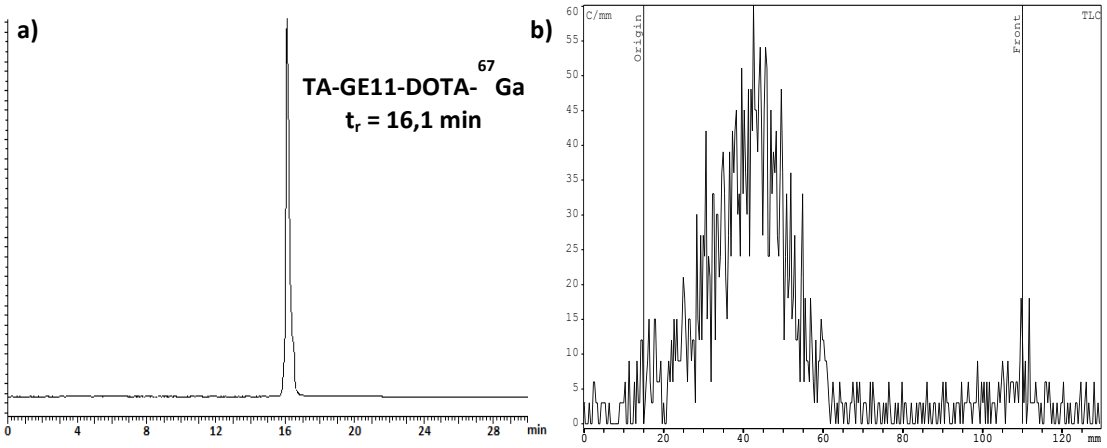

Figure 4.10: *Chromatographic analysis of* ***TA-GE11-DOTA-^{67}Ga****:* ***a)*** *HPLC chromatogram (100-10 C18, 0.1% TFA aqueous/CH_3CN);* ***b)*** *radiochromatogram (R_f = 0.2) obtained using ITLC-SG plates with 6 M HCl/MeOH (5:95) as eluent ($^{67}GaCl_3$ (R_f = 1)).*

Stability studies were performed for **TA-GE11-DOTA-^{67}Ga** in different media, including NaCl 0.9%, PBS 0.1 M, cell culture medium and apo-transferrin. After incubation at 37 ºC for a desired period of time, the different mixtures were analysed by HPLC. The results are shown in Figure 4.11.

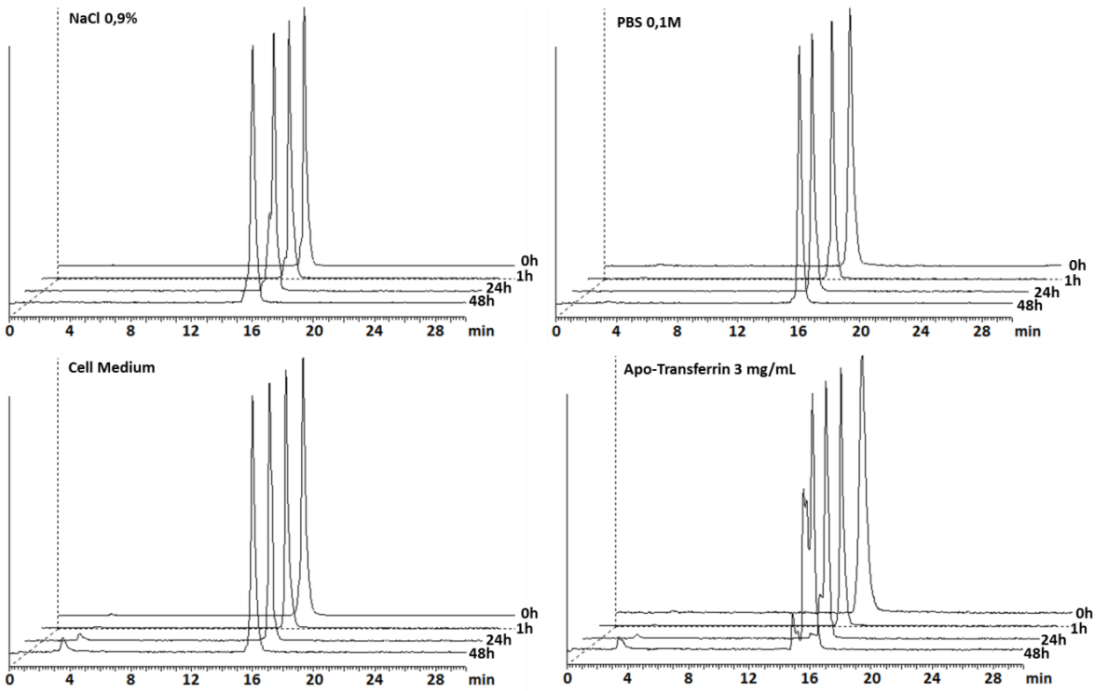

Figure 4.11: *Stability studies of* ***TA-GE11-DOTA-^{67}Ga*** *in the presence of physiological and biologically relevant media, performed by HPLC analyses (100-10 C18, 0.1% TFA aqueous/CH_3CN) of the different mixtures.*

TA-GE11-DOTA-^{67}Ga is stable in NaCl 0.9%, PBS 0.1 M and more importantly in cell medium, with no significant alterations in the HPLC chromatograms even after 48 h of incubation. In the presence of *apo*-transferrin the compound maintains a good stability up to 24 h of incubation; however, for longer periods it is detected the presence of radioactive impurities with lower retention times, as can be seen in Figure 4.12.

Overall, **TA-GE11-DOTA-^{67}Ga** displays an adequate stability in the different challenging media, and it was reasoned that it was worthwhile to study the use of **TA-GE11-DOTA** in the ^{67}Ga-labeling of AuNPs using the pre-labeling approach.

4.4.2 ^{67}Ga-labeling of the GE11-Containing AuNPs Using the Pre- and Post-Labeling Approaches: Synthesis and *In Vitro* Stability of the Resulting Nanoconstructs

Based on the post-labeling approach, the ^{67}Ga-labeling of **DTAu-GE11-DOTA** was achieved by reaction of the AuNPs with $^{67}GaCl_3$ in ammonium acetate buffer (pH ≈ 7), upon heating at 70 ºC for 15 min (Scheme 4.4). For the pre-labeling approach, **AuNP-DTDTPA** was reacted with **TA-GE11-DOTA-^{67}Ga**, which has been obtained as described

previously by ^{67}Ga-labeling of the cold peptide (0.08 mg). The radiopeptide solution was placed in the presence of **AuNP-DTDTPA** (0.4 mg), and the reaction mixture was stirred at room temperature for 2 h (Scheme 4.3). Purification of the radiolabeled AuNPs was done by ultra-filtration and their radiochemical purity was assessed by TLC (Figure 4.12). These procedures led to the synthesis of **Post-DTAu-GE11-DOTA-^{67}Ga** and **Pre-DTAu-GE11-DOTA-^{67}Ga**, which were obtained with radiochemical yields of ≈ 70% and 60% respectively.

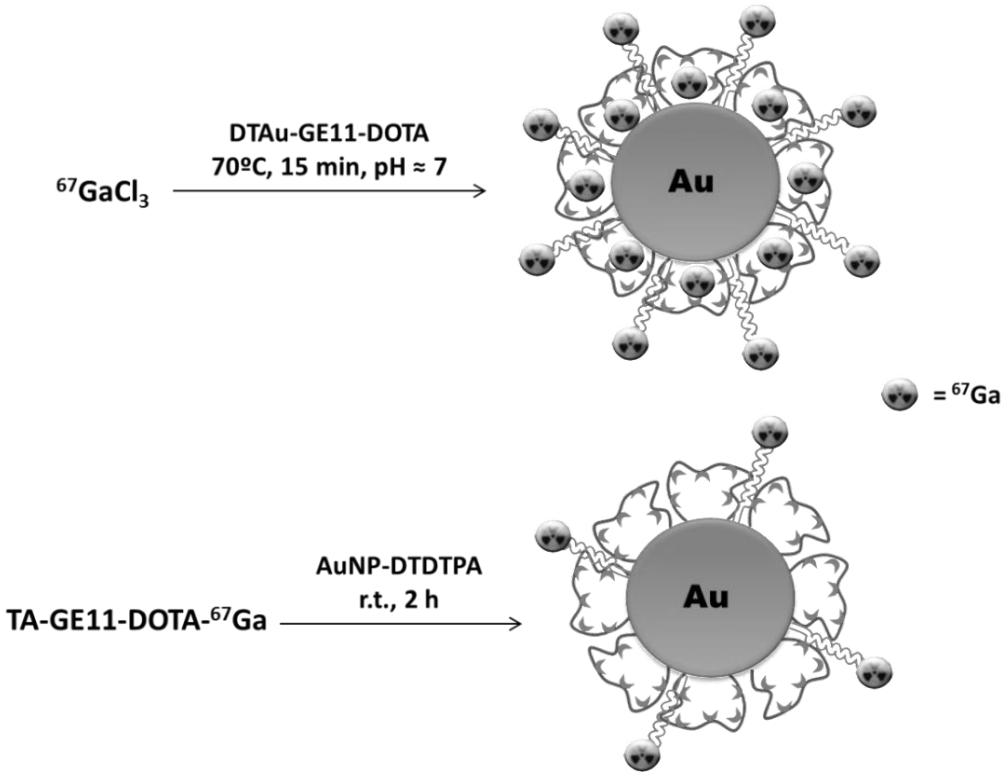

Scheme 4.4: *Synthesis of* ***Post-DTAu-GE11-DOTA-^{67}Ga*** *(above) and* ***Pre-DTAu-GE11-DOTA-^{67}Ga*** *(below).*

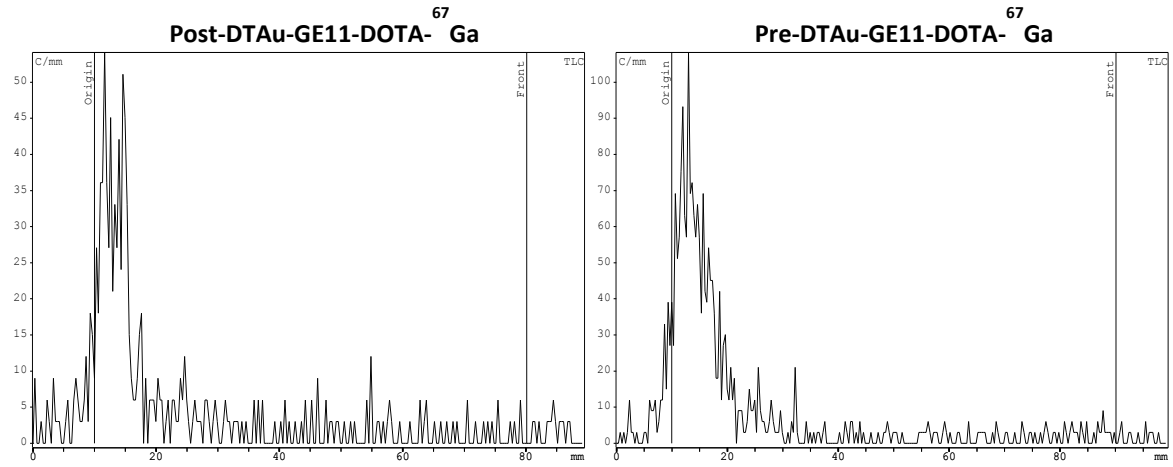

Figure 4.12: *Radiochromatograms of* ***Post-DTAu-GE11-DOTA-^{67}Ga*** *(R_f = 0) and* ***Pre-DTAu-GE11-DOTA-^{67}Ga*** *(R_f = 0) obtained using ITLC-SG plates with 6M HCl/MeOH (5:95) as eluent ($^{67}GaCl_3$ (R_f = 1)).*

The stability of both types of AuNPs, **Post-DTAu-GE11-DOTA-^{67}Ga** and **Pre-DTAu-GE11-DOTA-^{67}Ga**, in terms of release of ^{67}Ga, was studied in the presence of different challenging media (NaCl 0.9%, PBS 0.1 M, cell culture medium and *apo*-transferrin), as described in previous Chapters. The results obtained are shown in Figure 4.13.

The stability studies of **Post-DTAu-GE11-DOTA-^{67}Ga** indicated that these radiolabeled AuNPs are unable to maintain efficient ^{67}Ga coordination. After 3 h of incubation at 37 ºC, in the presence of cell culture medium and apo-transferrin, less than 30% of the ^{67}Ga is still coordinated on the AuNPs. In NaCl 0.9% and PBS 0.1 M, it is also observed a slight release of ^{67}Ga from the AuNPs, however not as significant as in the presence of the other media. This behaviour is very similar to that exhibited by **AuNP-DTDTPA-^{67}Ga** and **BBN-AuNP-DTDTPA-^{67}Ga**, which have been described in Chapter 2. This trend seems to indicate that ^{67}Ga is being coordinated preferably by the **DTDTPA** coating of **Post-DTAu-GE11-DOTA-^{67}Ga** instead of DOTA. As seen in Chapter 3, **AuNP-TDOTA-^{67}Ga** and **BBN-AuNP-TDOTA-^{67}Ga** display a much higher capability to maintain stable ^{67}Ga coordination if compared with the **AuNP-DTDTPA** counterparts. Eventually, these findings can be accounted by the formation of kinetically favored gallium complexes (i.e. with the **DTDTPA** coating), instead of the more thermodynamically stable ones (i.e. those with the DOTA derivative).

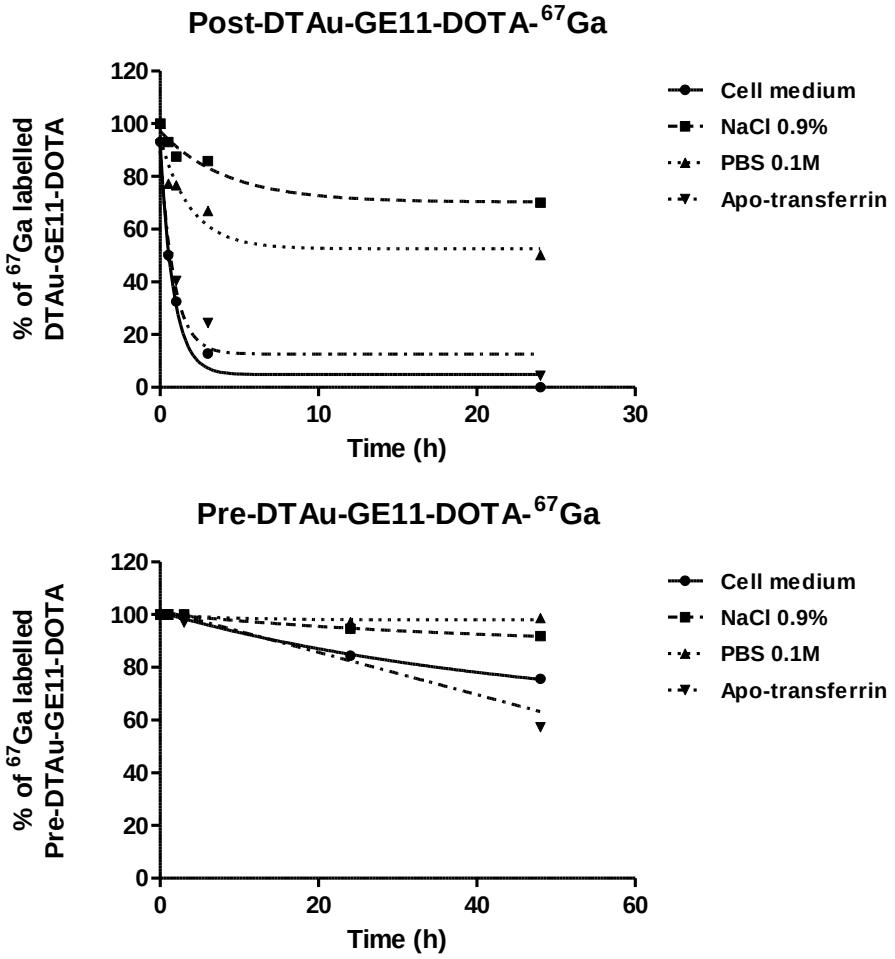

Figure 4.13: *Stability studies of* ***Post-DTAu-GE11-DOTA-^{67}Ga*** *and* ***Pre-DTAu-GE11-DOTA-^{67}Ga*** *in the presence of physiological and biologically relevant media.*

In contrast, **Pre-DTAu-GE11-DOTA-^{67}Ga** showed a good to reasonable stability in the presence of all challenging media, although being more reactive in the presence of *apo*-transferrin. In the presence of the later, roughly 60% of the ^{67}Ga radioactivity is retained by the AuNPs at 48 h. This result is similar to what was observed for **TA-GE11-DOTA-^{67}Ga**, which showed a slight degradation after 48 h of incubation in the presence of *apo*-transferrin (Figure 4.12).

Nonetheless, the overall stability displayed by **Pre-DTAu-GE11-DOTA-^{67}Ga** is significantly higher than that of **Post-DTAu-GE11-DOTA-^{67}Ga**. In particular, it has not been detected any species with R_f = 0.3, characteristic of **TA-GE11-DOTA-^{67}Ga**, which is indicative that no dissociation of the radiolabeled peptide had occurred.

4.5 Biological Studies

Following the ^{67}Ga-labeling of the GE11 containing AuNPs, preliminary biological studies have been performed for **TA-GE11-DOTA-^{67}Ga**, **Post-DTAu-GE11-DOTA-^{67}Ga** and **Pre-DTAu-GE11-DOTA-^{67}Ga**, which included biodistribution studies in normal mice and cell internalization studies in cervical carcinoma A431 cells that overexpress EGFr.[237,238] Also, the effect of cold **TA-GE11-DOTA** and **DTAu-GE11-DOTA** in the proliferation of this cell line was studied by MT assay.

4.5.1 *In Vitro* Evaluation of DTAu-GE11-DOTA by MTT Assay

In order to have some insight on the effect of **DTAu-GE11-DOTA** in the cell proliferation of cervical carcinoma A431 cells, the cells were incubated with increasing amounts of the nanoparticles, and the cell viability assessed by the MTT assay. For comparison purposes, the studies were also performed for **TA-GE11-DOTA** using the same methodology. The results obtained are presented in Figure 4.14.

TA-GE11-DOTA exerts some cytotoxic effect in A431 cells at concentrations higher than 1x10^{-5} M, being observed a cell viability of ca. 60%. As seen in Figure 4.10, **DTAu-GE11-DOTA** has a similar cytotoxicity profile, although the cell viability is still significantly high (≈ 80%) for the highest concentration studied (40.0 μg/mL). It should be mentioned that the concentrations of AuNPs used in subsequent biological studies were much lower than this value.

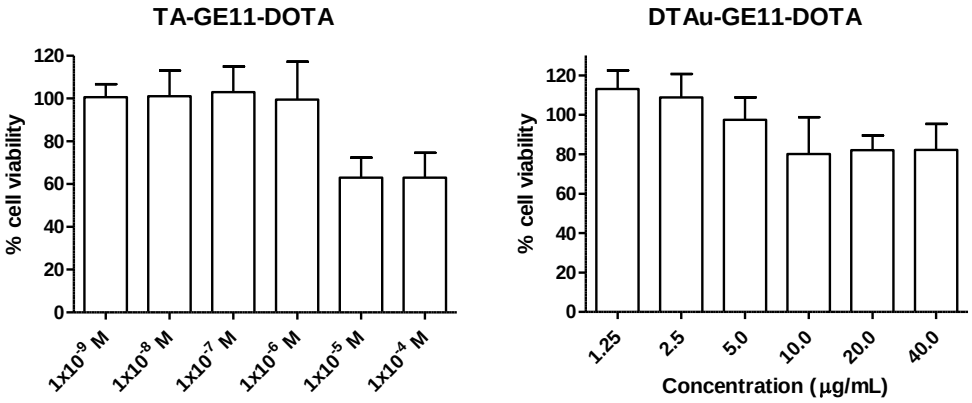

Figure 4.14: *Cell viability (mean ± SD, n=4) of A431 cells exposed to increasing concentrations of* ***TA-GE11-DOTA*** *and* ***DTAu-GE11-DOTA****, evaluated using the MTT assay.*

Interestingly, at lower concentrations (< 2.5 µg/mL), **DTAu-GE11-DOTA** led to a roughly 15% increase in cell viability. As mentioned in the introductory Chapter, GE11 displays a slight mitogenic effect when interacting with EGFr, which consequently can lead to an increase in cell viability.[230] These results seem to indicate that **DTAu-GE11-DOTA** retains the ability of interacting with EGFr. However it is not clear why the cell viability decreases as the concentration of the nanoparticles increases, and why **TA-GE11-DOTA** does not display a similar behavior.

4.5.2 Cellular Uptake

Internalization studies in the A431 cell line were performed for **TA-GE11-DOTA-^{67}Ga**, **Post-DTAu-GE11-DOTA-^{67}Ga** and **Pre-DTAu-GE11-DOTA-^{67}Ga** by incubation of the radioactive compounds with the cells, at 37 ºC and for different time points. In these assays, the cells were placed in culure medium without the standard growth factors used for cell proliferation, immediately before the addition of the tested compounds. In this way, it was intended to avoid competition between these growth factors and the compounds in the interaction with EGFr. The results obtained are presented in Figure 4.15.

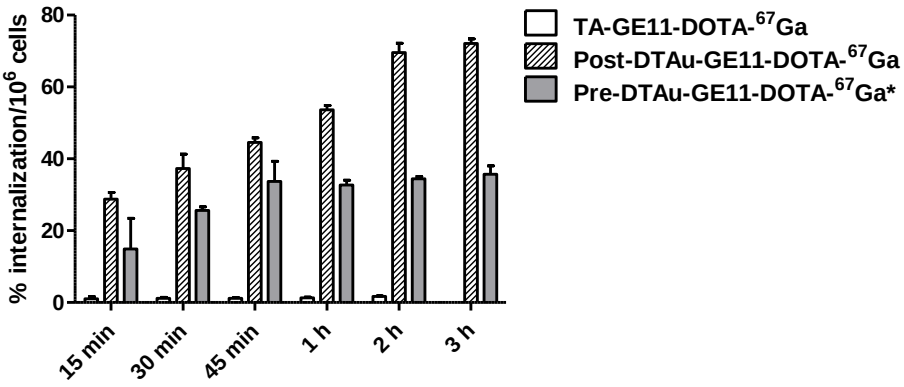

Figure 4.15: *Cellular uptake (mean ± SD, n=4) of* ***TA-GE11-DOTA-^{67}Ga****,* ***Post-DTAu-GE11-DOTA-^{67}Ga*** *and* ***Pre-DTAu-GE11-DOTA-^{67}Ga*** *in A431 cells after incubation at 37 ºC at different intervals of time. Internalization is expressed as percentage of the total radioactivity added to the cells.*

For **TA-GE11-DOTA-^{67}Ga**, the cellular internalization is very low. Even after 2 h of incubation the percentage of internalized radioactivity remained as low as 1.6%. In contrast, the internalization observed for the radiolabeled AuNPs is much higher and very fast with 14.0% and 28.7% internalized radioactivity for **Pre-DTAu-GE11-DOTA-^{67}Ga** and **Post-DTAu-GE11-DOTA-^{67}Ga**, respectively, after only 15 min of incubation.

The maximum amount of internalized radioactivity observed for **Pre-DTAu-GE11-DOTA-^{67}Ga** was 35.7%, after 3 h of incubation. **Post-DTAu-GE11-DOTA-^{67}Ga** displayed a remarkably high value of 72.1% for the internalized radioactivity, after 3 h of incubation. This result certainly reflects the higher amount of conjugated **TA-GE11-DOTA** in this nanoconstruct (≈ 104 molecules per nanoparticle) compared with **Pre-DTAu-GE11-DOTA-^{67}Ga** (≈ 4-5 molecules per nanoparticle). However, it should be taken into account that **Post-DTAu-GE11-DOTA-^{67}Ga** displays a lower stability in cell medium compared with **Pre-DTAu-GE11-DOTA-^{67}Ga** (Figure 4.14). Therefore, one can not exclude that its internalization rate migh also partially reflect some uptake due to released ^{67}Ga.

In a way, the highest rate of internalization of the ^{67}Ga-labeled GE11-containing AuNPs in comparison to **TA-GE11-DOTA-^{67}Ga** is consistent with recent results reported by other authors. Levitzki *et al.* verified that polyethyleneimine-polyethyleneglycol (PEI-PEG) conjugates containing several copies of GE11 showed nanomolar affinities towards EGFr, while GE11 as a free ligand displayed much lower affinity for the receptor.[231] In a similar trend, GE11-containing liposomes, reported by Xu *et al.*, were also able to bind specifically and efficiently to EGFr-overexpressing cancer cells.[239] These findings suggest that the incorporation of GE11 into polymeric or nanoparticle platforms seem to enhance significantly its internalization in EFGr-positive cells.

In order to assess the influence of EGFr blockade in the cell uptake of **Post-DTAu-GE11-DOTA-^{67}Ga** and **Pre-DTAu-GE11-DOTA-^{67}Ga**, studies of these AuNPs were performed in the presence of EGF. Results are shown in Figure 4.16.

For **Post-DTAu-GE11-DOTA-^{67}Ga**, it was found a slight blocking effect due to the presence of EGF, with a reduction of ca. 14% in internalized radioactivity after 3 h of incubation. In the case of **Pre-DTAu-GE11-DOTA-^{67}Ga**, the blocking effect is much more accentuated, with ≈ 28% reduction in internalized radioactivity. These findings are indicative that, to some degree, the internalization pathway of these pre-labeled AuNPs is mediated by the interaction with EGFr. The less pronounced blocking effect observed for **Post-DTAu-GE11-DOTA-^{67}Ga** might also indicate that part of its cell uptake is due eventually to released ^{67}Ga, not attached to the AuNPs, as above discussed.

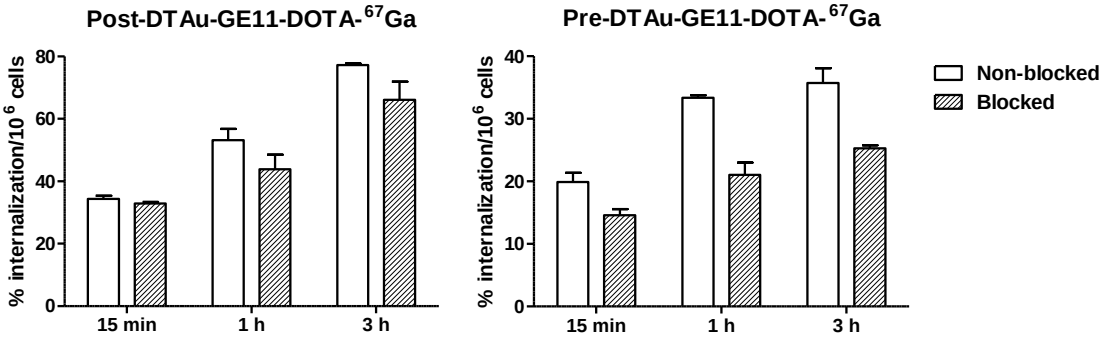

Figure 4.16: *Cellular uptake (mean ± SD, n=4) of* ***DTAu-GE11-DOTA-^{67}Ga****,* ***Pre-DTAu-GE11-DOTA-^{67}Ga*** *in A431 after incubation at 37 ºC cells, treated with EGF (blocked) or non-treated. Internalization is expressed as percentage of the total compound added to the cells.*

4.5.3 *In Vivo* – Biodistribution Studies

Biodistribution studies were performed in normal mice for **Post-DTAu-GE11-DOTA-^{67}Ga** and **Pre-DTAu-GE11-DOTA-^{67}Ga**. These studies were expected to provide a first insight in the biodistribution profile of these ^{67}Ga-labeled nanoconstructs, in terms of blood clearance, excretion pathways and *in vivo* stability. These studies were performed at 1 h p.i. in groups of three CD-1 mice, which were injected in the tail vein with aliquots of 100 µL of the AuNP solutions (pH ≈ 7). The results obtained are shown in Table 4.2 and Figure 4.17

At 1 h p.i., the biodistribution profile of **TA-GE11-DOTA-^{67}Ga** is notably different from those of **Post-DTAu-GE11-DOTA-^{67}Ga** and **Pre-DTAu-GE11-DOTA-^{67}Ga**. **TA-GE11-DOTA-^{67}Ga** displays a very fast excretion (52.9 ± 4.6 %I.D./g) compared with **Post-DTAu-GE11-DOTA-^{67}Ga** and **Pre-DTAu-GE11-DOTA-^{67}Ga** (2.1 ± 0.2 and 4.3 ± 0.7 %I.D./g, respectively). For **TA-GE11-DOTA-^{67}Ga** the excretion is predominantly done through a renal pathway, as seen by the high kidney uptake (50.1 ± 4.5 %I.D..g). The high kidney retentioncertainly reflects the presence of the extra lysines in the structure of the peptide.[240]

By contrast, **Post-DTAu-GE11-DOTA-^{67}Ga** has a very low kidney uptake (2.2 ± 0.2 %I.D./g), while **Pre-DTAu-GE11-DOTA-^{67}Ga** displays some significant uptake (12.6 ± 1.7 %I.D./g). As expected, the AuNPs excretion follows a hepatobilar pathway, as indicated by the high uptakes in the liver (62.2 ± 6.3 and 69.6 ± 9.4 %I.D./g). This is due to the large

size of these nanoparticles which enhances their uptake in macrophage-containig organs like liver and spleen.[140]

Regarding the blood clearance, there is a significant difference between both nanconstructs, **Post-DTAu-GE11-DOTA-^{67}Ga** has a slower blood clearance compared with **Pre-DTAu-GE11-DOTA-^{67}Ga** (5.0 ± 0.1 *vs* 1.3 ± 0.1 %I.D./g). Also, **Post-DTAu-GE11-DOTA-^{67}Ga** displays slightly higher bone uptake (2.2 ± 0.3 vs 1.6 ± 0.7 %I.D./g). These differences may be related with the possible enhanced tendency of **Post-DTAu-GE11-DOTA-^{67}Ga** to release ^{67}Ga if compared with **Pre-DTAu-GE11-DOTA-^{67}Ga**.

Table 4.2: *Biodistribution results (mean ± SD, n=3; expressed as %I.D./g of organ) for* ***TA-GE11-DOTA-^{67}Ga****,* ***DTAu-GE11-DOTA-^{67}Ga*** *and* ***Pre-DTAu-GE11-DOTA-^{67}Ga*** *after i.v. administration in CD-1 mice at 1 h p.i..*

Organ	% I.D./g		
	TA-GE11-DOTA-^{67}Ga	**Post-DTAu-GE11-DOTA-^{67}Ga**	**Pre-DTAu-GE11-DOTA-^{67}Ga***
Blood	2.4 ± 1.3	5.0 ± 0.1	1.3 ± 0.1
Liver	1.7 ± 0.5	62.2 ± 6.3	69.6 ± 9.4
Intestine	1.3 ± 0.8	1.00 ± 0.01	0.7 ± 0.5
Spleen	3.4 ± 1.6	39.4 ± 13.0	14.6 ± 2.6
Heart	2.2 ± 1.2	1.8 ± 0.2	0.64 ± 0.07
Lung	4.3 ± 1.9	4.3 ± 0.7	2.0 ± 0.5
Kidney	50.1 ± 4.5	2.2 ± 0.2	12.6 ± 1.7
Muscle	1.8 ± 0.4	0.68 ± 0.05	0.20 ± 0.02
Bone	1.2 ± 0.2	2.2 ± 0.3	1.6 ± 0.7
Stomach	2.4 ± 0.4	1.4 ± 0.8	1.8 ± 0.9
Pancreas	1.2 ± 0.7	1.0 ± 0.2	0.31 ± 0.04
Brain	0.06 ± 0.03	0.18 ± 0.05	0.06 ± 0.03
Excretion (%I.D.)	52.9 ± 4.6	2.1 ± 0.2	4.3 ± 0.7

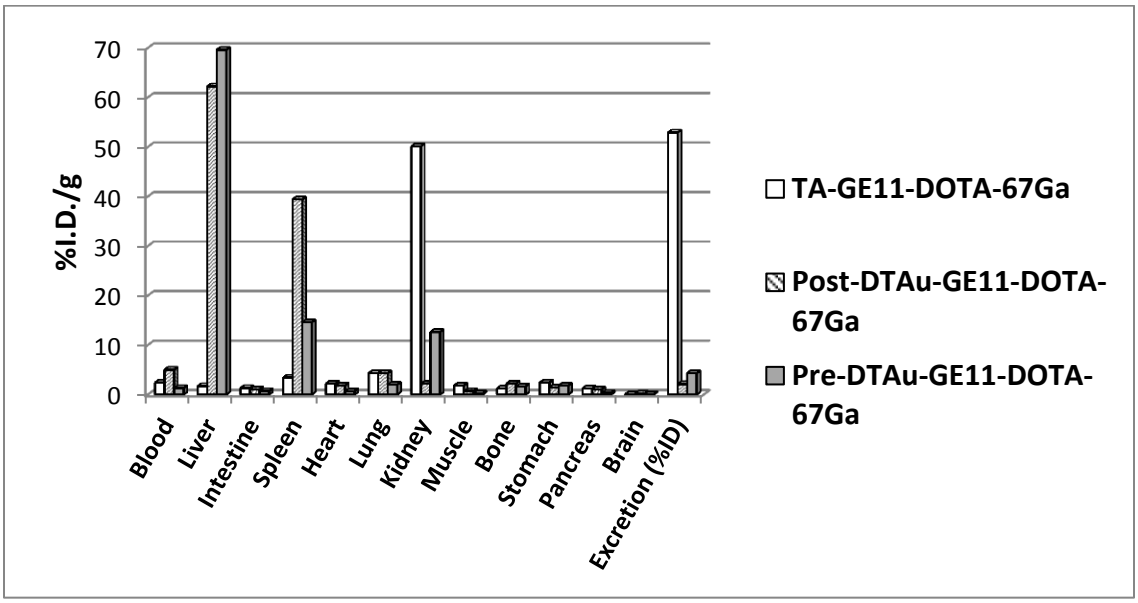

Figure 4.17: *Biodistribution results (mean ± SD, n=3; expressed as %I.D./g of organ) for* ***TA-GE11-DOTA-^{67}Ga****,* ***Post-DTAu-GE11-DOTA-^{67}Ga*** *and* ***Pre-DTAu-GE11-DOTA-^{67}Ga*** *after i.v. administration in CD-1 mice at 1 h p.i..*

In brief, **Pre-DTAu-GE11-DOTA-^{67}Ga** showed promising *in vitro* and *in vivo* biological results, to be further evaluated as a radiolabeled nanoconstruct for specific targeting of EGFr. It has shown a fast blood clearance and low bone uptake, which can be considered an evidence of high *in vivo* stability. Also, it displays a considerable internalization in cervical carcinoma A431 cells, which appears to be EGFr-mediated, as indicated by the performed blockade experiments.

Chapter 5: Gallium Complexes Containing N_2O_2-donor Ligands

5.1 Introduction

The design of new chelator systems for the development of perfusion or target-specific gallium ($^{67/68}$Ga) radiopharmaceuticals is still to this day an area that gets a lot focus by many research groups. Furthermore, the increasing impact of nanomaterials in radiopharmaceutical sciences also motivates the finding of suitable chelating molecules that can effectively be conjugated to nanoparticles while maintaining optimal Ga(III) coordination.

Macrocyclic chelators, like NOTA and DOTA, are known to afford gallium complexes with high kinetic inertness and high thermodynamic stability.[85,241] However, the synthesis of macrocyclic bifunctional chelators suitable for the conjugation of the biomolecules and still capable of stabilizing the metal ion can be considerably challenging, as only one of the pendant arms must be selectively functionalized with the targeting molecule. For this reason, many research groups have pursued in recent years with the synthesis and evaluation of alternative acyclic chelators suitable for the stable complexation of ^{67}Ga and ^{68}Ga under physiological conditions.

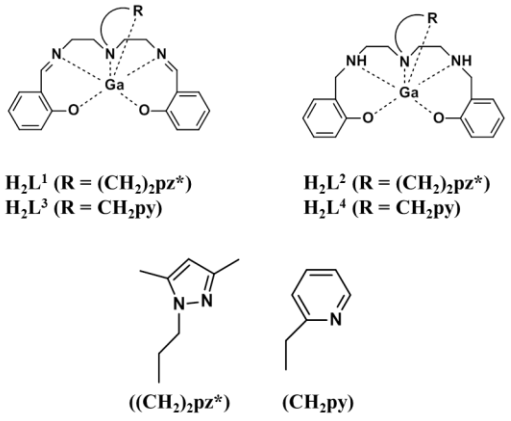

Figure 5.1: *Chemical structures of* ***H_2L^1 - H_2L^4*** *with a generic representation of their coordination to Ga(III).*

As reviewed in Chapter 1, several N,O-donor acyclic and hexadentate ligands were reported to afford stable Ga(III) complexes, which in some cases were successfully applied in $^{67/68}$Ga-labeling of pepides and proteins.[87,242-244] These encouraging findings have prompted the synthesis of new N_4O_2-donor acyclic chelators (Figure 5.1) and the evaluation of their coordination capability towards Ga(III), aiming to have an insight on their potential usefulness for radiopharmaceutical research.

The new N_4O_2-donor chelators featuring a N-heterocyclic pendant arm and two phenolate coordinating groups, have been designed based on the diethylenetriamine framework, and comprise compounds of the Schiff base type (**H_2L^1** and **H_2L^3**) and the respective reduced forms (**H_2L^2** and **H_2L^4**, Figure 5.1). The N-heterocyclic groups are of the pyridyl and pyrazolyl type, which have a well documented capacity of coordinating different metal ions under the aqueous conditions required in radiopharmaceutical chemistry.[87,243,245-247]

As described in this Chapter, the assessment of the relevance of these new N_4O_2-donor chelators for radiopharmaceutical development involved the following studies:

i) Synthesis and characterization of the N_4O_2-donor chelators (**H_2L^1** - **H_2L^4**).
ii) Evaluation on the capacity of **H_2L^1** - **H_2L^4** to coordinate natural gallium: Synthesis and characterization of the resulting complexes.
iii) Radiolabelling studies of selected N_4O_2-donor chelators using ^{67}Ga.
iv) Biological evaluation: biodistribution and *in vivo* stability studies in mice.

5.2 Synthesis and Characterization of the N_4O_2-donor Chelators

The new N_4O_2-donor chelators (**H_2L^1** - **H_2L^4**) were obtained by a multistep synthetic approach as depicted in Scheme 5.1. The synthesis was initiated with the introduction of the pyrazolyl- and pyridyl-containing pendat arms at the central nitrogen of the BOC protected dien backbone (**9**). This led to the synthesis of the previously reported compound (2-((2-tert-butoxycarbonylaminoethyl)-[2-(3,5-dimethylpyrazol-1-yl)-ethyl]amino)ethyl) carbamic acid tert-butyl ester (**10**), which was obtained by the literature method.[248] The pyridyl congener (**12**) was obtained in a similar way by N-alkylation of **10** with 1-bromomethylpyridine.

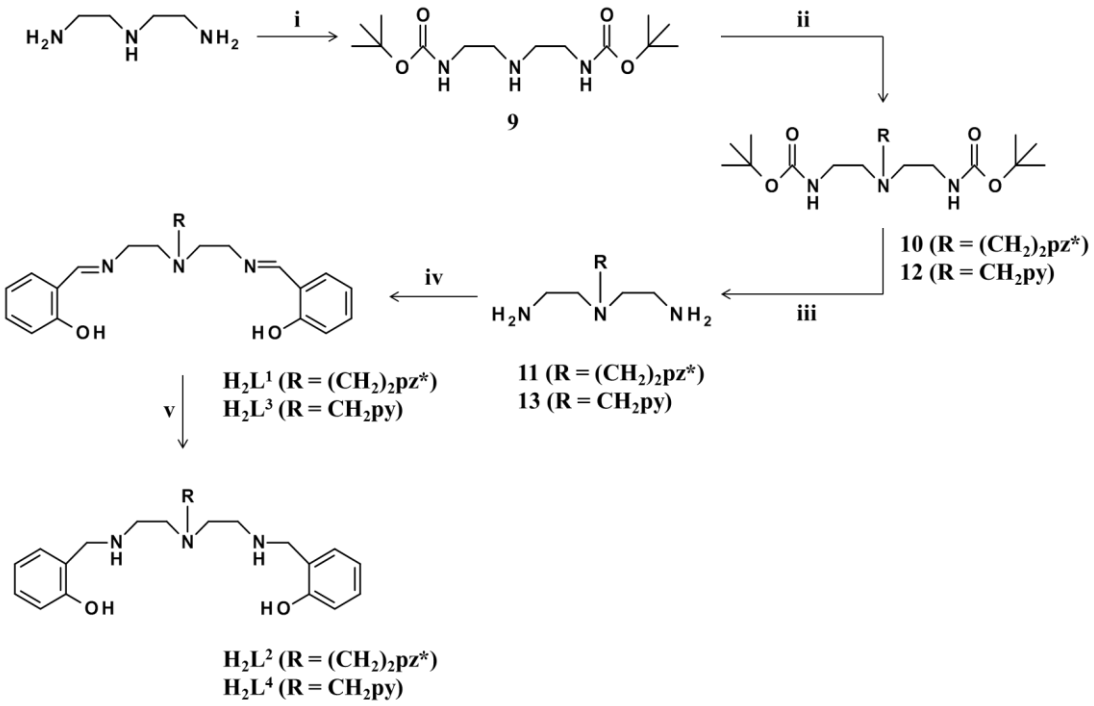

Scheme 5.1: *Synthesis of the N_2O_4-donor chelators.* ***i)*** *$O(BOC)_2$, THF, r.t., o.n.;* ***ii)*** *$BrCH_2CH_2$(3,5-Me_2pz) or 2-$BrCH_2$py , K_2CO_3, KI, THF, reflux, 24 h;* ***iii)*** *HCl/MeOH, r.t., 2 h;* ***iv)*** *salicylaldehyde, MeOH, reflux, 4h;* ***v)*** *$NaBH_4$, MeOH, r.t., o.n.*

Removal of the BOC protecting groups of **10** and **12**, under acid hydrolysis, afforded compounds **11** and **13**, respectively. Treatment of **11** and **13** with salicylaldehyde in refluxing methanol, using a 1:2 molar ratio of the reagents, gave the Schiff-base chelators $\mathbf{H_2L^1}$ and $\mathbf{H_2L^3}$, respectively. The corresponding reduced derivatives, $\mathbf{H_2L^2}$ and $\mathbf{H_2L^4}$, were synthesized by reaction of $\mathbf{H_2L^1}$ and $\mathbf{H_2L^3}$ with sodium borohydride in methanol. After appropriate work-up, these new N_2O_4-donor chelators ($\mathbf{H_2L^1}$-$\mathbf{H_2L^4}$) were obtained as pale yellow oils in moderate to high yield ranging between 45 - 97%.

The characterization of $\mathbf{H_2L^1}$-$\mathbf{H_2L^4}$ was done by ESI-MS, IR, ^{1}H and ^{13}C-NMR spectroscopy. The spectroscopic data obtained for $\mathbf{H_2L^1}$-$\mathbf{H_2L^4}$ are preseted in Tables 5.1 and 5.2.

Table 5.1: *^{1}H and ^{13}C-NMR data of* ***H_2L^1-H_2L^4*** *in $CDCl_3$.*

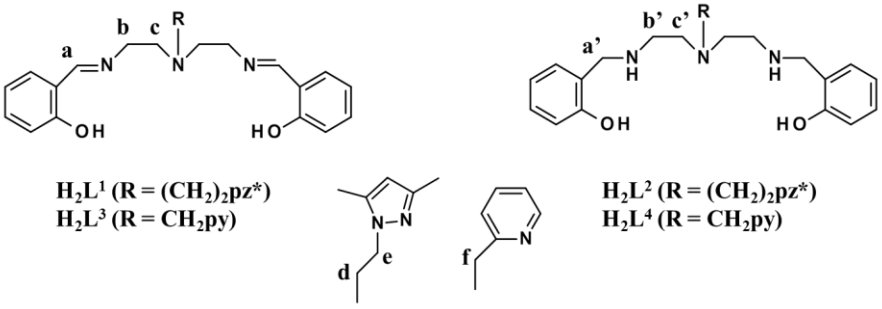

H_2L^1 (R = $(CH_2)_2$pz*)
H_2L^3 (R = CH_2py)

H_2L^2 (R = $(CH_2)_2$pz*)
H_2L^4 (R = CH_2py)

Compound	^{1}H-NMR (ppm)	^{13}C-NMR (ppm)
H_2L^1	2.03 (pz-CH_3), 2.19 (pz-CH_3), 2.83 (**c**), 2.96 (**d**), 3.54 (**b**), 3.89 (**e**), 5.70 (H(4)-pz), 6.78 (Ph), 6.90 (Ph), 7.00 (Ph), 7.26 (Ph), 8.05 (**a**), 13.38 (OH)	10.84 (pz-CH_3), 13.49 (pz-CH_3), 47.08 (**c**), 54.93 (**d**), 55.73 (**b**), 57.84 (**e**), 104.77 (C(4)-pz), 116.91 (Ph), 118.46 (Ph), 118.66 (Ph), 131.27 (Ph), 132.11 (Ph), 139.35 (C3/5-pz), 147.32 (C3/5-pz), 161.16 (Ph), 165.95 (**a**).
H_2L^2	1.87 (pz-CH_3), 2.20 (pz-CH_3), 2.56 (**c'**), 2.62 (**b'**), 2.74 (**d**), 3.89 (**a'**), 4.01 (**e**), 5.71 (H(4)-pz), 6.75-6.81 (Ph), 6.98 (Ph), 7.13 (Ph)	10.70 (pz-CH_3), 12.69 (pz-CH_3), 45.62 (**c'**), 46.56 (**b'**), 52.06 (**d**), 53.28 (**a'**), 53.54 (**e**), 105.04 (C(4)-pz), 115.96 (Ph), 118.60 (Ph), 122.21 (Ph), 128.25 (Ph), 128.27 (Ph), 134.41 (C3/5-pz), 146.98 (C3/5-pz), 158.06 (Ph).
H_2L^3	2.89 (**c**), 3.62 (**b**), 3.82 (**f**), 6.76 (Ph), 6.91 (Ph), 6.97 (Ph), 711 (py), 7.27 (py), 7.41 (py), 8.05 (**a**), 8.51 (py).	55.28 (**c**), 57.50 (**b**), 60.84 (**f**), 116.83 (Ph), 118.35 (Ph), 118.60 (Ph), 121.94 (py), 122.78 (py), 131.18 (Ph), 132.00 (Ph), 136.42 (py), 148.72 (py), 159.42 (py), 161.10 (Ph), 165.76 (**a**).
H_2L^4	2.64 (**c'**+**b'**), 3.66 (**f**), 3.80 (**a'**), 5.23 (NH), 6.71 (4Ph), 6.85 (Ph), 7.05-7.20 (Ph+py), 7.59 (py), 8.40 (py).	45.93 (**c'**), 52.44 (**b'**), 54.22 (**a'**), 60.19 (**f**), 116.21 (Ph), 118.82 (Ph), 122.53 (py), 122.80 (py), 123.32 (Ph), 128.25 (Ph), 128.48 (Ph), 136.63 (py), 149.37 (py), 158.16 (Ph), 159.10 (py).

Table 5.2: *Relevant IR and ESI-MS data of* ***H_2L^1-H_2L^4****.*

Compound	IR (KBr, ν/cm^{-1})[a]	ESI-MS (m/z) (calculated / found)[b]
H_2L^1	1634 (N=C)	434.3 / 434.3
H_2L^2	3286 (N-H)	438.3 / 438.4
H_2L^3	1634 (N=C)	403.2 / 403.3
H_2L^4	3418 (N-H)	407.2 / 407.4

[a] IR spectra were recorded as KBr pellets; [b] ESI-MS results shown correspond to $[M+H]^+$.

The ESI-MS and spectroscopic characterization (IR and NMR) of **H_2L^1-H_2L^4** provided data that are consistent with the formulations proposed for these compounds. In particular, the ^{1}H-NMR spectra of **H_2L^1** and **H_2L^3** in $CDCl_3$ showed a downfield singlet at 8.05 ppm due to the imine N=CH-Ph proton.[249] These imine proton resonances are absent in the ^{1}H-NMR spectra of **H_2L^2** and **H_2L^4** confirming the reduction of the imine function, which is further corroborated by the presence of a singlet at 3.89 and 3.80 ppm, respectively, due to the protons of the new CH_2 groups.

In agreement, the IR spectra of **H_2L^1** and **H_2L^3** display an absorption band centered at 1634 cm^{-1}, characteristic of the imine C=N bond.[249] By contrast, in the IR spectra of **H_2L^2** and **H_2L^4** there is no band assignable to the ν(C=N) stretching mode, being observed broad bands centered at 3286 and 3418 cm^{-1}, respectively, which are consistent with the formation of the secondary amines.[249]

5.3 Synthesis and Characterization of the Complexes with Natural Gallium

5.3.1 Synthesis of the Complexes

The attempts to synthesize Ga(III) complexes with **H_2L^1-H_2L^4** were made by reaction of Ga(III) nitrate with the respective chelator in methanol in the presence of sodium acetate, followed by precipitation with $NaClO_4$ (Scheme 5.2).

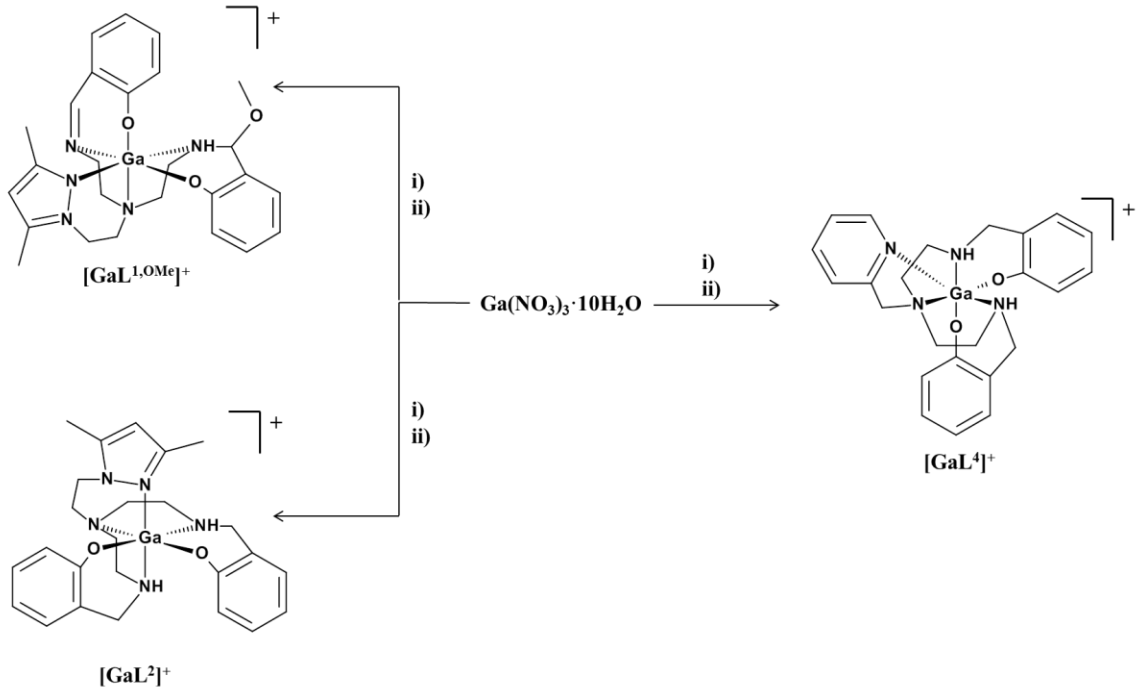

Scheme 5.2: *Synthesis of the isolated non-radioactive gallium complexes.* ***i)*** $H_2L^1/H_2L^2/H_2L^4$, *$NaCH_3COO$, MeOH, r.t., o.n.;* ***ii)*** *$NaClO_4$.*

For the pyrazolyl-containing Schiff base chelator, $\mathbf{H_2L^1}$, the final compound was obtained after precipitation at low temperature and washing with cold methanol. The isolated complex was $\mathbf{GaL^{1,OMe}}$, corresponding to a Ga(III) species that contains a modified ligand ($\mathbf{L^{1,OMe}}$), as a result of the attack of one of the imine groups of $\mathbf{L^1}$ by methanol. This attack led to the formation of a hemiaminal derivative as confirmed by the full characterization of $\mathbf{GaL^{1,OMe}}$, which is discribed below. The isolated complex was obtained in a yield of 36%.

In the reaction of $Ga(NO_3)_3$ with the similar pyridyl-containing Schiff base $\mathbf{H_2L^3}$, one of the species formed was GaL_3 as indicated by ESI-MS analysis of the solid that precipitated from the reaction mixture after treatment with $NaClO_4$ (Figure 5.2). Besides the peak due $\mathbf{[GaL^3]^+}$ (m/z = 469.3), the positive ESI-MS spectrum of this precipitate has shown another prominent peak at m/z = 365.2 displaying an isotopic pattern compatible with the presence of a second monomeric gallium species. This second Ga(III) species does not correspond to the hemiaminal congener of $\mathbf{[GaL^{1,OMe}]^+}$, which should display a molecular ion heavier than $\mathbf{[GaL^2]^+}$. Instead, it could correspond to the $[M+H]^+$ ion of a Ga(III) species containing a $\mathbf{L^1}$ ligand that has suffered hydrolysis of one of the

salicylaldiimine groups. Despite the several extraction, washing and/or recrystallization attempts that have been done, using different solvents (e.g. chloroform, acetonitrile or methanol) or mixtures of solvents (e.g. chloroform/n-hexane or methanol/diethyleter), it was not possible to purify the complexes that resulted from the reaction of Ga(III) with **H_2L^3.**

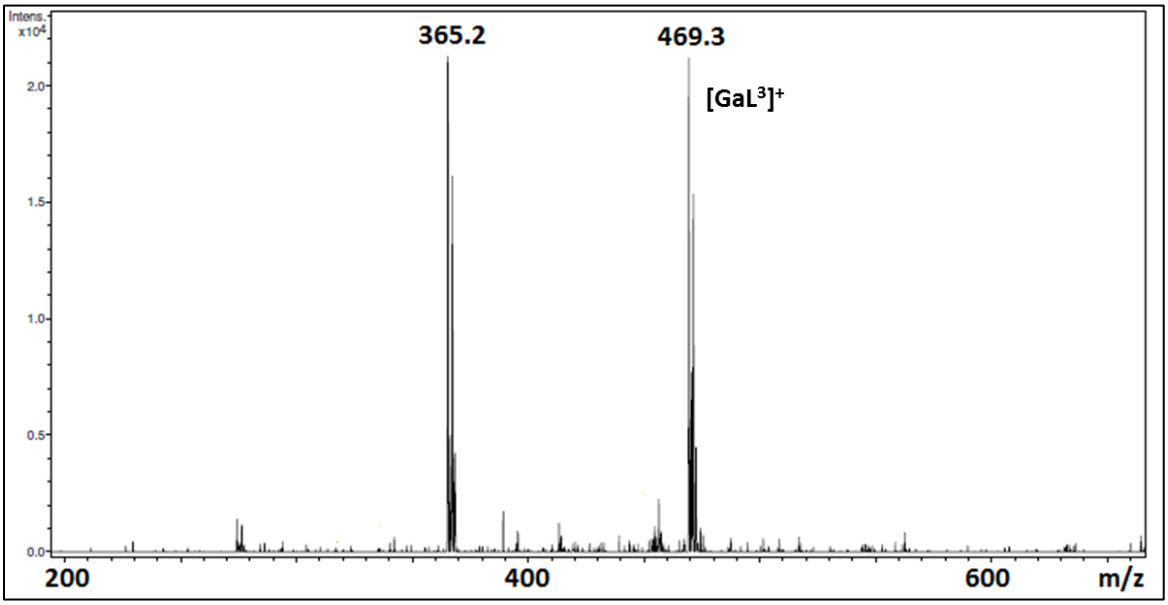

Figure 5.2: *ESI-MS spectrum of the precipitate obtained after treatment with $NaClO_4$ of the mixture resulting from the reaction of $Ga(NO_3)_3$ with* ***H_2L^3****.*

In the case of **H_2L^2** and **H_2L^4** the reactions with $Ga(NO_3)_3$ led to the formation of the expected compounds, i.e. **GaL^2** and **GaL^4**. After addition of $NaClO_4$, **GaL^2** was recovered as a microcrystaline solid that precipitated at low temperature, and was filtered and washed with cold MeOH. **GaL^4** was extracted with $CHCl_3$ from the dried reaction mixture, after treatment with $NaClO_4$. **GaL^2** and **GaL^4** were isolated in low to moderate yield: 34% and 22%, respectively.

5.3.2 Characterization of the Gallium Complexes

The Ga(III) compounds isolated in a pure form, i.e. **$GaL^{1,OMe}$**, **GaL^2** and **GaL^4**, were characterized by ESI-MS, C,H,N analysis, X-ray diffraction analysis, IR and 1D and 2D multinuclear NMR, as discussed below.

5.3.2.1 IR Spectroscopy and Mass Spectrometry

Relevant IR and ESI-MS data of **GaL^{1,OMe}**, **GaL^{2}** and **GaL^{4}** are shown in Table 5.3. As indicated in Table 5.3, the ESI-MS spectra of **GaL^{1,OMe}**, **GaL^{2}** and **GaL^{4}** have shown the presence of single peaks at m/z values corresponding to the respective molecular-ions ($[M+H]^+$), and presenting splitting patterns consistent with the expected isotopic distribution. The IR spectrum of **GaL^{1,OMe}** showed the presence of absorption bands corresponding to the stretching vibration modes of the imine C=N bonds and amine N-H bonds at 1643 cm^{-1} and 3379 cm^{-1}, respectively. In the IR spectra of complexes **GaL^{2}** and **GaL^{4}** there are also intense and broad bands centered at 3429 and 3200 cm^{-1}, respectively, which are due to ν(N-H).

Table 5.3: *Relevant IR and ESI-MS data for **GaL^{1,OMe}**, **GaL^{2}** and **GaL^{4}**.*

Compound	IR (KBr, v/cm^{-1})[a]	ESI-MS (m/z) (calculated / found)[b]
GaL^{1,OMe}	1643 (N=C), 3379 (N-H)	532.2 / 532.3
GaL^{2}	3429 (N-H)	504.2 / 504.2
GaL^{4}	3200 (N-H)	473.1 / 473.3

[a] IR spectra were recorded as KBr pellets; [b] ESI-MS results shown correspond to $[M+H]^+$.

5.3.2.2 Solid State Molecular Structures

Crystals of **GaL^{1,OMe}**, **GaL^{2}** and **GaL^{4}** suitable for X-ray diffraction analysis were obtained from slow evaporation of concentrated solutions of the compounds in methanol. For **GaL^{2}**, X-ray quality crystals were also grown from a concentrated solution of the compound in chloroform. A selection of bond lengths and angles for all complexes is presented in Table 5.4.

The X-ray structural analysis of **GaL^{1,OMe}** showed that the corresponding cations consist on Ga(III) ions coordinated by a hemiaminal derivative of **L^{1}**,[250,251] as can be verified in the ORTEP diagram presented in Figure 5.3. The Ga(III) ion is in a distorted-octaedral environment being coordinated by a N_4O_2-donor atom set, which comprises the two phenolate oxygen atoms, the pyrazolyl nitrogen atom, an imine nitrogen atom and a secondary amine nitrogen atom. The pyrazolyl ring is *trans* to the aliphatic nitrogen atom from the hemiaminal that resulted from the nucleophilic attack of **L^{1}** by methanol (N1-Ga1-N4 = 167.40(11)º), while the two phenoxide groups exhibit a *cis* orientation (O1-Ga1-O2 =

99.20(10)º). The N3-C12 distance of 1.293(4) Å is consistent with the presence of a C=N double bond, confirming that one of the imine groups did not suffer the nucleophilic attack.

***Table 5.4**: Selected bond lengths (Å) and angles (º) for the gallium complexes.*

	$GaL^{1,OMe}$ (MeOH)	**GaL^{2} (MeOH)**	**GaL^{2} ($CHCl_3$)**	**GaL^{4} (MeOH)**	
				Molecule A	**Molecule B**
Ga1-O1	1. 908(2)	1.9158(17)	1.886(2)	1.9021(12)	1.9003(12)
Ga1-O2	1. 902(2)	1.8879(19)	1.874(2)	1.8800(12)	1.8753(12)
Ga1-N1	2.135(3)	2.127(2)	2.121(3)	2.0900(15)	2.0870(15)
Ga1-N2	2.185(3)	2.165(2)	2.157(3)	2.1329(15)	2.1389(15)
Ga1-N3	2.042(2)	2.073(2)	2.116(3)	2.1203(15)	2.1220(14)
Ga1-N4	2.099(3)	2.121(2)	2.144(3)	2.0941(14)	2.0838(14)
O1-Ga1-O2	92.20(10)	94.12(8)	97.64(10)	95.91(5)	95.40(5)
O1-Ga1-N1	90.77(10)	90.71(8)	91.87(10)	90.74(5)	90.11(6)
O2-Ga1-N1	91.10(11)	90.77(9)	90.42(10)	97.74(5)	99.21(6)
O1-Ga1-N4	85.86(10)	84.72(8)	84.77(10)	85.13(5)	86.17(5)
O2-Ga1-N4	101.14(11)	96.05(8)	97.15(9)	99.89(6)	98.72(6)
N1-Ga1-N4	167.40(11)	172.04(9)	172.05(10)	162.32(6)	161.95(6)
O1-Ga1-N3	172.86(11)	172.77(9)	171.32(10)	172.65(6)	172.58(6)
O2-Ga1-N3	89.95(11)	92.24(9)	90.70(10)	90.42(5)	91.32(5)
N1-Ga1-N3	96.00(11)	92.63(9)	90.46(10)	92.12(6)	91.93(6)
N4-Ga1-N3	87.04(11)	91.21(9)	91.84(10)	90.12(6)	89.70(6)
O1-Ga1-N2	98.12(10)	93.64(8)	91.61(10)	92.14(5)	91.15(5)
O2-Ga1-N2	165.87(10)	169.14(8)	168.20(10)	171.92(5)	173.25(5)
N1-Ga1-N2	79.19(11)	81.54(9)	81.93(10)	82.85(6)	82.40(6)
N4-Ga1-N2	89.26(11)	92.22(9)	90.95(9)	80.14(6)	80.03(6)
N3-Ga1-N2	80.99(11)	80.53(9)	80.44(10)	81.50(6)	82.06(6)

The X-ray structural analysis of **GaL^{2}** and **GaL^{4}** (Figures 5.3 and 5.4, respectively) indicate that both compounds possess three chiral coordinated nitrogen atoms. For **GaL^{2}**, the measured crystals presented a unique enantiomeric form in the asymmetric unit, having S, R and R absolute configurations at the N1, N2 and N3 nitrogen atoms, either when the crystals were obtained from concentrated methanol or chloroform solutions of the compound. By contrast, for **GaL^{4}** there are two independent molecules in the asymmetric unit, which correspond to two different enantiomers that are non-superimposable mirror images of each other.

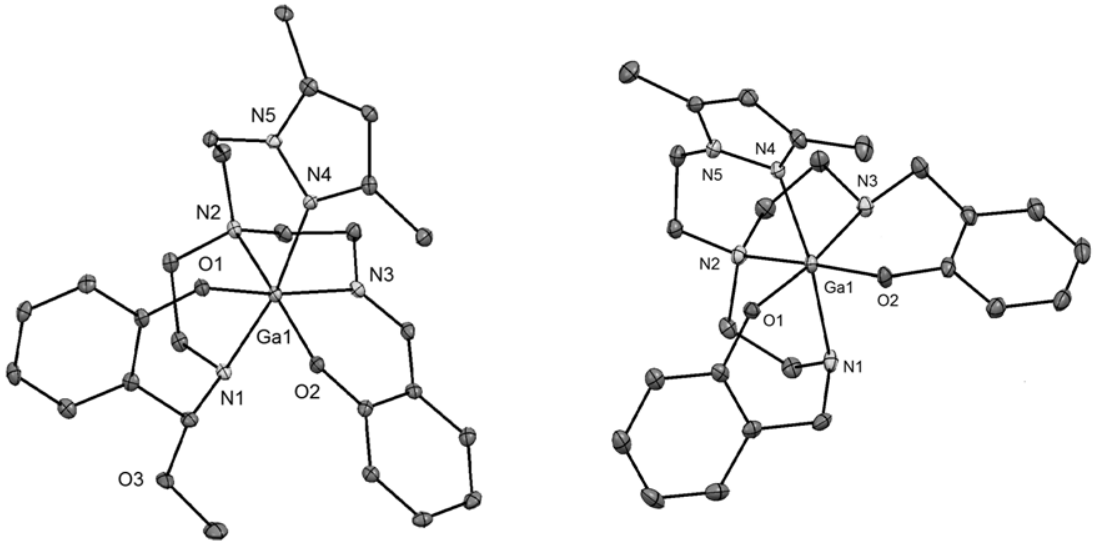

$[GaL^{1,OMe}]^+$ $[GaL^{2}]^+$

Figure 5.3: *ORTEP drawing at the 40% probability level for* ***GaL^{1,OMe}*** *and* ***GaL^{2}*** *cations. Hydrogen atoms are omitted for clarity.*

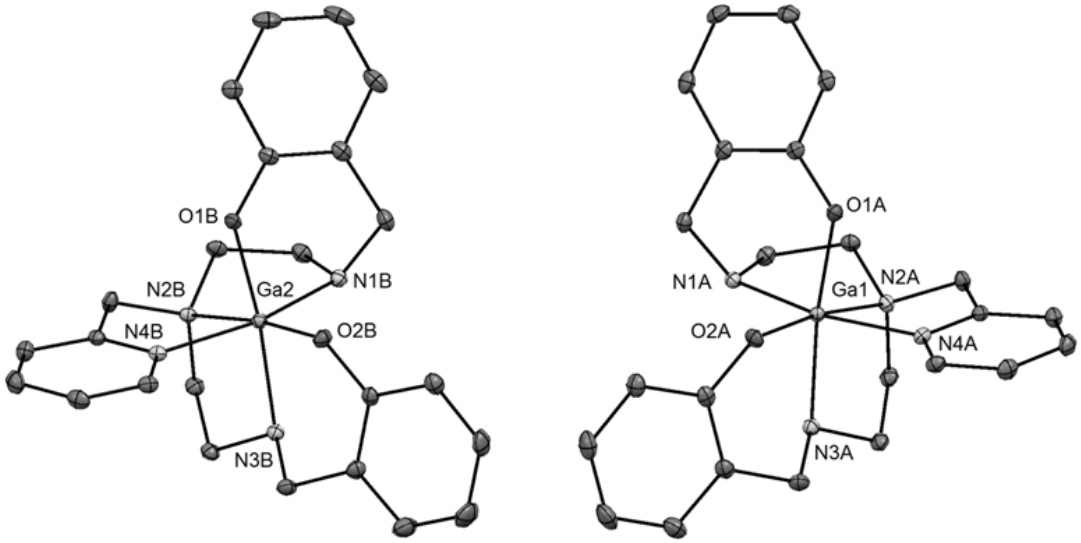

Molecule B **Molecule A**

Figure 5.4: *ORTEP drawing at the 40% probability level for two enantiomers of the* ***GaL^{4}*** *cation. Hydrogen atoms are omitted for clarity.*

The Ga-O, Ga-N_{pz} and Ga-N_{py} bond distances of **GaL^{1,OMe}**, **GaL^{2}** and **GaL^{4}** span in the ranges 1.874(2) - 1.9158(17) Å, 2.099(3) - 2.144(3) Å and 2.0838(14) - 2.0941(14) Å, respectively. These distances compare well with those reported for other Ga(III)

complexes containing phenoxide, pyrazolyl and pyridyl coordinating groups.[87,249,252,253] As expected, the Ga-N_{imine} bond distance of 2.042(3) Å (Ga-N3) found for **GaL^{1,OMe}** is shorter than the Ga-N bond distances measured for the coordinated aliphatic amines which vary between 2.0838(14) and 2.185(3) Å for all set of complexes.

The Ga-N bond distances of the coordinated pyrazolyl ring in **GaL^{2}**, Ga-N = 2.121(2) Å in crystals obtained from MeOH and Ga-N = 2.144(3) Å in crystals obtained from $CHCl_3$, are slightly longer than the Ga-N bond distances found for the coordinated pyridyl rings in the two enantiomeric forms that are present in the measured crystal of **GaL^{4}** (Ga-N = 2.0941(14) Å in Molecule A and Ga-N = 2.0838(14) Å in Molecule B). This trend reflects most probably the poorer electron-releasing properties of pyrazolyl, together with the greatest rigidity inherent to the pyridyl-containing five-membered [GaN_2C_2] chelating ring in comparison with the pyrazolyl-containing six-membered [GaN_3C_2] chelating ring.

5.3.2.3 Solution NMR Structural Analysis

Complexes **GaL^{1,OMe}**, **GaL^{2}** and **GaL^{4}** were also studied by a variety of multinuclear and bidimensional NMR techniques including Nuclear Overhauser Effect Spectroscopy (NOESY), Correlation Spectroscopy (COSY), Total Correlation Spectroscopy (TCOSY) and Heteronuclear Single Quantum Coherence (HSQC), to identify the number of species in solution and assign the coordination mode of the respective chelators in solution.

Table 5.5 displays the ^{1}H and ^{13}C-NMR spectroscopic data of the major species in solution for **GaL^{1,OMe}**, **GaL^{2}** and **GaL^{4}**.

Table 5.5: *^{1}H and ^{13}C-NMR data of the major species found in solution for* ***GaL^{1,OMe}***, ***GaL^{2}*** *and* ***GaL^{4}*** *in CD_3CN.*

Compound	^{1}H-NMR (ppm)	^{13}C-NMR (ppm)
GaL^{1,OMe}	1.99 (pz-CH_3), 2.36 (pz-CH_3), 2.46 (CH_2), 2.67 (2xCH_2), 2.78 (CH_2), 2.98 (CH_2), 3.11 (CH_2), 3.15 (O-CH_3), 3.22 (CH_2), 3.52 (CH_2), 3.63 (CH_2), 4.09 (N-H), 4.22 (CH_2), 4.92 (CH_2), 5.49 (CH), 6.07 (H(4)-pz), 6.63 (Ph), 6.71 (Ph), 6.81-6.87 (Ph), 7.18 (Ph), 7.35 (Ph), 7.41-7.47 (Ph), 8.54 (N=CH)	10.927 (CH_3), 12.36 (CH_3), 35.07 (CH_2), 43.31 (CH_2), 51.80 (CH_2), 53.03 (CH_2), 53.50 (CH_2), 56.68 (OCH_3), 57.75 (CH_2), 88.46 (CH), 107.41 (C(4)-pz), 116.80 (Ph), 119.18 (Ph), 122.39 (Ph), 122.93 (Ph), 127.93 (Ph), 130.88 (Ph), 135.49 (Ph), 136.61 (Ph), 143.70 (C(3)-pz), 150.41 (C(5)-pz), 160.65 (Ph), 166.83 (Ph), 171.64 (CH=N).
GaL^{2}	2.35 (2xpz-CH_3), 2.20 (CH_2), 2.50 (CH2), 2.63 (CH_2), 2.73 (CH_2), 2.90 (CH_2), 3.20-3.00 (CH_2), 3.69-3.49 (2xN-H + 2xCH_2), 3.74 (CH_2), 3.97 (CH_2), 4.22 (CH_2), 4.45 (CH_2), 4.74 (CH_2), 6.14 (H(4)-pz), 6.40 (Ph), 6.59 (Ph), 6.66 (Ph), 6.78 (Ph), 7.04 (Ph), 7.11 (Ph), 7.18 (Ph)	11.27 (CH_3), 14.15 (CH_3), 41.395 (CH_2), 44.02 (CH_2), 45.44 (CH_2), 50.69 (CH_2), 51.71 (CH_2), 52.78 (CH_2), 56.83 (CH_2), 108.66 (C(4)-pz), 116.312 (Ph), 116.77 (Ph), 118.99 (Ph), 120.96 (Ph), 121.70 (Ph), 123.12 (Ph), 129.74 (Ph), 130.13 (Ph), 130.81 (Ph), 145.03 (C(3)-pz), 153.03 (C(5)-pz), 161.37 (Ph), 164.06 (Ph)
GaL^{4}	2.52 (CH_2), 2.67 (CH_2), 2.88 (CH_2), 3.03 (CH_2), 3.26 (CH_2), 3.63 (2xCH_2), 4.03 (CH_2), 4.32 (N-H), 4.34 (CH_2), 4.72 (NH), 6.38 (Ph), 6.56 (Ph), 6.72 (Ph), 6.96 (Ph), 7.06 (Ph), 7.21 (Ph), 7.61 (py), 8.1 (py), 9.05 (py)	42.37 (CH_2), 42.78 (CH_2), 44.31 (CH_2), 44.93 (CH_2), 51.71 (CH_2), 52.14 (CH_2), 52.71 (CH_2), 54.09 (CH_2), 54.62 (CH_2), 55.66 (CH_2), 56.50 (CH_2), 57.84 (CH_2), 58.32 (CH_2), 63.00 (CH_2), 78.65 (CH_2), 116.23 (Ph), 119.37 (Ph), 121.14 + 121.50 (py), 123.64 + 124.57 + 125.56 (Ph), 129.96 + 130.54 + 131.13 (Ph), 142.14 + 142.57 (py), 146.73 (py), 148.55 (py), 153.93 (py), 163.48 + 164.28 (Ph)

The ^{1}H and ^{13}C-NMR analysis of **GaL^{1,OMe}** and **GaL^{2}** in acetonitrile solution revealed the presence of major species in solution, as can be checked in the ^{1}H-NMR spectra presented in Figure 5.5. The assignment of the different diastereotopic methylenic protons and corresponding carbon atoms for **GaL^{1,OMe}** and **GaL^{2}** was achieved by means of COSY and HSQC spectra (A3 - A6 of the Annex section).

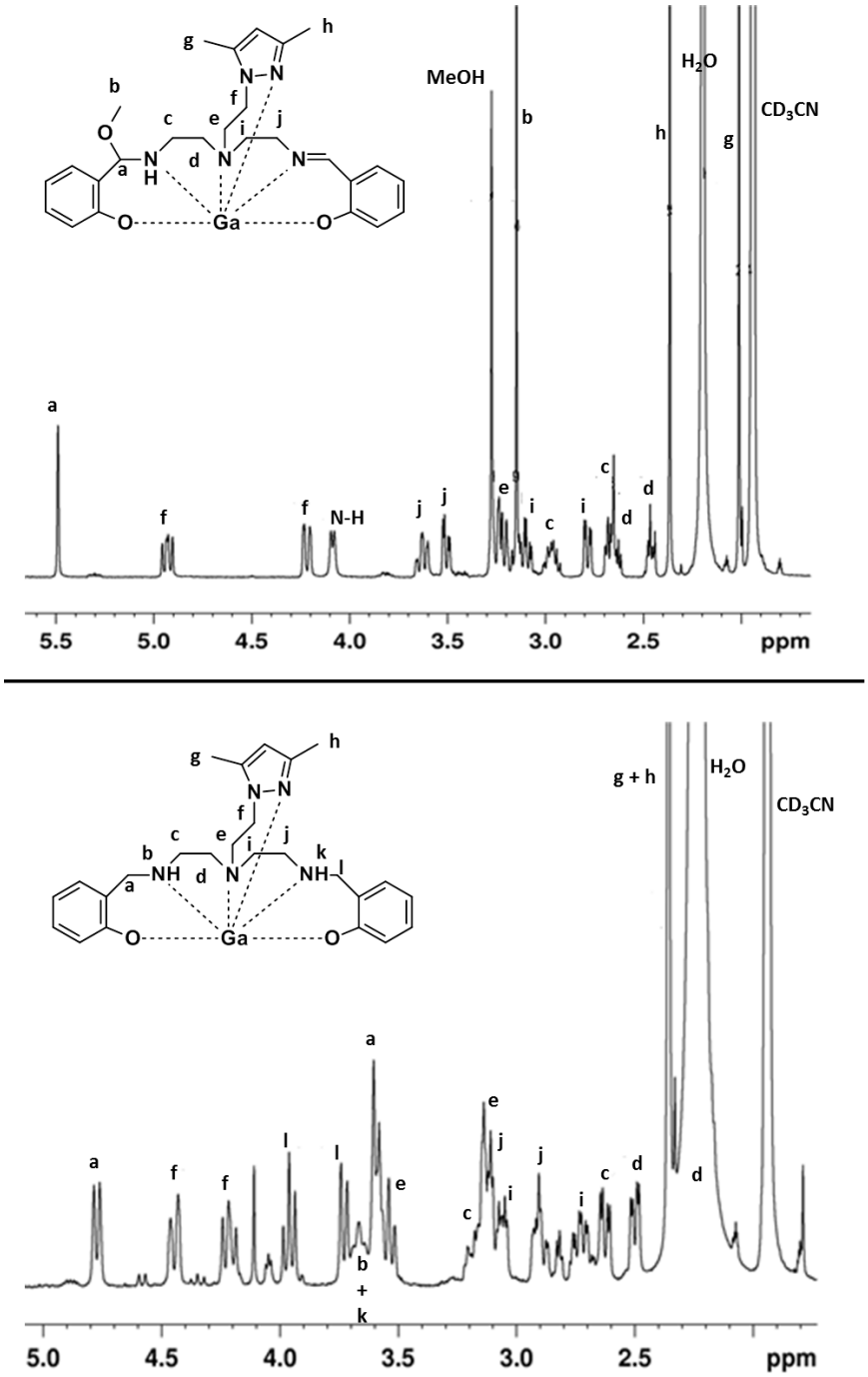

Figure 5.5: *Aliphatic region of the ^{1}H-NMR spectra of* ***GaL^{1,OMe}*** *(above) and* ***GaL^{2}*** *(below) in CD_3CN.*

For **GaL^{1,OMe}**, the NOESY experiments confirmed that the coordinated pyrazolyl nitrogen atom lies in an axial position *trans* to the NH group, being the two phenoxide oxygens bonded to the metal in *cis-cis* positions relative to the pyrazolyl ring. This ligand arrangement was corroborated by the long range correlations between NH at 4.09 ppm

and the methylenic proton at 3.11 ppm, which is pointing downward and belongs to the five-membered chelating ring that contains both aliphatic amines coordinated in an equatorial fashion (Figure 5.6).

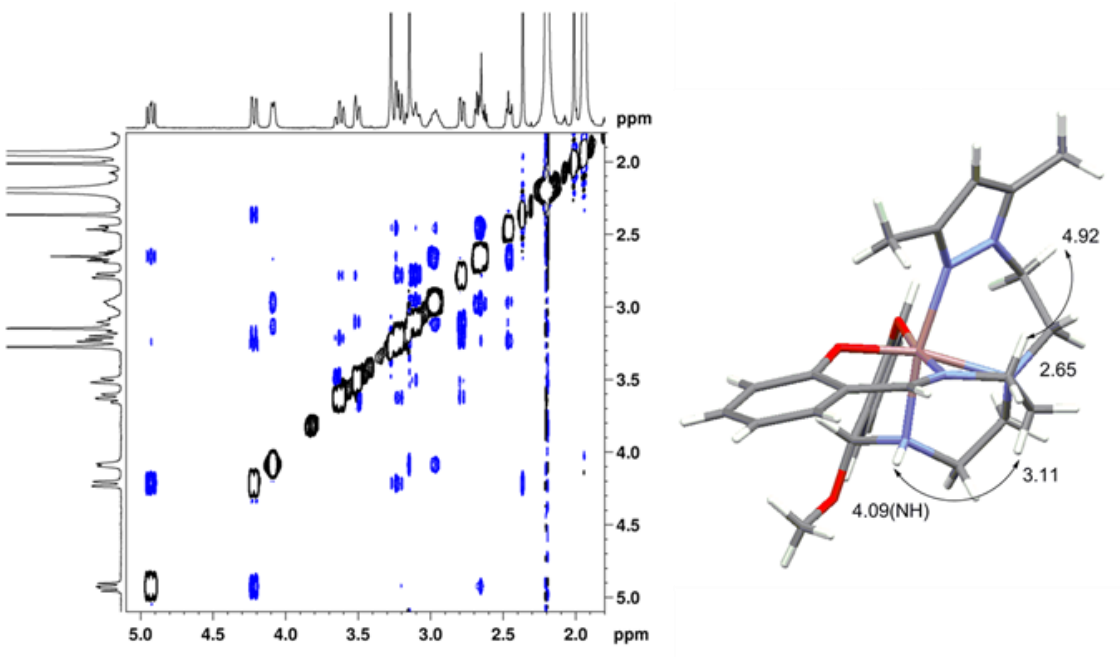

Figure 5.6: *Aliphatic region of the NOESY spectrum of* ***GaL^{1,OMe}*** *in CD_3CN (left), and relevant NOE (Nuclear Overhauser Effect) enhancements used to confirm the cis-cis coordination of* ***L^1*** *(right).*

As a consequence of the conformation adopted by the pyrazolyl arm in **GaL^{1,OMe}**, the methylenic proton from the pyrazolyl-containing six-membered chelating ring resonating at 4.92 ppm correlates via long range NOE with CH_2 proton at 2.65 ppm from the five-membered ring containing the aliphatic amines coordinated in an axial-equatorial mode.

The NOESY spectrum of **GaL^2** (Figure 5.7) shows negative NOE cross peaks between each pair of diastereotopic protons, which denotes slow exchange between enantiomers. This process also gives rise to indirect NOE effects.

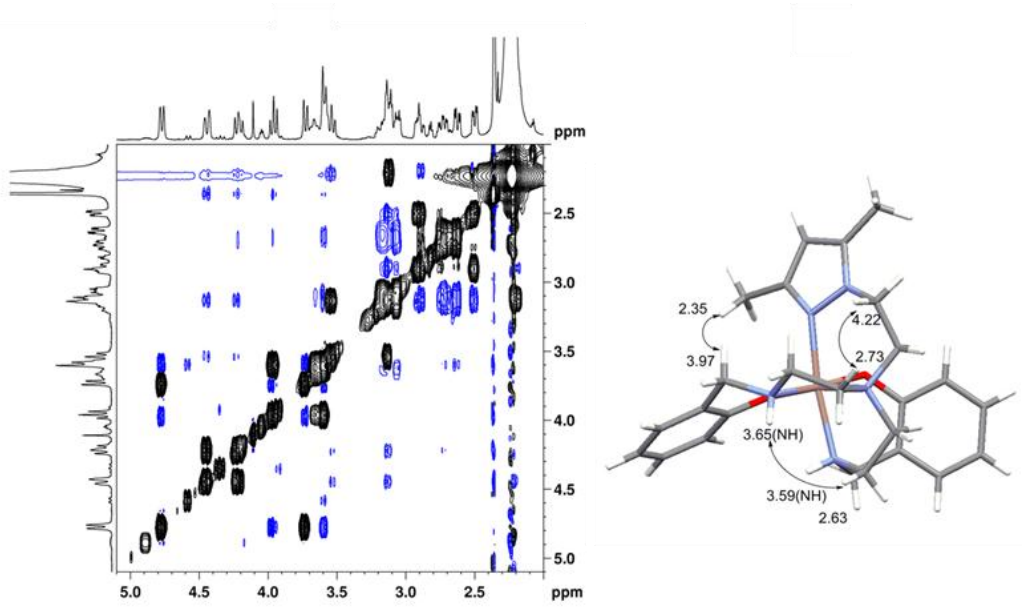

Figure 5.7: *Aliphatic region of the NOESY spectrum of* ***GaL^2*** *in CD_3CN (left), and relevant NOE (Nuclear Overhauser Effect) enhancements used to confirm the cis-cis coordination of* ***L^2****(right).*

To aid in the assignment of the coordination geometry of complex **GaL^2** a series of selective NOE 1D spectra were also performed, as seen in Figure 5.8.

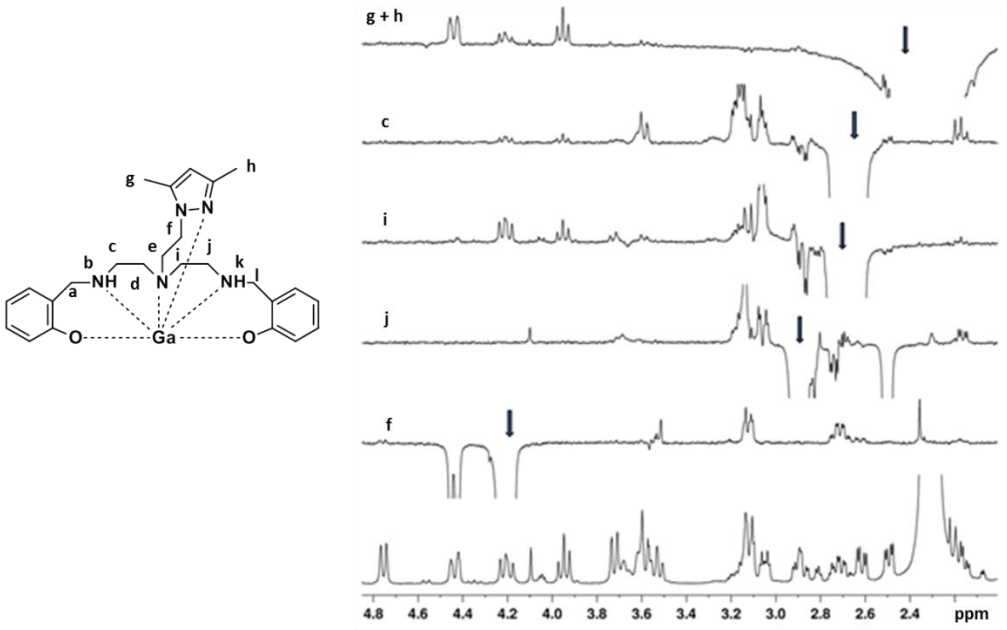

Figure 5.8: *Series of NOE 1D spectra of* ***GaL^2*** *in CD_3CN. The irradiated protons are indicated. Strong negative peaks are due to saturation transfer.*

Based on these data, it was reasoned that the pyrazolyl ring in **GaL^2** occupies an axial position of the octahedron, while the opposite axial position is occupied by the NH group at 3.59 ppm (Figure 5.7). In agreement with this coordination mode, the protons from the pyrazolyl methyl substituent appearing at 2.35 ppm are NOE-correlated with a CH_2 proton at 3.97 ppm from one of the six-membered rings containing a phenoxide group. The NH proton at 3.65 ppm points downward and is only correlated with a CH_2 proton at 2.63 ppm from one of the five-membered chelating ring containing axial and equatorially coordinated aliphatic amine groups.

Furthermore, the CH_2 proton of the pyrazolyl arm at 5.22 ppm is closer to an axial proton at 2.73 ppm from the same five-membered chelating ring. On contrary, its germinal counterpart at 4.45 ppm has no NOE correlations with any of the CH_2 protons of the other five-membered chelating ring.

Unlike **GaL^{1,OMe}** and **GaL^2**, the dissolution of **GaL^4** in acetonitrile originates three species detectable by NMR. As seen in Figures 5.9 and 5.10, there are two major species (**A** and **B**) and a minor species (**C**). **A** and **B** are coordination isomers and **C** is in exchange with **A**. This exchange is due most probably to the replacement of the pyridyl arm by the adventitious water.

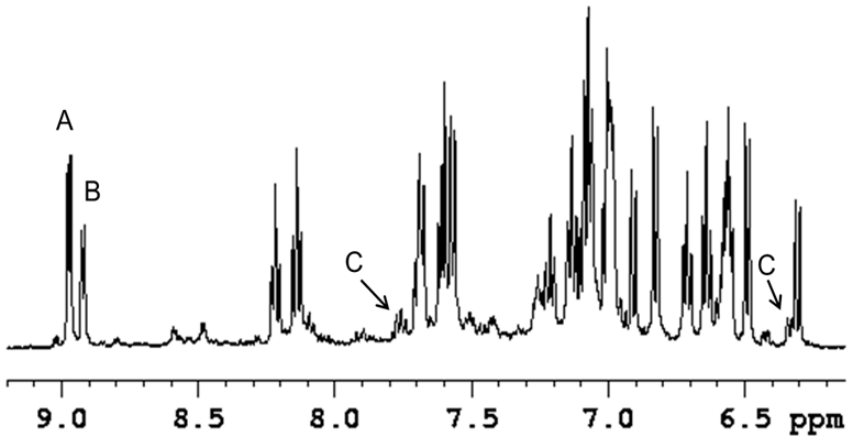

Figure 5.9: *Aromatic region of the ^{1}H-NMR spectrum of **GaL^4** in CD_3CN showing the presence of two major isomers **A** and **B** in a 1:0.6 ratio. Some peaks of the minor species **C** are also identified.*

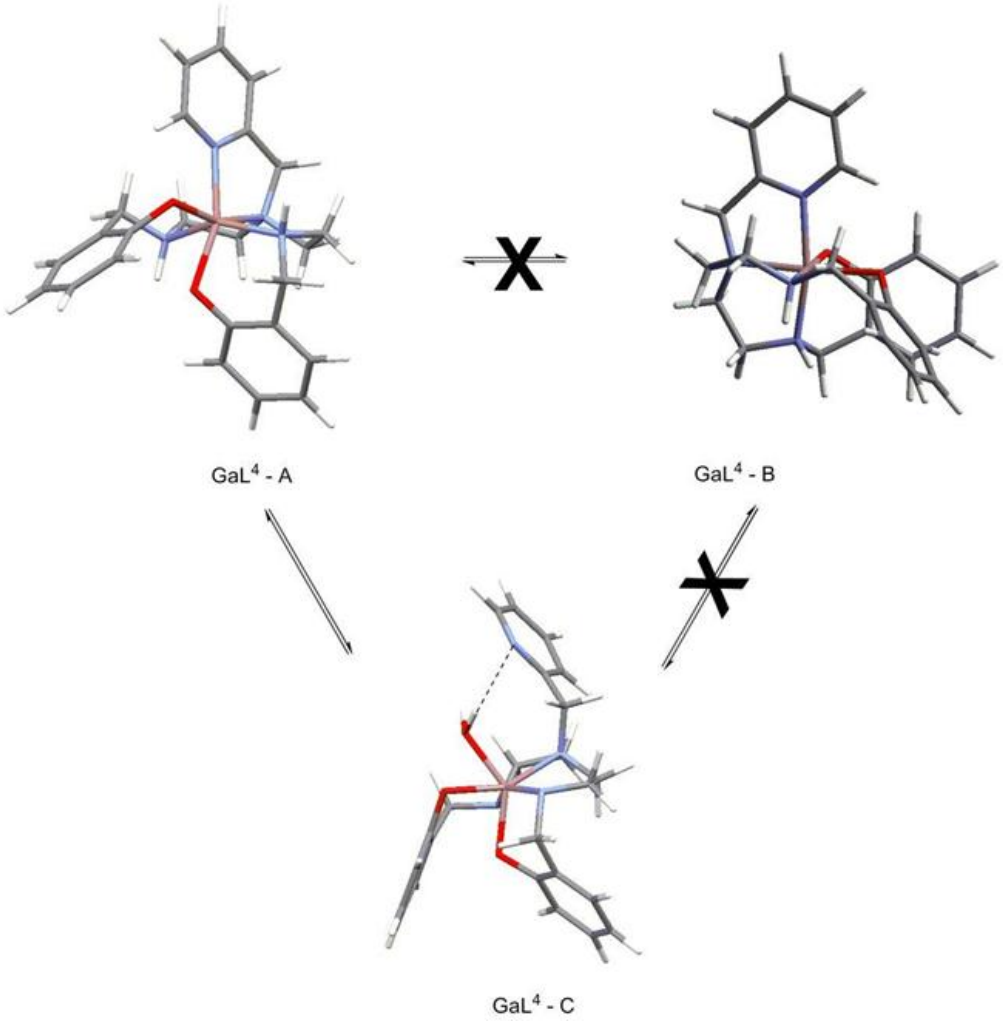

***Figure 5.10: GaL^4** species present in CD_3CN solution.*

The assignment of the diastereotopic methylenic protons in species **A** and **B** was achieved by combining the results of several NMR experiments such as COSY, TOCSY and HSQC (A7 - A9 of the Annex section). The ^{1}H and ^{15}N-NMR chemical shifts of the coordinated NH groups (Figures 5.11 and 5.12) are in general very similar for the three species indicating closely related structures in solution.

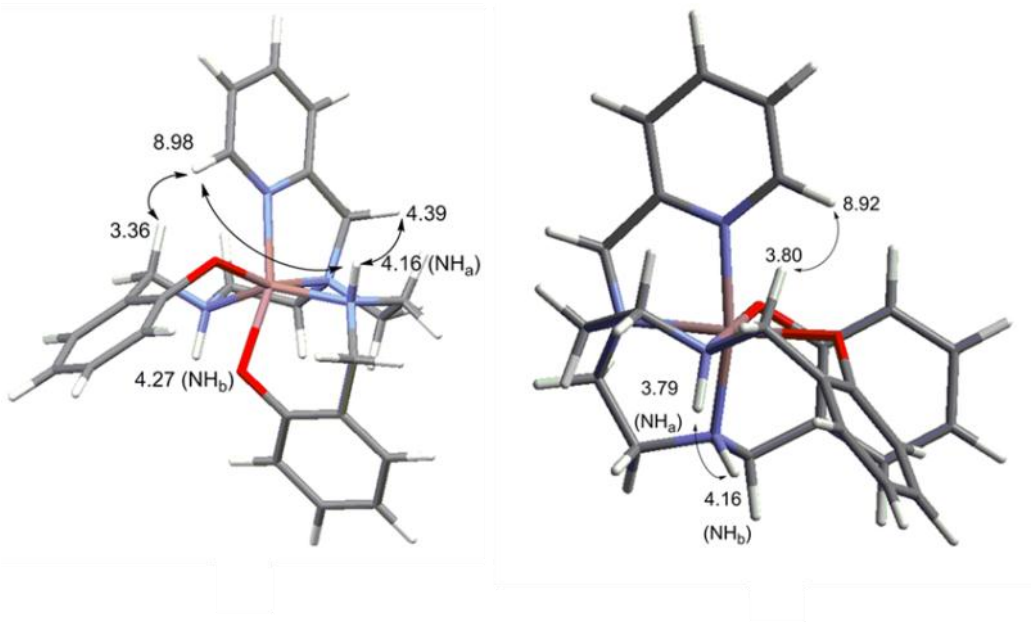

Figure 5.11: *Relevant NOE enhancements used to confirm the* cis-trans *coordination in isomer* ***A*** *(left) and the cis-cis coordination in isomer* ***B*** *(right) of* ***GaL^4*** *in CD_3CN.*

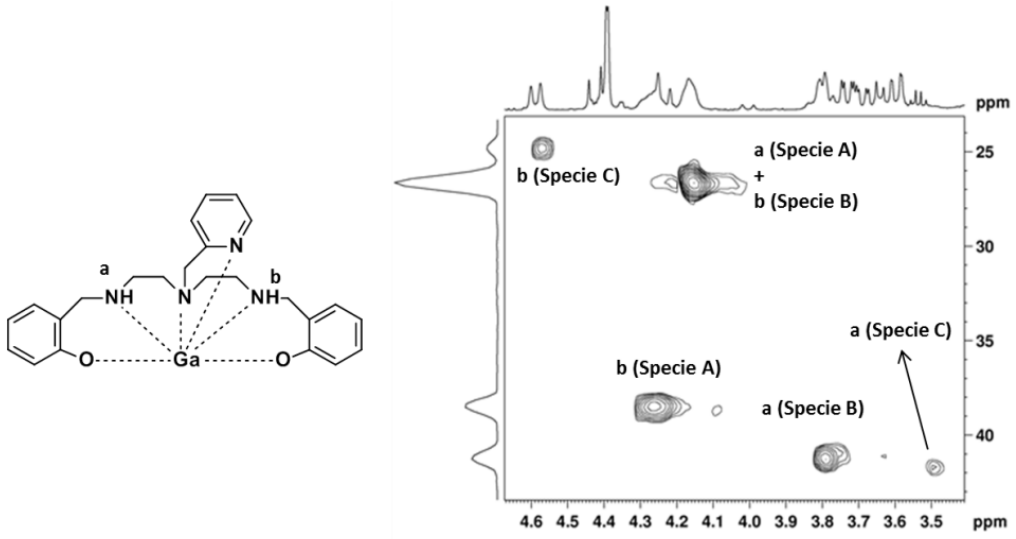

Figure 5.12: *^1H-^{15}N HSQC spectrum of* ***GaL^4*** *in CD_3CN. The NH cross peaks of species* ***A***, ***B*** *and* ***C*** *are assigned.*

For all species, the coordination geometry around the gallium ion is octahedral, as suggested by the careful analysis of the proton-proton correlations in the NOESY spectra (Figure 5.14). The aromatic region of the spectrum shows a long range NOE between proton **a** (Figures 5.11 and 5.12) at 4.16 ppm, and the *ortho* proton of the pyridyl ring in **A**

at 8.97 ppm. In species **B** this proton is correlated with an axial CH_2 proton at 3.80 ppm, from one of the phenolate-containing six-membered chelaing ring.

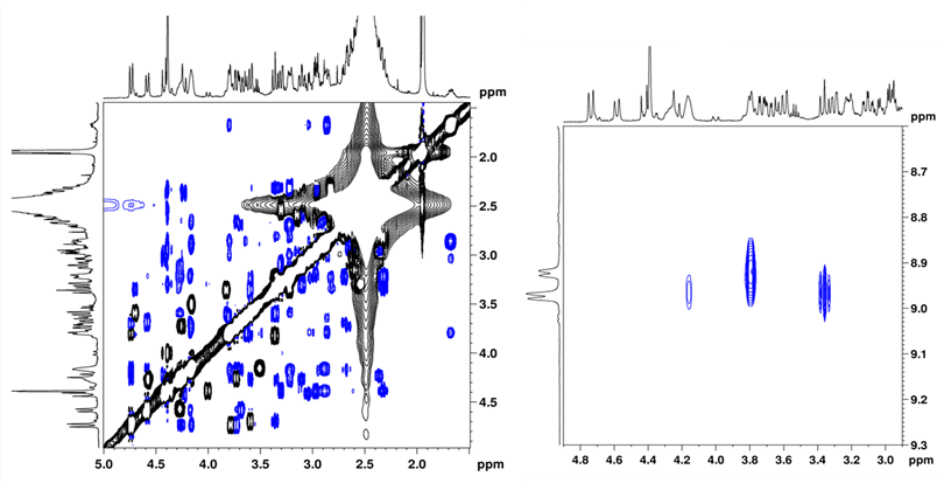

Figure 5.13: *NOESY spectrum of the methylenic protons of* ***GaL^4*** *in CD_3CN (left). The spectrum is dominated by NOE cross peaks of major species* ***A*** *and* ***B*** *in blue. The slow interconversion of species* ***A*** *and* ***C*** *gives rise to the exchange cross peaks in black. NOESY spectrum of the aromatic region of* ***GaL^4*** *in CD_3CN (right).*

In species **A** the pyridyl arm is *trans* to a phenolate oxygen and togheter with the three amine nitrogen donor atoms define two adjacent faces of an octahedral (Figure 5.10). This corresponds to a type of *cis-trans* configuration because one phenolate oxygen is *cis* to the pyridyl arm and the other one is *trans*.

The two-five-membered chelating rings containing the aliphatic amines are arranged in a similar way but one of the NH protons (**a**) lies on the same side as the pyridyl group while the other is pointing downward in the opposite direction (**b**) (Figure 5.11). Thus, proton **a** at 4.16 ppm has a long range NOE with CH_2 of the pyridyl arm resonating at 4.39 ppm while proton **b** at 4.27 ppm does not correlate with these protons. The amine proton **a** has also a very weak cross peak with the pyridyl proton doublet at 8.97 ppm. This *ortho* proton shows another correlation with a CH_2 proton at 3.36 ppm from the phenoxide-containing six-membered ring in the opposite side of the molecule.

The isomer **B** possesses also an octahedral geometry but the pyridyl is *trans* to the **a** proton (Figure 5.11). The other two amine nitrogen atoms and **a** belong to the same face of the octahedron. Proton **b** at 3.79 ppm points downwards relative to the pyridyl arm and is directed towards **a** at 4.16 ppm. Thus, **b** has long range NOE with **a**, and an axial CH_2

proton at 3.80 ppm from one of the phenoxide-containing six-membered chelating ring correlates with the *ortho* proton from the pyrydyl ring at 8.92 ppm (Figures 5.11 and 5.13). All these findings are consistent with solid state molecular structures depicted in Figure 5.5. This isomer **B** is considered of the type *cis-cis* because both phenoxide oxygens are *cis* to the pyridyl.

The NOESY spectrum of **GaL^4** (Figure 5.13) in CD_3CN also shows negative cross peaks as a results of a slow exchange process that interconverts species **A** and **C** (black peaks). The *ortho* proton of the pyridyl ring in species **C** resonates at 8.22 ppm being considerably shifted towards upfield when compared with the same proton (8.92 ppm) in species **A**, and approaching the chemical shift of the ortho pyridyl proton in the free **H_2L^4** (8.45 ppm). These data are consistent with the dissociation of the pyridyl group in **A**, which is most likely accompanied by the coordination of a solvent molecule.

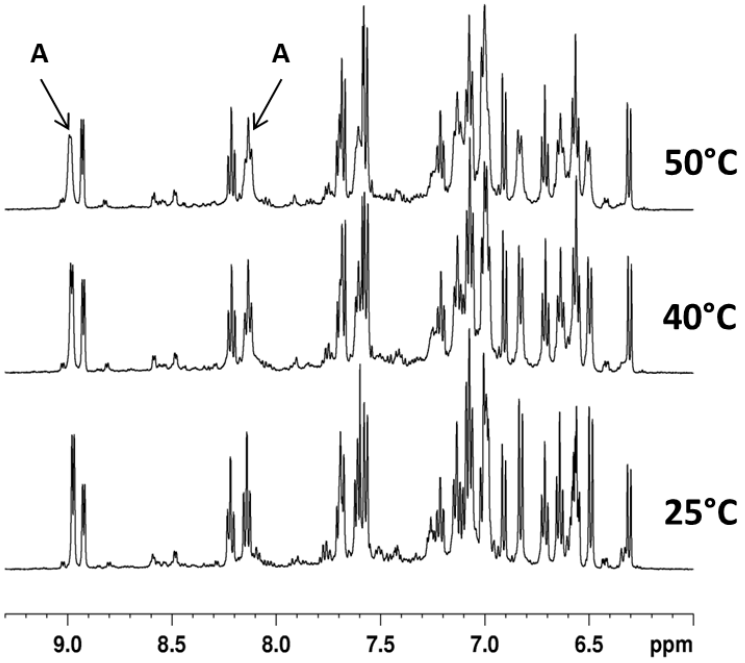

Figure 5.14: *^{1}H-NMR spectra of **GaL^4** in CD_3CN at various temperatures, showing broadening of the sginals for isomers **A** as the temperature is raised.*

Variable temperature ^{1}H-NMR spectra of **GaL^4** in CD_3CN (Figure 5.14) have shown the broadening of the resonances from species **A** with temperature, which further confirms its involvement in an exchange process. Unfortunately, rapid exchange in solution hampered the identification of this solvent molecule by NMR but it is reasoned that

adventitious water is probably replacing the pyridine arm instead of the acetonitrile (Figure 5.10). H_2O is a harder donor ligand than CH_3CN and, therefore, is expected to be a better ligand towards the oxophilic Ga(III). Indeed, the ^{1}H-NMR spectrum of **GaL^4** in D_2O shows that **B** and **C** are the predominant species in aqueous solution (Figure 5.15).

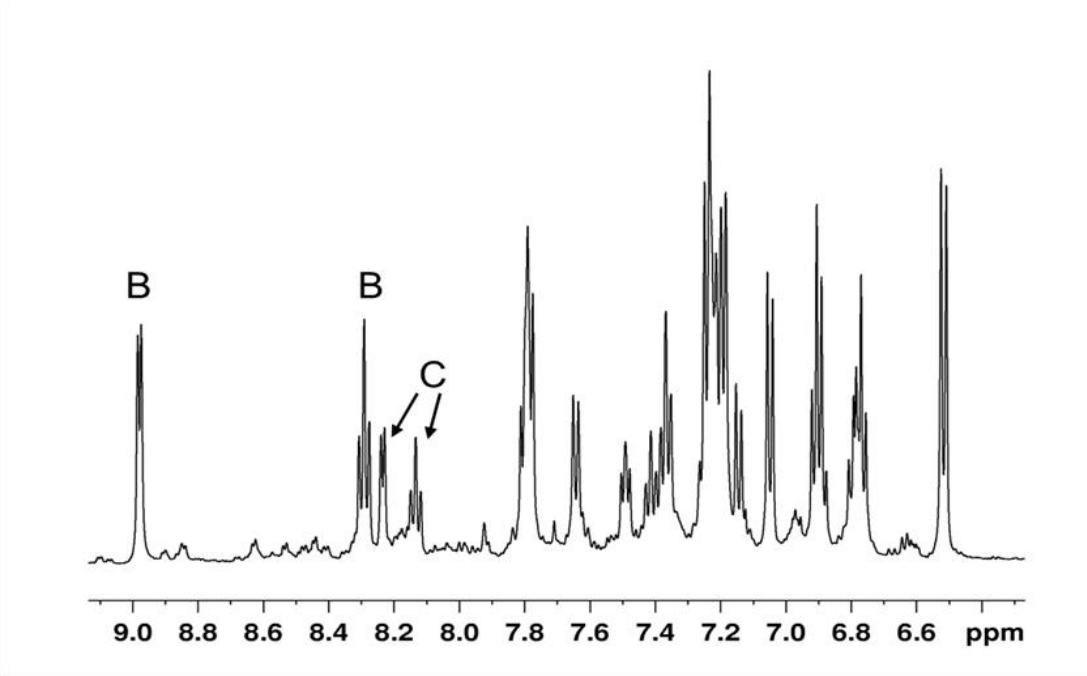

Figure 5.15: *Aromatic region of the ^{1}H-NMR spectra of **GaL^4** in D_2O showing the presence of two major isomers **B** and **C** in a 1:0.7 ratio.*

The NOESY spectrum of **GaL^4** (Figure 5.16) in D_2O also shows negative cross peaks as a result of a slow exchange process that interconverts species **C** and **A**. The variable temperature (Figure 5.17) also confirms the presence of this process.

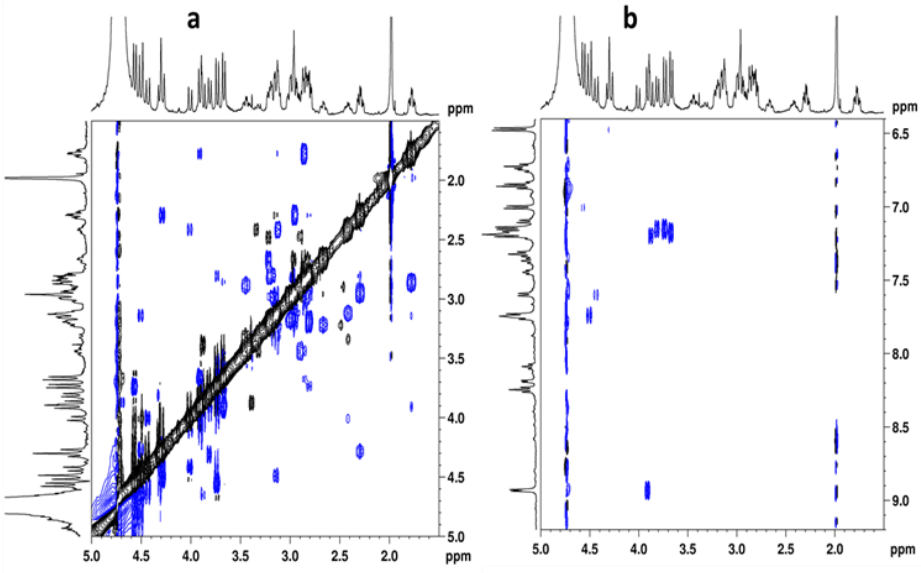

Figure 5.16: a) *Crowded methylenic region of the NOESY spectrum of* ***GaL^4*** *in D_2O. The spectrum is dominated by noe cross peaks of major species* ***B*** *and* ***C*** *in blue. The slow interconversion of species* ***A*** *and* ***C*** *gives rise to the exchange cross peaks (in black).* ***b)*** *Aromatic region of the spectrum. The ortho proton of the pyridyl ring in* ***C*** *at 8.19 ppm shows no long range noe correlations.*

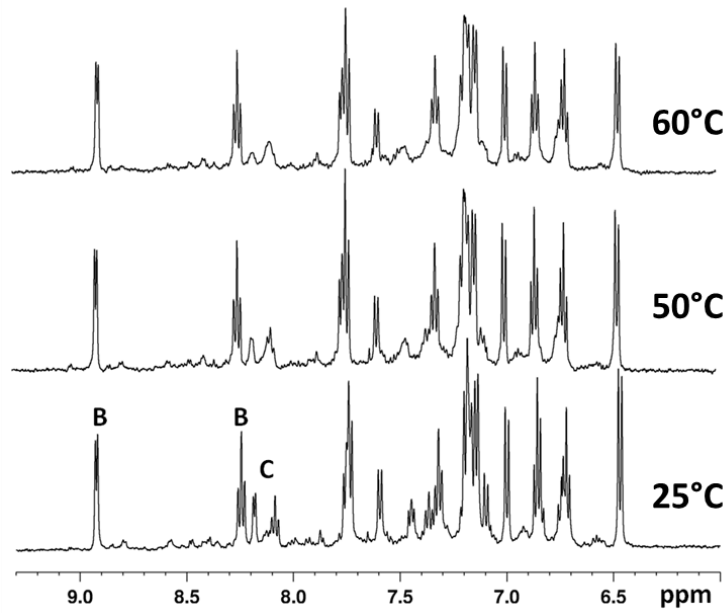

Figure 5.17: *^{1}H-NMR of spectra of* ***GaL^4*** *in D_2O at various temperatures, showing broadening of the signals for* ***C*** *as temperature is raised. Signals from isomer* ***B*** *remain sharp.*

The assignement of the diastereotopic CH_2 protons (Figure 5.18), based on a variety of 2D experiments (A10 - A12 of the Annex section), associated with the fine analysis of the NOESY, confirmed that the structure of **B** is maintained in D_2O solution. Due to deuteration of NH protons and the scarce number of noe contacts observed for **C**, it was not possible to confirm that the ligand arrangement in **C** matches that in **A**. However, the downfield shift of some CH_2 protons in **C** (Figure 5.18) is also observed in **A**, which seems to indicate that the ligand arrangement in these interconverting species is similar. The exception is the presence of a free pyridyl group in **C**, as indicated by the presence of *ortho* protons resonating at 8.19 ppm and with long range noe contacts (Figure 5.16).

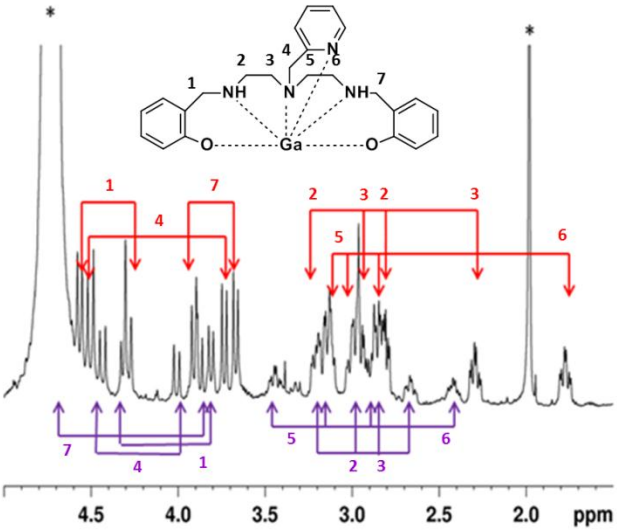

Figure 5.18: *Aliphatic region of the ^{1}H-NMR spectrum of **GaL^4** in D_2O showing the assignment of methylenic protons of **B** in red and **C** in purple. Peaks from solvent and impurities are assigned by an *.*

Despite the presence of two coordination isomers in solution, the ^{71}Ga-NMR spectrum of **GaL^4** in CD_3CN (Figure 5.19) displays a single but relatively broad resonance ($\Delta\nu_{1/2} \approx 5700$ Hz) centered at 102 ppm, which can be attributed to the presence of the same donor-atom set in isomers **A** and **B**. The broadness of the ^{71}Ga signal is higher in the ^{71}Ga-NMR spectra of **GaL^{1,OMe}** (53 ppm, $\Delta\nu_{1/2} \approx 12000$ Hz) and **GaL^2** (68 ppm, $\Delta\nu_{1/2} \approx 12000$ Hz) (Figure 5.19), indicating a larger asymmetry of the coordination environment around Ga(III) in these complexes.

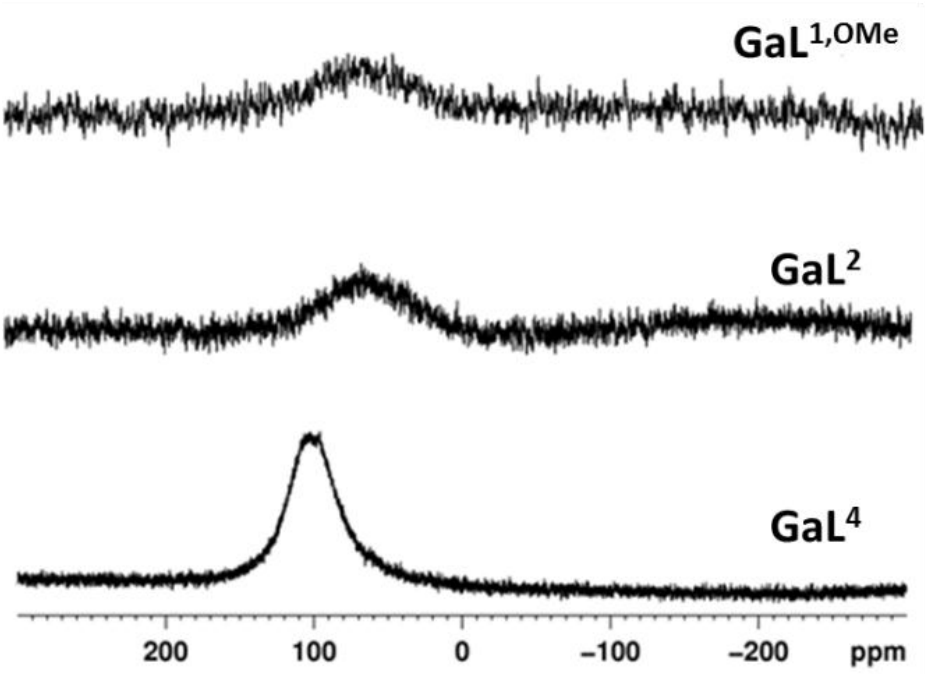

Figure 5.19: *^{71}Ga-NMR spectra of **GaL^{1,OMe}**, **GaL^{2}** and **GaL^{4}** in CD_3CN.*

In summary, the larger *trans* influence of a phenolate oxygen when compared to an aliphatic amine can certainly account that the pyridyl arm is labile in species **A** but not in species **B**.[254,255] Such *trans* effect may also justify the coordination of both phenoxide groups in *cis* position relatively to the pyrazolyl arm in **GaL^{1,OMe}** and **GaL^{2}**, observed either in solution or in the solid state.

5.4 Synthesis, Characterization and Biological evaluation of ^{67}Ga complexes

As seen previously, **H_2L^2** and **H_2L^4** were the only chelators able to coordinate in an intact form the Ga(III) ion, giving well defined complexes that were fully characterized. Therefore, only these chelators were further evaluated with carrier-free ^{67}Ga with the aim of assessing their relevance for radiopharmaceutical applications.

5.4.1 Radiolabeling and *In Vitro* Evaluation Studies

The synthesis of the radiocomplexes was attempted by treating a $^{67}GaCl_3$ solution in acetate buffer (pH ≈ 5) with ethanolic solutions of the chelators (**H_2L^2** and **H_2L^4**).

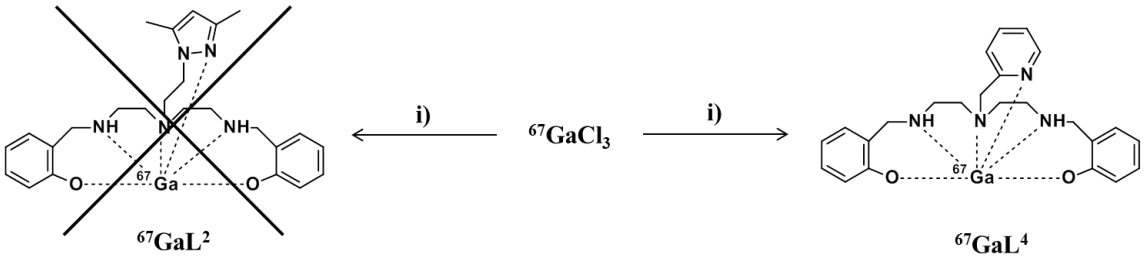

Scheme 5.3: *Radiolabeling of selected N_4O_2-donor chelators with ^{67}Ga.* ***i) H_2L^2/H_2L^4****, $NaCH_3COO$ (pH ≈ 5), EtOH/H_2O.*

For a final $\mathbf{H_2L^4}$ concentration of $5x10^{-5}$ M and after heating at 85 ºC for 15 min, the resulting radiolabeled compound ($\mathbf{^{67}GaL^4}$) was obtained with a radiochemical yield of > 95%, as checked by TLC and HPLC analysis (Figures 5.20 and 5.21, respectively).

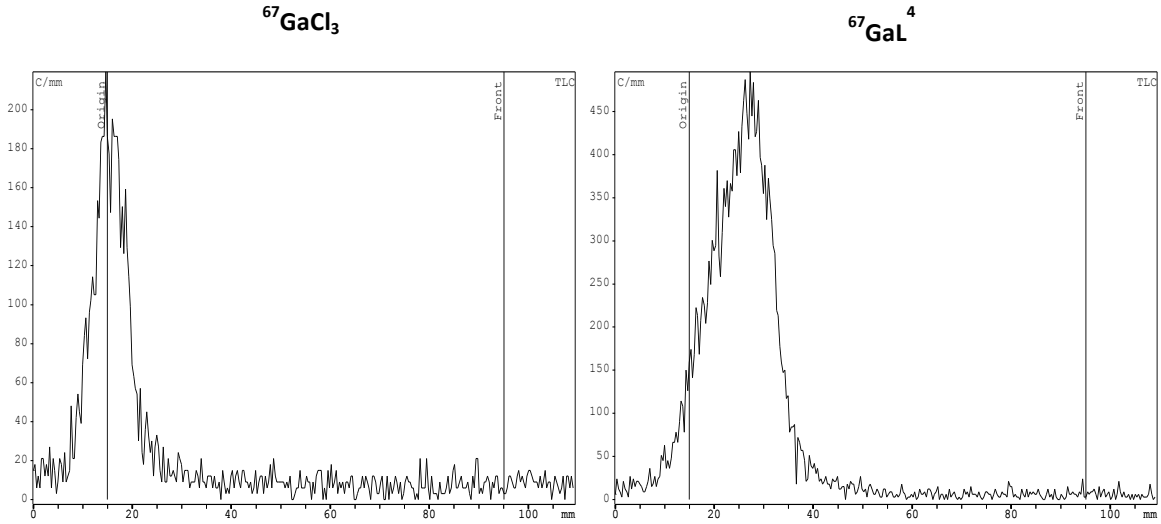

Figure 5.20: *Radiochromatograms of $^{67}GaCl_3$ (R_f = 0) and* ***$^{67}GaL^4$*** *(R_f = 0.2) obtained using RP-TLC plates with MeOH/0.9% NaCl (8:2) as eluent.*

HPLC was also used to assign the chemical identity of the $\mathbf{^{67}GaL^4}$ upon comparison with the natural gallium congener ($\mathbf{GaL^4}$) (Figure 5.21). The HPLC analysis of the reaction mixture has shown the presence of a single radioactive peak (t_R = 18.3 min). This peak was assigned to $\mathbf{^{67}GaL^4}$ since its retention time is well-matched with the one of $\mathbf{GaL^4}$ (t_R = 18.2 min). The slight difference of 0.1 min is due to the flow of the analyte in the HPLC system which passes through the UV detector first, and then through the gamma detector. It is worthwhile to notice that $\mathbf{GaL^4}$ gave rise to a unique peak in the HPLC chromatograms independently of the used elution conditions, which corroborates the

similarities of the physico-chemical properties of its coordination isomers, as discussed previously.

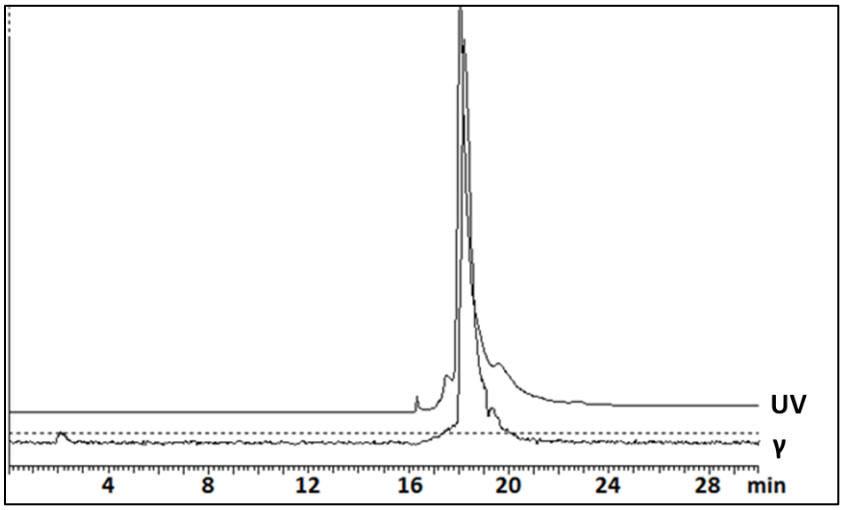

Figure 5.21: *HPLC chromatograms (100-5 C18, 0.9% NaCl/EtOH) of* ***GaL^4*** *(UV detection) and reaction mixture of the radiolabeling of* ***H_2L^4*** *with $^{67}GaCl_3$ (γ detection).*

On contrary to **H_2L^4**, **H_2L^2** provided only very low amounts (< 10%) of the desired radioactive compound (**$^{67}GaL^2$**) even when a final **H_2L^2** concentration as high as ≈ $1x10^{-3}$ M was used (Figure 5.22).

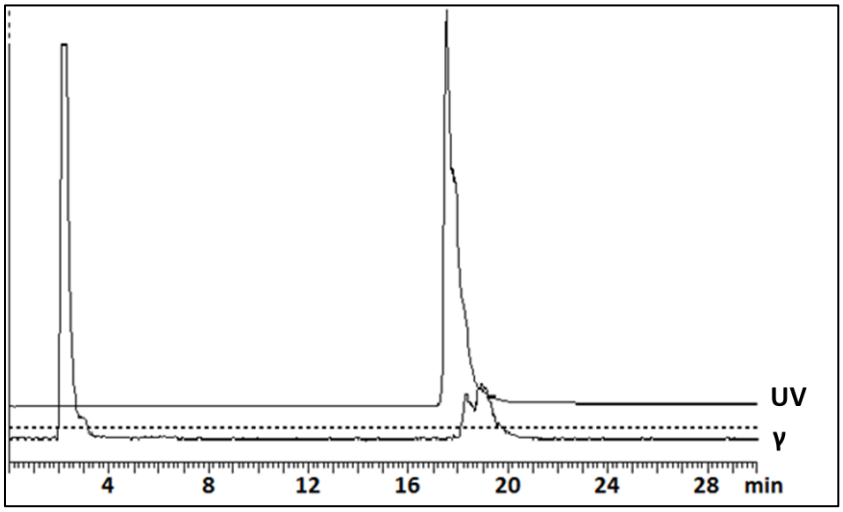

Figure 5.22: *HPLC chromatograms (100-5 C18, 0.9% NaCl/EtOH) of* ***GaL^2*** *(UV detection) and reaction mixture of the radiolabeling of* ***H_2L^2*** *with $^{67}GaCl_3$ (γ detection).*

The reasons that justify the striking differences on the behavior of **H_2L^2** and **H_2L^4** in the reactions with $^{67}GaCl_3$ are no completely clear. Such differences are not explained by

the weaker basicity of the pyrazolyl arm (pKa = 2.5 for protonated pyrazole) if compared with the pyridine arm (pKa = 5.2 for protonated pyrazole),[256] as this implies a larger percentage of non-protonated pyrazole available for complexation to the metal. This must reflect the weaker coordination capability of the pyrazolyl ring, although differences on the stability of the formed five-membered (**H_2L^2**) and six-membered (**H_2L^4**) chelating rings can also play a role.

To have further insight on the interest of **H_2L^4** as a new framework for the design of gallium radiopharmaceuticals, it was proceeded with its *in vitro* evaluation, which comprised the measurement of lipophilicity and challenge experiments with human *apo*-transferrin.

The lipophilicity of compound **$^{67}GaL_4$** was evaluated by determination of the partition coefficient (Log $D_{o/w}$) using the multiple extraction method, which is described in more detail in the experimental section of this thesis.[257] The value of Log $D_{o/w}$ found for **$^{67}GaL_4$** was **-0.53 ± 0.04**, which indicates that the complex is hydrophilic.

As already mentioned, the high affinity of Ga(III) for transferrin explains that radiocomplexes of gallium are usually tested in challenge experiments against this protein, particularly when evaluating new chelator systems, as in the present case. These challenge experiments are useful to predict the *in vivo* kinetic inertness of the complexes towards transchelation reactions. **$^{67}GaL^4$** was incubated with an excess of *apo*-transferrin in the presence of bicarbonate at 37 ºC and the reaction mixture was analyzed by HPLC at different time points, as seen in Figure 5.23. For comparison purposes, *apo*-transferrin was radiolabeled with ^{67}Ga. Briefly, *apo*-transferrin was reacted with $^{67}GaCl_3$ at pH ≈ 7 and incubated for 15 min at 37 ºC. HPLC analysis of the radiolabeled transferrin is depicted in Figure 5.24 along with that of $^{67}GaCl_3$.

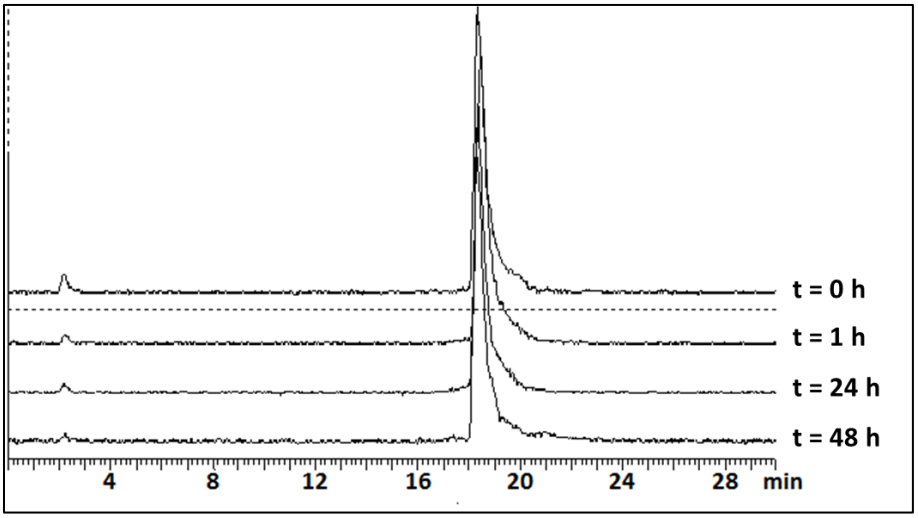

Figure 5.23: *HPLC chromatograms (100-5 C18, 0.9% NaCl/EtOH) of* ***GaL^4*** *in the presence of* apo-*transferrin after 0 h, 1 h, 24 h and 48 h of incubation at 37 ºC.*

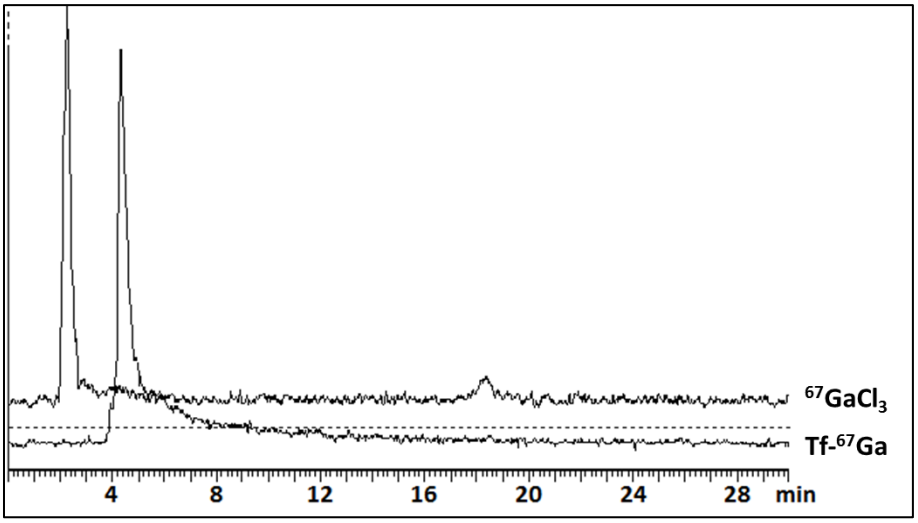

Figure 5.24: *HPLC chromatograms (100-5 C18, 0.9% NaCl/EtOH) of $^{67}GaCl_3$ (t_r = 2.3 min) and ^{67}Ga-labeled apo-transferrin (t_r = 4.3 min).*

No transchelation was observed even after 48 h of incubation, which confirms that **^{67}GaL^4** displays high *in vitro* stability and further corroborates that **H_2L^4** can stabilize Ga(III) under the conditions that are required in the preparation of radiopharmaceuticals.

5.4.2 Biological Studies

To ascertain the biokinetics and *in vivo* stability of **^{67}GaL^4**, biodistribution studies were carried out in CD-1 mice at 1 h and 4 h after intravenous administration. Total

radioactivity excretion was also assessed at both time points. The most relevant data from these studies are summarized in Table 5.6 and Figure 5.25.

^{67}GaL^4 shows a fast blood clearance (0.20 ± 0.08 %ID/g at 1 h p.i.) and a moderately fast overall excretion (35.3 ± 2.4 %ID/g at 1 h p.i.). Noticeably, **^{67}GaL^4** showed a much better blood clearance than ^{67}Ga complexes with pyridyl-containing acyclic chelators that have been recently reported, like the compound ^{67}Ga-dedpa (Figure 1.16) developed by the group of Orvig et al..[87] According to these authors, the retention of ^{67}Ga-dedpa in the blood compartment could be explained by a strong association with serum proteins due to the secondary amine groups of the chelator. However, this is not observed for **^{67}GaL^4** despite the presence of two secondary amines in the structure of the complex.

Table 5.6: *Biodistribution results (mean ± SD, n=3; expressed as %I.D./g of organ) for **^{67}GaL^4** after i.v. administration in CD-1 mice.*

Organ	%I.D./g	
	1 h	4 h
Blood	0.20 ± 0.08	0.20 ± 0.06
Liver	4.3 ± 1.4	4.3 ± 2.5
Intestine	13.2 ± 1.8	12.9 ± 2.6
Spleen	0.29 ± 0.1	0.18 ± 0.04
Heart	0.05 ± 0.01	0.07 ± 0.03
Lung	0.17 ± 0.02	0.14 ± 0.03
Kidney	2.3 ± 0.6	1.8 ± 0.2
Muscle	0.05 ± 0.01	0.03 ± 0.01
Bone	0.06 ± 0.02	0.08 ± 0.01
Stomach	0.14 ± 0.05	0.09 ± 0.04
Brain	0.02 ± 0.00	0.01 ± 0.00
Excretion (%I.D.)	35.3 ± 2.4	41.9 ± 10.2

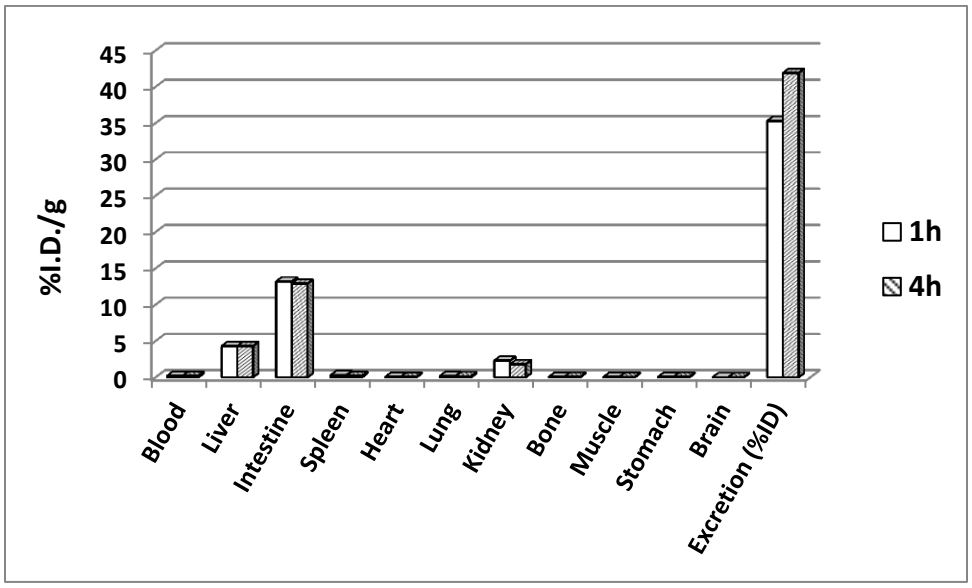

Figure 5.25: *Biodistribution results (mean, n=3; expressed as %I.D./g of organ) of* ^{67}***GaL*^{4}** *after i.v. administration in CD-1 mice.*

In general, ^{67}**GaL**^{4} presented a pronounced clearance from most organs and tissues with the exception of those involved in the excretion of the compound, such as kidney, liver and intestine. In the elimination of the complex there is a significant contribution of the hepatobiliary excretion pathway. In particular, there is a negligible bone uptake (< 0.1 %ID/g at 4 h p.i.), which indicates a high *in vivo* stability for this complex.

The *in vivo* stability of ^{67}**GaL**^{4} was further confirmed by HPLC analysis of the blood serum and urine from the CD-1 mice injected with the radiocomplex. The chromatograms obtained (Figure 5.26) display the presence of a single peak corresponding to that of ^{67}**GaL**^{4} (t_R = 18.2 min).

Altogether, the biodistribution profile of ^{67}**GaL**^{4} is consistent with a remarkably high *in vivo* stability. This might indicate that ^{67}**GaL**^{4} must correspond essentially to the coordination isomer **B**, which has been identified by solid state and NMR structural studies performed with natural gallium. The alternative isomer **A** has shown a rather labile pyridyl arm, which should enable easier transchelation processes with expected slow clearance from blood and background tissues, just the opposite behavior that has been found for ^{67}**GaL**^{4}. In addition, this seems to be consistent with the fact that isomer **B** is the dominant species in D_2O solutions of non-radioactive **GaL**^{4}, as above discussed.

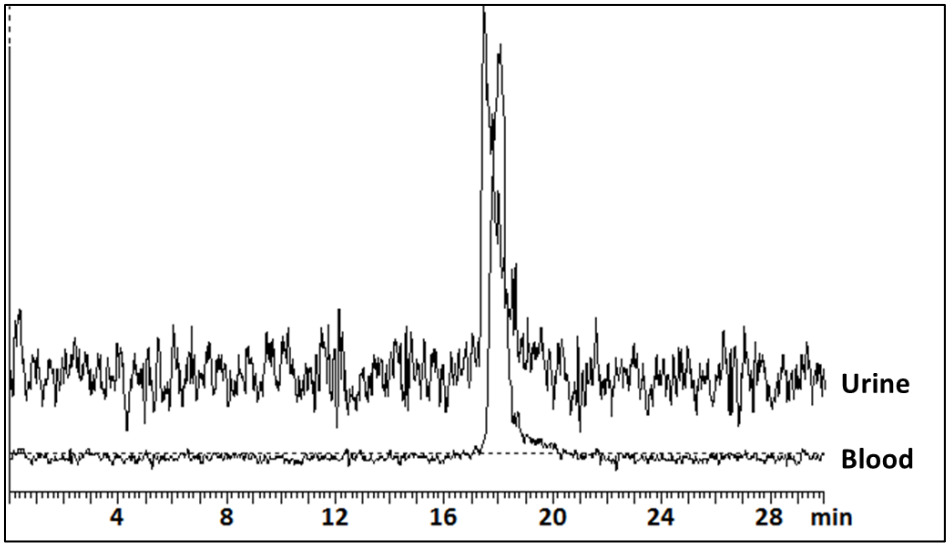

Figure 5.26: *HPLC chromatograms (100-5 C18, 0.9% NaCl/EtOH) of urine and blood serum from CD-1 mice injected with* ***GaL^4*** *at 4 h p.i..*

Chapter 6: Conclusions and Future Perspectives

The main goal of this work was to study new nanosized and molecular tools for the design of gallium radiopharmaceuticals. Having this in mind, two different topics were explored. The first one dealt with the evaluation of the potential of AuNPs, decorated with adequate chelator moieties and functionalized with tumor-seeking vectors, as theranostic tools for the delivery of radiogallium to tumor tissues. The second topic was focused in the evaluation of the coordination properties of new chelators of the N_2O_4-donor type towards Ga(III), aiming to assess their potential for the design of novel gallium radiopharmaceuticals.

AuNPs stabilized with different types of thiolated chelators were developed in this work. The initial approach included the use of a thiol-containing DTPA derivative (**DTDTPA**) to effectively stabilize AuNPs, which successfully afforded small core (2-3 nm) nanoparticles designated **AuNP-DTDTPA**. The studies showed that **AuNP-DTDTPA** can suitably coordinate natural gallium (non radioactive) with a homogeneous distribution of the metal within the **DTDTPA** coating around the AuNP core.

A thioctic acid derivative of BBN (**TA-BBN**) was conjugated to **AuNP-DTDTPA** in order to confer target specificity towards GRPr overexpressing cancer cells. Initial studies with the resulting AuNPs (**BBN- AuNP-DTDTPA**) demonstrated high affinity (IC_{50} ≈ 0.1 μg/mL) of the nanoconstruct towards human prostate PC3 cells.

Radiolabeling with ^{67}Ga of **AuNP-DTDTPA** and **BBN-AuNP-DTDTPA** was achieved with adequate radiochemical yields (85% and 80%, respectively); however, stability studies demonstrated that in certain physiological media, *e.g*. apo-transferrin and cell culture medium, the radiolabeled AuNPs show a high tendency to release the radionuclide. *In vitro* studies showed a low internalization of these AuNPs in PC3 cells with no significant distinction between **AuNP-DTDTPA-^{67}Ga** and **BBN-AuNP-DTDTPA-^{67}Ga**.

Biodistribution studies of **AuNP-DTDTPA-^{67}Ga** in human PC3 xenograft Balb/c mice showed high uptakes in liver and spleen, attributed to the high hydrodynamic size of these AuNPs, and only a slight uptake in the tumor (1.1 ± 0.6 I.D./g at 24 h p.i.). For **BBN-AuNP-DTDTPA-^{67}Ga**, the liver and spleen uptakes were much lower but a significant tumor uptake was observed (5.8 ± 0.7% I.D./g at 24 h p.i.); however, this result might be related to eventual release of ^{67}Ga from the AuNPs *in vivo*. This is in agreement with

stability studies performed *in vitro*, as well as eith the similitude of its biological profile with that of ^{67}Ga-citrate, which undergoes extensive transchelation to circulating transferrin.

Due to the stability issues associated with the use of the **DTDTPA** stabilized AuNPs, macrocyclic chelators were used instead of **DTDTPA**, expecting to ensure more efficient ^{67}Ga coordination in physiological media. For this purpose, a new thiolated DOTA derivative (**TDOTA**) was synthesized, which was able to stabilize small core (4-5 nm) AuNPs. The resulting AuNPs, **AuNP-TDOTA**, were successfully decorated with two BBN derivatives (**TA-BBN** and **C-KKK-BBN**). **TA-BBN** afforded a five times higher amount of conjugated peptide ($8.58x10^{-4}$ mmol) to the AuNPs surface compared with **C-KKK-BBN** ($1.68x10^{-4}$ mmol).

AuNP-TDOTA, **BBN-AuNP-TDOTA** and **CBBN-AuNP-TDOTA** were successfully labeled with ^{67}Ga and the resulting AuNPs displayed good stability properties under physiological conditions, regarding their capacity to maintain ^{67}Ga coordination, especially when compared to the **DTDTPA** stabilized AuNPs (**AuNP-DTDTPA** and **BBN-AuNP-DTDTPA**).

In vitro studies showed a very high internalization of **BBN-AuNP-TDOTA-^{67}Ga** in PC3 cells (> 24% at 15 min) when compared with **AuNP-TDOTA-^{67}Ga** and **CBBN-AuNP-TDOTA-^{67}Ga**. This indicates that the presence of the BBN derivative is enhancing the internalization of the AuNPs into the cells; the fact that **CBBN-AuNP-TDOTA-^{67}Ga** does not display such a high internalization is most likely due to the lower amount of conjugated peptide in its composition which may limit its interaction with the GRPr.

Although **BBN-AuNP-TDOTA-^{67}Ga** displayed a very high internalization in PC3 cells, the blocking studies performed in the presence of BBN did not affect the cell uptake of these AuNPs. However, when evaluated in non-GRPr overexpressing cells, like MCF7 and B16F1, the internalization of these AuNPs is significantly lower.

It has been reported in literature that large sized nanoparticle decorated with targeting molecules can interact with a large number of membrane receptors and hence lead to an easier saturation of these receptors, and consequently inhibiting the interaction of other nanoparticles.[101] Taking into account the relatively large hydrodynamic size of **BBN-AuNP-TDOTA-^{67}Ga** (214.7 nm (PDI = 0.269)), this can be the case of these nanoparticles.

The biodistribution studies in mice of **BBN-AuNP-TDOTA-^{67}Ga** and **CBBN-AuNP-TDOTA-^{67}Ga** showed high uptake in the liver and spleen after i.v. injection, which is characteristic for large sized nanoparticles. A similar amount of radioactivity uptake was observed in the tumor for both nanoconstructs, in a significant degree. It was reasoned that due to the large hydrodynamic size of these AuNPs they are rapidly being uptaken by organs of the RES (e.g liver and spleen), and therefore only a few amount of AuNPs are available to reach the pancreas and tumor site.

The i.p. administration of **BBN-AuNP-TDOTA-^{67}Ga** in tumor bearing mice led to a remarkable difference in the biodistribution profile of these AuNPs, compared with the profile obtained using i.v. administration. The liver, spleen and lung uptakes were significantly decreased, and in contrast, a high uptake in the pancreas was observed (> 9% at 4 h p.i.). After i.p. administration, the congener without peptide, **AuNP-TDOTA-^{67}Ga**, showed a similar biodistribution profile but with a lower uptake in the pancreas. Probably, the higher pancreas uptake found for **BBN-AuNP-TDOTA-^{67}Ga** reflects the presence of the conjugated BBN molecules. However, the tumor uptake for these two nanoconstructs was very similar. This finding points out for the involvement of mechanisms of tumor uptake non-mediated by GRPr, namely those related with the EPR effect.

BBN-AuNP-TDOTA-^{67}Ga displayed very promising *in vitro* biological properties but these did not translate to its *in vivo* profile. One of the major factors that is influencing significantly the *in vivo* biological behavior of these AuNPs is its hydrodynamic size, which is significantly large. The conjugation of PEG molecules to the surface of these AuNPs may effectively decrease their hydrodynamic size and significantly alter its biological profile by reducing its uptake by the RES organs, providing a more suitable biodistribution for radioimaging applications. Additionally, the suitability of DOTA to coordinate a variety of medically relevant d- and f- transition elements, like trivalent radiometals (e.g. ^{111}In or ^{90}Y) for nuclear medicine applications or gadolinium for MRI, encourages the further evaluation of **BBN-AuNP-TDOTA** in the design of multiomodal tools for cancer theranostics.

GE11-containing AuNPs were synthesized in this PhD work with the intent of obtaining nanoconstructs for the delivery of radiogallium to EGFr-positive cancers. For this purpose, it has been designed a new multifunctional DOTA derivative, **TA-GE11-DOTA**, containing a dithiotic moiety for coupling to the AuNP surface and the GE-11 peptide

sequence. Initially, it has been synthesized the PEGylated nanoconstruct **PEG-AuNP-GE11-DOTA**, which displayed the lowest hydrodynamic size (49.26 nm (PDI = 0.382)) of all the nanoparticles studied in this thesis. This would make it an interesting candidate for biomedical applications, since their lower hydrodynamic size could eventually minimize their uptake by the RES organs. However, it was not possible to successfully radiolabel these AuNPs with ^{67}Ga after several different attempts, most likely due to the low amount of available **TA-GE11-DOTA** in the nanoparticle surface.

In alternative, it has been studied the conjugation of **TA-GE11-DOTA** to **AuNP-DTDTPA**. The resulting AuNPs (**DTAu-GE11-DOTA** and **Pre-DTAu-GE11-DOTA**) displayed similar physico-chemical properties to those of BBN loaded **DTDTPA**-stabilized AuNPs, in regard to their hydrodynamic size and zeta-potential. The corresponding radiolabeled AuNPs, **DTAu-GE11-DOTA-^{67}Ga** and **Pre-DTAu-GE11-DOTA-^{67}Ga**, were obtained based on the post- and pre-labeling approaches, respectively. **DTAu-GE11-DOTA-^{67}Ga** showed a poorer ability to maintain ^{67}Ga coordination, in the presence of different challenging media. This difference certainly reflects the use of two different methodologies in the radiolabeling of these nanoconstructs. In the post-labeling approach, a significant part of ^{67}Ga is most likely coordinated by the **DTDTPA** molecules, while in the case of the pre-labeling approach the coordination to the metal is done exclusively, in a well-defined way, by the DOTA chelating unit, affording more inert and stable ^{67}Ga complexes.

Cell studies of nanoconstructs **DTAu-GE11-DOTA-^{67}Ga** and **Pre-DTAu-GE11-DOTA-^{67}Ga** have showed significant cellular internalization in EGFr expressing cells. The highest uptake was obtained for **DTAu-GE11-DOTA-^{67}Ga** (> 70% at 3 h), in agreement with the higher amount of conjugated GE11 derivative; however, blocking studies with EGF indicated that the uptake of **Pre-DTAu-GE11-DOTA-^{67}Ga** is more affected by the presence of EGF, which points out for a more probable involvement of an EGFr-mediated mechanism of uptake in the case of these AuNPs.

The significant cellular uptake of **Pre-DTAu-GE11-DOTA-^{67}Ga,** mediated apparently by the interaction with EGFr, together with its high *in vitro* and *in vivo* stability towards release of radiogallium, indicates that this radiolabeled nanoconstruct has favorable features to be further investigated for the targeted delivery of gallium to EGFr-expressing tumors. In the next future, further studies with these AuNPs will include biodistribution in A431 xenograft mice. Moreover, it will be performed the measurement of

the binding affinity of the non-radioactive counterparts by competition binding assays using radioiodinated EGF, as well as Western blot assays to verify any effect of these AuNPs in EGFr phosphorylation.

As demonstrated in this PhD thesis, **AuNP-DTDTPA** can be easily functionalized with dithiotic-containing biomolecules through formation of Au-S bonds. Moreover, recent reports have also shown that the **AuNP-DTDTPA** platform can be decorated with biologically relevant molecules by conjugation to the carboxylic acids of the **DTDTPA** coating through formation of amide bonds.[258] This approach may pave the way for the development of AuNPs stabilized with the **DTDTPA** moiety and functionalized with a variety of target specific vectors, while maintaining the capability to be functionalized with thiolated radioactive chelates. It is worth mentioning, that the new chelator **TDOTA** might be an interesting choice to provide the stable attachment of biomedically relevant metals to the **AuNP-DTDTPA** platform. In summary, the use of **AuNP-DTDTPA,** in combination with the pre-labelling approach, offers many possibilities for the design of nanoradiopharmaceuticals for cancer theranostics.

Finally, new N_4O_2-donor Schiff base chelators (**H_2L^1** and **H_2L^3**) and the reduced counterparts (**H_2L^2** and **H_2L^4**) were obtained based on the dien backbone and by introducing pyrazolyl and pyridyl arms at the central nitrogen atom. The coordination behavior towards Ga(III) was evaluated for all these chelators in order to assess their suitability for the design of gallium radiopharmaceuticals.

For the Schiff base chelators, the reactions performed at macroscopic level were accompanied by transformation of the ligands. In the case of **H_2L^1**, the unique gallium complex that was isolated and characterized was **$GaL^{1,OMe}$**, which corresponds to a relatively rare example of a metal complex containing a O-methyl hemiaminal derivative whose structure has been confirmed by solid state X-ray diffraction analysis.

These results confirm the well known tendency of Schiff base ligands to undergo nucleophilic addition reactions at the imine functions, which may hamper their use in radiopharmaceutical research, as observed herein for **H_2L^1** and **H_2L^3**.

The amine derivatives, **H_2L^2** and **H_2L^4**, afforded the expected complexes **GaL^2** and **GaL^4**, respectively, containing N_4O_2-hexadentate ligands, as confirmed by X-ray diffraction

analysis. The presence of a pyrazolyl ($\mathbf{H_2L^2}$) or a pyridyl ($\mathbf{H_2L^4}$) arm on the ligand framework strongly influences the solution behavior of the complexes and the possibility of preparing the radioactive congeners using ^{67}Ga. In fact, $\mathbf{^{67}GaL^4}$ was obtained in almost quantitative radiochemical yield using relatively low chelator concentration, while $\mathbf{^{67}GaL^2}$ was hardly formed even using a 50-fold higher concentration of $\mathbf{H_2L^2}$. Such differences eventually reflect he poorer electron-releasing properties and the larger flexibility of the pyrazolyl arm that forms six-membered chelating rings, on contrary to the pyridyl arm that forms more stable five-membered chelating rings.

$\mathbf{^{67}GaL^4}$ has shown a favourable biodistribution profile in mice, consistent with a remarkably high *in vivo* stability. It was reasoned that $\mathbf{H_2L^4}$ has the necessary requisites to be used in the development of gallium radiopharmaceuticals. It may have relevance for the design of perfusion agents, e.g. for cardiac imaging, as different substituents can be introduced at the secondary amine, pyridyl and phenolate rings to tune the lipophilicity of the corresponding gallium complex. However, the $\mathbf{H_2L^4}$ backbone can also be explored to design bifucntional chelators for target-specific radiopharmaceuticals because the pyridyl ring is easily replaceable by picolinic acid derivatives presenting carboxylic groups for linkage to targeting biomolecules.

Altogether, these results highlighted that the combination of the dien framework with N-heterocyclic and phenol coordinating groups can provide N_4O_2-donor chelators suitable to stabilize Ga(III) complexes for *in vivo* studies. The encouraging results obtained for $\mathbf{H_2L^4}$ justify further studies aiming at a better understanding of the structural factors (e.g. nature of the N-heterocyclic group and spacer length) that determine the performance of this type of compounds as chelators for the design of radiopharmaceuticals.

Chapter 7: Experimental Section

7.1 Solvents and reagents

Handling of air- and/or moisture-sensitive compounds was performed in an inert atmosphere, using vacuum lines and Schlenk techniques.

All commercially acquired chemical reagents and solvents were of pro-analysis quality, and were used without any additional purification.

Solvents were dried and distilled in accordance to literature[259]:

- THF distilled in the presence of sodium/benzophenone
- CH_2Cl_2 and CH_3CN distilled in the presence of calcium hydride.
- MeOH distilled in the presence of metallic magnesium and molecular iodine.

The solvents were stored under N_2 atmosphere and kept over 4 Å molecular sieves or 3 Å molecular sieves in the case of CH_3CN.

7.2 Analytical Techniques

7.2.1 Nuclear Magnetic Resonance Spectroscopy (NMR)

The ^{1}H and ^{13}C NMR spectra of organic compounds and ligands were recorded on a Varian Unity operating at 300 and 75 MHz, respectively. The ^{1}H, ^{13}C, ^{71}Ga and ^{15}N NMR spectra of the Ga(III) complexes were recorded on a Bruker Avance III spectrometer operating at 500, 125, 152 and 50 MHz, respectively. Chemical shifts of ^{1}H and ^{13}C spectra (δ, ppm) are reported relative to the residual solvent peaks relative to $SiMe_4$. Spectra in D_2O are referenced to trimethylsilyl propionate (TSP). For ^{71}Ga and ^{15}N spectra, external references were used: $Ga(NO_3)_3$ in D_2O (δ = 0 ppm) and neat CH_3NO_2 (δ = 381.7 ppm relative to liquid NH_3), respectively. The peak assignments in the spectra of the Ga(III) complexes were achieved via the use of COSY, TOCSY, HSQC, NOESY and selective NOEs at 500 MHz. The NMR characterization of the Ga(III) complexes was done in collaboration with Prof. José R. Ascenso and Dr. M. João Ferreira from CQE/IST.

7.2.2 Infra-red Spectroscopy (IR)

IR spectra were recorded as KBr pellets in a Bruker Tensor 27 spectrometer.

7.2.3 Mass Spectroscopy (MS)

Mass spectra were done in an ESI/QITMS Bruker HCT by Dr.Joaquim Marçalo and Dr.Célia Fernandes (CTN/IST), using electrospray ionization in positive ion mode

7.2.4 Elemental Analysis (CHN)

Elemental analyses were performed by Vânia Sousa (CTN/IST), in an automated analyzer EA 110 CE Instruments.

7.2.5 X-ray Diffraction

Crystals of the Ga(III) complexes suitable for X-ray diffraction analysis were mounted on a loop with protective oil. The X-ray diffraction data were collected on a Bruker APEXII CCD diffractometer using graphite monochromated Mo-Kα radiation (λ = 0.71069 Å), equipped with an Oxford Cryosystems low-temperature device at 150 K, operated in the ω and φ scans mode. A summary of the crystal data, structure solution and refinement parameters are given in the Annex Section (A13). A semi empirical absorption correction was carried out using SADABS.[260] Data collection, cell refinement and data reduction were done with the SMART and SAINT programs.[261] The structures were solved by direct methods using SIR97[262] and refined by full-matrix least-squares methods with the SHELXL97[263] program using the WINGX[264] software package. A full-matrix least-squares refinement was used for the non-hydrogen atoms with anisotropic thermal parameters. All hydrogen atoms connected to carbons were inserted in idealized positions and allowed to refine riding in the parent carbon atom; hydrogen atoms bonded to nitrogen atoms were located in a difference map. Molecular graphics were prepared using MERCURY 1.4.2..[265] X-ray diffraction analysis were performed by Dr.Isabel C. Santos (CTN/IST).

7.2.6 UV-Vis Spectroscopy

UV-Vis spectra were recorded at room temperature using a Varian Cary 50 UV/Vis spectrophotometer in disposable or quartz cuvettes with a 10 mm path length.

7.2.7 Inductive Coupled Plasma – Optical Emission Spectrometry (ICP-OES)

The samples for ICP-OES analysis were initially digested in *aqua regia* and submitted to microwave heating. The ICP-OES measurements were performed on a Varian Vista – Pro CCD simultaneous inductively coupled plasma – optical emission spectrometer. ICP-OES analysis were performed in the Laboratório de Análises of IST by Eng. Miguel Baião and Eng. Mário Dias.

7.2.8 Atomic Absorption Spectrometry (AAS)

Samples for AAS were initially digested in *aqua regia*. The AAS measurements were performed in a Perkin Elmer (Norwalk, CT) Model 5100 atomic absorption spectrometer with graphite furnace.

7.2.9 Transmission Electron Microscopy (TEM)

TEM images were obtained on a JOEL 1400 transmission electron microscope, JEOL, LTD., Tokyo, Japan. TEM samples were prepared by placing 5 µL of nanoparticle solution on a 300 mesh carbon coated copper grid allowed to dry. The average size and size distribution of the nanoparticles were determined by processing the TEM image in Adobe Photoshop with Fovea Pro plug-in.

7.2.10 Scanning Transmission Electron Microscopy (STEM) and High Angle Annular Dark Field (HAADF), Energy-Dispersive X-ray Spectroscopy (EDS) and Electron Energy Loss Spectroscopy (EELS)

The samples were prepared by placing 5 µL of nanoparticle solution on a 300 mesh carbon coated copper grid allowed to dry

STEM images in-tandem with HAADF were obtained on a FEI Tecnai F30 G2 Twin Microscope (300 kV), Hillsboro, Oregon 97124 USA. EDS spectra were performed with a FEI Quanta 600 FEG Extended Vaccum Scanning Electron Microscope. EELS analyses were performed with a probe corrected JEM-ARM200cF at 200 kV.

The analyses were performed at Florida State University by Dr.Wen Ritts.

7.2.11 Dynamic Light Scattering (DLS) and Zeta-Potential Measurements

Samples were prepared by dissolving the AuNPs in H_2O in a final concentration of $8x10^{-2}$ mg/mL, and placed in a clear disposable zeta cell. DLS and zeta-potential measurements were performed in a Malvern Zetasizer ZS (Malvern Instruments Ltd. USA) equipped with a 633-nm He-Ne laser and operating at an angle of 173º. The data collected were analyzed using the Dispersion Technology Software version 5.10 from Malvern. The intensity of size distribution, the Z-average diameter and the PDI were obtained from the autocorrelation function using the "general purpose mode" for all nanoparticle samples. The zeta-potential measurements were obtained using a combination of electrophoresis and laser Doppler velocimetry, with acquisition in Huckel

7.2.12 Nanoparticle Tracking Analysis (NTA)

NTA analysis was performed in a Nanosoght LM10-HSGFT system configured with a temperature controlled LM14G sample viewing unit equipped with a 535 nm (green) laser (NanoSight Limited, Amesbury, UK). Video tracking of the nanoparticles based on Raleigh scattering was captured with a monochrome Marlin CCD camera (Allied Vision Technologies, Germany). A 1 mL syringe (Becton Dickinson, NJ) was used to deliver the samples to the viewing chamber and the temperature was held constant at 22 ºC. nanoSight 2.2 program was used to collect and analyze the sample data. The samples were diluted 30-fold relatie to the stock AuNP concentration prior to NTA measurements. This dilution was selected such that ≈ 900 nanoparticles were tracked in a 30 second video.

7.2.13 X-ray Photoelectron Spectroscopy (XPS)

XPS analysis of **AuNP-DTDTPA-Ga** was performed using a Kratos Axis His XPS instrument. A solution of the nanoparticles was placed onto a piece of clean silicon wafer and allowed to dry and then measured in a 90º take-off-angle (TOA) yielding a sampling depth of ≈ 10 nm. The analyses were performed with a monochromatic Al kα X-ray source powered at 15 kV and 15 mA. Energy scales of the spectra are referenced to the C2s C-C/C-H signal at 285.0 eV.

XPS analysis of **BBN-AuNP-DTDTPA** was performed by Rocky Mountain Labs Inc., Colorado, USA.

XPS analysis of **AuNP-TDOTA** was performed in a Kratos XSAM800 spectrometer, operated in the fixed analyser transmission (FAT) mode, with a pass energy of 20 eV, a power of 120 W and using non-monochromatic Al Kα and Mg Kα radiations (hv = 1486.6 eV and 1253.6 eV, respectively). Spectra were collected with a step of 0.1 eV, using a Sun SPARC Station 4 with Vision software from Kratos. X-ray source satellites were subtracted and Shirley backgrounds were used. The analyses were peformed by Dr.Ana Maria Botelho do Rego (IST) and Dr.Ana Ferraria (IST).

7.2.14 High Performance Liquid Chromatography (HPLC)

The HPLC analyses were performed in a Perkin-Elmer LC200 pump with a UV-Vis Shimadzu LC290 and a Berthold LB-507A γ-detector. The solvents used were HPLC grade; H_2O was bidistilled and filtered in 0.22 μm milipore filters.

General conditions of the HPLC analyses performed in this thesis:

Column: Macherey-Nagel EC 250/4 Nucleosil 100-10 C18 (or 100-5 C18).

Flow: 1.0 mL/min (or 0.5 mL/min for column 100-5 C18).

UV detection: 280 nm for the peptides, 220 nm for the gallium complexes.

7.2.14.1 HPLC analysis of peptides

The supernatants and control solutions of the peptides used in the synthesis of the peptide-conjugated AuNPs were analysed using different HPLC gradient elution conditions, as described below.

i) BBN-AuNP-DTDTPA, **BBN-AuNP-TDOTA** and **PEG-AuNP-GE11-DOTA**:

Method 1 - Eluents: A – TFA 0.1% (aqueous); B – CH_3CN.

Step	t (min)	A (%)	B (%)	Curve
0	5.0	100	-	-
1	3.0	100	-	-
2	0.1	75	25	1
3	5.9	75	25	-
4	0.1	66	34	1
5	5.9	-	100	1

t_R (**TA-BBN**) = 10.92 min

t_R (**TA-GE11-DOTA**) = 8.41 min

ii) CBBN-AuNP-TDOTA, **DTAu-GE11-DOTA** and **Pre-DTAu-GE11-DOTA:**

Method 2 - Eluents: A – TFA 0.1% (aqueous); B – CH_3CN.

Step	t (min)	A (%)	B (%)	Curve
0	5.0	100	-	-
1	5.0	100	-	-
2	10	-	100	1
3	10	-	100	-

t_R (**C-KKK-BBN**) = 4.64 min

t_R (**TA-GE11-DOTA**) = 15.23 min

7.2.16.2 HPLC Analysis of Gallium Complexes:

Method 3 - Eluents: A – NaCl 0.9% (aqueous); B – EtOH.

Step	t (min)	A (%)	B (%)	Curve
0	5.0	100	-	-
1	10	100	-	-
2	5	-	100	1
3	5	-	100	-
4	1	100	-	1
5	4	100	-	0

7.2.15 Thin Layer Chromatography (TLC)

TLC analyses of reaction mixtures were done in silica-gel 0.25 mm, in aluminum support (Merck). The chromatograms were revealed with UV radiation at a wavelength of 254 nm, or in an iodine chamber.

TLC analyses of radiolabelled compounds were performed in ITLC-SG (Agilent Technologies) or RP-TLC (Macharey-Nagel). The radiochromatograms were revealed in a Raytest γ-miniGITA TLC scanner.

7.3 Synthetic Protocols and Characterization of Molecular Compounds and Nanoparticles

7.3.1 Synthesis and Characterization of the Organic Compounds

7.3.1.1 2-[bis[2-[carboxymethyl-[2-oxo-2-(2-sulfanylethylamino)ethyl]amino]ethyl] amino]acetic acid (DTDTPA)[208]

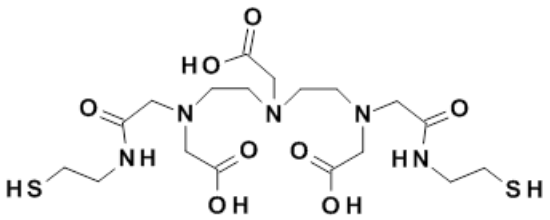

In a round bottom flask, 2 g (5.6 mmol) of DTPA-bis(anhydride) were dissolved in 40 mL of DMF and heated to 70 ºC. 1.4 g (12.3 mmol) of aminoethanehiol dissolved in 15

mL of DMF and 1.74 mL of triethylamine, were added. The resulting mixture was left to stir at 70 ºC overnight. The mixture was cooled to room temperature and placed in a freezer until formation of a white precipitate (NEt_3·HCl) was observed. The solution was filtered and the filtrate was concentrated at low pressure. 20 mL of $CHCl_3$ were added to the filtrate which led to the formation of a white powder. After filtration, the white powder was washed with $CHCl_3$ and dried under vacuum.

Yield: 1.89 g (66%).

ESI-MS: m/z calcd for $[M+H]^+$ 403.2; found 403.3.

^{1}H-NMR ($CDCl_3$): δ_H 2.90 (4H, t, 2-CH_2), 3.26 (4H, t, 2-CH_2), 3.46 (4H, t, 2-CH_2), 3.56 (4H, t, 2-CH_2), 3.76 (2H, s, CH_2), 4.04 (4H, s, 2-CH_2), 4.08 (4H, s, 2-CH_2).

^{13}C-NMR ($CDCl_3$): δ_c 36.92 (CH_2), 38.01 (CH_2), 50.23 (CH_2), 52.08 (CH_2), 52.87 (CH_2), 55.02 (CH_2), 56.22 (CH_2), 167.22 (C=O), 169.76 (C=O), 171.95 (C=O).

7.3.1.2 Tert-butyl N-(2-bromoethyl)carbamate (1)[266]

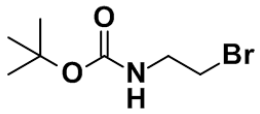

4 g (19.5 mmol) of 2-bromoethanamine·HBr were dissolved in 60 mL of 1,4-dioxane. 6 mL (43.0 mmol) of triethylamine were added and the mixture was stirred for 10 min. A solution of 6.8 g (31.2 mmol) of tert-butoxycarbonyl tert-butyl carbonate in 20 mL of 1,4-dioxane was added slowly at room temperature and the mixture was stirred overnight. The solvent was removed at reduced pressure and the compound redissolved in CH_2Cl_2 and then washed with H_2O. The solvent was removed under vacuum.

Yield: 3.9 g (89%).

^{1}H-NMR ($CDCl_3$): δ_H 1.39 (9H, s, 3-CH_3), 3.40 (2H, t, CH_2), 3.47 (2H, t, CH_2).

7.3.1.3 Tert-butyl N-[2-(1,4,7,10-tetrazacyclododec-1-yl)ethyl]carbamate (2)[267]

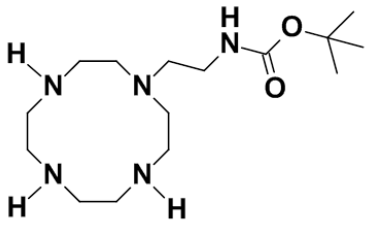

1.0 g (4.5 mmol) of **1** was added to a stirring solution of 1.92 g (11.1 mmol) of cyclen in 60 mL of dry toluene and the mixture was refluxed overnight under N_2. The solution was extracted with 3 x 100 mL of H_2O. The aqueous layer was extracted with 3 x 75 mL of CH_2Cl_2 and the combined CH_2Cl_2 extracts were dried over $MgSO_4$. The solvent was evaporated at reduced pressure and the compound washed with diethyl ether and then dried again under reduced pressure.

Yield: 652 mg (45%).

^{1}H-NMR ($CDCl_3$): δ_H 1.28 (9H, s, -C(CH_3)$_3$), 2.43 (14H, b, 7-CH_2), 2.69 (4H, b, 2-CH_2), 3.05 (2H, b, CH_2), 5.61 (1H, s, NH).

^{13}C-NMR ($CDCl_3$): δ_c 25.13 (CH_3), 38.15 (CH_2), 45.65 (CH_2), 46.73 (CH_2), 47.36 (CH_2), 51.64 (CH_2), 53.76 (CH_2), 78.41 (C(CH_3)$_3$), 155.70 (C=O).

7.3.1.4 Methyl 2-[4-[2-(tert-butoxycarbonylamino)ethyl]-7,10-bis(2-methoxy-2-oxo-ethyl)-1,4,7,10-tetrazacyclododec-1 yl]acetate (3)[268]

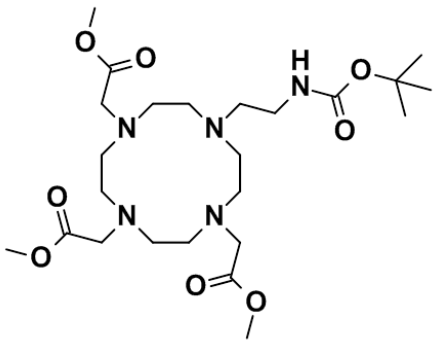

A solution of **2** (600.0 mg, 1.9 mmol), Na_2CO_3 (1.6 mg, 15.2 mmol) and methylbromoacetate (0.65 mL, 6.65 mmol) in 70 mL of CH_3CN was stirred at 70 ºC

overnight. The solvent was evaporated under low pressure and the residue was dissolved in 20 mL of CH_2Cl_2. The solution was filtered and the filtrate was evaporated under reduced pressure and purified by column chromatography (silica gel, 5% MeOH in CH_2Cl_2, R_f = 0.4).

Yield: 810 mg (82%).

ESI-MS: m/z calcd for $[M+H]^+$ 532.3, found 532.3.

^{1}H-NMR ($CDCl_3$): δ_H 1.24 (9H, s, -C(CH_3)$_3$), 2.23-2.71 (18H, m, 9-CH_2), 3.06 (2H, s, CH_2), 3.09 (2H, s, CH_2), 3.17 (4H, s, 2-CH_2), 3.56 (3H, s, CH_3), 3.63 (6H, s, 2-CH_3), 5.43 (1H, s, NH).).

^{13}C-NMR ($CDCl_3$): δ_c 27.7 ((CH_3)$_3$), 36.9 (CH_2), 49.7 (CH3), 51.0 (CH_3), 51.7 (CH_2), 51.98 (CH_2), 54.1 (CH_2), 54.6 (CH_2), 55.1 (CH_2), 78.3 (C(CH_3)$_3$), 156.3 (N-C=O), 173.2 (O-C=O), 173.5 (O-C=O).

7.3.1.5 Methyl 2-[4-(2-aminoethyl)-7,10-bis(2-methoxy-2-oxo-ethyl)-1,4,7,10-tetrazacyclododec-1-yl]acetate (4)[268]

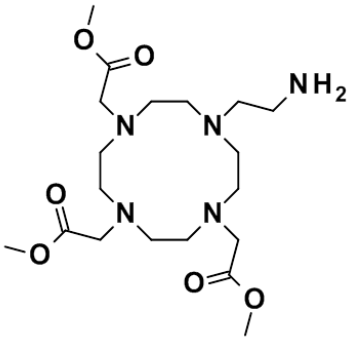

A solution of **3** (500 mg, 0.94 mmol) in TFA (2 mL) and CH_2Cl_2 (8 mL) was stirred at room temperature for 2 h. The solvent was evaporated under reduced pressure and the residue was dissolved in 2 mL of MeOH, followed by dropwise addition of diethylether at 0 ºC and then stirred for 1 h at room temperature. Any insoluble material was removed by filtration and the solvent was evaporated under low pressure. The residue was redissolved in 5 mL of H_2O, the resulting solution was neutralized by addition of 1 M Na_2CO_3, and the solvent evaporated under reduced pressure at 50 ºC.

Yield: 288 mg (71%).

ESI-MS: m/z calcd for $[M+H]^+$ 432.2, found 432.3.

^{1}H-NMR ($CDCl_3$): δ_H 3.15 (20H, b, 10-CH_2), 3.79 (6H, b, 3-CH_2), 4.85 (9H, s, 3-CH_3).

^{13}C-NMR ($CDCl_3$): δ_c 36.02 (CH_3), 51.89 (CH_2), 52.91 (CH_2), 52.99 (CH_2), 53.14 (CH_2), 55.35 (CH_2), 56.23 (CH_2), 56.86 (CH_2), 175.74 (C=O), 176.27 (C=O).

7.3.1.6 3-tritylsulfanylpropanoic acid (5)

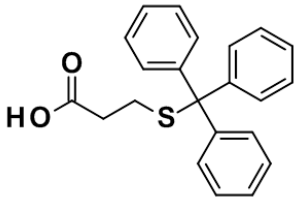

Tritylthiol (3.0 g, 10.8 mmol) in THF (15 mL) was added over 5 min to pentane-washed NaH (435.0 mg, 10.8 mmoL) in THF (5 mL) at 0 ºC. The mixture was stirred at room temperature for 10 min. It was then placed in an ice bath and 3-bromopropionic acid (2.18 g, 10.8 mmol) was added. After stirring at room temperature for 30 min the mixture was concentrated and partitioned between EtOAc (20 mL) and H_2O (10 mL). The organic layer was dried over $MgSO_4$ and the solvent evaporated under low pressure.

Yield: 4.06 g (95%).

^{1}H-NMR ($CDCl_3$): δ_H 2.14 (2H, t, CH2), 2.39 (2H, t, CH2), 7.12-7.24 (12H, m, H-Ph), 7.36 (3H, d, H-Ph).

^{13}C-NMR ($CDCl_3$): δ_c 26.47 (CH_2), 33.05 (CH_2), 55.77 ($C(Ph)_3$), 126.72 (Ph), 127.94 (Ph), 129.53 (Ph), 146.91 (Ph), 156.29 (C=O).

7.3.1.7 (2,5-dioxopyrrolidin-1-yl) 3-tritylsulfanylpropanoate (6)

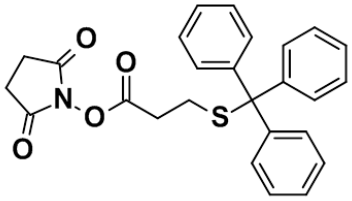

To a solution of compound **5** (1.0 g, 2.9 mmol) in CH_2Cl_2 (10 mL) was added NHS (409 mg, 3.48 mmol). The mixture was then placed in an ice bath and EDC (674 mg, 3.48 mmol) was added. The solution was stirred at room temperature over night. The solvent was evaporated under reduced pressure and the residue washed with H_2O.

Yield: 0.939 g (73%).

^{1}H-NMR ($CDCl_3$): δ_H 2.29 (2H, t, CH_2), 2.44 (2H, t, CH_2), 2.69 (4H, s, 2-CH_2), 7.12-7.28 (12H, m, H-Ph), 7.36 (3H, d, H-Ph).

^{13}C-NMR ($CDCl_3$): δ_c 25.49 (CH2), 26.05 (CH2), 30.45 (CH2), 67.08 ($C(Ph)_3$), 126.80 (Ph), 128.02 (Ph), 129.47 (Ph), 144.29 (Ph), 168.84 (C=O), 191.25 (C=O).

7.3.1.8 Methyl 2-[4,7-bis(2-methoxy-2-oxo-ethyl)-10-[2-(3-tritylsulfanyl propanoylamino)ethyl]-1,4,7,10-tetrazacyclododec-1-yl]acetate (7)

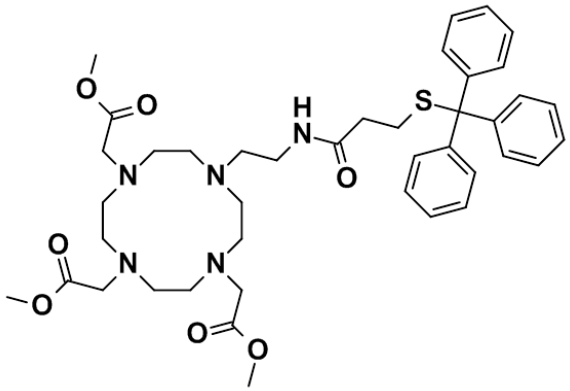

Compound **4** (1.17 g, 2.7 mmol) was dissolved in DMF (5 mL) and DIPEA was added to reach pH ≈ 7-8. In a separated flask, **6** (1.2 g, 2.7 mmoL) was dissolved in DMF (5 mL) and then added to the solution of compound **4**. The pH of the mixture was adjusted to ≈ 9 with DIPEA and the stirred at room temperature overnight. The solvent was

evaporated under reduced pressure and the residue redissolved in CH_2Cl_2. The solution was washed with 2x20 mL of H_2O and the organic phase was dried under low pressure.

Yield: 2.0 g (99%).

ESI-MS: m/z calcd for $[M+H]^+$ 762.3, found 762.4.

^{1}H-NMR ($CDCl_3$): δ_H 2.20-2.63 (20H, m, 10-CH_2), 2.94 (2H, t, CH_2), 3.16-3.34 (6H, m, 3-CH_2), 3.63 (9H, s, CH_3), 7.11-7.23 (12H, m, H-Ph), 7.31 (3H, d, H-Ph).

^{13}C-NMR ($CDCl_3$): δ_c 27.40 (CH_2), 28.29 (CH_2), 34.60 (CH_2), 36.04 (CH_2), 50.10 (CH_2), 52.23 (CH_2), 52.49 (CH_2), 53.97 (CH_2), 54.86 (CH_2), 55.17 (CH_2), 66.34 ($C(Ph)_3$), 126.43 (Ph), 127.68 (Ph), 129.39 (Ph), 144.64 (Ph), 172.42 (C=O), 173.45 (C=O), 173.83 (C=O).

7.3.1.9 2-[4,7-bis(carboxymethyl)-10-[2-(3-tritylsulfanylpropanoylamino)ethyl]-1,4,7,10-tetrazacyclododec-1-yl]acetic acid (8)

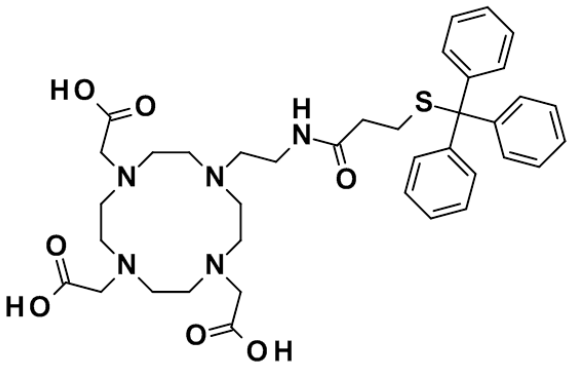

A solution of **7** (887 mg, 1.16 mmol) in 10 mL of THF:MeOH:H_2O (3:2:2) was stirred for 15 min in an ice bath and then LiOH (55 mg, 1.3 mmol) was added. The mixture was stirred for 3 h at room temperature. The solvent was evaporated at reduced pressure and the residue redissolved in 3 mL of H_2O. The solution was placed in a C18 column. The column was initially eluted with 20 mL of H_2O and each additional elution had an increment of 10% MeOH until a final elution of 100% MeOH. The recovered fractions were dried under reduced pressure and the desired compound was tracked by ^{1}H-NMR analysis of selected fractions.

Yield: 541 mg (65%).

ESI-MS: m/z calcd for $[M-H]^-$ 718.9, found 718.5.

^{1}H-NMR (D_2O): δ_H 1.84-2.63 (20H, m, 10-CH_2), 2.98-3.55 (6H, m, 3-CH_2), 3.99 (2H, t, CH_2) 6.75 (9H, m, H-Ph), 7.05 (6H, m, H-Ph).

^{13}C-NMR (D_2O): δ_c 23.50 (CH_2), 28.03 (CH_2), 34.93 (CH_2), 35.93 (CH_2), 50.35 (CH_2), 52.73 (CH_2), 58.66 (CH_2), 66.65 (CH_2), 127.07 (Ph), 128.19 (Ph), 129.55 (Ph), 144.68 (Ph), 172.63 (C=O), 179.51 (C=O), 180.03 (C=O).

7.3.1.10 2-[4,7-bis(carboxymethyl)-10-[2-(3-sulfanylpropanoylamino)ethyl]-1,4,7,10-tetrazacyclododec-1-yl]acetic acid (TDOTA)

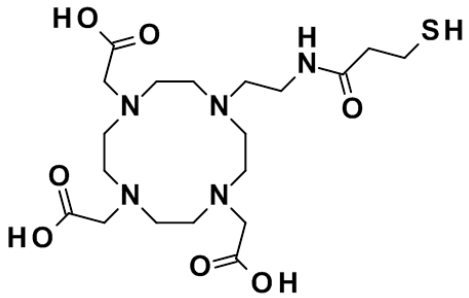

Compound **8** (322 mg, 0.45 mmol) was dissolved in a mixture of TFA:H_2O:tthioanisole:1,2-dithiolethane (94:2.5:1:2.5) (10 mL) and stirred for 2 h at room temperature. The mixture was dried under low pressure. The residue was redissolved in 10 mL of H_2O and washed with 3x10 mL of CH_2Cl_2. The aqueous phase was dried under reduced pressure.

Yield: 262 mg (98%) (2xTFA molecules).

ESI-MS: m/z calcd for $[M+H]^+$ 478.2, found 478.4.

^{1}H-NMR (D_2O): δ_H 2.33 (2H, t, CH_2), 2.49 (2H, t, CH_2), 2.70-3.10 (10H, m, CH_2), 3.10-3.50 (8H, m, CH_2), 3.97 (1H, b, NH).

^{13}C-NMR (D_2O): δ_c 21.54 (CH_2), 35.89 (CH_2), 40.89 (CH_2), 50.10 (CH_2), 50.56 (CH_2), 51.92 (CH_2), 53.43 (CH_2), 54.78 (CH_2), 56.19 (CH_2), 170.85 (C=O), 175.87 (C=O), 176.77 (C=O).

7.3.1.11 Tert-butyl N-[2-[2-(tert-butoxycarbonylamino)ethylamino]ethyl]carbamate (9)[269]

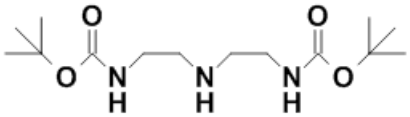

Diethylenetriamine (1.87 g, 18.0 mmol) was dissolved in 20 mL of THF. The solution was placed in an ice bath and BOC-ON (8.96 g, 36.0 mmol) in 10 mL of THF was added over a period of 90 min. The mixture was stirred for 2 h in the ice bath and then stirred at room temperature over night. The solvent was evaporated under reduced pressure and the residue was purified by silica-gel chromatography ($CHCl_3$/MeOH, 95:5).

Yield: 3.2 g (56%).

^{1}H-NMR ($CDCl_3$): δ_H 1.41 (18H, s, 6-CH_3), 2.90 (4H, t, 2-CH_2), 3.38 (4H, t, 2-CH_2).

7.3.1.12 1-(2-bromoethyl)-3,5-dimethyl-pyrazole

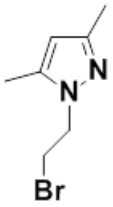

To a solution of 3,5-dimethyl-pyrazole (2.3 g, 23.9 mmol) in 15 mL of 40% NaOH (aqueous), 15 mL (32.7 mmol) of 1,2-dibromoethane were added. The mixture was stirred at room temperature over night. The solution was dried under low pressure and the residue was purified by silica-gel chromatography (100% ethyl acetate).

Yield: 2.3 g (48%).

^{1}H-NMR ($CDCl_3$): δ_H 2.10 (3H, s, CH_3), 2.25 (3H, s, CH_3), 3.67 (2H, t, CH_2), 4.30 (2H, t, CH_2), 5.78 (1H, s, H(4)-pz).

7.3.1.13 tert-butyl N-[2-[2-(tert-butoxycarbonylamino)ethyl-[2-(3,5-dimethylpyrazol-1-yl)ethyl]amino]ethyl]carbamate (10)[248]

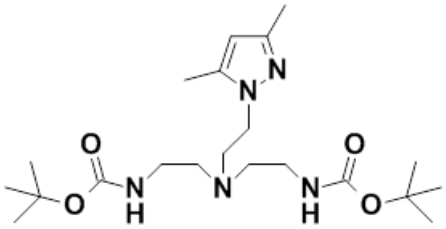

A mixture of **9** (1.6 g, 5.1 mmol), 1-(2-bromoethyl)-3,5-dimethyl-pyrazole (837 mg, 4.04 mmol), K_2CO_3 (710 mg, 5.1 mmol) and KI (70 mg, 0.42 mmol) in THF (30 mL) was refluxed over night. The solven was evaporated under low pressure and the residue was purified by silica-gel chromatography (CH_2Cl_2/MeOH, 95:5).

Yield: 829 mg (48%).

^{1}H-NMR ($CDCl_3$): δ_H 1.46 (18H, s, 6-CH_3) 2.25 (3H, s, CH_3), 2.28 (3H, s, CH_3), 2.53 (4H, t, 2-CH_2), 52.71 (2H, t, CH_2), 3.05 (4H, t, 2-CH_2), 4.02 (2H, t, CH_2), 5.86 (1H, s, H(4)-pz).

7.3.14 N'-(2-aminoethyl)-N'-[2-(3,5-dimethylpyrazol-1-yl)ethyl]ethane-1,2-diamine (11)

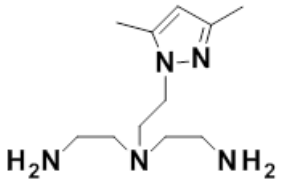

To solution of compound **11** (826 mg, 3.20 mmol) in MeOH (25 mL), at 0 ºC, were added 6 mL of 12 M HCl. The reaction mixture was left to stir at room temperature for 24 h. Then, the solvent was evaporated under vacuum, the pH was adjusted to pH=5-6 by addition of 40 % aqueous NaOH and the mixture extracted with CH_2Cl_2 (3x20 mL). The organic phase was dried over $MgSO_4$, filtered and the filtrate was dried under vacuum to afford the title compound as a pale yellow oil.

Yield: 341 mg (0.79 mmol, 79 %).

^{1}H-NMR (CD_3OD): δ_H 2.17 (3H, s, CH_3), 2.22 (3H, s, CH_3), 2.51 (4H, tr, CH_2), 2.68 (4H, t, CH_2), 2.82 (2H, t, CH_2), 4.00 (2H, tr, CH_2), 5.75 (1H, s, H(4)-pz).

^{13}C-NMR ($CDCl_3$): δ_c 10.84 (CH_3), 13.11 (CH_3), 38.96 (CH_2), 38.96 (CH_2), 46.54 (CH_2), 53.68 (CH_2), 55.45 (CH_2), 104.78 (C(4)-pz), 138.58 (C(3/5)-pz), 146.85 (C(3/5)-pz).

7.3.1.15 Tert-butyl N-[2-[2-(tert-butoxycarbonylamino)ethyl-(2-pyridylmethyl)amino] ethyl]carbamate (12)

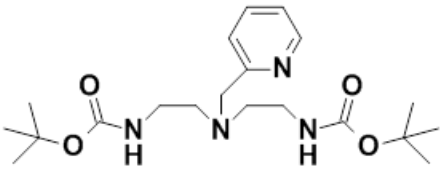

In a 100 mL flask, **9** (700 mg, 2.26 mmol), 2-bromomethyl-pyridine (628 mg, 2.48 mmol), K_2CO_3 (685 mg, 4.96 mmol) and KI (41 mg, 0.25 mmol)) were mixed in 30 mL of dried THF. The mixture was refluxed overnight. The solution was filtered and the solvent was evaporated under reduced pressure to afford the final product.

Yield: 786 mg (99%).

^{1}H-NMR ($CDCl_3$): δ_H 1.42 (18H, s, 2-C(CH_3)$_3$, 2.62 (4H, t, 2-CH_2), 3.15 (4H, t, 2-CH_2), 3.74 (2H, s, CH_2), 5.51 (2H, b, 2-NH), 7.15 (1H, t, py), 7.29 (1H, d, py), 7.62 (1H, t, py), 8.52 (1H, d, py).

^{13}C-NMR ($CDCl_3$): δ_c 28.32 (CH_3), 38.34 (CH_2), 54.03 (CH_2), 59.80 (CH_2), 78.71 (C(CH_3)$_3$), 121.98 (py), 122.83 (py), 136.37 (py), 148.99 (py), 156.17 (py), 159.37 (C=O).

7.3.1.16 N'-(2-aminoethyl)-N'-(2-pyridylmethyl)ethane-1,2-diamine (13)

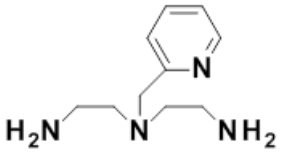

25 mL of MeOH were added to compound **12** (1.0 g, 2.5 mmol) in a 50 mL flask. The solution was placed in an ice bath and 12 M HCl (6 mL) was added. The mixture was stirred at room temperature for 24 h. The solvent was evaporated under reduced pressure

and to the resulting residue was added 40% aqueous NaOH until pH=5-6. The compound was then extracted with $CHCl_3$ (3x20 mL), dried with $MgSO_4$ and the organic solvent evaporated under vacuum.

Yield: 466mg (96%).

^{1}H-NMR ($CDCl_3$): δ_H 2.56 (4H, t, 2-CH_2), 2.73 (4H, t, 2-CH_2), 3.72 (2H, s, CH_2), 7.13 (1H, t, py), 7.37 (1H, d, py), 7.62 (1H, t, py), 8.49 (1H, d, py).

^{13}C-NMR ($CDCl_3$): δ_c 39.58 (CH_2), 57.59 (CH_2), 60.78 (CH_2), 122.00 (py), 122.89 (py), 136.44 (py), 149.04 (py), 159.83 (py).

7.3.1.17 (2-[(E)-2-[2-(3,5-dimethylpyrazol-1-yl)ethyl-[2-[(E)-(2-hydroxyphenyl) methyleneamino]ethyl]amino]ethyliminomethyl]phenol) (H_2L^1)

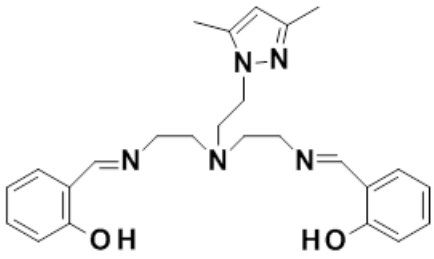

A solution of compound **11** (296 mg, 1.31 mmol) and salicylaldehyde (321 mg, 2.63 mmol) in MeOH (15 mL) was refluxed under N_2 for 4 h, and then evaporated to dryness under reduced pressure. The residue was extracted several times with diethyl ether (3x25 mL) and the ether fractions were filtered to remove an insoluble orange material. The solvent was dried under low pressure.

Yied: Yield: 256 mg (45%).

ESI-MS: m/z calcd for $[M+H]^+$, 434.3; found 434.3.

IR (KBr, v/cm^{-1}): 3428w, 3019m; 2952m; 2901m, 2253w, (N=C, sharp) 1634vs, 1582m 1553w, 1498m; 1461m; 1280s; 1216s; 1152w; 1117w; 1072w; 1041w; 900s; 760s; 669sh,m; 650mw; 556w; 464w.

^{1}H-NMR ($CDCl_3$) δ_H 2.03 (3H, s, CH_3), 2.19 (3H, s, CH_3), 2.83 (4H, t, 2-CH_2), 2.96 (2H, tr, CH_2), 3.54 (4H, tr, 2-CH_2), 3.89 (2H, tr, CH_2), 5.70 (1H, s, H(4)-pz), 6.78 (2H, tr,

Ph), 6.90 (2H, d, Ph), 7.00 (2H, d, Ph), 7.26 7.00 (2H, tr, Ph), 8.05 (2H, s, CH=N), 13.38 (2H, br, OH).

^{13}C-NMR ($CDCl_3$) δ_c 10.84 (CH_3), 13.49 (CH_3), 47.08 (CH_2), 54.93 (CH_2), 55.73 (CH_2), 57.84 (CH_2), 104.77 (C(4)-pz), 116.91 (Ph), 118.46 (Ph), 118.66 (Ph), 131.27 (Ph), 132.11 (Ph), 139.35 (C3/5-pz), 147.32 (C3/5-pz), 161.16 (Ph), 165.95 CH=N).

7.3.1.18 (2-[(E)-2-[2-[(E)-(2-hydroxyphenyl)methyleneamino]ethyl-(2-pyridylmethyl) amino]ethyliminomethyl]phenol) (H_2L^2)

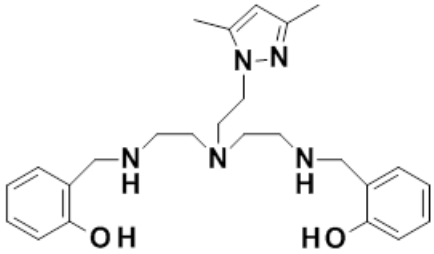

A solution of compound **11** (390 mg, 1.73 mmol) and salicylaldehyde (423 mg, 3.46 mmol) in MeOH (20 mL) was refluxed under N_2 for 4 h. After cooling to room temperature, solid $NaBH_4$ (200 mg, 5.29 mmol) was added to the reaction mixture and the resulting clear solution was stirred overnight at room temperature. The solvent was evaporated under reduced pressure, the oily residue was redissolved in CH_2Cl_2 and then washed with a saturated $NaHCO_3$ aqueous solution. The organic phase was separated, the solvent removed under vacuum and the crude was purified by silica-gel column chromatography using CH_2Cl_2/MeOH/NH_4OH (90/30/2) (R_f = 0.40) as the eluent. Removal of the solvent from the collected fractions gave the desired compound.

Yield: 774 mg (85%).

ESI-MS: m/z calcd for $[M+H]^+$ 403.2, found 403.3.

IR (KBr, v/cm^{-1}): 3286w, 3239w, 2951m, 2840m, 2361w, 1591s, 1552m, 1459s, 1419m, 1260s, 1184w, 1151w, 1104m, 1025m, 933w, 845w, 802wm, 756s, 720w, 625w, 544w, 458w.

^{1}H-NMR ($CDCl_3$): δ_H 2.89 (4H, t, 2-CH_2), 3.62 (4H, t, 2-CH_2), 3.82 (2H, s, CH_2), 6.76 (4H, t, Ph), 6.91 (2H, d, Ph), 6.97 (2H, d, Ph), 711 (1H, t, py), 7.27 (1H, d, py), 7.41 (1H, t, py), 8.05 (2H, s, 2-N=CH), 8.51 (1H, d, py).

^{13}C-NMR ($CDCl_3$): δ_c 55.28 (CH_2), 57.50 (CH_2), 60.84 (CH_2), 116.83 (Ph), 118.35 (Ph), 118.60 (Ph), 121.94 (py), 122.78 (py), 131.18 (Ph), 132.00 (Ph), 136.42 (py), 148.72 (py), 159.42 (py), 161.10 (Ph), 165.76 (N=CH).

7.3.1.19 (2-[[2-[2-(3,5-dimethylpyrazol-1-yl)ethyl-[2-[(2-hydroxyphenyl)methylamino] ethyl]amino]ethylamino]methyl]phenol) (H_2L^3)

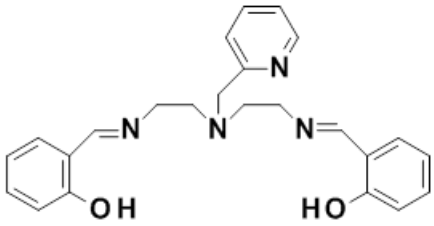

Compound **13** (440 mg, 2.26 mmol) and salicylaldehyde (552 mg, 476 µL, 4.52 mmol) were dissolved in dried MeOH (10 mL). The mixture was refluxed under N_2 for 3 h. After evaporation of the solvent, the crude product was extracted with diethyl ether. The ether was dried under reduced pressure to afford the final product.

Yield: 423 mg (56%).

ESI-MS: m/z calcd for $[M+H]^+$ 438.3, found 438.4.

IR (KBr, v/cm^{-1}): 3059w, 3009w, 2846w, 2362w, 1634s, 1588m,1498m, 1460m, 1372w, 1280m, 1208w, 1152m, 1116m, 1077m, 895w, 85w, 757s, 641w, 624w, 558w, 460w.

^{1}H-NMR ($CDCl_3$): δ_H 1.87 (3H, s, CH_3), 2.20 (3H, s, CH_3), 2.56 (4H, m, 2-CH_2), 2.62 (2H, m, CH_2), 2.74 (2H, tr, CH_2), 3.89 (4H, s, CH_2), 4.01 (2H, tr, CH_2), 5.71 (1H, s, H(4)-pz), 6.75-6.81 (4H, tr, Ph), 6.98 (2H, d, Ph), 7.13 (2H, d, Ph).

^{13}C-NMR ($CDCl_3$): δ_c 10.70 (CH_3), 12.69 (CH_3), 45.62 (CH_2), 46.56 (CH_2), 52.06 (CH_2), 53.28 (CH_2), 53.54 (CH_2), 105.04 (C(4)-pz), 115.96 (Ph), 118.60 (Ph), 122.21 (Ph), 128.25 (Ph), 128.27 (Ph), 134.41 (C3/5-pz), 146.98 (C3/5-pz), 158.06 (Ph).

7.3.1.20 (2-[[2-[2-[(2-hydroxyphenyl)methylamino]ethyl-(2-pyridylmethyl)amino]ethyl amino]methyl]phenol) (H_2L^4)

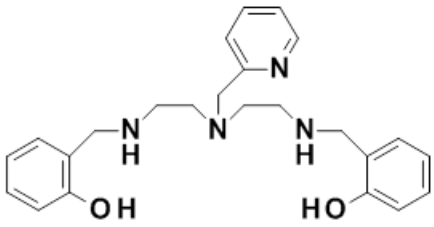

To a solution of **H_2L^3** (362 mg, 0.9 mmol) in MeOH (10 mL), $NaBH_4$ (102 mg, 2.7 mmol) was added. The solution was stirred overnight at room temperature. The solvent was evaporated under reduced pressure, the oily residue was redissolved in CH_2Cl_2 and filtered. The solvent was removed under vacuum and the residue washed with diethyl ether. After drying under vacuum, the final compound was obtained as a dark brown oil.

Yield: 353 mg (97%).

ESI-MS: m/z calcd for $[M+H]^+$ 407.2, found 407.4.

IR (KBr, v/cm^{-1}): 3418s (N-H), 3418s, 3054m, 2948m, 2845m, 2362w, 1592vs, 1475s, 1435sh,s, 1260s, 1151m, 1104m, 1000w, 936w, 843w, 756s, 736m, 702w, 624w, 459w.

^{1}H-NMR ($CDCl_3$): δ_H 2.64 (8H, m, 4-CH_2), 3.66 (2H, s, CH_2), 3.80 (4H, s, 2-CH_2), 5.23 (s, NH), 6.71 (4H, t, Ph), 6.85 (2H, d, Ph), 7.05-7.20 (4H, m, Ph+py), 7.59 (1H, t, py), 8.40 (1H, d, py).

^{13}C-NMR ($CDCl_3$): δ_c 45.93 (CH_2), 52.44 (CH_2), 54.22 (CH_2), 60.19 (CH_2), 116.21 (Ph), 118.82 (Ph), 122.53 (py), 122.80 (py), 123.32 (Ph), 128.25 (Ph), 128.48 (Ph), 136.63 (py), 149.37 (py), 158.16 (Ph), 159.10 (py).

7.3.2 Synthesis of the Peptides

The peptides **TA-BBN** and **TA-GE11-DOTA** were custom synthesized by CPC Scientific; the company confirmed their formulation and purity (> 95%) by ESI-MS and HPLC analysis. ESI-MS and HPLC analyses were also performed after delivery of the peptides, at CTN/IST (**TA-BBN**: m/z calcd for $[M+H]^+$, 1129.4, found, 1129.0. t_R (HPLC,

Method 1) = 10.92 min; **TA-GE11-DOTA**: m/z calcd for $[M+H+Na]^{2+}$, 1336.2, found, 1335.6. t_R (HPLC, Method 2) = 15.23 min).

Synthesis of **C-KKK-BBN** was performed by Fmoc-based Solid Phase Peptide Synthesis in a CEM 12-Channel Automated Peptide Synthesizer (scale 0.1 mM), using microwave irradiation and rink amide resin (MBHA). The peptide was cleaved from the resin by treatment with a mixture of TFA:thioanisole:1,2-dithiolethane:H_2O (96:2:1:1) for 2 h. The cleavage solution was separated from the resin by filtration and concentrated under N_2. The crude peptide was precipitated, washed with cold diethylether and vacuum-dried. After dissolution in H_2O, the peptide was purified by HPLC (Macherey-Nagel EC 250/4 Nucleosil 100-10 C18, Method 2); the collected fractions were lyophilized and analysed by HPLC and ESI-MS (ESI-MS: m/z calcd for $[M+H]^{1+}$, 1428.8, found, 1429.2. t_R (HPLC, Method 2) = 4.64 min).

7.3.3 Synthesis and Characterization of the Gold Nanoparticles

7.3.3.1 AuNP-DTDTPA

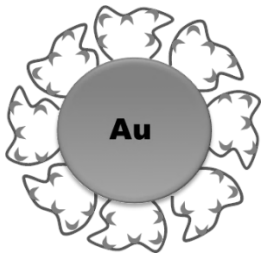

200 mg (0.51 mmol) of $HAuCl_4.3H_2O$ was dissolved in 120 mL of methanol in a 500 mL round bottom flask. In a separate flask, 482 mg (0.94 mmol) of **DTDTPA** was dissolved in 40 mL of methanol and 2 mL of glacial acetic acid. This solution was added with continuous stirring to aqueous solution of gold salt to produce an orange solution. To this mixture, 190 mg (5 mmol) of $NaBH_4$ dissolved in 14 mL of water was added under vigorous stirring at room temperature. Immediately after addition of $NaBH_4$, the solution became dark brown followed by appearance of black flocculate. The resultant mixture was allowed to stir for 1 h at room temperature and then 5 mL of 1 M aqueous HCl was added. This black solution of gold nanoparticles was then subjected to centrifugation at 7000 rpm for 20 min. The supernatant was removed and the particles were washed twice with 0.01 M HCl keeping the centrifugation parameters same as above. The particles were further

washed thoroughly and successively with water followed by diethyl ether. The resulting black powder of AuNPs was dried under low pressure.

UV-Vis: 520 nm.

TEM: 2.28 ± 1.32 nm.

DLS (H_2O): 100.6 nm, PDI = 0.111.

Zeta-Potential (H_2O): -80.7 ± 15.6 mV.

7.3.3.2 AuNP-DTDTPA-Ga

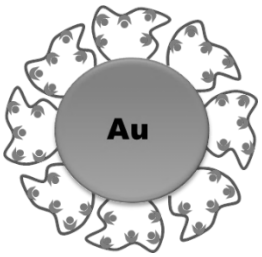

In 20 mL vial, a 1 mL solution of **AuNP-DTDTPA** (1 mg/mL) was prepared using an aqueous 0.01 M NaOH. 5 mg ($19.6x10^{-3}$ mmol) of $Ga(NO_3)_3$ was added and the mixture was stirred for 2 h at room temperature. The reaction mixture was the centrifuged at 15000 rpm for 5 min and the obtained pellet was washed three times with H_2O and dried under low pressure.

UV-Vis: 520 nm.

TEM: 2.61 ± 1.31 nm.

DLS (H_2O): 177.3 nm, PDI = 0.226.

Zeta-Potential (H_2O): +27.1 ± 5.4 mV.

7.3.3.3 BBN-AuNP-DTDTPA

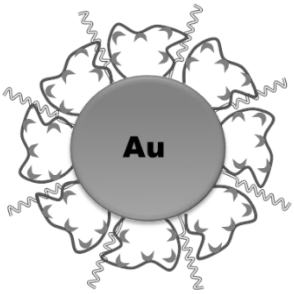

In a 20 mL vial, 1 mL of a solution of **AuNP-DTDTPA** (1 mg/mL) using a H_2O/MeOH mixture (1:9) was prepared. **TA-BBN** (5 mg, 4.43 X 10^{-3} mmol) was dissolved in 4 mL of MeOH and then added to the nanoparticles solution while stirring vigorously. Formation of a dark brown precipitate was observed after some time. The reaction was continued to stir for 1 h at room temperature. The mixture was centrifuged (10000 rpm for 10 min at 10 °C) and the supernatant was removed. The precipitated AuNPs were washed two times with MeOH and three times with water and then dried under low pressure.

UV-Vis: 520 nm.

TEM: 2.02 ± 0.88 nm.

DLS (H_2O): 148.2 nm, PDI = 0.162.

Zeta-Potential (H_2O): -71.5 ± 9.1 mV.

7.3.3.4 AuNP-TDOTA

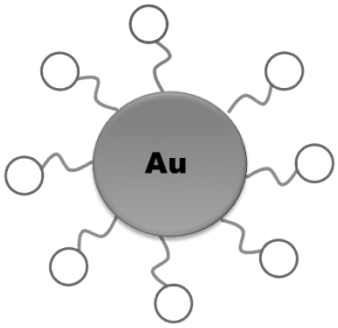

TDOTA·2TFA (68 mg, 0.115 mmol) was dissolved in 10 mL of a MeOH/H_2O solution (7:3), and added to 4.5 mL of a solution of $HAuCl_3 \cdot 3H_2O$ (1 mM) in MeOH. The mixture was stirred at room temperature for 5 min and then 0.3 mL of a solution of $NaBH_4$

(0.295 M) was added while vigorously stirring. There was an immediate formation of a dark precipitate. The reaction was stirred for an additional hour at room temperature. The solution was centrifuged at 1000 rpm for 20 min and the obtained pellet was washed two times with MeOH and two times with H_2O. The nanoparticles were then dried at reduce pressure.

UV-Vis: 520 nm.

TEM: 4.29 ± 1.60 nm.

DLS (H_2O): 489.3 nm, PDI = 0.520.

Zeta-Potential (H_2O): -20.4 ± 5.5 mV.

7.3.3.5 BBN-AuNP-TDOTA

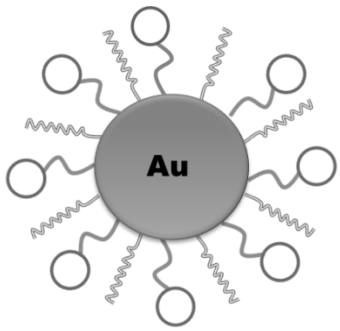

500 µL of a solution of **AuNP-TDOTA** (5 mg/mL) was placed in a 10 mL vial and 500 µL of MeOH were added. While stirring vigorously, 2 mg ($1.77x10^{-3}$ mmol) of **TA-BBN** in 1 mL of MeOH were added. The mixture was stirred at room temperature for 2 h. The solution was ultra-centrifuged at 12000 rpm for 5 min. The nanoparticles were washed with MeOH and H_2O and dried at low pressure.

UV-Vis: 520 nm.

TEM: 4.79 ± 1.50 nm.

DLS (H_2O): 214.7 nm, PDI = 0.269.

Zeta-Potential (H_2O): -22.6 ± 5.6 mV.

7.3.3.6 CBBN-AuNP-TDOTA

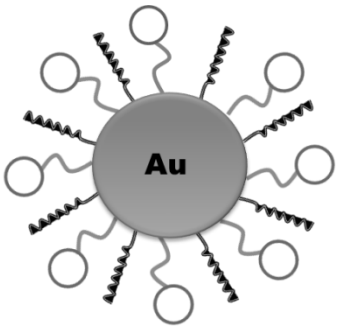

500 µL of a solution of **AuNP-TDOTA** (5 mg/mL) was placed in a 10 mL vial and 500 µL of MeOH were added. While stirring vigorously, 2 mg ($1.42x10^{-3}$ mmol) of **C-KKK-BBN** in 1 mL of MeOH were added. The mixture was stirred at room temperature for 2 h. The solution was ultra-centrifuged at 12000 rpm for 5 min. The nanoparticles were washed with MeOH and H_2O and dried at low pressure.

UV-Vis: 520 nm.

TEM: 4.04 ± 1.52 nm.

DLS (H_2O): 313 nm, PDI = 0.37.

Zeta-Potential (H_2O): -15.0 ± 8.7 mV.

7.3.3.7 PEG-AuNP-GE11-DOTA

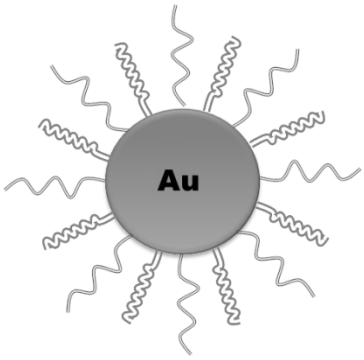

2 mL of AuNP-citrate (1.86 mg(Au)/mL, 0.95 mmol(Au)) were placed in a 20 mL vial and 2 mL of H_2O were added. A solution of mPEG-SH (Mw = 750) (14.18 mg, 1.9 mmol) in H_2O (1 mL) and **TA-GE11-DOTA** (5.0 mg, 0.19 mmol) in H_2O (1 mL) were

prepared. While stirring vigorously, 100 µL of the mPEG-SH solution was added to the AuNP-citrate, followed by the addition of 100 µL of the **TA-GE11-DOTA** solution. This process was repeated until complete addition of the mPEG-SH and **TA-GE11-DOTA** solutions. The mixture was left to stir at room temperature for 2 h. The solution was centrifuged at 15000 rpm for 10 min and the nanoparticles were washed with H_2O.

UV-Vis: 525 nm.

TEM: 11.99 ± 1.49 nm.

DLS (H_2O): 49.3 nm, PDI = 0.382.

Zeta-Potential (H_2O): -65.8 ± 35.7 mV.

7.3.3.8 DTAu-GE11-DOTA

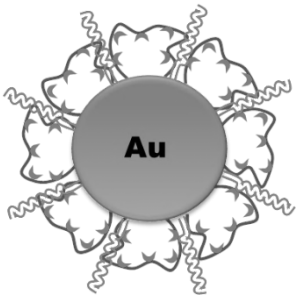

2 mg (7.5×10^{-4} mmol) of **TA-GE11-DOTA** was dissolved in 1 mL of H_2O and then added to a 10 mL vial containing 1 mL of a 1 mg/mL solution of **AuNP-DTDTPA** in H_2O, while stirring. The reaction was continued to stir for 2h at room temperature. The mixture was centrifuged (10000 rpm for 10 min) and the supernatant was removed. The nanoparticles were washed with H_2O and then dried under low pressure.

UV-Vis: 520 nm.

TEM: 2.26 ± 1.45 nm.

DLS (H_2O): 167.2 nm, PDI = 0.228.

Zeta-Potential (H_2O): -53.1 ± 10.0 mV.

7.3.3.9 Pre-DTAu-GE11-DOTA

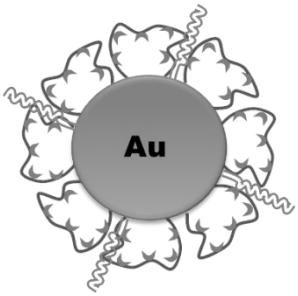

To 25 µL of a solution of **TA-GE11-DOTA** ($1x10^{-3}$M, H_2O), 125 µL of sodium acetate buffer (0.4 M, pH ≈ 5) were added. To this mixture, 100 µL of HCl (0.1 M) were added and the reaction was heated at 70 ºC for 30 min. The mixture was then transferred to a 10 mL vial containing 80 µL a solution of **AuNP-DTDTPA** (5 mg/mL, H_2O) and stirred at room temperature for 2 h. The solution was ultrafiltered in an Amicon Ultra 10K filter. The nanoparticles were washed with H_2O and then dried under low pressure.

UV-Vis: 520 nm.

TEM: 2.45 ± 1.35 nm.

DLS (H_2O): 149.5 nm, PDI = 0.167.

Zeta-Potential (H_2O): -52.9 ± 8.5 mV.

7.2.4 Determination of the Amount of Conjugated Peptides to the AuNPs

For the reactions of peptide conjugation to the AuNPs, an initial solution of the respective peptide was prepared. Part of the peptide solution was used for the reaction with the AuNPs and an equal part was used to prepare the control solution. The control solution was diluted in order to have the same volume as the reaction mixture. The control solution and the supernatant of the reaction mixtures were analysed by HPLC using identical equipment parameters. The difference in the peak areas found in the chromatograms was used to determine the amount of conjugated peptide (see Table 7.1).

Table 7.1: *Peak areas of the control solutions and supernatants obtained in the HPLC analysis of the conjugation reactions of the peptides to the AuNPs.*

Bioconjugated AuNP (Au:Peptide)*	Amount of starting AuNP (mg)	Amount of starting peptide (mg)	Peak area of control solution	Peak area of supernatant
BBN-AuNP-DTDTPA (1:0.24)	1	0.6	557581	521809
BBN-AuNP-DTDTPA (1:0.4)	1	1	974731	833139
BBN-AuNP-DTDTPA (1:0.8)	1	2	1804145	1593173
BBN-AuNP-DTDTPA (1:2)	1	5	4363538	4137768
BBN-AuNP-DTDTPA (1:4)	1	10	8569382	8330907
BBN-AuNP-TDOTA	1	2	1742879	896505
CBBN-AuNP-TDOTA	1	2	2633590	2321230
PEG-AuNP-GE11-DOTA	1	2	11232618	9649608
DTAu-GE11-DOTA	1	2	201508	1715623
Pre-DTAu-GE11-DOTA	0.4	0.08	4693743	104808

***** Au:Peptide molar ratios used in the reaction

7.3.5 Synthesis of the Gallium Complexes

7.3.5.1 $GaL^{1,OMe}$

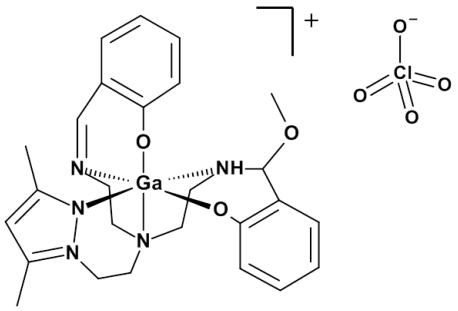

To a solution of $Ga(NO_3)_3.10H_2O$ (111 mg, 0.26 mmol) in MeOH (5 mL) was added dropwise a solution of **H_2L^1** (130 mg, 0.32 mmol) also in MeOH (5 mL). To the resulting clear solution, was added $NaCH_3COO.3H_2O$ (87 mg, 0.64 mmol) dissolved in 5 mL of MeOH, and the reaction mixture was stirred overnight at room temperature. Then, the mixture was treated with $NaClO_4.H_2O$ (44 mg, 0.31 mmol) and was let to stand in the refrigerator. After several days, a white crystalline solid precipitated, which was formulated as **$[GaL^{1,OMe}](ClO_4)$**.

Yield: 65 mg (36%).

CHN: $C_{26}H_{32}N_5O_7ClGa.CH_3OH$ (696.83), calcd. C 48.26, H 5.93, N 10.05; found C 48.02, H 7.38, N 10.02.

ESI-MS: m/z calcd for $[M]^+$, 532.2, found .532.3.

IR (KBr, v/cm^{-1}): 3379m (N-H), 3229mw, 2928w, 1643s (N=C), 1603m, 1551m, 1472sh,m, 1455s, 1306s, 1084s (C-O) , 975mw, 894m, 858mw, 752m, 622m, 607sh,m, 534w, 472w, 414w.

^{1}H-NMR (CD_3CN): δ_H 1.99 (3H, s, CH_3), 2.36 (3H, s, CH_3), 2.46 (1H, m, CH_2), 2.67 (1+1H, m, CH_2), 2.78 (1H, dd, CH_2), 2.98 (1H, m, CH_2), 3.11 (1H, m, CH_2), 3.15 (3H, s, OCH_3), 3.22 (1H, m, CH_2), 3.52 (1H, m, CH_2), 3.63 (1H, m, CH_2), 4.09 (1H, d, NH), 4.22 (1H, d, CH_2), 4.92 (1H, tr, CH_2), 5.49 (1H, s, CH), 6.07 (1H, s, H(4)-pz), 6.63 (1H, d, Ph), 6.71 (1H, tr, Ph), 6.81-6.87 (1+1H, m, Ph), 7.18 (1H, tr, Ph), 7.35 (1H, d, Ph), 7.41-7.47 (1+1H, m, Ph), 8.54 (1H, s, CH=N).

^{13}C-NMR (CD_3CN): δ_C10.927 (CH_3), 12.36 (CH_3), 35.07 (CH_2), 43.31 (CH_2), 51.80 (CH_2), 53.03 (CH_2), 53.50 (CH_2), 56.68 (OCH_3), 57.75 (CH_2), 88.46 (CH), 107.41 (C(4)-pz), 116.80 (Ph), 119.18 (Ph), 122.39 (Ph), 122.93 (Ph), 127.93 (Ph), 130.88 (Ph), 135.49 (Ph), 136.61 (Ph), 143.70 (C(5)-pz), 150.41 (C(3)-pz, 160.65 (Ph), 166.83 (Ph), 171.64 (CH=N).

7.3.5.2 GaL^2

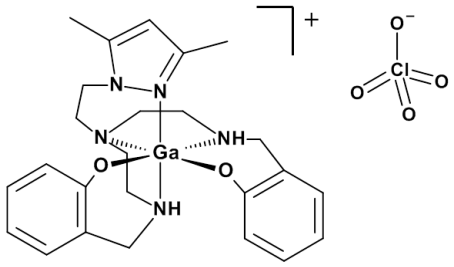

To a solution of $Ga(NO_3)_3.10H_2O$ (100 mg, 0.23 mmol) in MeOH (5 mL) was added dropwise a solution of **H_2L^2** (125 mg, 0.29 mmol) also in MeOH (2 mL). To the resulting clear solution, was added $NaCH_3COO.3H_2O$ (80 mg, 0.59 mmol) dissolved in 5 mL of MeOH, and the reaction mixture was stirred overnight at room temperature. The mixture was treated with $NaClO_4.H_2O$ (40 mg, 0.29 mmol) and let to stand overnight in the refrigerator. The formed white precipitate was separated by filtration, dried and formulated as **[GaL^2](ClO$_4$)**.

Yield: 52 mg (34%).

CHN: $C_{25}H_{33}N_5O_6ClGa{\cdot}3CH_3OH$ (668.82), calcd. C 47.98, H 6.47, N 9.99; found C 47.50, H 6.85, N 10.60.

ESI-MS: m/z calcd for $[M]^+$, 504.2, found .504.2.

IR (KBr, v/cm^{-1}): 3429m (N-H), 3238w, 2926w, 1548m, 1483s, 1454m, 1298m, 1274m, 1085s, 881mw, 756mw, 622mw, 524w, 476w.

t_R (HPLC): 17.5 min.

^{1}H-NMR ($CDCl_3$): δ_H 2.35 (6H, s, CH_3), 2.20 (H, m, CH_2), 2.50 (1H, dd, CH2), 2.63 (1H, dd, CH_2), 2.73 (1H, m, CH_2), 2.90 (1H, m, CH_2), 3.20-3.00 (4H, m, CH_2), 3.69-3.49

(4H, m, 2NH+2CH_2), 3.74 (1H, d, CH_2), 3.97 (1H, t, CH_2), 4.22 (1H, t, CH_2), 4.45 (1H, d, CH_2), 4.74 (1H, d, CH_2), 6.14 (1H, s, H(4)-pz), 6.40 (1H, d, Ph), 6.59 (1H, t, Ph), 6.66 (1H, t, Ph), 6.78 (1H, d, Ph), 7.04 (1 +1H, d, Ph), 7.11 (1, t, Ph), 7.18 (1H, t, Ph).

^{13}C-NMR (CD_3CN): δ_C 11.27 (CH_3), 14.15 (CH_3), 41.395 (CH_2), 44.02 (CH_2), 45.44 (CH_2), 50.69 (CH_2), 51.71 (CH_2), 52.78 (CH_2), 56.83 (CH_2), 108.66 (C(4)-pz), 116.312 (Ph), 116.77 (Ph), 118.99 (Ph), 120.96 (Ph), 121.70 (Ph), 123.12 (Ph), 129.74 (Ph), 130.13 (Ph), 130.81 (Ph), 145.03 (C(5)-pz), 153.03 (C(3)-pz, 161.37 (Ph), 164.06 (Ph).

7.3.5.3 GaL^4

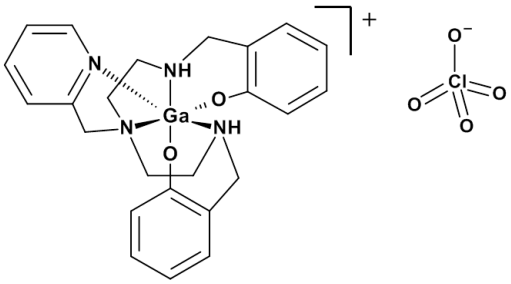

To a solution of **H_2L^4** (173 mg, 0.43 mmol) in MeOH (10 mL) was added a $Ga(NO_3)_3.10H_2O$ (148 mg, 0.34 mmol) dissolved in MeOH (5 mL). To the resulting clear solution, was added $NaCH_3COO{\cdot}3H_2O$ (70.5mg, 0.86 mmol) dissolved in 5 mL of MeOH. The reaction mixture was stirred overnight at room temperature. The solution was treated with $NaClO_4{\cdot}H_2O$ (59 mg, 0.43 mmol) and again stirred overnight at room temperature. The solvent was dried at low pressure and the compound was extracted with 5x10 mL $CHCl_3$. The final compound displayed a light brown color and was formulated as **[GaL^4](ClO$_4$)**.

Yield: 36 mg (22.4%).

CHN: $C_{24}H_{28}N_4O_6ClGa.CH_3OH$ (605.73), calcd. C 49.57, H 5.32, N 9.25; found C 49.14, H 5.99, N 9.12.

ESI-MS: m/z calcd for $[M]^+$ 473.1, found 473.3.

IR (KBr, v/cm^{-1}): 3429m (N-H), 3238w, 2926w, 1548m, 1483s, 1454m, 1298m, 1274m, 1085s, 881mw, 756mw, 622mw, 524w, 476w.

t_R (HPLC): 18.2 min.

^{1}H-NMR ($CDCl_3$): δ_H 2.52 (1H, m, CH_2), 2.67 (1H, d-d, CH_2), 2.88 (1H, d-d, CH_2), 3.03 (2H, m, CH_2), 3.26 (2H, m, CH_2), 3.63 (4H, m, 2-CH_2), 4.03 (1H, d, CH_2), 4.32 (1H, d, NH), 4.34 (2H, m, CH_2), 4.72 (1H, d, NH), 6.38 (1H, d, Ph), 6.56 (1H, t, Ph), 6.72 (1H, t, Ph), 6.96 (2H, t, ph), 7.06 (2H, d, Ph), 7.21 (1H, d, Ph), 7.61 (2H, m, py), 8.1 (1H, t, py), 9.05 (1H, d, py);

^{13}C-NMR (CD_3CN): δ_C 42.37 (CH_2), 42.78 (CH_2), 44.31 (CH_2), 44.93 (CH_2), 51.71 (CH_2), 52.14 (CH_2), 52.71 (CH_2), 54.09 (CH_2), 54.62 (CH_2), 55.66 (CH_2), 56.50 (CH_2), 57.84 (CH_2), 58.32 (CH_2), 63.00 (CH_2), 78.65 (CH_2), 116.23 (Ph), 119.37 (Ph), 121.14 + 121.50 (py), 123.64 + 124.57 + 125.56 (Ph), 129.96 + 130.54 + 131.13 (Ph), 142.14 + 142.57 (py), 146.73 (py), 148.55 (py), 153.93 (py), 163.48 + 164.28 (Ph).

7.4 Radiolabeling Studies with ^{67}Ga

7.4.1 General Considerations

All procedures that involved the manipulation of non-sealed radioactive substances were performed in a laboratory following the required radiation protection rules. Manipulations of the ^{67}Ga solutions were done using a lead protection barrier with a glass visor containing lead salts. The vials that contained radioactive solutions were placed inside lead containers with adequate thickness.

7.4.2 Preparation of $^{67}GaCl_3$

$^{67}GaCl_3$ was prepared following a protocol previously described in literature.[270] Briefly, ^{67}Ga-Citrate (Mallinckrodt) (2.2 mL) was placed in a SEP-PAK SI cartridge (Waters) which was previously conditioned with 10 mL of H_2O. After addition of the ^{67}Ga-citrate, 10 mL of H_2O were passed through the cartridge and then dried with air. This was followed up with the addition of 5x500 µL of 0.1 M HCl, where the five fractions were collected separately. The obtained $^{67}GaCl_3$ in 0.1 M HCl was directly used in this manner for the radiolabeling procedures.

7.4.3 Radiolabeling of the AuNPs

All the ^{67}Ga-labeled AuNPs described in this thesis were radiolabeled using identical concentrations of the nanoparticles and in the same kind of buffer solution. Briefly, 20 µL of the respective AuNP solution (5 mg/mL, H_2O) were added to 350 µL of ammonium acetate buffer (0.4 M, pH ≈ 7). To this mixture, 250 µL of $^{67}GaCl_3$ in 0.1 M HCl were added. The final solutions (pH ≈ 7) were heated at different temperatures and reaction times, depending on the nanoparticle to be labeled (see Table 7.2).

Table 7.2: *Temperature and reaction times used for the different radiolabeling protocols.*

Nanoparticle	Temperature (ºC)	Reaction time (min)
AuNP-DTDTPA	50	15
BBN-AuNP-DTDTPA	Room temperature	15
AuNP-TDOTA	50	30
BBN-AuNP-TDOTA	50	30
CBBN-AuNP-TDOTA	50	30
DTAu-GE11-DOTA	70	15

The radiochemical yields were checked by TLC analysis. In order to purify the AuNPs, the solutions were placed in an Amicon Ultra 10K filter (Millipore) and ultra-filtered in a centrifuge at 12000 rpm for 5 min. The AuNPs were further washed with H_2O and then used for posterior studies.

7.4.4 Radiolabeling of TA-GE11-DOTA

20 µL of a solution of **TA-GE11-DOTA** ($1x10^{-3}$ M, H_2O) were added to 80 µL of sodium acetate buffer (0.4 M, pH ≈ 5). To this mixture, 100 µL of $^{67}GaCl_3$ (0.1 M HCl) were added. The final mixture (pH ≈ 5) was heated at 70 ºC for 30 min. Radiochemical yield was checked by HPLC and TLC analysis. Due to the almost quantitative radiochemical yield (> 99%), the resulting **TA-GE11-DOTA-^{67}Ga** was used in further studies without any purification.

7.4.5 Radiolabeling of H_2L^4

To 20 µL of **H_2L^4** in EtOH ($1x10^{-3}$ M) was added 200 µL of acetate buffer (0.4 M, pH ≈ 5) and then 100 µL of $^{67}GaCl_3$ (0.1 M HCl). The reaction mixture was heated at 85 ºC for 15 min. Radiochemical yield was checked by HPLC. Due to the almost quantitative radiochemical yield (>95%), the resulting **GaL^4** was used in further studies without any purification.

7.5 *In Vitro* Stability Studies

All the *in vitro* stability studies described in this thesis were performed in a similar manner in the presence of NaCl 0.9%, PBS 0.1 M, cell culture medium or human *apo*-transferrin. Briefly, 30 µL aliquots of aqueous solutions containing the radiolabeled compound under study were added to 120 µL of each medium, and the mixtures were incubated at 37 ºC. Analyses of the solutions were performed at specific time points by TLC.

The human *apo*-transferrin solution was prepared in $NaHCO_3$ (10 mM, H_2O) with a concentration of 3 mg/mL.

The cell culture medium used for the *in vitro* stability studies described in Chapters 2 and 3 was a mixture of RPMI 1640 medium supplemented with 10% heat-inactivated fetal bovine serum (FBS) and 1% penicillin/ streptomycin antibitiotic solution (all from Invitrogen). The cell culture medium used for the studies described in Chapter 4 was a mixture of Dulbecco's modified Eagle's medium containing Glutamax I (DMEM Glutamax I) supplemented with 10% FBS and 1% penicillin/ streptomycin antibitiotic solution.

7.6 Lipophilicity Determination

Lipophilicity of compound **$^{67}GaL_4$** was evaluated by determination of the partition coefficient (log $D_{o/w}$) of the compound in the biphasic system n-octanol/PBS 0.1M (pH ≈ 7.4), using the multiple extraction method.[257]

A mixture of 1 mL of PBS 0.1M and 1 mL of octanol (1:1) (pH ≈ 7.4) was vortexed for 1 min. 100 µL of a **$^{67}GaL_4$** solution were added and the mixture was vortexed again for 1 min. The solution was centrifuged for 10 min at 3000 rpm. Three aliquots of 100 µL each

were taken from the aqueous and the organic phases and their radioactivity was measured in a γ counter.

The partition coefficient ($P_{o/w}$) was calculated in the following way:

$P_{o/w}$ = C1/C2

C1 = radioactivity in the organic phase (octanol)

C2 = radioactivity in the aqueous phase (PBS 0.1M)

The result was presented in the form of Log $P_{o/w}$.

7.7 Biological Studies

7.7.1 Cell Culture

PC3 human prostate carcinoma cells (ATCC, Spain) were grown in RPMI 1640 medium supplemented with 10% heat-inactivated fetal bovine serum (FBS) and 1% penicillin/ streptomycin antibitiotic solution (all from Invitrogen).

The cervical carcinoma A431 cells, murine melanoma B16F1 cells and human breast cancer MCF7 cells were maintained in Dulbecco's modified Eagle's medium containing Glutamax I (DMEM Glutamax I) supplemented with 10% FBS and 1% penicillin/ streptomycin antibitiotic solution.

Cells were cultured in a humidified atmosphere of 95% air and 5% CO_2 at 37 ºC (Heraeus, Germany), with the medium changed every other day. The cells were adherent in monolayers and when confluent were harvested from the cell culture flasks with trypsin–EDTA (Invitrogen) and seeded further apart.

7.7.2 Cytotoxicity Studies

Cytotoxic studies were performed by MTT (3-(4,5-dimethylthiazol-2-yl)-2,5-diphenyltetrazolium bromide) assays which evaluate the viability of cells upon exposure to the studied compounds. The mitochondria of the cells that remain viable reduce MTT to formazan. Hence, the detection of formazan is an indication of the integraty of the mitochondria and cell viability.

Briefly, the cells were placed in plaques with 96 wells in a ratio of 3000 cells per 100 µL in each well. After 24 h the cells were incubated at 37 ºC with different concentrations of the compounds under study (1 mL) for 24 h. Wells containing the same number of cells but without compound were used for control purposes. The cell medium was removed and the cells were incubated at 37 ºC with MTT (1 mg/mL) in RPMI for 4 h. Upon removal of the MTT solution isopropanol was added (100 µL/well). The absorvance was measured in an ELISA detector at 540 nm. The average optic density was then calculated for each evaluated concentration of the compound under study, as well as for the different controsl.

7.7.3 Receptor Binding Affinity Assays

The receptor binding affinity (IC_{50}) of the BBN-containing AuNPs was determined by a competitive cell-binding assay on PC3 cells using ^{125}I-Tyr$_4$-BBN (Perkin Elmer) as the GRP-specific radioligand. Cells were seeded in 24-well tissue culture plates and allowed to attach overnight. The medium was then replaced with 0.5 mL of medium containing 20,000 cpm of ^{125}I-Tyr$_4$-BBN and increasing amounts of the respective AuNPs in triplicate such that the final concentrations ranged from 0.001-100 µg/mL. The plates were incubated at 4 ºC for 1 h to avoid interference by the kinetics of internalization and degradation. After incubation, the medium was aspirated and the cells were washed twice with ice-cold phosphate-buffered saline and harvested. Cell associated radioactivity was determined by counting in a gamma counter. The percentage of ^{125}I-Tyr$_4$-BBN bound to cells was plotted against increasing concentrations of the respective AuNPs. IC_{50} values were calculated using GraphPad Software.

7.7.4 Cellular Internalization Assays

i) Internalization Assays for the GRPr-targeted AuNPs

Internalization assays of the BBN-containing AuNPs labeled with ^{67}Ga were performed in PC3 cells seeded at a density of 0.2 million per well in 24-well tissue culture plates and allowed to attach overnight. The cells were incubated at 37 ºC for a period of 15 min to 3 h with about 400,000 cpm of the respective AuNPs (≈ 3.5 µg/mL) in 0.5 mL of assay medium [RPMI with 25 mM N-(2- hydroxyethyl)piperazine-N'-ethanesulfonic acid and 0.2% BSA]. Incubation was terminated by washing the cells with ice-cold assay medium. Cell-surface-bound radioactivity was removed by two steps of acid wash (50 mM

glycine, HCl/100 mM NaCl, pH 2.8) at room temperature for 5 min. The pH was neutralized with cold PBS with 0.2% BSA, and subsequently the cells were lysed by 10 min incubation with 1 M NaOH at 37 ºC to determine internalized radioactivity. Each experiment was performed in quadruplicate. The radioactivity associated to each fraction and that in the cell lysates was measured in a gamma counter and expressed as the percentage of the total activity added to the cells and presented as an average plus the standard deviation.

ii) Internalization Assays for the EGFr-targeted AuNPs

Internalization assays of the GE11-containing AuNPs labeled with ^{67}Ga and **TA-GE11-DOTA-^{67}Ga**, were performed in A431 cells in DMEM Glutamax I following the procedure described above. However two hours before the incubation of the nanoparticles the medium was removed and replaced by FBS free medium.

iii) Blockade and Inhibition Studies

For the blockade studies, parallel experiments were performed following the procedure described above but the cells were pre-incubated in the presence of BBN (500 µL, 1 µM) for 30 min at 37 ºC. The blocking with AuNPs, the cells were pre-incubated in the presence of **BBN-AuNP-DTDTPA** (500 µL, 42 or 105 µg/mL) For the inhibition studies, the cells were pre-incubated for 30 min at 37 ºC in the presence of Amiloride (500 µL, 10 µM), Phenylarsine Oxide (500 µL, 1 nM) or Cadaverine (500 µL, 1 µM).

7.7.5 Biodistribution and In Vivo Stability Studies

i) Biodistribution

In vivo biological studies for the GRPr targeting compounds described in Chapters 2 and 3 were performed in human PC3 xenograft Balb/c mice, while the studies for the compounds described in Chapters 4 and 5 were performed in CD-1 mice. Animal experiments were conducted in conformity with the national law and with the EU Guidelines for Animal Care and Ethics in Animal Experimentation. The animals were housed in a temperature- and humidity-controlled room with a 12 h light/12 h dark schedule.

The animals were injected with 100 µL (50-100 µCi) of an aqueous solution of the radioactive compounds. For intravenous administration the animals were injected in the tail

vein. After specific time intervals varying from 15 min - 24 h after administration, the mice were sacrificed by cervical displacement. The administrated dose and radioactivity of the sacrificed animals were measured in an ionization chamber (Aloka, Curiemeter IGC-3). The difference in radioactivity between the injected animal and the sacrificed one was assumed as excretion. The tissue samples and organs were removed, weighted and the radioactivity measured in a γ counter (Berthold).

The biodistribution results are expressed as a percentage of the injected dose per gram of organ (%I.D./g). Regarding the blood, bone and muscle, the total activity was calculated assuming that these organs comprise 6, 10 and 40% of the total weight of the animal, respectively.

ii) Blockade Studies

Blockade studies were performed following the same procedure described above; however, BBN (100 µg, 100µL) was injected into the mice 30 min prior to the administration of the respective ^{67}Ga-labeled AuNPs.

iii) *In Vivo* Stability Studies

At the time of animal sacrifice, the urine was collected and filtered before injection in the HPLC. For the blood sample, it was collected during the animal sacrifice and was centrifuged at 2000 rpm for 15 min. The serum was separated and ethanol was added in a 2:1 (v/v) ratio (ethanol/serum). The mixture was cooled in ice and centrifuged at 3000 rpm for 10 min at 4 ºC. The resulting supernatant was analysed by HPLC.

References

(1) Erba, P. A.; Manfredi, C.; Lazzeri, E.; Minichilli, F.; Pauwels, E. K. J.; Sbrana, A.; Strauss, H. W.; Mariani, G. *Journal of Nuclear Medicine* **2010**, *51*, 775.

(2) *http://eco.iarc.fr/EUCAN/Country.aspx?ISOCountryCd=968 (visited 16, April, 2014)*.

(3) *American Cancer Society. Global Cancer Facts & Figures 2nd Edition* **2011**.

(4) Goustin, A. S.; Leof, E. B.; Shipley, G. D.; Moses, H. L. *Cancer Research* **1986**, *46*, 1015.

(5) *http://www.cancerresearchuk.org/cancer-help/about-cancer/what-is-cancer/ (visited 16, April, 2014)*.

(6) Sumer, B.; Gao, J. M. *Nanomedicine* **2008**, *3*, 137.

(7) Abercrom.M *In Vitro-Journal of the Tissue Culture Association* **1970**, *6*, 128.

(8) Batson, J.; Astin, J. W.; Nobes, C. D. *Journal of microscopy* **2013**, *251*, 232.

(9) Ostergaard, L.; Tietze, A.; Nielsen, T.; Drasbek, K. R.; Mouridsen, K.; Jespersen, S. N.; Horsman, M. R. *Cancer Research* **2013**, *73*, 5618.

(10) Jain, R. K. *Journal of Controlled Release* **2001**, *74*, 7.

(11) Baban, D. F.; Seymour, L. W. *Advanced Drug Delivery Reviews* **1998**, *34*, 109.

(12) Franses, J. W.; Drosu, N. C.; Gibson, W. J.; Chitalia, V. C.; Edelman, E. R. *International Journal of Cancer* **2013**, *133*, 1334.

(13) Jain, R. K. *Nature Medicine* **2001**, *7*, 987.

(14) Fukumori, Y.; Ichikawa, H. *Advanced Powder Technology* **2006**, *17*, 1.

(15) Brigger, I.; Dubernet, C.; Couvreur, P. *Advanced Drug Delivery Reviews* **2012**, *64*, 24.

(16) Jain, R. K. *Cancer Research* **1987**, *47*, 3039.

(17) Heldin, C.-H.; Rubin, K.; Pietras, K.; Ostman, A. *Nature Reviews Cancer* **2004**, *4*, 806.

(18) Bhatt, A. N.; Mathur, R.; Farooque, A.; Verma, A.; Dwarakanath, B. S. *Indian Journal of Medical Research* **2010**, *132*, 129.

(19) Weissleder, R.; Pittet, M. J. *Nature* **2008**, *452*, 580.

(20) Aina, O. H.; Sroka, T. C.; Chen, M. L.; Lam, K. S. *Biopolymers* **2002**, *66*, 184.

(21) Shadidi, M.; Sioud, M. *Drug Resistance Updates* **2003**, *6*, 363.

(22) Thundimadathil, J. *Journal of amino acids* **2012**, *2012*, 967347.

(23) Reubi, J. C. *Endocrine Reviews* **2003**, *24*, 389.

(24) Maecke, H. R.; Fani, M. *European journal of nuclear medicine and molecular imaging* **2012**, *39*, S11.

(25) Okarvi, S. M. *Medicinal Research Reviews* **2004**, *24*, 357.

(26) Cescato, R.; Maina, T.; Nock, B.; Nikolopoulou, A.; Charalambidis, D.; Piccand, V.; Reubi, J. C. *Journal of Nuclear Medicine* **2008**, *49*, 318.

(27) Dumont, R. A.; Tamma, M.; Braun, F.; Borkowski, S.; Reubi, J. C.; Maecke, H.; Weber, W. A.; Mansi, R. *Journal of Nuclear Medicine* **2013**, *54*, 762.

(28) Hutton, B. F. *European journal of nuclear medicine and molecular imaging* **2013**.

(29) Saha, B.; Gopal *Fundamentals of Nuclear Pharmacy, 5th Edition* **2003**, *Springer-Verlag Inc., New York*.

(30) Kuhn, F. E.; Herrmann, W. A.; Jurgens, S. *Journal of Organometallic Chemistry* **2014**, *751*, 83.

(31) Morais, G. R.; Paulo, A.; Santos, I. *Organometallics* **2012**, *31*, 5693.

(32) W.H., B. *Nuclear Medicine* **1971**, *2nd Edition, McGraw-Hill*.

(33) Welsh, J. S. *The Oncologist* **2006**, *11*, 181.

(34) Carrasquillo, J. A.; Larson, S. M.; Pandit-Taskar, N. *Journal of Nuclear Medicine* **2014**, *55*, 268.

(35) Howell, R. W. *International Journal of Radiation Biology* **2008**, *84*, 959.

(36) *http://hdl.handle.net/1807/17745 (visited 16, April, 2014)*.

(37) *Royal Society of Chemistry, Radiochemical Methods Group*, *5*.

(38) Wadsak, W.; Mitterhauser, M. *European Journal of Radiology* **2010**, *73*, 461.

(39) Fass, L. *Molecular Oncology* **2008**, *2*, 115.

(40) de Barros, A. B.; Tsourkas, A.; Saboury, B.; Cardoso, V. N.; Alavi, A. *EJNMMI research* **2012**, *2*, 39.

(41) *http://biomedfrontiers.org/cancer-201310-11/ (visited 16, April, 2014)*.

(42) Hadjipanayis, C. G.; Jiang, H. B.; Roberts, D. W.; Yang, L. *Seminars in Oncology* **2011**, *38*, 109.

(43) Hellebust, A.; Richards-Kortum, R. *Nanomedicine* **2012**, *7*, 429.

(44) Herranz, M.; Ruibal, A. *Journal of oncology* **2012**, *2012*, 863747.

(45) *https://www.miltenyibiotec.com/en/products-and-services/viscover-imaging/data-gallery/optical-imaging.aspx (visited 14, April, 2014)*.

(46) http://www.cancer.gov/cancertopics/factsheet/detection/CT *(visited 14, April, 2014)*.

(47) Kinsella, J. M.; Jimenez, R. E.; Karmali, P. P.; Rush, A. M.; Kotamraju, V. R.; Gianneschi, N. C.; Ruoslahti, E.; Stupack, D.; Sailor, M. J. *Angewandte Chemie-International Edition* **2011**, *50*, 12308.

(48) Badea, C. T.; Athreya, K. K.; Espinosa, G.; Clark, D.; Ghafoori, A. P.; Li, Y. F.; Kirsch, D. G.; Johnson, G. A.; Annapragada, A.; Ghaghada, K. B. *Plos One* **2012**, *7*.

(49) Lusic, H.; Grinstaff, M. W. *Chemical Reviews* **2013**, *113*, 1641.

(50) http://www.nanoprobes.com/newsletters/ImgGold.html *(visited 14, April, 2014)*.

(51) http://www.royalmarsden.nhs.uk/cancer-information/detection-diagnosis/pages/mri-scan.aspx *(visited 14, April, 2014)*.

(52) Houssami, N.; Hayes, D. F. *Ca-a Cancer Journal for Clinicians* **2009**, *59*, 290.

(53) Kirkham, A. P. S.; Emberton, M.; Allen, C. *European Urology* **2006**, *50*, 1163.

(54) Bruening, R.; Berchtenbreiter, C.; Holzknecht, N.; Essig, M.; Wu, R. H.; Simmons, A.; Heuck, A.; Maschek, A.; Meusel, M.; Williams, S. C. R.; Cox, T.; Knopp, M. V.; Reiser, M. *American Journal of Neuroradiology* **2000**, *21*, 1603.

(55) Li, Y.; Beija, M.; Laurent, S.; vander Elst, L.; Muller, R. N.; Duong, H. T. T.; Lowe, A. B.; Davis, T. P.; Boyer, C. *Macromolecules* **2012**, *45*, 4196.

(56) Na, H. B.; Song, I. C.; Hyeon, T. *Advanced Materials* **2009**, *21*, 2133.

(57) Chen, K. J.; Wolahan, S. M.; Wang, H.; Hsu, C. H.; Chang, H. W.; Durazo, A.; Hwang, L. P.; Garcia, M. A.; Jiang, Z. K.; Wu, L.; Lin, Y. Y.; Tseng, H. R. *Biomaterials* **2011**, *32*, 2160.

(58) Schoder, H.; Larson, S. M.; Yeung, H. W. D. *Journal of Nuclear Medicine* **2004**, *45*, 72S.

(59) Mariani, G.; Bruselli, L.; Kuwert, T.; Kim, E. E.; Flotats, A.; Israel, O.; Dondi, M.; Watanabe, N. *European journal of nuclear medicine and molecular imaging* **2010**, *37*, 1959.

(60) Rosales, R. T. M. *Journal of Labelled Compounds and Radiopharmaceuticals* **2014**, *doi: 10.1002/jlcr.3154*.

(61) Pichler, B. J.; Kolb, A.; Nagele, T.; Schlemmer, H. P. *Journal of Nuclear Medicine* **2010**, *51*, 333.

(62) Ramos-Font, C.; Gomez-Rio, M.; Rodriguez-Fernandez, A.; Jimenez-Heffernan, A.; Sanchez, R. S.; Llamas-Elvira, J. M. *Journal of Surgical Oncology* **2014**, *109*, 218.

(63) Lee, D. E.; Koo, H.; Sun, I. C.; Ryu, J. H.; Kim, K.; Kwon, I. C. *Chemical Society Reviews* **2012**, *41*, 2656.

(64) Toy, R.; Hayden, E.; Camann, A.; Berman, Z.; Vicente, P.; Tran, E.; Meyers, J.; Pansky, J.; Peiris, P. M.; Wu, H. P.; Exner, A.; Wilson, D.; Ghaghada, K. B.; Karathanasis, E. *Acs Nano* **2013**, *7*, 3118.

(65) Dai, Y. L.; Xiao, H. H.; Liu, J. H.; Yuan, Q. H.; Ma, P. A.; Yang, D. M.; Li, C. X.; Cheng, Z. Y.; Hou, Z. Y.; Yang, P. P.; Lin, J. *Journal of the American Chemical Society* **2013**, *135*, 18920.

(66) Lee, D. Y.; Li, K. C. P. *American Journal of Roentgenology* **2011**, *197*, 318.

(67) Del Vecchio, S.; Zanneti, A.; Fonti, R.; Pace, L.; Salvatore, M. *Quarterly Journal of Nuclear Medicine and Molecular Imaging* **2007**, *51*, 152.

(68) Funkhouser, J. *Current Drug Discovery* **2002**, *2*, 17.

(69) Svenson, S. *Molecular Pharmaceutics* **2013**, *10*, 848.

(70) Bartholoma, M. D.; Louie, A. S.; Valliant, J. F.; Zubieta, J. *Chemical Reviews* **2010**, *110*, 2903.

(71) Rosch, F. *Applied Radiation and Isotopes* **2013**, *76*, 24.

(72) *http://www.radiustech.it/prodotti_scheda.asp?l=1&c=1&p=17 (visited 14, April, 2014)*.

(73) Bernstein, L. R. *Pharmacological Reviews* **1998**, *50*, 665.

(74) Green, M. A.; Welch, M. J. *International Journal of Radiation Applications and Instrumentation* **1989**, *16*, 435.

(75) Edwards, C. L.; Hayes, R. L. *Journal of Nuclear Medicine* **1969**, *10*, 103.

(76) Amsterdam, J. A. G.; Nelemans, J. C. K.; van Eck-Smit, B. L. F.; Pauwels, E. K. J. *Annals of Hematology* **1996**, *72*, 202.

(77) Chitambar, C. R. *International Journal of Environmental Research and Public Health* **2010**, *7*.

(78) Ando, A.; Nitta, K.; Ando, I.; Sanada, S.; Katsuda, S.; Tonami, N.; Hiraki, T.; Hisada, K.; Ogawa, H. *European Journal of nuclear medicine* **1990**, *17*, 21.

(79) Chen, D. C. P.; Newman, B.; Turkall, R. M.; Tsan, M. F. *European Journal of nuclear medicine* **1982**, *7*, 536.

(80) Clausen, J.; Edeling, C. J.; Fogh, J. *Cancer Research* **1974**, *34*, 1931.

(81) Chitambar, C. R.; Zivkovic-Gilgenbach, Z. *Cancer Research* **1987**, *47*, 4468.

(82) C.R., C. *Expert Opinion on Investigational Drugs* **2004**, *13*, 531.

(83) L.R., B. *Pharmacology Reviews* **1998**, *50*, 665.

(84) Hongzhe, S.; Hongyan, L.; Sadler, P. J. *Chemical Reviews* **1999**, *99*.

(85) Price, E. W.; Orvig, C. *Chemical Society Reviews* **2013**, *43*, 260.

(86) Liu, S.; Edwards, D. S. *Bioconjugate Chemistry* **2001**, *12*, 7.

(87) Boros, E.; Ferreira, C. L.; Cawthray, J. F.; Price, E. W.; Patrick, B. O.; Wester, D. W.; Adam, M. J.; Orvig, C. *Journal of the American Chemical Society* **2010**, *132*, 15726.

(88) Notni, J.; Pohle, K.; Wester, H. J. *European journal of nuclear medicine and molecular imaging* **2012**, *2*, 28.

(89) Platas-Iglesias, C.; Blas, A. *Chemistry - A European Journal* **2004**, *10*, 3579.

(90) Afshar-Oromieh, A. *European journal of nuclear medicine and molecular imaging* **2013**, *40*, 486.

(91) Green, M. A.; Welch, M. J.; Mathias, C. J.; Fox, K. A. A.; Knabb, R. M.; Huffman, J. C. *Journal of Nuclear Medicine* **1985**, *26*, 170.

(92) Green, M. A.; Mathias, C. J.; Neumann, W. L.; Fanwick, P. E.; Janik, M.; Deutsch, E. A. *Journal of Nuclear Medicine* **1993**, *34*, 228.

(93) Hsiao, Y. M.; Mathias, C. J.; Wey, S. P.; Fanwick, P. E.; Green, M. A. *Nuclear Medicine and Biology* **2009**, *36*, 39.

(94) Cutler, C. S.; Giron, M. C.; Reichert, D. E.; Snyder, A. Z.; Herrero, P.; Anderson, C. J.; Quarless, D. A.; Koch, S. A.; Welch, M. J. *Nuclear Medicine and Biology* **1999**, *26*, 305.

(95) Hofmann, M.; Maecke, H.; Borner, R. *European Journal of nuclear medicine* **2001**, *28*, 1751.

(96) Breeman, W. A. P.; de Blois, E.; Chan, H. S.; Konijnenberg, M.; Kwekkeboom, D. J.; Krenning, E. P. *Seminars in Nuclear Medicine* **2011**, *41*, 314.

(97) Ambrosini, V.; Campana, D.; Tomassetti, P.; Grassetto, G.; Rubello, D.; Fanti, S. *European Journal of Radiology* **2011**, *80*, E116.

(98) Al-Nahhas, A.; Win, Z.; Szyszko, T.; Singh, A.; Nanni, C.; Fanti, S.; Rubello, D. *Anticancer Res.* **2007**, *27*, 4087.

(99) Froidevaux, S.; Calame-Christe, M.; Schuhmacher, J.; Tanner, H.; Saffrich, R.; Henze, M.; Eberle, A. N. *Journal of Nuclear Medicine* **2004**, *45*, 116.

(100) Schuhmacher, J.; Zhang, H.; Doll, J.; Macke, H. R.; Matys, R.; Hauser, H.; Henze, M.; Haberkorn, U.; Eisenhut, M. *Journal of Nuclear Medicine* **2005**, *46*, 691.

(101) Albanese, A.; Tang, P. S.; Chan, W. C. W. In *Annual Review of Biomedical Engineering, Vol 14*; Yarmush, M. L., Ed. 2012; Vol. 14, p 1.

(102) Cai, W.; Gao, T.; Hong, H.; Sun, J. *Nanotechnology, Science and Applications* **2008**, *1*.

(103) Buzea, C.; Pacheco, II; Robbie, K. *Biointerphases* **2007**, *2*, MR17.

(104) Roduner, E. *Chemical Society Reviews* **2006**, *35*, 583.

(105) Grainger, D. W.; Castner, D. G. *Advanced Materials* **2008**, *20*, 867.

(106) Alivisatos, A. P. *Science* **1996**, *271*, 933.

(107) Mody, V. V.; Siwale, R.; Singh, A.; Mody, H. R. *Journal of pharmacy & bioallied sciences* **2010**, *2*, 282.

(108) Faraji, A. H.; Wipf, P. *Bioorganic & Medicinal Chemistry* **2009**, *17*, 2950.

(109) Re, F.; Moresco, R.; Masserini, M. *Journal of Physics D-Applied Physics* **2012**, *45*.

(110) Loubaton, B.; Boisseau, P. *Comptes Rendus Physique* **2011**, *12*.

(111) Boulaiz, H.; Avarez, P. J.; Ramirez, A.; Marchal, J. A.; Prados, J.; Rodrígez-Serrano, F.; Péran, M.; Melguizo, C.; Aranega, A. *International Journal of Molecular Sciences* **2011**, *12*.

(112) Sahoo, S. K.; Parveen, S.; Panda, J. J. *Nanomedicine-Nanotechnology Biology and Medicine* **2007**, *3*, 20.

(113) Parveen, S.; Misra, R.; Sahoo, S. K. *Nanomedicine: Nanotechnology, Biology and Medicine* **2012**, *8*, 147.

(114) Xi, D.; Dong, S.; Meng, X. X.; Lu, Q. H.; Meng, L. J.; Ye, J. *Rsc Advances* **2012**, *2*, 12515.

(115) Popovtzer, R.; Agrawal, A.; Kotov, N. A.; Popovtzer, A.; Balter, J.; Carey, T. E.; Kopelman, R. *Nano Letters* **2008**, *8*, 4593.

(116) Sun, I. C.; Eun, D. K.; Na, J. H.; Lee, S.; Kim, I. J.; Youn, I. C.; Ko, C. Y.; Kim, H. S.; Lim, D.; Choi, K.; Messersmith, P. B.; Park, T. G.; Kim, S. Y.; Kwon, I. C.; Kim, K.; Ahn, C. H. *Chemistry-a European Journal* **2009**, *15*, 13341.

(117) Xing, H. Y.; Zheng, X. P.; Ren, Q. G.; Bu, W. B.; Ge, W. Q.; Xiao, Q. F.; Zhang, S. J.; Wei, C. Y.; Qu, H. Y.; Wang, Z.; Hua, Y. Q.; Zhou, L. P.; Peng, W. J.; Zhao, K. L.; Shi, J. L. *Scientific Reports* **2013**, *3*.

(118) Laurent, S.; Forge, D.; Port, M.; Roch, A.; Robic, C.; Elst, L. V.; Muller, R. N. *Chemical Reviews* **2010**, *110*, 2574.

(119) Hacliipanayis, C. G.; Bonder, M. J.; Balakrishanan, S.; Wang, X.; Mao, H.; Hadjipanayis, G. C. *Small* **2008**, *4*, 1925.

(120) Bu, L. H.; Xie, J.; Chen, K.; Huang, J.; Aguilar, Z. P.; Wang, A.; Sun, K. W.; Chua, M. S.; So, S.; Cheng, Z.; Eden, H. S.; Shen, B. Z.; Chen, X. Y. *Contrast Media & Molecular Imaging* **2012**, *7*, 363.

(121) Hayashi, K.; Nakamura, M.; Sakamoto, W.; Yogo, T.; Miki, H.; Ozaki, S.; Abe, M.; Matsumoto, T.; Ishimura, K. *Theranostics* **2013**, *3*, 366.

(122) Aryal, S.; Key, J.; Stigliano, C.; Ananta, J. S.; Zhong, M.; Decuzzi, P. *Biomaterials* **2013**, *34*, 7725.

(123) Rapoport, N.; Gao, Z. G.; Kennedy, A. *Journal of the National Cancer Institute* **2007**, *99*, 1095.

(124) Douma, K.; Prinzen, L.; Slaaf, D. W.; Reutelingsperger, C. P. M.; Biessen, E. A. L.; Hackeng, T. M.; Post, M. J.; van Zandvoort, M. *Small* **2009**, *5*, 544.

(125) Liu, H.; Xu, C. T.; Dumlupinar, G.; Jensen, O. B.; Andersen, P. E.; Andersson-Engels, S. *Nanoscale* **2013**, *5*, 10034.

(126) Sandiford, L.; Phinikaridou, A.; Protti, A.; Meszaros, L. K.; Cui, X. J.; Yan, Y.; Frodsham, G.; Williamson, P. A.; Gaddum, N.; Botnar, R. M.; Blower, P. J.; Green, M. A.; de Rosales, R. T. M. *Acs Nano* **2013**, *7*, 500.

(127) Madru, R.; Kjellman, P.; Olsson, F.; Wingardh, K.; Ingvar, C.; Stahlberg, F.; Olsrud, J.; Latt, J.; Fredriksson, S.; Knutsson, L.; Strand, S. E. *Journal of Nuclear Medicine* **2012**, *53*, 459.

(128) Zhang, R.; Xiong, C. Y.; Huang, M.; Zhou, M.; Huang, Q.; Wen, X. X.; Liang, D.; Li, C. *Biomaterials* **2011**, *32*, 5872.

(129) Welch, M. J.; Hawker, C. J.; Wooley, K. L. *Journal of Nuclear Medicine* **2009**, *50*, 1743.

(130) Liu, Y. J.; Welch, M. J. *Bioconjugate Chemistry* **2012**, *23*, 671.

(131) Sharma, R.; Xu, Y. W.; Kim, S. W.; Schueller, M. J.; Alexoff, D.; Smith, S. D.; Wang, W.; Schlyer, D. *Nanoscale* **2013**, *5*, 7476.

(132) Devaraj, N. K.; Keliher, E. J.; Thurber, G. M.; Nahrendorf, M.; Weissleder, R. *Bioconjugate Chemistry* **2009**, *20*, 397.

(133) Wang, E. C.; Wang, A. Z. *Integrative Biology* **2014**, *6*, 9.

(134) http://ts-1.eee.hku.hk/ccst9015sp13/p13/drug-delivery/cancer-3/ *(visited 14, April, 2014)*.

(135) Maeda, H.; Nakamura, H.; Fang, J. *Advanced Drug Delivery Reviews* **2013**, *65*, 71.

(136) Petros, R. A.; DeSimone, J. M. *Nature Reviews Drug Discovery* **2010**, *9*, 615.

(137) Saha, K.; Kim, S. T.; Yan, B.; Miranda, O. R.; Alfonso, F. S.; Shlosman, D.; Rotello, V. M. *Small* **2013**, *9*, 300.

(138) Nam, H. Y.; Kwon, S. M.; Chung, H.; Lee, S. Y.; Kwon, S. H.; Jeon, H.; Kim, Y.; Park, J. H.; Kim, J.; Her, S.; Oh, Y. K.; Kwon, I. C.; Kim, K.; Jeong, S. Y. *Journal of Controlled Release* **2009**, *135*, 259.

(139) Puckett, C. A.; Ernst, R. J.; Barton, J. K. *Dalton Transactions* **2010**, *39*, 1159.

(140) Walkey, C. D.; Olsen, J. B.; Guo, H. B.; Emili, A.; Chan, W. C. W. *Journal of the American Chemical Society* **2012**, *134*, 2139.

(141) Choi, H. S.; Liu, W.; Misra, P.; Tanaka, E.; Zimmer, J. P.; Ipe, B. I.; Bawendi, M. G.; Frangioni, J. V. *Nature Biotechnology* **2007**, *25*, 1165.

(142) Longmire, M.; Choyke, P. L.; Kobayashi, H. *Nanomedicine* **2008**, *3*, 703.

(143) Thorek, D. L. J.; Tsourkas, A. *Biomaterials* **2008**, *29*, 3583.

(144) Jokerst, J. V.; Lobovkina, T.; Zare, R. N.; Gambhir, S. S. *Nanomedicine* **2011**, *6*, 715.

(145) Ting, G.; Chang, C.-H.; Wang, H.-E.; Lee, T.-W. *Journal of Biomedicine and Biotechnology* **2010**, *vol. 2010, ID 953537*.

(146) Chanda, N.; Kattumuri, V.; Shukla, R.; Zambre, A.; Katti, K.; Upendran, A.; Kulkarni, R. R.; Kan, P.; Fent, G. M.; Casteel, S. W.; Smith, C. J.; Boote, E.; Robertson, J. D.; Cutler, C.; Lever, J. R.; Katti, K. V.; Kannan, R. *Proceedings of the National Academy of Sciences of the United States of America* **2010**, *107*, 8760.

(147) Rotello, V. M.; Ghosh, P.; Han, G.; De, M.; Kim, C. K. *Advanced Drug Delivery Reviews* **2008**, *60*, 1307.

(148) Freestone, I.; Meeks, N.; Sax, M.; Higgitt, C. *Gold Bulletin* **2007**, *40*, 270.

(149) Astruc, D.; Daniel, M.-C. *Chemical Reviews* **2004**, *104*.

(150) Turkavich, J.; Stevenson, P. C.; Hillier, J. *Discussions on the Faraday Society* **1951**, *11*, 55.

(151) Ross, R. D.; Roeder, R. K. *Journal of Biomedical Materials Research Part A* **2011**, *99A*, 58.

(152) Chen, S. W. *Langmuir* **1999**, *15*, 7551.

(153) Chen, S. W.; Murray, R. W. *Langmuir* **1999**, *15*, 682.

(154) Drezek, R.; Loo, C.; Lowery, A.; Halas, N.; West, J. *Nano Letters* **2005**, *5*, 709.

(155) Cheng, J.-X.; Wei, A.; Tong, L.; Zhao, Y.; Huff, T. B.; Hansen, M. N. *Advanced Materials* **2007**, *19*, 3136.

(156) El-Sayed, M. A.; Huang, X.; Jain, P. K.; El-Sayed, I. H. *Photochemistry and Photobiology* **2006**, *82*, 413.

(157) West, L.; Hirsch, L. R.; Serchen, S. R. *Proceedings of the National Academy of Sciences* **2003**, *100*, 13549.

(158) Visaria, R.; Griffin, R. J.; Williams, B. W. *Molecular Cancer Therapeutics* **2006**, *5*, 1014.

(159) *http://www.cytimmune.com/go.cfm?do=page.view&pid=26 (visited 16, April, 2014)*.

(160) Wang, J. *Journal of American Chemical Society Nano* **2011**, *5*, 3679.

(161) Sha, M. Y.; Xu, H.; Penn, S. G.; Cromer, R. *Nanomedicine* **2007**, *2*, 725.

(162) Huang, X.; El-Sayed, I. H.; Qian, W. *Nano Letters* **2007**, *7*, 1591.

(163) Laurent, G.; Felidj, N.; Truong, S. L. *Nano Letters* **2005**, *5*, 253.

(164) Adair, J. H.; Altinoglu, E. I. *Nanomedicine and Nanobiology* **2010**, *2*, 461.

(165) Morales-Avila, E.; Ferro-Flores, G.; Ocampo-García, B. E.; Ramírez, F. M. *InTech, Molecular Imaging, Prof. Bernhard Schaller (Ed.)* **2012**, *ISBN: 978-953-51-0359-2*.

(166) Harrington, K. J.; Mohammadtaghi, S.; Uster, P. S. *Clinical Cancer Research* **2001**, *7*, 243.

(167) Proffitt, R. T.; Williams, L. E.; Presant, C. A.; Tin, G. W.; Uliana, J. A.; Gamble, R. C.; Baldeschwieler, J. D. *Journal of Nuclear Medicine* **1983**, *24*, 45.

(168) Elbayoumi, T. A.; Torchilin, V. P. *European journal of nuclear medicine and molecular imaging* **2006**, *33*, 1196.

(169) Medina, O. P.; Kairemo, K.; Valtanen, H.; Kangasniemi, A.; Kaukinen, S.; Ahonen, I.; Permi, P.; Annila, A.; Sneck, M.; Holopainen, J. M.; Karonen, S. L.; Kinnunen, P. K. J.; Koivunen, E. *Anticancer Res.* **2005**, *25*, 33.

(170) Dagar, S.; Krishnadas, A.; Rubinstein, I.; Blend, M. J.; Onyuksel, H. *Journal of Controlled Release* **2003**, *91*, 123.

(171) Ogihara, I.; Kojima, S.; Jay, M. *Journal of Nuclear Medicine* **1986**, *27*, 1300.

(172) Petersen, A. L.; Binderup, T.; Rasmussen, P.; Henriksen, J. R.; Elema, D. R.; Kjaer, A.; Andresen, T. L. *Biomaterials* **2011**, *32*, 2334.

(173) Petersen, A. L.; Binderup, T.; Jolck, R. I.; Rasmussen, P.; Henriksen, J. R.; Pfeifer, A. K.; Kjaer, A.; Andresen, T. L. *Journal of Controlled Release* **2012**, *160*, 254.

(174) Kondo, M.; Asai, T.; Katanasaka, Y.; Sadzuka, Y.; Tsukada, H.; Ogino, K.; Taki, T.; Baba, K.; Oku, N. *International Journal of Cancer* **2004**, *108*, 301.

(175) Maeda, N.; Miyazawa, S.; Shimizu, K.; Asai, T.; Yonezawa, S.; Kitazawa, S.; Namba, Y.; Tsukada, H.; Oku, N. *Biological & Pharmaceutical Bulletin* **2006**, *29*, 1936.

(176) Lee, H. Y.; Li, Z.; Chen, K.; Hsu, A. R.; Xu, C.; Xie, J.; Sun, S.; Chen, X. *Journal of Nuclear Medicine* **2008**, *49*, 1371.

(177) Cai, W.; Chen, K.; Li, Z.-B.; Gambhir, S. S.; Chen, X. *Journal of Nuclear Medicine* **2007**, *48*, 1862.

(178) Chen, K.; Li, Z. B.; Wang, H.; Cai, W. B.; Chen, X. Y. *European journal of nuclear medicine and molecular imaging* **2008**, *35*, 2235.

(179) Duconge, F.; Pons, T.; Pestourie, C.; Herin, L.; Theze, B.; Gombert, K.; Mahler, B.; Hinnen, F.; Kuhnast, B.; Dolle, F.; Dubertret, B.; Tavitian, B. *Bioconjugate Chemistry* **2008**, *19*, 1921.

(180) McDevitt, M. R.; Chattopadhyay, D.; Kappel, B. J.; Jaggi, J. S.; Schiffman, S. R.; Antczak, C.; Njardarson, J. T.; Brentjens, R.; Scheinberg, D. A. *Journal of Nuclear Medicine* **2007**, *48*, 1180.

(181) Morales-Avila, E.; Ferro-Flores, G. *Bioconjugate Chemistry* **2011**, *22*, 913.

(182) Mendoza-Sanchez, A. N.; Ferro-Flores, G.; Ocampo-Garcia, B. E.; Morales-Avila, E.; Ramirez, F. D.; De Leon-Rodriguez, L. M.; Santos-Cuevas, C. L.; Medina, L. A.; Rojas-Calderon, E. L.; Camacho-Lopez, M. A. *Journal of Biomedical Nanotechnology* **2010**, *6*, 375.

(183) Alric, C.; Miladi, I.; Kryza, D.; Taleb, J.; Lux, F.; Bazzi, R.; Billotey, C.; Janier, M.; Perriat, P.; Roux, S.; Tillement, O. *Nanoscale* **2013**, *5*, 5930.

(184) Li, H. Y.; Diaz, L.; Lee, D. E.; Cui, L.; Liang, X.; Cheng, Y. *Molecular Imaging* **2013**, DOI 10.1007/s11547.

(185) Melancon, M. P.; Lu, W.; Yang, Z.; Zhang, R.; Cheng, Z.; Elliot, A. M.; Stafford, J.; Olson, T.; Zhang, J. Z.; Li, C. *Molecular Cancer Therapeutics* **2008**, *7*, 1730.

(186) Krishnan, S. *International Journal of Nanomedicine* **2011**, *6*, 259.

(187) Shao, X.; Zhang, H. A.; Rajian, J. R.; Chamberland, D. L.; Sherman, P. S.; Quesada, C. A.; Koch, A. E.; Kotov, N. A.; Wang, X. D. *Acs Nano* **2011**, *5*, 8967.

(188) Kang, K. W.; Nam, J. M. *Small* **2011**, *14*, 2052.

(189) Ferro-Flores, G. *Journal of Labelled Compounds and Radiopharmaceuticals* **2013**, *56*, 663.

(190) Frigell, J.; Garcia, I.; Gomez-Vallejo, V.; Llop, J.; Penades, S. *Journal of the American Chemical Society* **2014**, *136*, 449.

(191) Jensen, R. T.; Battey, J. F.; Spindel, E. R.; Benya, R. V. *Pharmacological Reviews* **2008**, *60*, 1.

(192) Pansky, A.; De Weerth, A.; Fasler-Kan, E.; Boulay, J. L.; Schulz, M.; Ketterer, S.; Selck, C.; Beglinger, C.; Von Schrenck, T.; Hildebrand, P. *Journal of the American Society of Nephrology* **2000**, *11*, 1409.

(193) Grider, J. R. *American Journal of Physiology-Gastrointestinal and Liver Physiology* **2004**, *287*, G1109.

(194) Hoffman, T. J.; Gali, H.; Smith, C. J.; Sieckman, G. L.; Hayes, D. L.; Owen, N. K.; Volkert, W. A. *Journal of Nuclear Medicine* **2003**, *44*, 823.

(195) Okarvi, S. M. *Cancer Treatment Reviews* **2008**, *34*, 13.

(196) Hoffman, T. J.; Quinn, T. P.; Volkert, W. A. *Nuclear Medicine and Biology* **2001**, *28*, 527.

(197) de Barros, A. L. B.; Mota, L. D.; Ferreira, C. D.; de Oliveira, M. C.; de Goes, A. M.; Cardoso, V. N. *Bioorganic & Medicinal Chemistry Letters* **2010**, *20*, 6182.

(198) Esteves, T.; Marques, F.; Paulo, A.; Rino, J.; Nanda, P.; Smith, C. J.; Santos, I. *Journal of Biological Inorganic Chemistry* **2011**, *16*, 1141.

(199) de Visser, M.; Bernard, H. F.; Erion, J. L.; Schmidt, M. A.; Srinivasan, A.; Waser, B.; Reubi, J. C.; Krenning, E. P.; de Jong, M. *European journal of nuclear medicine and molecular imaging* **2007**, *34*, 1228.

(200) Lears, K. A.; Ferdani, R.; Liang, K. X.; Zheleznyak, A.; Andrews, R.; Sherman, C. D.; Achilefu, S.; Anderson, C. J.; Rogers, B. E. *Journal of Nuclear Medicine* **2011**, *52*, 470.

(201) Zhang, X. Z.; Cai, W. B.; Cao, F.; Schreibmann, E.; Wu, Y.; Wu, J. C.; Xing, L.; Chen, X. Y. *Journal of Nuclear Medicine* **2006**, *47*, 492.

(202) Koumarianou, E.; Mikolajczak, R.; Pawlak, D.; Zikos, X.; Bouziotis, P.; Garnuszek, P.; Karczmarczyk, U.; Maurin, M.; Archimandritis, S. C. *Nuclear Medicine and Biology* **2009**, *36*, 591.

(203) Martin, A. L.; Hickey, J. L.; Ablack, A. L.; Lewis, J. D.; Luyt, L. G.; Gillies, E. R. *Journal of Nanoparticle Research* **2010**, *12*, 1599.

(204) Accardo, A.; Salsano, G.; Morisco, A.; Aurilio, M.; Parisi, A.; Maione, F.; Cicala, C.; Tesauro, D.; Aloj, L.; De Rosa, G.; Morelli, G. *International Journal of Nanomedicine* **2012**, *7*, 2007.

(205) Lee, C. M.; Jeong, H. J.; Cheong, S. J.; Kim, E. M.; Kim, D. W.; Lim, S. T.; Sohn, M. H. *Pharmaceutical Research* **2010**, *27*, 712.

(206) Chanda, N.; Shukla, R.; Katti, K. V.; Kannan, R. *Nano Letters* **2009**, *9*, 1798.

(207) Alric, C.; Taleb, J.; Le Duc, G.; Mandon, C.; Billotey, C.; Le Meur-Herland, A.; Brochard, T.; Vocanson, F.; Janier, M.; Perriat, P.; Roux, S.; Tillement, O. *Journal of the American Chemical Society* **2008**, *130*, 5908.

(208) Debouttiere, P. J.; Roux, S.; Vocanson, F.; Billotey, C.; Beuf, O.; Favre-Reguillon, A.; Lin, Y.; Pellet-Rostaing, S.; Lamartine, R.; Perriat, P.; Tillement, O. *Advanced Functional Materials* **2006**, *16*, 2330.

(209) *http://www.nanosight.com/technology/nanoparticle-tracking-analysis-nta (visited 14, April, 2014)*.

(210) Eccles, J. W. L.; Bangert, U.; Bromfield, M.; Christian, P.; Harvey, A. J.; Thomas, P. In *Electron Microscopy and Analysis Group Conference 2009*; Baker, R. T., Ed. 2010; Vol. 241.

(211) Chen, S. H.; Kimura, K. *Langmuir* **1999**, *15*, 1075.

(212) *http://50.87.149.212/sites/default/files/nanoComposix%20Guidelines%20for%20TEM%20Analysis.pdf (Visited 02, June, 2014)*.

(213) *http://nanocomposix.com/sites/default/files/handbooks/introduction.pdf*.

(214) *http://nanocomposix.com/sites/default/files/nanoComposix%20Guidelines%20for%20Zeta %20Potential%20Analysis%20of%20Nanoparticles.pdf (visited 14, April, 2014)*.

(215) *http://micron.ucr.edu/public/manuals/EDS-intro.pdf (visited 14, April, 2014)*.

(216) *http://www.kayelaby.npl.co.uk/atomic_and_nuclear_physics/4_2/4_2_1.html (visited 13, June, 2014)*.

(217) Nukala, H. *Quantitative Thickness Mapping in High-Angle Annular Dark-Field (HAADF) Scanning Transmission Electron Microscopy, University of Central Florida* **2004**.

(218) Egerton, R. F. *Reports on Progress in Physics* **2009**, *72*.

(219) *http://www.casaxps.com/help_manual/manual_updates/xps_spectra.pdf (visited 14, April, 2014)*.

(220) *NIST X-ray Photoelectron Spectroscopy Database, Version 4.1 (National Institute of Standards and Technology, Gaithersburg, 2012); http://srdata.nist.gov/xps/ (visited 14, April, 2014)*.

(221) Rogers, B. E.; Bigott, H. M.; McCarthy, D. W.; Della Manna, D.; Kim, J.; Sharp, T. L.; Welch, M. J. *Bioconjugate Chemistry* **2003**, *14*, 756.

(222) Montet, X.; Weissleder, R.; Josephson, L. *Bioconjugate Chemistry* **2006**, *17*, 905.

(223) Bockman, R. S.; Boskey, A. L.; Blumenthal, N. C.; Alcock, N. W.; Warrell, R. P. *Calcified Tissue International* **1986**, *39*, 376.

(224) Gronbeck, H.; Curioni, A.; Andreoni, W. *Journal of the American Chemical Society* **2000**, *122*, 3839.

(225) Lindner, S.; Michler, C.; Wangler, B.; Bartenstein, P.; Fischer, G.; Schirrmacher, R.; Wangler, C. *Bioconjugate Chemistry* **2014**, *25*, 489.

(226) Suresh, D.; Zambre, A.; Chanda, N.; Hoffman, T. J.; Smith, C. J.; Robertson, J. D.; Kannan, R. *Bioconjugate Chemistry* **2014**.

(227) Pedersen, M. W.; Meltorn, M.; Damstrup, L.; Poulsen, H. S. *Annals of Oncology* **2001**, *12*, 745.

(228) Harari, P. M. *Endocrine-Related Cancer* **2004**, *11*, 689.

(229) Mendelsohn, J.; Baselga, J. *Oncogene* **2000**, *19*, 6550.

(230) Li, Z. H.; Zhao, R. J.; Wu, X. H.; Sun, Y.; Yao, M.; Li, J. J.; Xu, Y. H.; Gu, J. R. *Faseb Journal* **2005**, *19*, 1978.

(231) Abourbeh, G.; Shir, A.; Mishani, E.; Ogris, M.; Rodl, W.; Wagner, E.; Levitzki, A. *Iubmb Life* **2012**, *64*, 324.

(232) Shetty, D.; Jeong, J.-M.; Shim, H. *International journal of molecular imaging* **2012**, *2012*, 817682.

(233) Dissoki, S.; Hagooly, A.; Elmachily, S.; Mishani, E. *Journal of Labelled Compounds & Radiopharmaceuticals* **2011**, *54*, 693.

(234) Cheng, L.; Huang, F. Z.; Cheng, L. F.; Zhu, Y. Q.; Hu, Q.; Li, L.; Wei, L.; Chen, D. W. *International Journal of Nanomedicine* **2014**, *9*, 921.

(235) *https://mospace.umsystem.edu/xmlui/bitstream/handle/10355/9779/RelativeStudyAntiEFGR%5babstract%5d.pdf?sequence=1 (visited 01 May 2014)*.

(236) Amendola, V.; Meneghetti, M. *Journal of Physical Chemistry C* **2009**, *113*, 4277.

(237) Kawamoto, T.; Sato, J. D.; Le, A.; Polikoff, J.; Sato, G. H.; Mendelsohn, J. *Proceedings of the National Academy of Sciences of the United States of America-Biological Sciences* **1983**, *80*, 1337.

(238) Distefano, J. F.; Cotto, C. A.; Lane, B.; Hagag, N. *Cancer Research* **1989**, *49*, 179.

(239) Song, S. X.; Liu, D.; Peng, J. L.; Sun, Y.; Li, Z. H.; Gu, J. R.; Xu, Y. H. *International Journal of Pharmaceutics* **2008**, *363*, 155.

(240) Tran, T. A.; Ekblad, T.; Orlova, A.; Sandstrom, M.; Feldwisch, J.; Wennborg, A.; Abrahmsen, L.; Tolmachev, V.; Karlstrom, A. E. *Bioconjugate Chemistry* **2008**, *19*, 2568.

(241) Zeglis, B. M.; Lewis, J. S. *Dalton Transactions* **2011**, *40*, 6168.

(242) Eder, M.; Wangler, B.; Knackmuss, S.; LeGall, F.; Little, M.; Haberkorn, U.; Mier, W.; Eisenhut, M. *European journal of nuclear medicine and molecular imaging* **2008**, *35*, 1878.

(243) Bailey, G. A.; Price, E. W.; Zeglis, B. M.; Ferreira, C. L.; Boros, E.; Lacasse, M. J.; Patrick, B. O.; Lewis, J. S.; Adam, M. J.; Orvig, C. *Inorganic Chemistry* **2012**, *51*, 12575.

(244) Berry, D. J.; Ma, Y. M.; Ballinger, J. R.; Tavare, R.; Koers, A.; Sunassee, K.; Zhou, T.; Nawaz, S.; Mullen, G. E. D.; Hider, R. C.; Blower, P. J. *Chemical Communications* **2011**, *47*, 7068.

(245) Banerjee, S. R.; Pullambhatla, M.; Foss, C. A.; Falk, A.; Byun, Y.; Nimmagadda, S.; Mease, R. C.; Pomper, M. G. *Journal of Medicinal Chemistry* **2013**, *56*, 6108.

(246) Maria, L.; Fernandes, C.; Garcia, R.; Gano, L.; Paulo, A.; Santos, I. C.; Santos, I. *Dalton Transactions* **2009**, 603.

(247) Goethals, L. R.; Santos, I.; Caveliers, V.; Paulo, A.; De Geeter, F.; Lurdes, P. G.; Fernandes, C.; Lahoutte, T. *Contrast Media & Molecular Imaging* **2011**, *6*, 178.

(248) Perez-Mayoral, E.; Soriano, E.; Cerdan, S.; Ballesteros, P. *Molecules* **2006**, *11*, 345.

(249) Silva, F.; Marques, F.; Santos, I. C.; Paulo, A.; Rodrigues, A. S.; Rueff, J.; Santos, I. *Journal of Inorganic Biochemistry* **2010**, *104*, 523.

(250) Brefuel, N.; Lepetit, C.; Shova, S.; Dahan, F.; Tuchagues, J. P. *Inorganic Chemistry* **2005**, *44*, 8916.

(251) Cooper, C. J.; Jones, M. D.; Brayshaw, S. K.; Sonnex, B.; Russell, M. L.; Mahon, M. F.; Allan, D. R. *Dalton Transactions* **2011**, *40*, 3677.

(252) Harpstrite, S. E.; Beatty, A. A.; Collins, S. D.; Oksman, A.; Goldberg, D. E.; Sharma, V. *Inorganic Chemistry* **2003**, *42*, 2294.

(253) Shakya, R.; Peng, F. Y.; Liu, J. G.; Heeg, M. J.; Verani, C. N. *Inorganic Chemistry* **2006**, *45*, 6263.

(254) Beran, G.; Carty, A. J.; Patel, H. A.; Palenik, G. J. *Journal of the Chemical Society D-Chemical Communications* **1970**, 223.

(255) Sinclair, I.; Small, R. W. H.; Worrall, I. J. *Acta Crystallographica Section B-Structural Science* **1981**, *37*, 1290.

(256) Marion, R.; Saleh, N. M.; Le Poul, N.; Floner, D.; Lavastre, O.; Geneste, F. *New Journal of Chemistry* **2012**, *36*, 1828.

(257) Troutner, D. E.; Volkert, W. A.; Hoffman, T. J.; Holmes, R. A. *International Journal of Applied Radiation and Isotopes* **1984**, *35*, 467.

(258) Zambre, A.; Silva, F.; Upendran, A.; Afrasiabi, Z.; Xin, Y.; Paulo, A.; Kannan, R. *Chemical Communications* **2014**, *50*, 3281.

(259) Perrin, D. D.; Armarego, W. L. F. *Purification of Laboratory Chemicals. 3th Edition, Pergamon Press, Oxford* **1988**.

(260) Sheldrick, G. M. *SADABS, Bruker AXS., Madison, Wisoncisn, USA* **2004**.

(261) Bruker *SMART and SAINT, Bruker AXS Inc., Madison, Winsconsin, USA* **2004**.

(262) Altomare, A.; Burla, M. C.; Camalli, M.; Cascarano, G. L.; Giacovazzo, C.; Guagliardi, A.; Moliterni, A. G. G.; Polidori, G.; Spagna, R. *Journal of Applied Crystallography* **1999**, *32*, 115.

(263) Sheldrick, G. M. *SHELXL97, Program for Crystal Structure Refinement, University of Goettingen, Germany* **1997**.

(264) Farrugia, L. J. *Journal of Applied Crystallography* **1999**.

(265) Macrae, C. F.; Edgington, P. R.; McCabe, P.; Pidcock, E.; Shields, G. P.; Taylor, R.; Towler, M.; van De Streek, J. *Journal of Applied Crystallography* **2006**, *39*, 453.

(266) Mougenot, P.; Mertens, P.; Nguyen, M.; Touillaux, R.; MarchandBrynaert, J. *Journal of Organic Chemistry* **1996**, *61*, 408.

(267) Duimstra, J. A.; Femia, F. J.; Meade, T. J. *Journal of the American Chemical Society* **2005**, *127*, 12847.

(268) Mishra, A.; Pfeuffer, J.; Mishra, R.; Engelmann, J.; Mishra, A. K.; Ugurbil, K.; Logothetis, N. K. *Bioconjugate Chemistry* **2006**, *17*, 773.

(269) Lane, S. R.; Veerendra, B.; Rold, T. L.; Sieckman, G. L.; Hoffman, T. J.; Jurisson, S. S.; Smith, C. J. *Nuclear Medicine and Biology* **2008**, *35*, 263.

(270) Scasnar, V.; Vanlier, J. E. *European Journal of nuclear medicine* **1993**, *20*, 273.

Annexes

Multidimensional NMR Spectra

A1: COSY spectrum of **TDOTA** in D_2O.

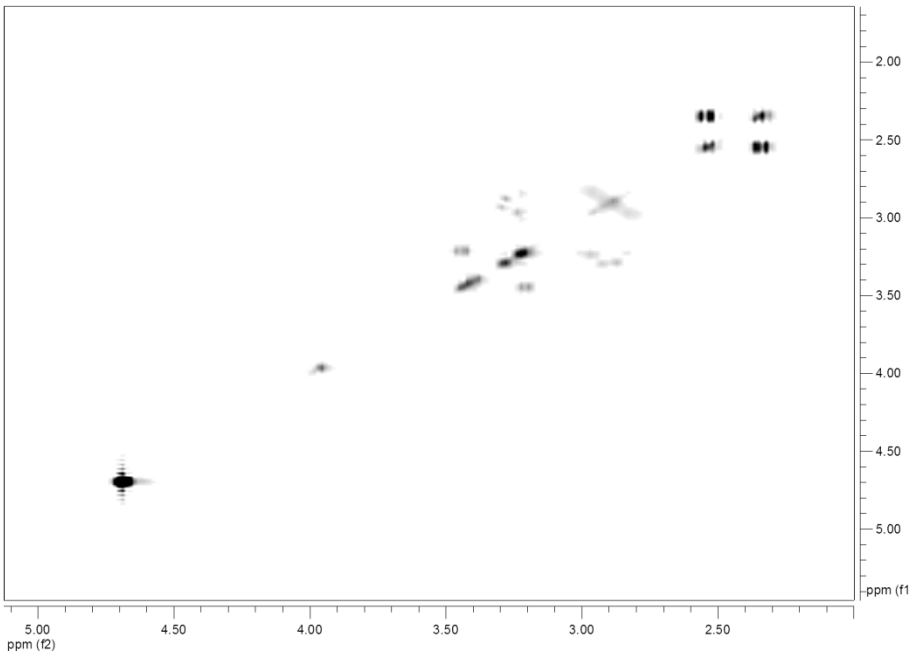

A2: HSQC spectrum of **TDOTA** in D_2O.

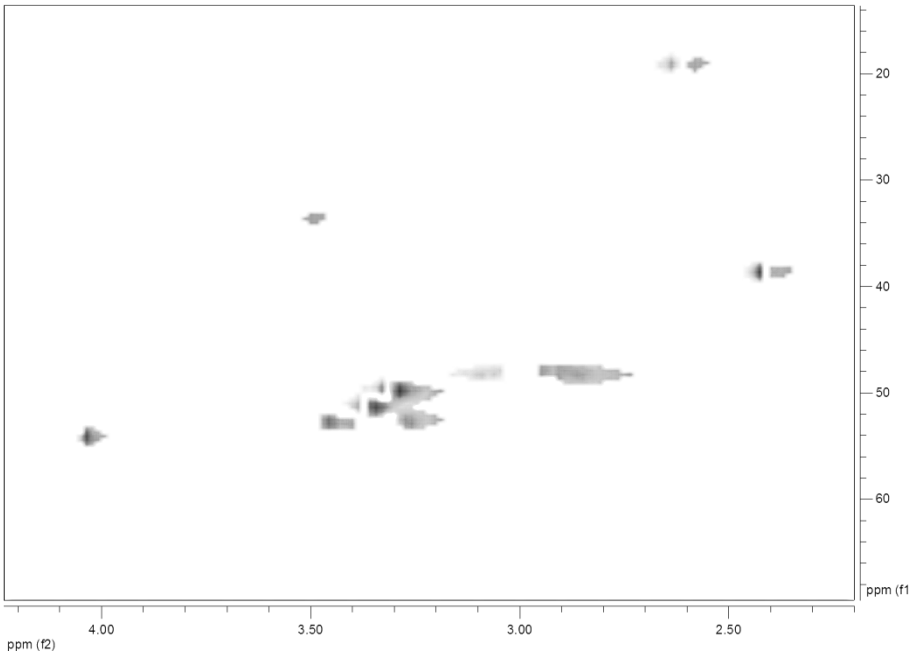

A3: COSY spectrum of **GaL^{1,OMe}** in CD_3CN.

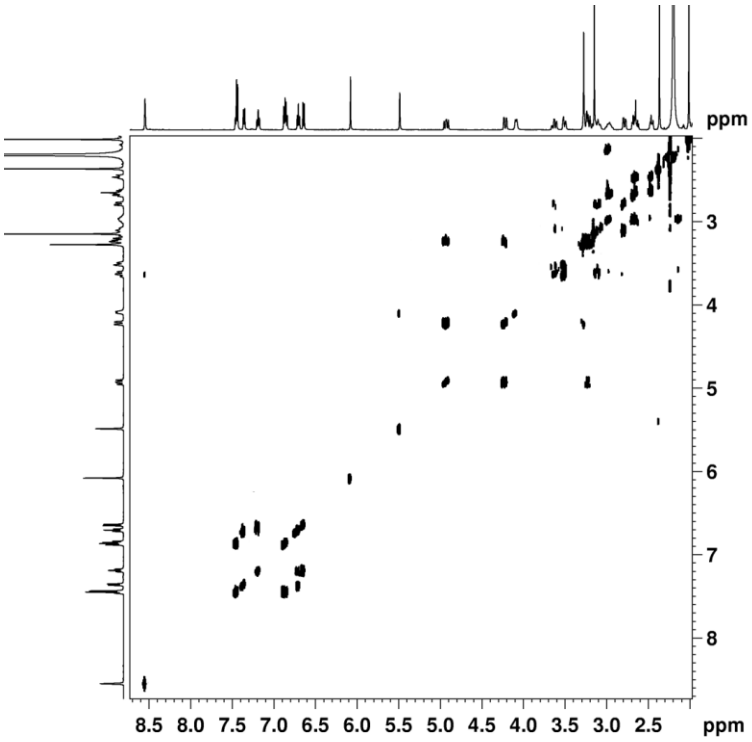

A4: HSQC spectrum of aliphatic carbons of **GaL^{1,OMe}** in CD_3CN.

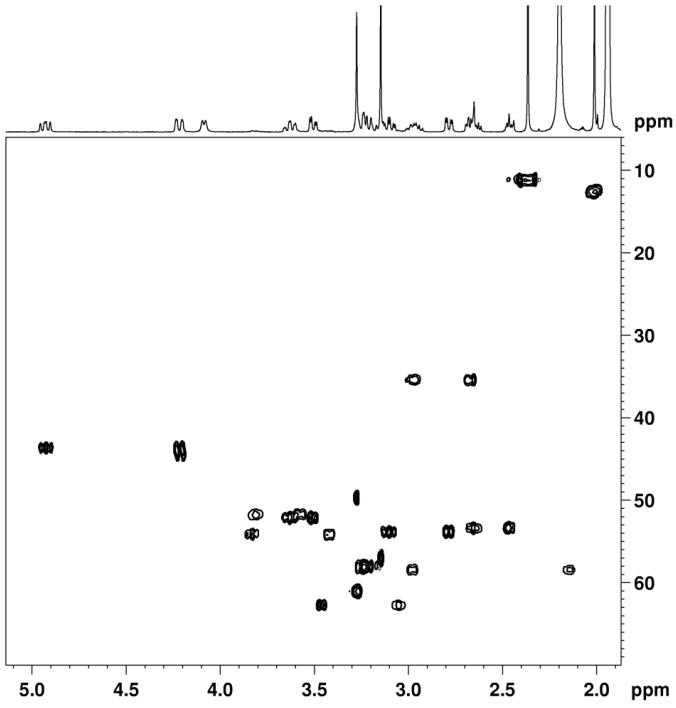

A5: COSY spectrum of **GaL^{2}** in CD_3CN.

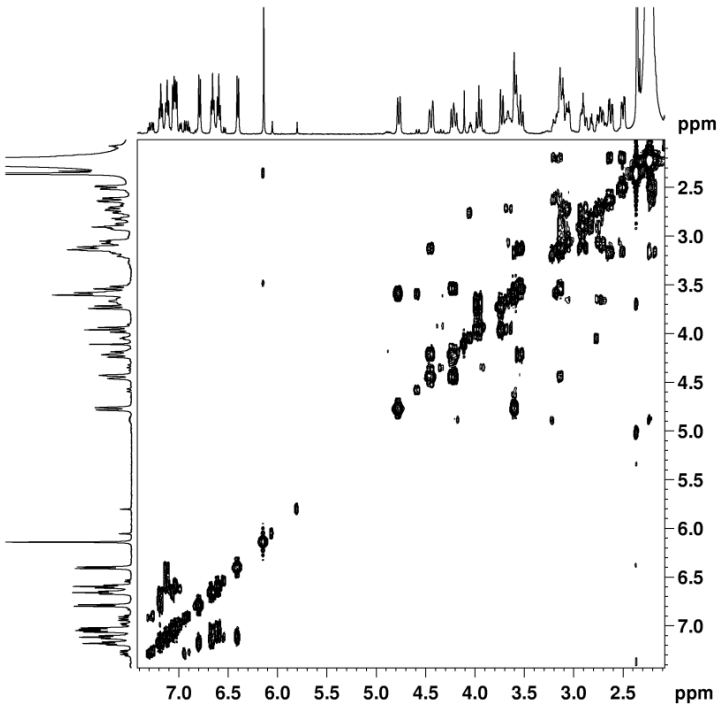

A6: HSQC spectrum of **GaL^2** in CD_3CN.

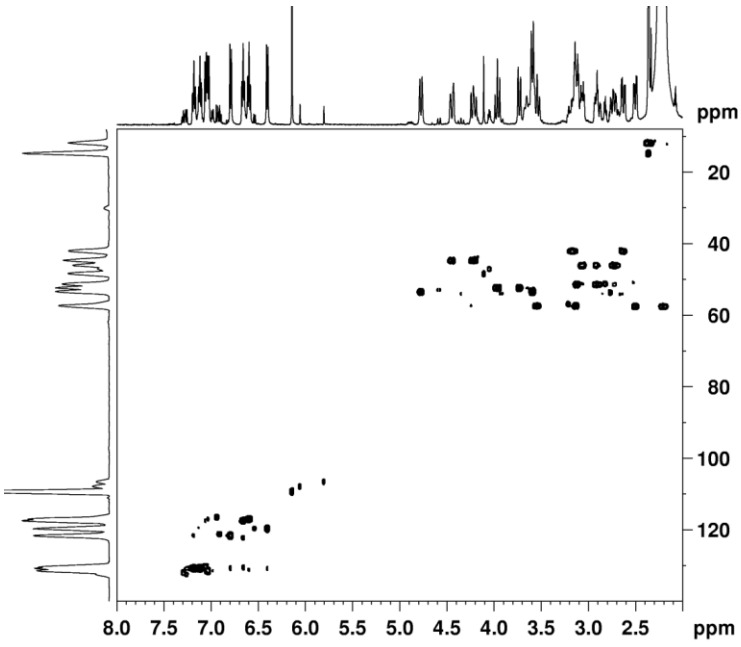

A7: COSY spectrum of the methylenic protons of **GaL^4** in CD_3CN.

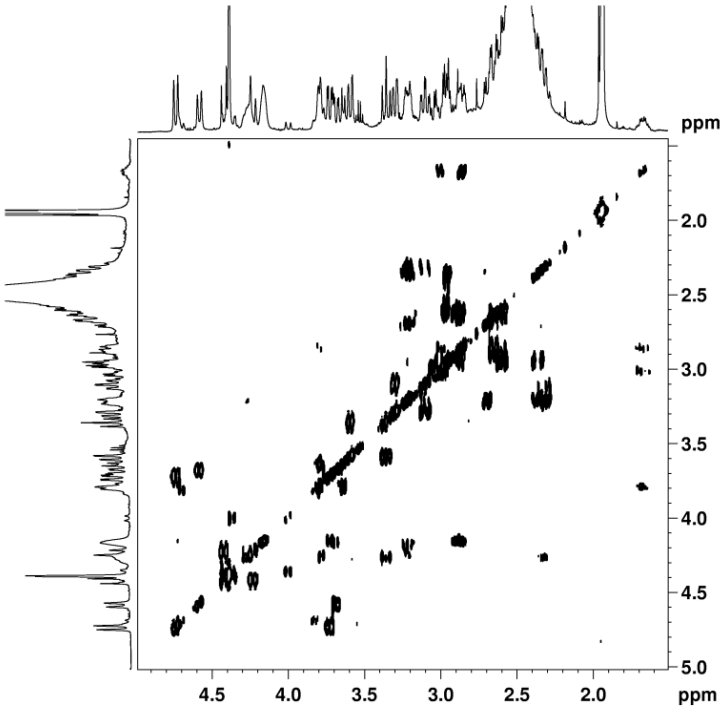

A8: TOCSY spectrum of the methylenic protons of **GaL**^{4} in CD_3CN.

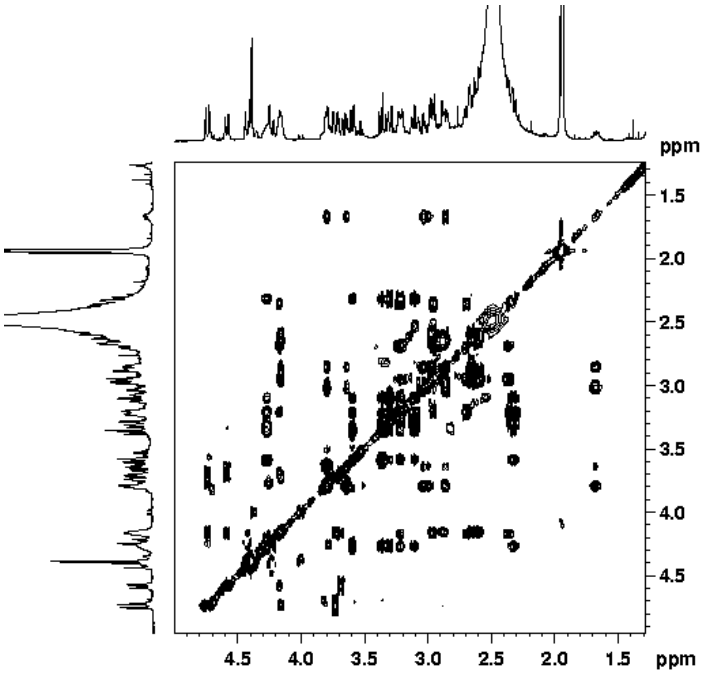

A9: HSQC spectrum of the methylenic protons of **GaL**^{4} in CD_3CN.

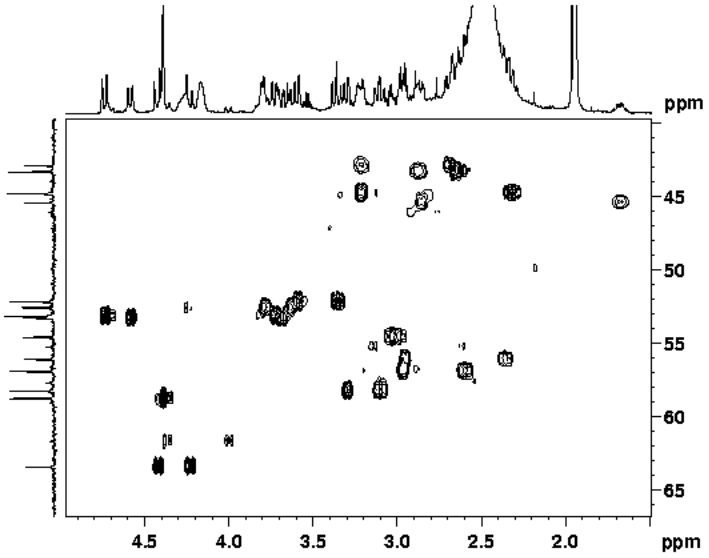

A10: COSY spectrum of **GaL^4** in D_2O.

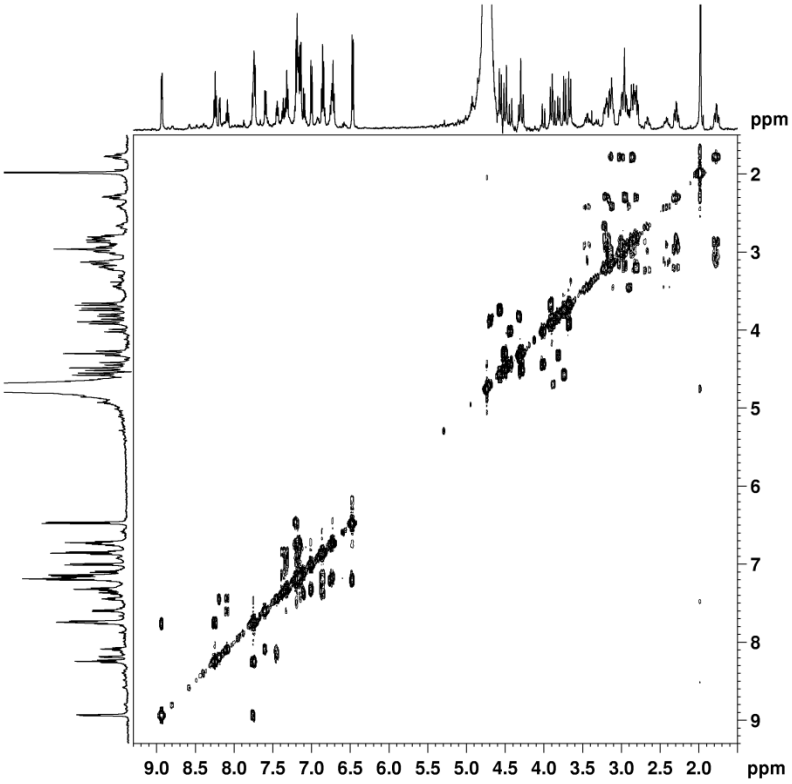

A11: TOCSY spectrum of the methylenic protons of **GaL^4** in D_2O.

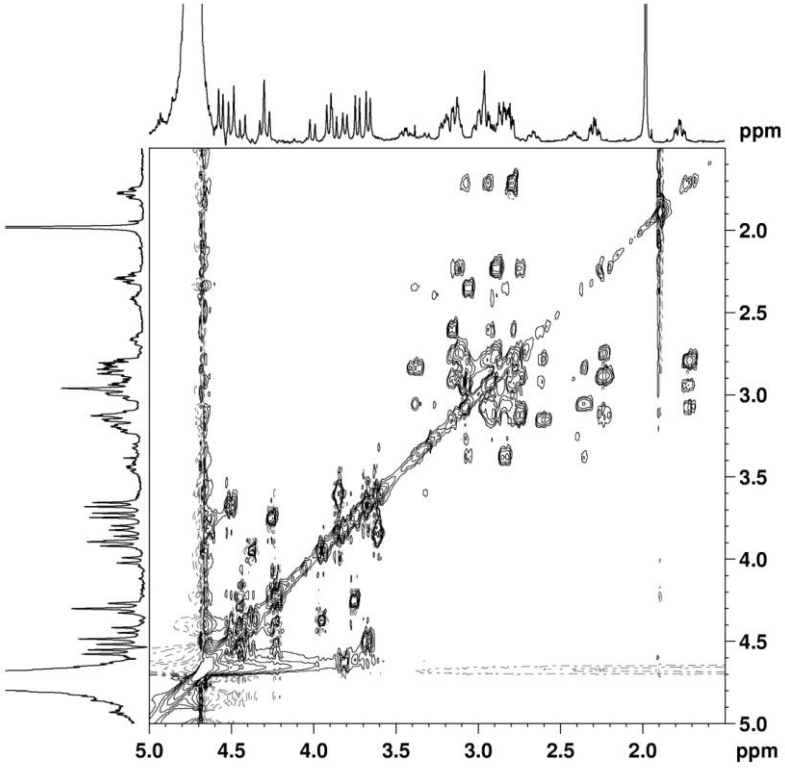

A12: HSQC spectrum of the methylenic protons of **GaL^4** in D_2O.

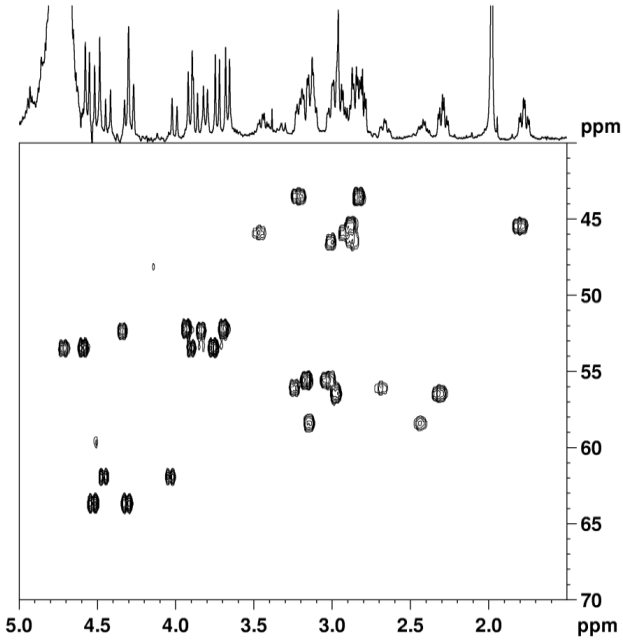

X-ray Diffraction Data

A13: Crystallographic details for the Gallium Complexes

	[GaL^{1,OMe}](ClO$_4$).(MeOH)	**[GaL^2](ClO$_4$).(**MeOH)	[**GaL^2](ClO$_4$).(**CHCl$_3$)	**[GaL^4](ClO$_4$).(**MeOH)
empirical form.	$C_{27}H_{37}N_5O_8ClGa$	$C_{26}H_{37}N_5O_7ClGa$	$C_{26}H_{34}N_5O_6Cl_4Ga$	$C_{24}H_{28}N_4O_6ClGa$
f_w	664.79	636.78	724.10	573.67
temp. (K)	150(2)	150(2)	150(2)	150(2)
cryst. system	triclinic	monoclinic	monoclinic	monoclinic
space group	P-1	P21/c	P21/c	P21/n
a (Å)	8.3515(2)	7.9018(3)	14.2384(5)	22.5793(5)
b (Å)	9.8243(3)	11.6269(4)	12.5399(4)	10.5056(2)
c (Å)	18.2097(5)	30.2610(11)	17. 0528(6)	23.2529(4)
α (deg)	78.347(1)	90	90	90
β (deg)	80.943(1)	91.358(1)	98.761(1)	117.545(1
γ (deg)	86.333(2)	90	90	90
V (Å^3)	1444.23(7)	2779.40(17)	3009.22(18)	4890.57(18)
Z, D_{calcd} (Mg/m^3)	2,1.529	4,1.522	4,1.598	8,1.558
μ (mm^{-1})	1.104	1.141	1.319	1.283
F(000)	692	1328	1488	2368
θ range (deg)	3.12-25.03	2.67-25.34	2.59-25.35	3.25-25.68
h,k,l range	-9/9,-11/11,-21/20	-9/9,-13/14,-36/30	-16/17,-15/11,-20/20	-27/19,-12/12,-24/28
reflns col./uniq.	15192/5017 [Rint=0.0634]	13307/5077 [Rint=0.0440]	21810/5497 [Rint=0.0552]	72909/9277 [Rint=0.0444]
T max./min.	0.9676/0.8095	0.8945 /0.7714	0.9018 /0.7601	0.8210 /0.6551
S on F^2	0.973	1.072	1.070	1.046
R1 (I > 2σ(I))	0.0437	0.0395	0.0432	0.0252
wR2 (all data)	0.1121	0.0942	0.1027	0.0609

[a]Definitions: $R1 = \sum||F_o| - |F_c||/\sum|F_o|$, $wR2 = [\sum w(F_o^2 - F_c^2)^2/\sum w(F_o^2)^2]^{1/2}$